The Impact of SSC on High-Latitude HF Communications.

A Thesis

Submitted for the Degree of

Doctor of Philosophy

in the

Department of Communications Systems

Lancaster University

Lancaster, UK

By

Samuel Esteban Ritchie

N.Dip.Tech, N.H.Dip.Tech, M.Dip.Tech, MSc, MBA, C.Eng

MIEI

September 2009

The Impact of SSC on High-Latitude HF Communications

Submitted for the Degree of Doctor of Philosophy

June 2009

by

Samuel Esteban Ritchie N.Dip.Tech, N.H.Dip.Tech, M.Dip.Tech, MSc, MBA, C.Eng MIEI

Abstract

The typical features of high-latitude HF radio communications following the onset of a disturbed ionosphere are threefold. These features are an increase in ionospheric absorption, a reduction in operational frequencies as electron density in the reflective layers changes and variations in the expected mode of propagation.

This thesis moves to model these changes based around a methodology of determining the change that occurs during disturbed periods relative to median quiet time values – for which it is accepted that the use of current propagation prediction methods is adequate. The key to this methodology is defining the point of transition between a quiet and a disturbed ionosphere. This transition point, defined as the occurrence of a storm sudden commencement (SSC), marks the change from a quiet to a disturbed ionosphere.

The three typical features following the onset of a disturbed ionosphere are clearly demonstrated in a multi-instrument case study that examines the effect of SSC on the high-latitude ionosphere. This case study clearly shows the complex mode changes that a high-latitude HF link experiences following SSC and demonstrates the further two effects that are investigated in detail in this thesis.

Firstly, sudden commencement absorption (SCA), the absorption spike that occurs coincidently with the SSC, is statistically analysed in detail and empirically modelled based on the change in interplanetary magnetic field (IMF) strength.

Secondly, an assessment is made of the variability of the Sporadic-E layer during disturbed periods. As part of this assessment of E-layer variability, it has been possible to empirically model the change from the quiet time critical frequency through the six hours immediately following the onset of a disturbed ionosphere. In addition, the value of E-layer critical frequency that can be used to indicate the onset of a fully-blanketing E-layer has been developed.

Contents

List of Figures

List of Tables

Declaration

The research presented in this thesis is my own work and has not been submitted in substantially the same form for the award of a higher degree elsewhere. Some of the research results have led to the publication of three scientific papers in refereed journals as follows:

Ritchie, S.E., and F. Honary, Observed characteristics of sudden commencement absorption, Journal of Atmospheric and Solar-Terrestrial Physics, Vol 71, Issue 5, p 306-617, ***doi:10.1016/j.jastp.2008.11.011*** *, 2009.*

Ritchie, S.E., and F. Honary, Storm Sudden Commencement and its Effect on High-Latitude HF Communication Links, Space Weather,7, SO6005, ***doi:10.1029/2008 SW00046****, 2009.*

Ritchie, S.E., and F. Honary, Observations on the variability and screening effect of Sporadic-E, Journal of Atmospheric and Solar-Terrestrial Physics, Vol 71, Issue 12, p 1353-1364, ***doi:10.1016/j.jastp.2009.05.008,*** *2009.*

As well as the publication of the following four refereed conference posters and papers:

Honary, F., and S.E.Ritchie, Sudden Commencement Events and Implications on Radio Propagation, 2nd International Riometer Workshop. Banff, Alberta, Canada. 25th February-26th March, 2006.

S. E. Ritchie and F. Honary. Prediction of Sudden Commencement Absorption, in Loughborough Antennas and Propagation Conference. Loughborough, UK. 11th-12th April pp. 113-116, 2006.

Ritchie, S.E., and F. Honary, Case Studies of enhanced E-layer formation at high-latitudes following SCA events, The 10th International Conference on Ionospheric Radio Systems and Techniques (IRST-2006), IC517, 18-21 July, The Royal Society of Medicine, London, UK, 2006.

Ritchie, S.E., and F. Honary, Advances in Ionospheric Propagation Modelling at High-Latitudes, The 11th International Conference on Ionospheric Radio Systems and Techniques (IRST-2009), CP-549, 28 April – 1 May, Edinburgh Conference Centre, Heriot-Watt University, Scotland, UK, 2009.

Acknowledgements

The research embodied in this Thesis was undertaken as a part-time, off-campus student, over a period of six years. There are a number of people and organisations that I would like to thank for all their support in helping make this happen:

My employer, the **Commission for Communications Regulation** (ComReg) for making it possible for me to study as a self-funded student by meeting all the costs involved and especially **Jim Connolly**, Senior Spectrum Advisor to the Commission for all his encouragement.

Professor Farideh Honary for taking me on a student and guiding me through this major project over these last six years. Her insight and knowledge are much appreciated, most especially when dealing with comments received in the peer review process.

Members of the Space Plasma Environment and Radio Science (SPEARS) group at the University of Lancaster, most notably **Andrew Kavanagh** and **Andrew Senior** – I aspire to be a researcher of your calibre. Also other members of the group, both past and present, who have been friendly, accommodating and a pleasure to visit – **Jim Wild, Mike Kosch, Emma Woodfield, Steve Marple, Patrick Daum and Martin Grill.**

People who freely shared their time, knowledge, resources, data and valuable insights with me, **Ruth Bamford** (RAL), **Les Barclay** (Barclay Associates Ltd), **Alan Stocker** (University of Leicester) and **Mary McCready** (SRI).

Barry McLaughlin of Source design for advice and assistance with posters, printing and design work.

Michelle McFadden for proofreading my work.

My parents **Samuel and Teresa Ritchie**, my sister **Lydia Ritchie** and my friends who put up with me studying.

A massive extra-special acknowledgment to my wife **Lorraine** for sacrificing our together-time, keeping me balanced and supporting me without hesitation through every stage and emotion.

CHAPTER 1

Introduction

1.0 Objectives of this Chapter

The objectives of this introductory chapter are to:

1. outline the relevance of the research undertaken through considering the use of HF communications at high-latitudes by introducing the types of services using the HF bands, detailing the requirements of these services and defining the role of propagation prediction models in ensuring that these requirements are achieved;
2. detail the connection of the high-lattiude ionosphere to the Sun by showing how the high-latitude ionosphere is directly under the control of solar-based phenomena and how the effects of these phenomena are transported by the solar wind via the magnetosphere to the high-latitude ionosphere where they may have severe consequences on radio communication systems operating at these latitudes.

It is assumed that the reader has an intermediate knowledge of HF propagation, and ionospheric and magnetospheric processes; this material is not repeated, but to assist, a glossary of terms is provided.

1.1 Services in the HF bands.

This section examines the use being made of the HF radio spectrum by introducing some of the services using the HF bands and the important role these services play at high latitudes. This reflects the importance of accurate propagation prediction methods to ensure the requirements of these services are met.

Services, as used in the context of this chapter, are defined by agreement through the International Telecommunications Union (ITU). The ITU, based in Geneva, is a specialist agency of the UN with 191 Member States and more than 700 Sector Members and Associates (ITU, 2007). This membership has established the Radio Regulations, a treaty-based arrangement which governs the use of the radio-frequency spectrum and the geostationary-satellite and non-geostationary-satellite orbits. This Treaty, known as the "Radio Regulations" can only be modified by a World Radiocommunications Conference which takes place every four years. Within the Radio Regulations "Services" are clearly defined in order to group spectrum users with similar technical requirements to facilitate the establishment of sharing criteria between the same services and other services which may be co-channel or in adjacent spectrum bands.

The ***Fixed Service*** is the main user of spectrum between 4 MHz and 30 MHz and is defined as a radiocommunication service between specified fixed points. Until the early 1980's these bands were very heavily loaded with long distance links, mainly providing telephony services in support of the international public telecommunications network. The heavy loading was reduced in the 1980's as a result of the reliability and reduced cost of undersea fibre-optic cables and it became

possible to transfer some of the Fixed Service allocations to other services with pressing needs, such as the broadcasting service. There remain even today HF radio systems providing telephonic services for the public network, operating on a continuous basis. These systems commonly use single sideband or independent sideband Amplitude Modulated duplex with a reduced carrier level conveying up to four analogue channels with a bandwidth of 3.0 kHz (ITU, 1990).

The Fixed Service has in total 12.6 MHz of allocated spectrum between 4 and 30 MHz across 30 different bands as indicated in figure 1. All these allocations are on a Primary basis with 40% being shared with other co-primary services.

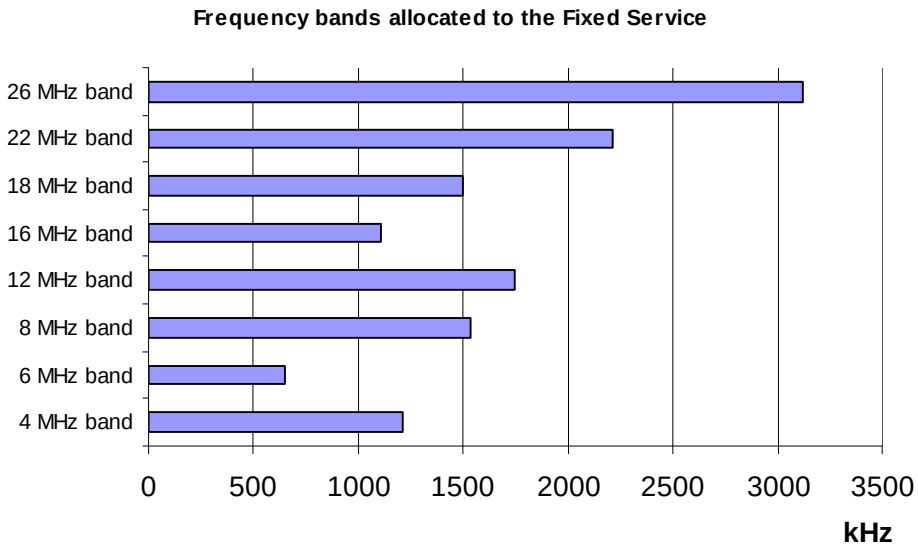

Figure 1. Amount of spectrum allocated to the Fixed Service

In central and western Europe, civilian use of the Fixed Service spectrum has decreased over the past few decades and the frequency bands are only used to a limited extend for embassy communications, a back-up system to the wired Interpol communication network with encrypted transmission of speech and data, the Red

Cross and a few other similar international networks. The traffic load on such channels varies between 300 and 700 hours per months. The majority of long distance services in Europe are used for Government communications, often military. The planning of fixed services is often considered as a subset of broadcasting planning as each service has parts of the techniques used in broadcast planning incorporated. However, the requirements for accurate predictions of ionospheric conditions in order to achieve an adequate quality of service for users remain the same.

The term ***Mobile Service*** is used to cover a number of different services, parts of which may not be mobile at all or are considered to be mobile even when not operated whilst in motion. These Mobile Services (MS) include the Maritime Mobile Service (MMS), the Aeronautical Mobile Service (AMS) and the Land Mobile Service (LMS). The usual communication mode is between a mobile station and a land station (a mobile station operated at a fixed position), but nothing prohibits communications between mobile and mobile, which does occur for instance between ships. The planning of mobile services is often considered as a subset of broadcasting planning; as each service has parts of the techniques used in broadcast planning incorporated e.g. area coverage. However, the requirements for accurate predictions of ionospheric conditions are similar.

The ***Science Service*** acquires information directly by observations of nature using sensors that function within the radio spectrum allocated to the Science Service. Passive sensors take the form of sensitive radiometers, which measure the strength of natural radiation and are by definition radars that analyse radiation returned from a target illuminated by the active sensor. A special case is the Radio Astronomy Service (RAS), which is a passive service and observes emissions of natural origin. A

relevant example is the frequency band 37 500 – 38 250 kHz. This is the prime band for the operation of Riometers: for example, the University of Lancaster Riometer at Kilpisjärvi operates at 38.2 MHz within this band. This band is allocated internationally on a primary basis to the Fixed and the Mobile services and then to the Radio Astronomy Service on a secondary basis. However, as these Riometers are usually in remote locations the sharing with services of a higher status is not normally problematic. One known exception is the HAARP Riometer operating on 30 MHz, which suffers occasional interference caused by broadcast stations (HAARP, 2008).

The ***Broadcasting Service*** is a radiocommunication service in which transmissions are intended for direct reception by the general public. The planning of many other services is recognised as a subset of the tasks that need to be undertaken for the broadcast services. This service is detailed further in this chapter's case study.

The use of the radio spectrum by the ***Military*** is an issue of National Sovereignty and as a result there has been worldwide reluctance to include these services under the ITU Rules and Regulations. During peacetime the military attempt to co-exist with civil users and maintain tight control on their spectrum usage keeping, for example, the fixed service within the designated fixed service bands and even co-ordinating operations with the broadcast and other services. However, during military operations in a time of war or limited conflict all such rules and practices are suspended. Within Europe, to ensure interoperability between NATO and its Partners, a significant amount of standardisation and agreement has taken place.

Other services not detailed further include the Amateur Service, Radiodetermination Service (which includes Radionavigation and Radiolocation Services), Meteorological Aids Service and the Standard Frequency and Time Service (ITU, 2003).

1.1.1 Services at High Latitudes.

HF remains the key to coverage outside satellite cover above 70^0 north and below 70^0 south and is often the only available media from 60^0 north and below 60^0 south as the look angle to the geostationary orbit is limiting, especially for mobile and covert type users utilising compromise antenna. HF remains the predominant media in the Baltic and southern region maritime nations, as well as providing coverage of vast areas outside Europe and North America where satellite resources are much less concentrated.

Military Land Forces need HF communications to ensure effective Consultation, Command and Control, both within NATO and with Partner Nations. In addition, HF Combat Net Radio communications are used at lower echelons as primary or secondary means where terrain, distance, or mobility requirements preclude reliance on Tactical Area Communications Systems. Within the maritime community, HF is widely fitted throughout NATO and Partner-for-Peace (PfP) nations, and is common to virtually all warships. Significant work has been done by the military forces of a number of countries to find solutions to HF propagation problems at high latitudes (e.g. Ames et al., 1970 and Trautmann, 2004).

The civilian and military Aeronautical Services make extensive use of HF at all latitudes. The increase in commercial flights across the north polar regions to connect

Asia to Europe and Europe to the USA has resulted in new HF infrastructure investments in recent years (Cabral, 2003). As high-latitude areas are increasingly populated there is a need to provide HF broadcasting and other services using the HF bands.

1.2 Requirements of HF Spectrum Users.

The international community has long recognized that the HF skywave channel is a valuable resource and has, through the ITU, developed methods that can be applied by users for optimisation of communication and broadcast performance, while limiting the potential for interference with other users. These methods represent the best the community can agree on or achieve in the prediction of ionospheric behaviour.

Different types of services have different requirements e.g. unidirectional flow of information as in the broadcasting service and either unidirectional or bi-directional flow of information as in the fixed and mobile services. Table 1 summarises the three main radio services and their requirements.

	Fixed Service	**Mobile Service**	**Broadcasting Service**
Communication Type	Point-to-point	Point-to-point and/or Point-to-area	Point-to-area
Information Flow	Bi- or Uni-directional	Bi-directional	Uni-directional
Frequency Agility	Changed as and when required		Frequency set well in advance.

	Fixed Service	Mobile Service	Broadcasting Service
Transmitter Power	Medium	Medium to low	High
Receiver Sensitivity/ Antenna gain	High/high	High/limited	Low/low
User	Technical	Technical	Non-technical
Minimum Audio Quality	Just intelligible	Just intelligible	Good

Table 1. Radio Service and User Requirements.

For these requirements to be met, long-term predictions based on estimates of expected propagation conditions are needed for radio circuit design. Ray-path launch angle and arrival angle data is essential data for optimum antenna design. Studies of the relationships between transmitter power and received signal strengths at a range of frequencies enables the necessary provisioning of transmitter plant and antenna farms. To date, relatively little effort has been applied on a worldwide scale to the optimisation of the different radio services, except in the case of HF broadcasting, and as a result the development of many services has been in a haphazard fashion. Frequency sharing is a useful means of optimising spectrum utilisation and for the reduction of unintentional interference. There is plenty of scope for further studies based on long-term predictions to determine the ideal service planning strategies (Bradley, 1996).

1.2.1 Required Signal to Noise Ratio.

The key output of planning tools based on propagation prediction is to determine the expected signal-to-noise ratio (S/N) (or carrier-to-noise ratio (C/N) for digital systems). The parameter S/N defines the transmission quality of the radio link, along with the percentage of the time a threshold of S/N is achieved at the receiving point. The minimum acceptable value is determined by the quality demands placed on the class of emission used. A reception quality in the class 'just usable' might be quite acceptable to a skilled operator, but for a subscriber to a public system, it might not be generally adequate. Table 2 is an extract from a table included in ITU-R Recommendation 339, which gives values for the signal-to-noise ratio for a few different technologies (ITU, 2006) and shows the typical wide-ranging differences in requirements.

Class of emission	Pre-detection bandwidth of receiver (Hz)	Post-detection bandwidth of receiver (Hz)	Grade of service	Audio signal-to-noise ratio (1) (dB)	RF signal-to-noise density ratio (dB)		
					Stable condition	Fading condition (4) non-diversity	Fading condition (5) dual diversity
A1 A Telegraphy 8 bauds	3000	1500	Aural reception	−4	31	38	
A1 B Telegraphy 50 bauds, printer	250	250	Commercial grade	16	40		58
A1 B Telegraphy 120 bauds, undulator	600	600		10	38		49
A2 A Telegraphy 8 bauds	3000	1500	Aural reception	−4	35	38	
A2 B Telegraphy 24 bauds	3000	1500	Commercial grade	11	50	56	

Table 2. Extract from ITU-R Recommendation 339 (2006).

1.3 Defining the Usable Field Strength.

In order to calculate the signal-to-noise or the carrier-to-noise ratio at the receiver two parameters are required; firstly the total strength of the signal arriving at the receiver and secondly the noise at the receiver. The minimum usable field strength (MUFS) is

that value of the field strength necessary to permit the desired reception quality, taking into account the specific receiving conditions, in the presence of natural noise and man-made noise but without the presence of interference from other transmitters.

The lower absolute lowest limit on the minimum usable field strength is set by the sensitivity of the receiver. The wanted usable field strength (WUFS) is then the minimum usable field strength as defined above plus sufficient power to overcome interfering signals in the area of reception. External noise enters the receiving system via the antenna together with the wanted signal and often with interference from co-channel and adjacent channel transmitters. More noise is generated by various mechanisms within the receiver. All of the noise and interference degrades the receiver performance and it is necessary to design the system so that the ratio between the power of the received carrier of the wanted signal and the total noise including an allowance for interference is high enough to achieve the performance objectives.

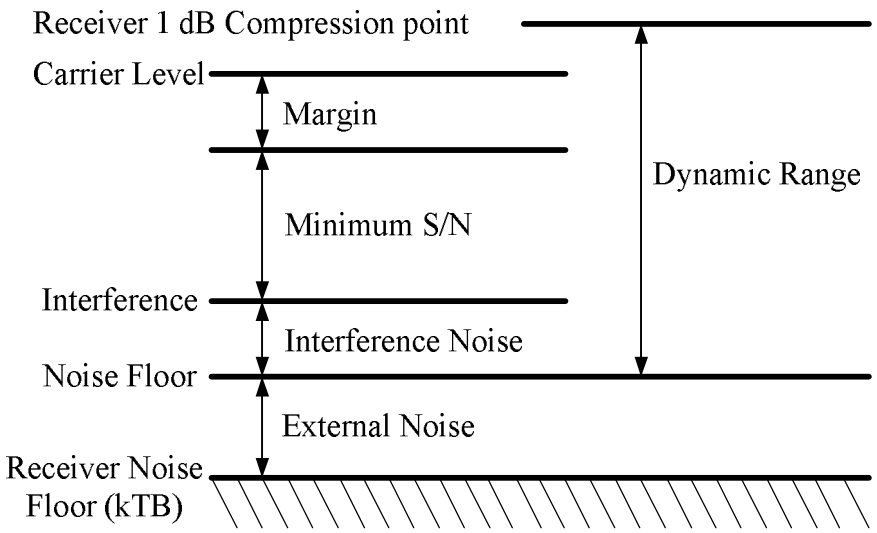

Figure 2. Defining signal levels

Figure 2 indicates the receiver noise floor, which includes the thermal noise of the system including the noise figure of the receiver. Once the external noise is added into the equation the actual noise floor to be overcome is determined. Adding the interference expected at the receiver increases the overall noise power floor. The wanted signal must be greater than the minimum S/N referenced to the interference noise floor which includes the contribution from both internal and external noise and the local interference level in the area of the receiver. The diagram also shows that if the carrier level exceeds the required S/N level then a margin is available to overcome unexpected degradations. The overall limit to how much signal the receiver can handle is given by the dynamic range at which point any strong unwanted input signals cause non-linearitys in the receiver. In considering the effect of noise on system performance, it is usual to find the sum of all the noise contributions from both internal and external sources. It is beyond the scope of this chapter to look into each internal and external noise source that needs to be considered and how the contribution from each source is summed.

1.4 Introduction to Propagation Prediction

The term “prediction” in the context of this chapter is understood as the forecast of the expected state of a specific phenomenon at a certain time in the future. In the context of the work undertaken in this thesis, this is a prediction of the state of the ionospheric path a radiowave must traverse.

Predictions are less valuable than accurate computations based on firmly established laws, for example, the calculation of a solar eclipse using celestial mechanics. On the other hand, they are more valuable than limited empirical evidence or, at worse, non-

scientific guesses often guided by intuition than precise application of the laws of nature. Prediction methods are the only recourse when the information available is incomplete, inaccurate or unreliable. The greater the extent to which predictions are based on deterministic calculations, the greater the degree of accuracy.

The information about a given phenomenon may become so complete and accurate that over the course of time predictive estimates are gradually replaced by deterministic calculations with an accurate estimate of the errors involved. For example, during quiet periods there are fairly accurate computations of propagation conditions for mid-latitude paths, the uncertainty for disturbed periods' results in the use of statistical probability for these disturbed periods. At high latitudes, other relationships governing the change in the ionosphere, involving unpredictable sporadic disturbances, have not yet been sufficiently understood or defined in order for us to incorporate them into prediction models.

There are two fundamental approaches to prediction, the statistical and the deterministic approach. The statistical approach is based on qualitative and quantitative information obtained by statistical processing of data obtained by long-term observations and therefore a definitive probability can be assigned to each prediction. The deterministic approach to prediction is based on rigid quantitative descriptions of physical effects and all the relationships involved in the process. As applied to the ionosphere, a deterministic approach would have to be based on a sufficiently reliable theory of ionosphere formation and its change with respect to all solar and geophysical forces.

Two other methods of prediction that have been/are used and must be mentioned are the intuitive and the inertial methods of prediction. The intuitive method of prediction is essentially a subjective method. Certain relationships are used to reach the final conclusions intuitively, either through experience or by chance. The inertial method is based on the principle "what happens today, should also happen tomorrow": this is a valid prediction method when the changes that can take place happen over periods of more than one day. This method is partially used in the National Oceanic and Atmospheric Administration (NOAA) space weather 3-day predictions[1] of solar radiation that, outside the periods of solar flares, uses the inertial method since the typical period in solar radiation is about 5 days.

The function of propagation prediction, when used as an engineering planning tool, is to ensure, as best as possible, that an adequate service can be provided to spectrum users. The term 'adequate service' has two components that must be satisfied. The first component is the delivery of a wanted usable field strength to the reception point. The second component is that this wanted usable field strength is available for the required length of time. Different services place different emphases on the availability of the wanted usable field strength. For example, in the HF broadcasting service the broadcaster is interested in reaching listeners only during a few hours of the day when spare time permits listening to the radio. As indicated in broadcaster schedules, this period for Europe is 18:00 – 21:00 local time in the reception area and for Africa the period is 05:00 – 09:00 and 17:00 – 20:30 local time. On the other hand, for the aviation air traffic control service, a safety of life service, the communications link is required 100% of the time.

[1] NOAA – 3 Day Solar Weather Prediction: http://www.sec.noaa.gov/ftpdir/latest/daypre.txt

In the last three decades numerous HF-propagation prediction methodologies and software programs have been developed. Most of the programs take transmitter and receiver locations, time, month, year, and usually the number of sunspots as input, and provide median values of MUF, LUF, mode structure, antenna headings, great-circle distance and root-mean-square median-field-strength values for mid-latitude HF paths. The calculation of signal strength is especially difficult, because the exact mode structure on a particular path is not accurately known and all the path losses (in the D region, in the transmission line of the antenna, and from mismatch, ground reflection, etc.) are difficult to accurately characterise. It is surprising that the process yields any useful results, yet it often does and is used extensively in HF broadcast planning and other spectrum management activities where significant lead times between planning and operation are involved.

Irrespective of the particular method employed in making a prediction there is the problem of predicting the expected levels of solar and geomagnetic activities. The sunspot number (SSN) is an input parameter in the derivation of long-term predictions. On the other hand, the correlation between the critical frequency of the F-layer (f_0F) and SSN is valid only on the average, and there is no correlation if, for instance, the comparison is made on specific days. The reason for this is that the F-region is sensitive to the flux of solar short-wave radiation, which itself correlates with the sunspot number only on the average. It is a fact that the daily electron concentrations in the F-layer maximum may differ by more than a factor of two, even on two days in near succession, and even if both days are magnetically quiet. This may be due to changes in the flux of solar radiation, which clearly cannot be taken into consideration when establishing the prediction. Practical radiocommunications for tactical operations, where instant communications are required at any time of day

and night, must be based on the true state of the ionosphere on a specific day, which may be very different from the predicted monthly average.

Another very complex problem connected with the calculation and presentation of electron concentration profiles is the prediction of solar radiation and the level of geomagnetic activity, the input parameters of several ionospheric models. The prediction of perturbed conditions in the ionosphere is a problem to which no answer has as yet been found. This is due to the difficulty of predicting the geomagnetic indexes, Ap and Kp, and to the complexity of planetary distribution and temporal variation of the disturbed conditions in the ionosphere.

Figure 3 depicts the hierarchy of ionospheric disturbances and provides an estimate of the typical duration for each type of disturbance – which varies from 1μs to 12 years.

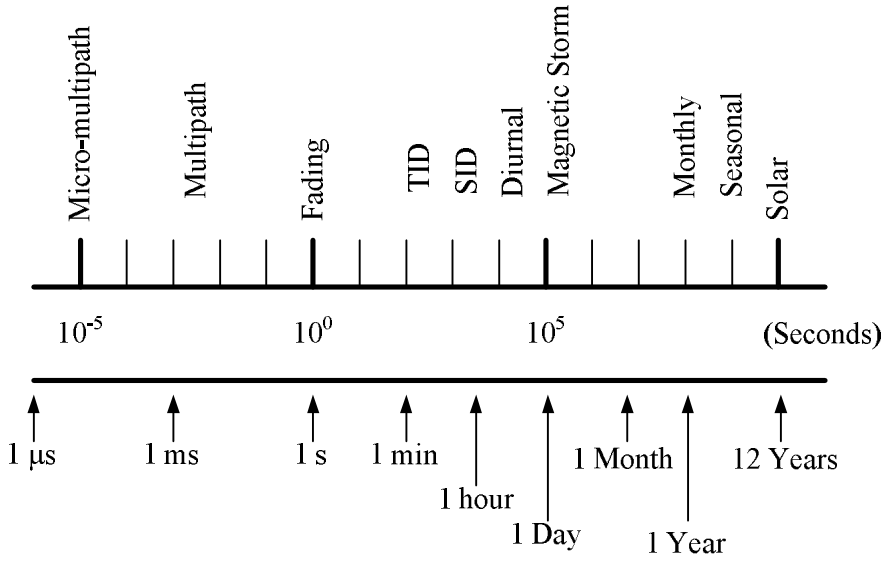

Figure 3. Hierarchy of ionospheric disturbances

The nature of ionospheric variability is quite complex, since it arises from temporal and geographic variabilities in upper atmospheric chemistry, ionisation production and loss mechanisms, particle diffusion and electro-dynamical phenomena. Generally, the trends are fairly well modelled, and much of the variability is understood from a physical point of view. Unfortunately, an understanding of cause and effect does not always translate into being able to make predictions in the time period desired.

1.5 The Function of Propagation Prediction and Planning Tools.

Predictions have improved in the last decade as a result of the evolution of computers, along with associated advanced computational methods and the development of advanced sensors and telemetry. Figure 4 is a flowchart showing in a simplistic manner the task that propagation prediction and planning tools must perform.

The first function of propagation prediction is to evaluate the state of the ionosphere at some point in the future. Having entered the station parameters, which as a minimum must be the location of the transmitter and the location of the receiver as well as a number of expected or predicted ionospheric parameters - which as a minimum is some form of the Smoothed Sunspot Number (SSN) - the state of the ionosphere for the wanted time is forecast. Based on the forecast, the Maximum Usable Frequency (MUF), the Lowest Usable Frequency (LUF) and sometimes the Optimum Usable Frequency (FOT) are calculated. If these parameters do not meet the requirements, no link is possible. If the calculation of MUF, LUF and FOT meet the requirements, then it is possible to predict the usable field strength that will be delivered to the receiver.

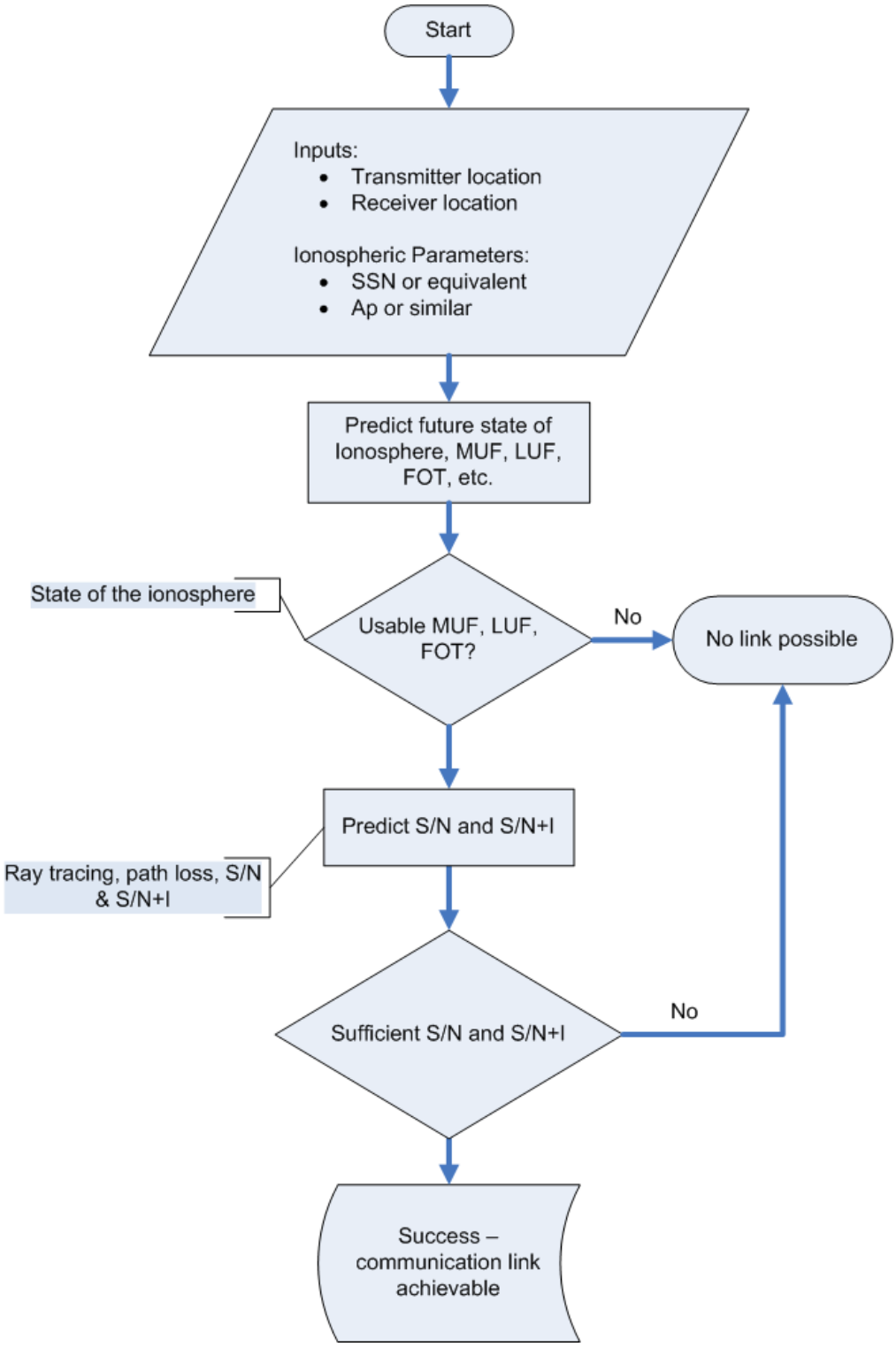

Figure 4. Flowchart indicating the tasks that propagation prediction and planning tools must perform.

The second function of the prediction process is to determine if an adequate field strength is delivered. Using further transmitter parameters, such as transmitter effective radiated power (e.r.p), take-off angle form the antenna, receive antenna gain and noise level at the receiver, the signal to noise ratio is predicted. If a database of all transmitters that can be received in the reception area is available (as is the case in international HF broadcasting), the signal to noise plus interference ratio can be determined.

As indicated in figure 4 this process can be broken down into the following stages:

i. Determination of a representative model of the electron concentration over the propagation path, taken as being the great circle between transmitter and receiver;
ii. some kind of ray path assessment leading to an estimation of the modes available;
iii. calculation of the received signal intensity using a transmission-loss calculation;
iv. estimation of the atmospheric noise, background man-made noise and noise arising from unintentional co-channel emissions;
v. statistical quantification of the random variability of signal and noise intensities;
vi. check of grade of service based on some choice of reference signal/noise ratio.

One of the most important parameters in the prediction of HF propagation is the maximum electron density of the ionosphere, since this determines the communication coverage at a specified frequency. The ordinary ray critical frequency, f_oF_2, may be

directly related to maximum F_2 layer electron density and f_oF_2, together with the effective ray launch angle, determines the MUF for a specified transmission distance. Thus, the ability to predict the f_oF_2 by knowing the maximum electron density of the ionosphere by some method is the first step in predicting HF propagation. This is usually accomplished by generating a model of the vertical distribution of electron concentration/density in the E and F regions. This needs to take account of the known large geographic and temporal variations in the ionosphere.

Models of the vertical distribution of electron density may be empirical (statistical), semi-empirical or theoretical. Empirical models are based on the generalization of a number of observations of individual ionospheric parameters, which may be presented in graphs, tables or formulas. Statistical models involve charts of planetary distribution of ionospheric parameters as a function of the coordinates, the local time and the level of solar activity.

A short survey of freely available amateur and professional propagation prediction software is presented in the appendix to this thesis.

1.6 Case Study: The Broadcasting Service

The broadcast services have one of the most highly developed regulatory frameworks on an international scale. This is largely because of the political importance of broadcasting both within a country's border and, for some countries, external to their borders. Bands between 6 MHz and 26 MHz that are used exclusively for the broadcast service are used for broadcasting to both domestic and foreign audiences. Because of problems that have occurred in the past, the Radio Regulations require the

power of transmitters to be limited to what will provide a national service, except in the bands exclusively for international broadcasting[2], and a prohibition on broadcasting from ships or aircraft outside national territory.

HF propagation characteristics require that a family of frequencies be used in order to provide sufficient coverage of particular target areas. In 2001 the BBC world service made use of 176 HF frequencies which all required co-ordination in accordance with the procedures described the Radio Regulations. The typical HF traffic load for big broadcasters such as the BBC World Service is approximately 6 000 transmitted hours per week. A total of 4.35 MHz or 15.5% of the HF bands is assigned to the Broadcasting Services as shown in figure 5.

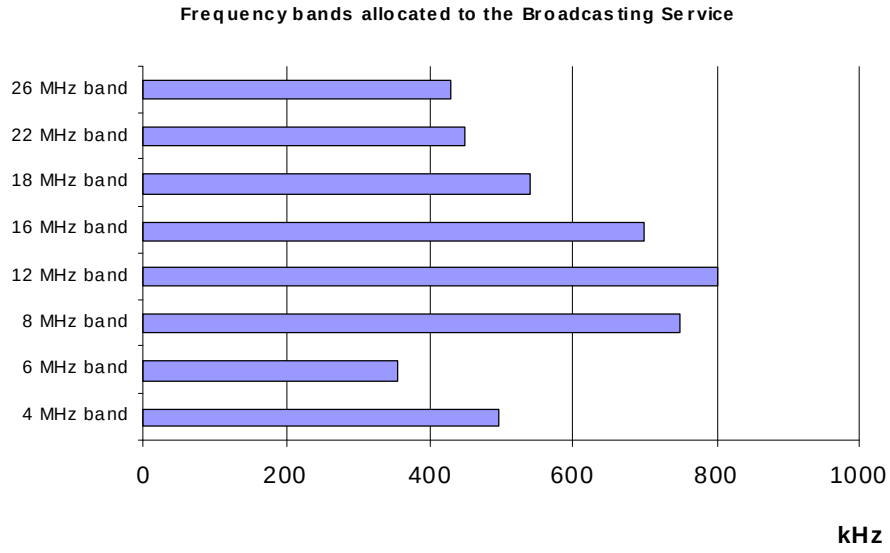

Figure 5. Amount of spectrum assigned to HF broadcasting.

The requirements of the broadcast services are unique in that they are aimed at providing service to an area as opposed to a single location and that the receivers most

[2] See ITU Radio Regulation 23.3.

commonly used are consumer products and not high specification professional equipment. This results in planning systems with extreme stability, with special care taken to avoid interference and the use of high transmitter power to provide adequate coverage. The management of broadcast frequency assignments differs from the procedures to assign spectrum to a fixed service or a maritime service for example. The special assignment of frequencies to broadcasting in the HF bands is necessary because of the intense pressure on the radio spectrum for broadcasting, the long reach of interference at HF and the uncertainties of HF radio propagation.

Listeners of civilian broadcasts are disadvantaged as they have no access to sophisticated radio equipment, no real-time feedback capability and, due to cost factors, are limited in sensitivity and selectivity. For this reason, the minimum signal-to-noise ratio for an average AM receiver is 40 dBμV/m. For digital modes this level is 10 to 20 dB above the minimum usable field strength required. The broadcasting community therefore needs a credible long- term prediction capability before they can offer (and advertise) a reasonable set of reliable broadcast channels to listeners in designated reception areas.

Of all HF spectrum users broadcasters face the greatest challenge when it comes to planning services. Factors that contribute to this are the requirements to:

i. notify frequency assignments up to 6 months before operation commences;
ii. lay down a signal to cover reception areas that are widely spaced geographically;
iii. compensate for skip zone variations even when the diurnal period of transmission is limited.

1.6.1 The Broadcasting Propagation Model.

The only model internationally accepted for use in determining the interference potential of broadcast services is known as ITU Recommendation P.533 (ITU, 1995). The roots of this model known as P.533 are in CCIR Report 252-2 (CCIR, 1970), which was adopted at the 1970 plenary of the International Radio Consultative Committee (CCIR[3]). It was the first of three computer methods for field strength prediction that were sanctioned by the CCIR. It is also the method that IONCAP (Lane, 2001) uses for estimating the median signal strength and the day-to-day variability (termed the 'excess system loss') of the median value. This was followed in 1982 by a supplement to CCIR Report 252-2 (CCIR, 1982) which was more complex than the method of CCIR 252-2 in a number of respects, and the machine time required reflected this additional complexity. The major change in this supplement is the consideration of longitudinal gradients for the first time.

CCIR Report 894 (CCIR, 19864) followed in 1984 to assist in an international HF Broadcast Conference by producing a rapid computational method. This document was the result of deliberations to produce a prediction program for use in planning by the HF broadcast service and an improved estimate of field strength was made possible by taking the antenna gain (of appropriate broadcast antennas) into account when selecting modes to be included in the calculations. Following 15 more years of work, in 1995 the ITU published Recommendation P.533 (ITU, 1995). Recommendation P.533 provides estimates of the monthly median values of the

[3] In 1992 at an Additional Plenipotentiary Conference the ITU was dramatically remodelled. As a result of the reorganization, the Union was streamlined into three Sectors, corresponding to its three main areas of activity Telecommunication Standardization (ITU-T), Radiocommunication (ITU-R) and Telecommunication Development (ITU-D). The name CCIR was dropped as this point.

maximum usable frequency (MUF), received signal strength, available receiver power, signal-to-noise ratio, reliability and lowest usable frequency (LUF) between two locations for any specified time and level of solar activity.

The term “basic MUF” as used in P.533 is defined as the highest frequency at which a radiowave can propagate between given terminals on a specific occasion by ionospheric refraction alone. MUF (Maximum Usable Frequency) is a function of path length, geographic position and time. Methods of predicting MUF are restricted to determining smoothed monthly median values and to providing statistical parameters descriptive of daily figures. The monthly median path basic MUF is taken as the highest monthly median basic MUF of any mode reflected from the different layers, so that it is necessary to first determine the separate E and F_2 MUFs depending on path length.

The term “operational MUF” as used in P.533 is the highest frequency that will give acceptable operation between two terminals on a specific occasion; under the same operational conditions it is greater than the basic MUF. The operational MUF depends, among other factors, upon the types of antenna used, the transmitter power, class of emission, information rate and required signal-to-noise ratio. The differences between the operational MUF and the basic MUF can be explained by various ionospheric phenomena, such as scattering in the E- and F-regions, off-great-circle propagation and propagation by unusual modes when ionisation irregularities exist; also spread F may be an important factor.

Control Points

The first step in P.533 is the determination of a number of ionospheric characteristics and propagation parameters at specified 'control points'. The control points are the locations along the great-circle path where the radio wave interacts with the ionosphere. For example, for path lengths up to 2 000 km only the mid-point of the path is assessed for both the E and F layers. The same method applies to ionospheric absorption; it is only evaluated at the mid point for paths less than 2 000 km – no attempt is made to evaluate D-region absorption as part of the ray tracing.

Ray Path Assessment

A ray path assessment is carried out in order to estimate control points and possible modes present. Recommendation P.533 applies a ray-path analysis for paths up to 7 000 km, empirical formulations from the fit to measured data beyond 9 000 km, and a smooth transition between these approaches over the 7 000-9 000 km distance range.

E-layer basic MUF

For the E-layer the method of calculation of the monthly median critical frequency (f_0E) is based on all published data over the years 1944-1973 from 55 ionospheric stations. Four factors are combined in an empirical formula: solar activity; season; latitude; and time-of-day. The virtual height of the E-layer is set, for all calculations, at 110 km.

The basic MUF of an n-hop E mode over a path length D is given in terms of the hop length, f_0E and the secant of the angle of incidence at a mid-hop mirror reflection height of 110 km. The E-layer basic MUF for the path is that appropriate to the lower-order E mode. The maximum length for a single-hop is 2 000 km and E modes

are only determined for paths up to 4 000 km. The E-layer operational MUF is taken as equal to the basic E-layer MUF.

F2-layer basic MUF

Monthly median values of f_oF_2 are obtained from a numerical map function **Ω (λ, θ, T)**. The function **Ω** has the form of a Fourier time series with 988 coefficients. The lowest-order mode (minimum elevation of 3^0) is initially determined from geometrical considerations, using an estimate for mirror reflection height (h_r) at the mid-path control point. The parameter d_{max}, which is the maximum possible path length for a single-hop mode depends on the underlying ionisation, indicated by the ratio $x = f_oF_2/fo_E$, and the characteristic $M(3000)F_2$ which is the MUF required for a path length of 3 000 km.

For the lowest order mode, the F_2-layer basic MUF is a function of factors including the hop length d, d_{max} and the critical frequency. For paths lengths of d_{max} and less, calculations are based on propagation via the ionosphere given at the mid-path position. For F_2 modes the ITU-R has adopted empirical relationships giving mean mirror-reflection height as a function of time, location and path length. The values of the parameters of this model are given in terms of the average of the predicted ionospheric characteristics f_oE, f_oF_2 and $M(3000)F_2$ along the path.

Field strength

Once all existing modes and their associated elevation angles are known, the next stage is to evaluate the corresponding signal intensities at the receiver. Monthly median values of field strength E_{tw} for each propagation mode w at frequency f are

determined in terms of transmitter-radiated power, transmitting antenna gain and the transmission losses.

$$E_{tw} = 136.6 + P_t + G_t + 20\log f - L \qquad (dBmV/m)$$

where:

P_t = transmitter power (dB(1kW))

G_t = transmitting antenna gain (decibels relative to an isotropic antenna)

L = summed transmission losses (dB)

The resultant equivalent median sky-wave field strength, E_{ts}, is taken as the root-sum-squares (RSS) for up to N modes where N encompasses the three strongest F_2 modes and also, in the case of path lengths to 4 000 km, the two strongest E modes.

Median available receiver power

For each mode *w* the corresponding available signal power P_{rw} (dBW) from a lossless receiving antenna of gain G_{rw} (dB relative to an isotropic radiator) in the direction of signal incidence is:

$$P_{rw} = E_{tw} + G_{rwt} - 20\log f - 107.2 \qquad (dBW)$$

From the above modes, the resultant root-sum-square (RSS) monthly median receiver power P_{sr} (dBW) is calculated by taking up to the three strongest F2 modes and additionally the two strongest E modes for ranges up to 4 000 km. Predictions for path lengths longer than 9 000 km are made by dividing the path into the minimum of equal length hops, none of which exceeds 4 000 km.

For predictions for path length between 7 000 and 9 000 km RSS field strength and RSS available receiver power are obtained by using a weighted interpolation procedure from the two values obtained respectively from the methods used for the two other path lengths for the required distance.

Transmission with Absorption Loss

In the equation for fields strength the parameter *L* represents a number of summed transmission losses (dB) represented by:

$$L_t = 32.45 + 20\log f + 20\log p' + L_i + L_m + L_g + L_h + L_z \qquad (dB)$$

where:

p' = virtual slant range (km) (Free-space loss);

L_m = "above-the-MUF" loss if applicable;

L_g = summed ground-reflection loss at intermediate reflection points;

L_z = a term containing those effects in sky-wave propagation not otherwise included in this method. This factor, currently set at 9.9 dB, is added to make the model match up to a measurement database;

L_i = absorption loss (dB) factor, which occurs largely in the E and D regions and is expressed as a function of the solar zenith angle, χ; While the formula is complex and involved this term only deals with absorption as a function of solar zenith angle;

L_h = factor to allow for auroral and other signal losses, dB.

Model Flaws

There are a number of recognised flaws in P.533:

- The degree of detail in the numerical maps used to determine the parameters of the F-layer depends on the spacing of measuring stations and the highest order of the harmonic coefficient used. The stations used were never uniformly spread across the globe and the numbers of high-latitudes stations were limited. In addition, different stations were in operation for different time periods over which measurements were taken and the harmonic coefficients were truncated for economy. This has resulted in the maps becoming smoothed and hence a loss of some ionospheric features such as troughs and auroral activity.
- F_oE is calculated for four factors using mainly mid-latitude ionosondes – this methodology does not capture the effects of ionisation due to particle precipitation – which will be shown to be in control of E-layer formation.
- The virtual height of the E-layer is set for all calculations at 110 km – the case study in chapter 2 will show how this is a very limiting assumption at high latitudes.
- Estimations of absorption are done only at the mid-path control point and not where the ray passes through the D-region.

These flaws need to be recognised when using the model in practice.

1.7 The Ionosphere

The ionised region in the Earth's atmosphere extending from about 50 km to roughly 2 000 km above the surface is called the ionosphere. The ionosphere is that part of the atmosphere where free electrons occur in an appreciable density so as to influence the

propagation of radio waves. For reasons related to the historical development of ionospheric research, the ionosphere is conventionally described in terms of three principal regions, the D, E and F regions respectively, in order of increasing altitude as shown in figure 6. Subdivisions of these regions may exist under certain conditions; for example, F_1 and F_2 layers during daylight hours.

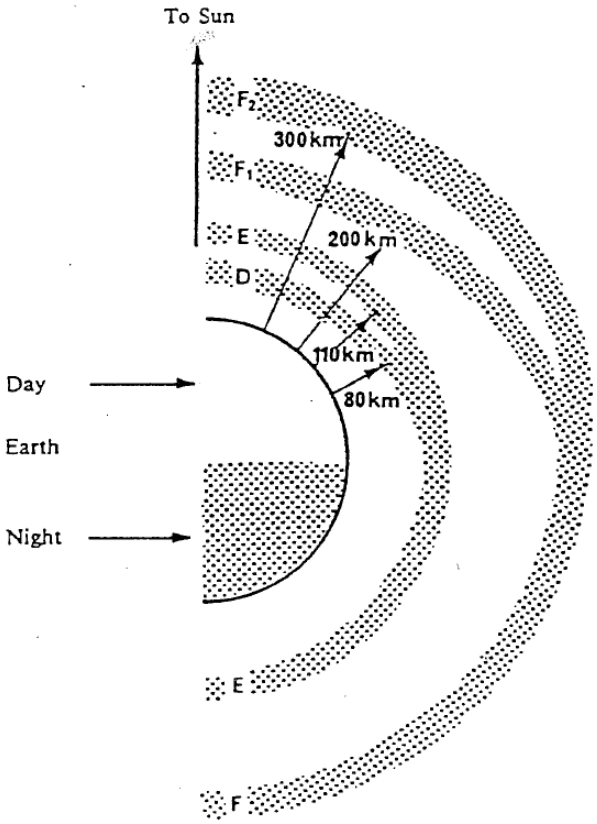

Figure 6. Ionospheric regions as a function of height above the Earth's surface. (ITU, 1998)

Radiowaves in the low frequency to high frequency bands are receivable over long distances because they can be reflected by these ionised regions of the atmosphere. From the viewpoint of HF propagation, the E and F regions act principally as

radiowave reflectors[4], and permit long range propagation between terrestrial terminals. The transmission channel for radiowave propagation at HF includes much of the Earth's atmosphere between the transmitter and receiver terminals. The varying ionisation in the upper atmosphere is the major cause of changes in the transmission channel and therefore in the path loss between terminals (ITU, 1998). These variations in ionisation are due to a number of causes, all related to the solar influence on the Earth's atmosphere. Regular variations are classified according to period, e.g. multiple years, year, season, day. Annual and diurnal variations, which are often a function of geographic locations, have also been identified.

The most important ionospheric parameter, from the view of radiowave propagation, is electron density. The electron density at any given point in space and time is a function of three competing physical processes; production, loss and transport. These three processes in practice involve a multitude of complex photochemical and electrodynamic processes which are influenced by a variety of external conditions within the atmosphere and the magnetosphere.

1.7.1 Ionospheric Regions

With reference to figure 6, the D region is the zone between about 50 km and about 90 km above the Earth. The ionisation found here is that which is mainly responsible for absorption of those high frequency radio waves which are reflected by higher layers with electron concentrations that generally decrease with decreasing altitude, reaching

[4] It is convention to speak about ionospheric reflections as if they were occurring from a mirror surface. It is understood, however, that the radiowave is returned to the Earth's surface by a number of refractions that overall have the same effect as a single reflection.

vanishingly small values under normal conditions below about 60 km. The electron density in the D region exhibits a marked diurnal variation, with peak densities shortly after local noon (typically 10^8 to 10^9 electrons.m^{-3}) and very small values at night. There is also a pronounced seasonal variation with maximum densities in summer.

The E-region is the zone between about 90 km and about 140 km above the Earth in which the normal daytime E-layer is usually found. The E-region often conforms closely to a Chapman model with a maximum density near noon and a seasonal maximum in summer. This region also exhibits solar cycle dependence with maximum densities occurring at solar maximum. The E-region reaches a peak concentration of about 10^{11} electrons.m^{-3} near 110 km although this height varies with local time (ITU, 1998). The (mid-to-low latitude) quiet time E-region is very predictable as compared to the F_2 layer. A large volume of vertical-incidence ionosonde data has been collected over more than four solar cycles and the characteristics of the Low and Mid latitude E-region are well known. For these latitudes the minimum vertical height of the E-region and the variation of the maximum electron density (N_e) have been recorded as a function of time and geographical location. As a guide the maximum electron density occurs during the day at ~ 110 km and the semi-thickness is ~ 20 km (Frihagen, 1965). Usually for propagation prediction purposes the E-layer critical frequency (F_oE) is calculated via an empirical equation involving the sunspot number and the zenith angle of the Sun.

Within the E-region there also exists an ill-predicated layer known as sporadic-E (E_s). This layer often forms at about ~ 105 km altitude and may be optically dense and spatially thin. In such cases it reflects radio signals well. Sporadic-E, however, also includes partially transparent layers and irregular patches of ionisation in which case

signals may be reflected, or scattered, or little affected by the layer. The mechanisms producing sporadic-E are not well understood (Cannon, 1994).

The F region, the zone above about 150 km, is where the most important reflecting layer, F_2, is usually found. Other stratifications in this zone are also derived with the prefix F, e.g. the temperate latitude regular stratification F_1 and the low-latitude semiregular stratification $F_{1.5}$. The bulk of the free ionisation in the ionosphere is found here in the F region with a peak concentration of electrons of about 10^6 electrons/ m^3 near 300 km altitude. The F_2 layer is the highest layer and generally exhibits the greatest electron densities and in general is the only layer which persists to any degree during the night. The F_2 layer is not well represented by the Chapman formulation since it is strongly influenced by neutral winds, diffusion and other electrodynamic effects. The relationship between the direction of the geomagnetic fields and the direction of the neutral winds and electrodynamic drifts plays a major role in the structure of the F_2 layer. It is the plasma response to the dynamic processes in the presence of the geomagnetic field that gives rise to the observed geographical and temporal variations in the F_2 layer (ITU, 1998).

A number of anomalies have been identified in the F layer including the diurnal anomaly, the seasonal anomaly and the equatorial anomaly. At high latitudes a variety of anomalous features are also observed, some of which are associated with charged particle precipitation. The F-region “trough” is a pronounced depression in the F_2-layer electron density resulting from magnetospheric convection. The trough extends from about 2 to 10 degrees equatorward from the auroral oval in the late afternoon and night-time ionosphere.

1.7.2 Ionisation: Production, Loss and Transport

The formation of the ionosphere is ultimately due to the ionisation of the neutral constituents of the atmosphere by solar extreme ultraviolet (EUV) and X-rays, with a much smaller contribution from particle-induced ionisation in general. Therefore, the structure of the ionosphere is strongly influenced by solar activity, since the Sun's output in these portions of the spectrum is increased when the Sun is active, both on the long-term scale (e.g. the peak of the solar cycle) and on the short-term timescale (e.g. in response to individual active regions on the Sun).

This response to solar activity comes about through two related but distinct mechanisms. First, ionising radiation is more intense under active solar conditions, leading to generally higher concentrations of electrons and secondly, the increase in the temperature of the neutral upper atmosphere when the Sun is active causes redistribution in the ionisation, with peak concentrations occurring at higher altitudes, especially in the case of the F region. Although the overall cause of these variations is well understood, the quantitative details are still unclear, since the ionising and heating radiations cover a wide spectral range with an extremely complex variation with solar activity.

Figure 7 indicates approximately the portions of the solar spectrum which are responsible for the different regions of the ionosphere. In the X-ray region, from about 0.1 to 1nm wavelength, the absorption cross section is comparatively small and the radiation penetrates the upper regions of the ionosphere with negligible attenuation, ionising only in the D-region. The wavelength band from about 1 to 12 nm, where the ionisation cross section is higher, is one of the major sources of E-

region ionisations, whereas the EUV band from 12 to 76,9 nm is the principal source of the F region.

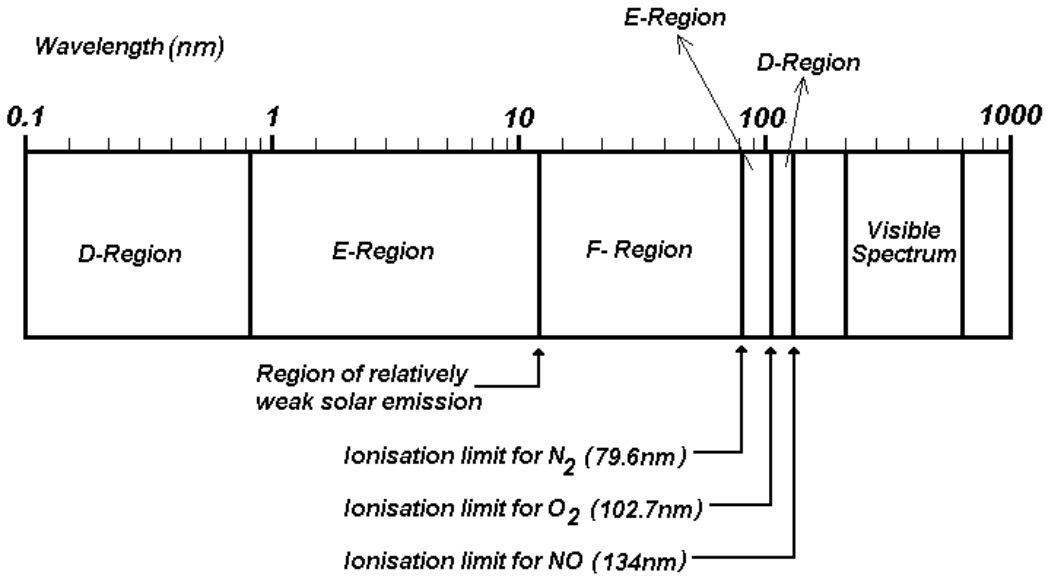

Figure 7. Approximate regions of the solar spectrum responsible for the different regions of the ionosphere (based on Reid, 1972)

With further reference to figure 7, the upper wavelength limit of 79.6nm corresponds to the maximum wavelength capable of ionising molecular nitrogen. On the long wave side of this band, the cross section drops again and there is a region from about 79.6 to 102.7nm that is again an important source of E-region ionisation with the upper limit of 102.7nm corresponding to the maximum wavelength capable of ionising molecular oxygen. At wavelengths longer than 102.7, the major constituents of the atmosphere cannot be ionised, but certain minor constituents of the D-region are still available. Chief amongst these is Nitric Oxide, which is readily ionised by the extremely intense H I Lyman – α line at 121.6 nm. It has also been established that the band 102.7 to 111.8nm is capable of ionising molecular oxygen in the electronically excited metastable state and that this region of the atmosphere normally

contains sufficiently large concentrations of these exited molecules that they form an important source of D-region ionisation (Hunten and McElroy, 1968). At wavelengths longer than about 130nm, only the alkali metals can still be ionised, and although trace elements of these metals, especially sodium, do exist in the upper mesosphere and lower thermosphere, they are unlikely to form any appreciable contribution to the ionosphere (Ivanov-Kholodny and Mikhailov, 1986). As mentioned, the structure of the ionosphere is strongly influenced by solar activity. This is shown for the sunspot cycle in figure 8 and a significant variation can be seen in ionisation (electron density vs. height above the Earth's surface) on a long-term scale as the Sun cycles through a sunspot cycle, from a sunspot minimum to a sunspot maximum over a period of 11-12 years.

The production of free ionisation by solar radiation (and charged particles) is counter-balanced by ionisation loss processes, principally the recombination of electrons and positive ions following collision, and the attachment of electrons to neutral gas atoms and molecules. It is possible to determine, from physical principles, a reasonably realistic mathematical description of the altitude distribution of ionisation, based on estimates of the solar ionising flux, the vertical distribution of neutral atmospheric constituents and their absorption efficiency, and the solar zenith angle.

One of the first models, which are fairly accurate at low and mid-latitudes during "quiet solar" periods, was by Chapman (1931) for a single constituent, isothermal atmospheric ionised by monochromatic solar radiation.

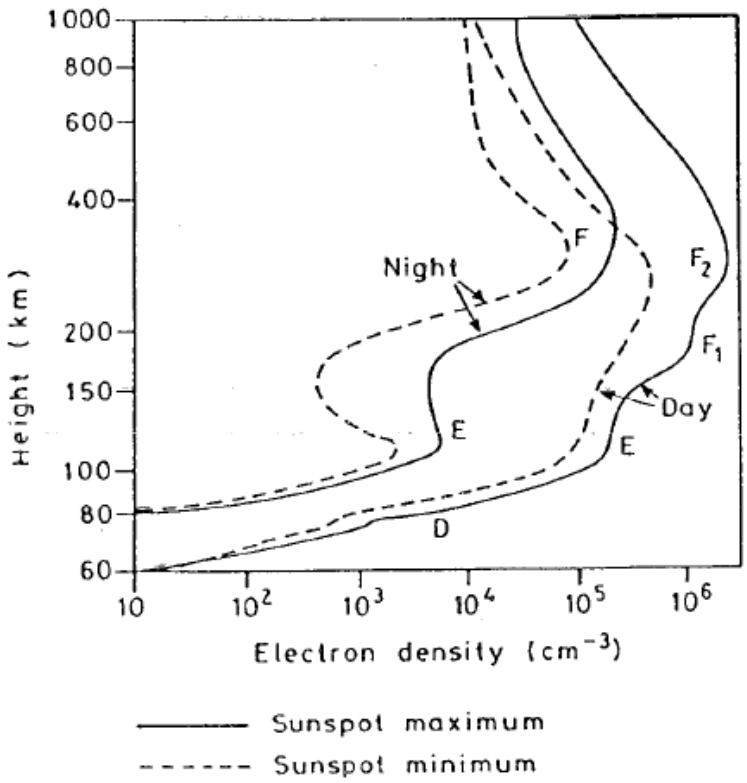

Figure 8. Representation of the Ionosphere layers for sunspot maximum and minimum (After Jursa, 1985)

At the height of the F_2 layer the transport of ionisation is important. This movement can be caused by diffusion, neutral atmospheric winds and electromagnetic drift. Plasma diffusion occurs along magnetic field lines and is greatest at the magnetic poles where the electrons and ions can move nearly vertically along the field lines. The effect on ionisation distribution is not a strong as the effect of neutral winds that are driven from the hotter dayside to the cooler nightside of the Earth. The winds move the ionisation through neutral-ion collisions and thence the electrons by Coulomb attraction. In the F_2 region electromagnetic drift (E×B), caused by interaction of ionised particles with the Earth's magnetic field (B) and electric fields (E) in the ionosphere, is important because it accounts for ionisation moving across

magnetic field lines. Electric fields cause vertical drifts near the equator and horizontal drifts in the auroral zones and polar caps (Rishbeth, 1989).

1.7.3 Predicting the State of the Ionosphere

In order to reach a general characterisation of the problems involved in the prediction of the ionosphere, we must consider the factors determining the state of the ionosphere to understand why it is very difficult with current knowledge to produce a fully deterministic calculation (Ivanov-Kholodny and Mikhailov, 1986). To do this we need to consider: a) the fundamental parameters of the ionosphere; b) their spatial and temporal distribution; and c) their dependence on solar and geomagnetic activities.

a. The state of the ionosphere is determined by a large number of different parameters and the characteristics of the ionised part of the upper atmosphere such as electron concentration, ion composition, electron and ion temperatures, particle fluxes and drifts, constitute the basic physical parameters of the ionosphere.
b. The parameters of the ionosphere undergo considerable changes with altitude. The concentrations of ions, n_i, and electrons n_e, at certain altitudes have characteristic maximum peaks, forming the ionospheric layers, E, F_1 and F_2. As a result, the stratified structure of the ionosphere may be characterized by a set of parameters: the concentration of electron density (n_e) at layer maximum, layer altitude and widths, the depths and widths of the troughs between layers etc. This group of parameters describes the special features of the distribution of n_e over the altitude h or, as it is usually referred to, the profile, $n_e(h)$. In addition to variation with altitude, ionospheric parameters also vary with the

geographical coordinates (latitude φ, longitude λ), and with the geomagnetic coordinates. The properties of the ionosphere are known to undergo significant changes in the equatorial and auroral latitudes. Accordingly, a distinction is made between low-, mid- and high-latitude ionospheric regions. Knowledge of the relationship governing the variation of the ionosphere with time is particularly important in prediction. It has been found that there are variations in parameters not only between daytime and night time, but also that there were sharp variations between values for the daytime, even noontime, from one place to another. Indeed there are features which depend on the season of the year, for example, giving rise to the so-called winter anomaly. Thus, any description of the variation of the ionosphere with time must include several parameters.

c. Some variations in the ionosphere were found to be caused by the variation of active factors such as solar radiation and geomagnetic activity. Therefore, the ionosphere is not merely a geophysical, but also a helio-geophysical entity. Owing to the abundance of the parameters required to describe it, and since each parameter varies differently with the coordinates, time, and activity factors, the behaviour of the ionosphere is extremely complex. As a result, both the study of the ionosphere and its description are very complex tasks.

Ideally, any method of ionospheric prediction needs to calculate of all the ionospheric parameters as well as their global and altitude distributions at any future point in time. The present-day limitations to this ideal are as follows:

a. Limitations due to incomplete information, which might become more complete at some future date or they may be intrinsic to the phenomenon itself.

For example, the detail in ionospheric charts of the different ionospheric depends on the accuracy with which each parameter can be determined, and on the extent of its variation from one point to another is known;

b. How detailed should the description of the parameters as a function of time be, bearing in mind that a change of longitude of 15^o corresponds to a one-hour time difference. Clearly, if only 10% accuracy is required in describing n_e in the F_2-region, it is sufficient to take observations every hour, or even every 1½ - 2 hours, except perhaps at sunrise and sunset. This is not sufficient for disturbed periods when changes happen quickly;

c. As with other types of prediction, the nature and reliability of ionospheric prediction not only depends on an accurate and reliable knowledge of the relationships governing the evolution of the ionosphere, but also on the accuracy and the completeness of empirical and other information which is used in predictive computations. The prediction of data concerning geomagnetic perturbations is of very limited value; nevertheless, such data are used as the input data in all atmospheric predictions. A highly accurate prediction of short-wave radiation is only possible one or two days ahead. Long-range predictions – several months ahead – are based on the grosser estimates of average short-wave solar radiation or SSN, which at best yield median MUF frequency values.

1.7.4 The High-Latitude Ionosphere

It is convention to also divide the ionosphere into three regions that have different properties according to their geomagnetic latitude. The mid-latitude region is the most completely explored and understood region. In the mid-latitude region

ionisation is produced almost entirely by ultra-violet and X-ray emissions from the Sun, and is removed again by chemical recombination processes that involve the neutral atmosphere as well as the ionised species (Hunsucker and Hargreaves, 2003). The movement of ions and the balance between production and loss are affected by winds in the neutral air. These mid-latitude processes also operate in low- and high latitudes but with additional processes coming into play.

The low-latitude zone spanning 20^o to 30^o either side of the magnetic equator is also strongly influenced by electromagnetic forces that arise because the geomagnetic field runs horizontally over the magnetic equator. As a result, the electrical conductivity is abnormally large over the equator causing a strong electric current (the electrojet) to flow in the E-region and the F-region is subject to electrodynamic lifting and a fountain effect that distorts the general form of the ionosphere throughout the low-latitude zone.

At high latitudes the opposite occurs. Here the geomagnetic field runs nearly vertical which leads to an ionosphere that is considerably more complex than in the other two zones. This happens because the magnetic field lines connect the high latitudes to the outer part of the magnetosphere which is driven by the solar wind, whereas the ionosphere at middle latitudes is connected to the inner magnetosphere which essentially rotates with the Earth and so is less sensitive to external influence. There are four general consequences of the high-latitude ionosphere connection to the outer magnetosphere (Hunsucker and Hargreaves, 2003):

1. The high-latitude ionosphere is dynamic and circulates in a pattern mainly under the control of the solar wind which is itself variable;

2. This region is more accessible to energetic particle emissions from the Sun that can produce additional and sometimes substantial ionisation;
3. The auroral zones occur in the high-latitude region. The location of the auroral zones is directly linked to the magnetosphere and to the distorted tail of the magnetosphere. Auroral phenomena include electrojets which cause magnetic perturbations and there are substorms in which the rate of ionisation is greatly increased by the arrival of energetic electrons;
4. A trough of lesser ionisation is often formed between the auroral and the mid-latitude ionospheres. Part of the cause of the trough appears to be the difference in circulation patterns between the inner and outer parts of the magnetosphere.

It is apparent from the brief list above that the **magnetosphere** has a major role to play in the structure of the high-latitude ionosphere.

1.8 The Magnetosphere

Radiant energy from the Sun determines the surface temperature of the Earth and supplies virtually all the energy for natural processes on the Earth's surface and in its atmosphere (Jursa, 1985). The Earth's upper atmosphere is ionised by radiations, both electromagnetic and corpuscular, from the Sun. The electromagnetic radiations such as radio, infrared, ultraviolet, extreme ultraviolet and X-rays travel directly between the Sun and Earth at the free space speed with a transit time of approximately 8.3 minutes.

In addition to the electromagnetic radiations the Sun emits a stream of charged corpuscles (mostly electrons and protons) which is called the solar wind. The solar wind originates in the Sun's corona which is the tenuous halo or crown overlaying the chromosphere. The corona is very dynamic and contributes to the general outflow of material from the Sun into interplanetary space. It is this outflow or stream of charged corpuscles which is known as the solar wind. The solar wind flows at a speed of normally about 400 $km.s^{-1}$ and takes about 5 days for individual particles to travel from the Sun to the Earth. The fully-ionised electrical neutral plasma that makes up the solar wind carries the Sun's magnetic field outward from the inner solar corona at all times.

Since the conductivity of the solar wind is extremely high, there is essentially no diffusion of the plasma transverse to the magnetic field and the field is said to be "frozen in" to the flow (Parker, 1963). As the Sun is rotating, the solar wind does not flow straight out from the Sun but in a spiral – the analogy of a garden sprinkler is often used to describe the effect. The imbedded magnetic field gives the solar wind plasma, fluid properties so that frictional or viscous-like interactions can take place between the streaming solar wind and the magnetic fields of any planet it interacts with. On approaching the Earth, the magnetised collisionless solar wind confines the magnetic field of the Earth to a region around the planet called a magnetosphere. The magnetosphere is therefore the region of near-Earth space where the dynamics are governed by the internal geomagnetic field. The solar wind flows past the Earth distorting the otherwise dipole field to compress it on the dayside and elongate it to a long geomagnetic tail on the nightside.

The principle features of the Earth's magnetosphere are shown schematically in figure 9 and figure 10 and the terms used are defined in the glossary.

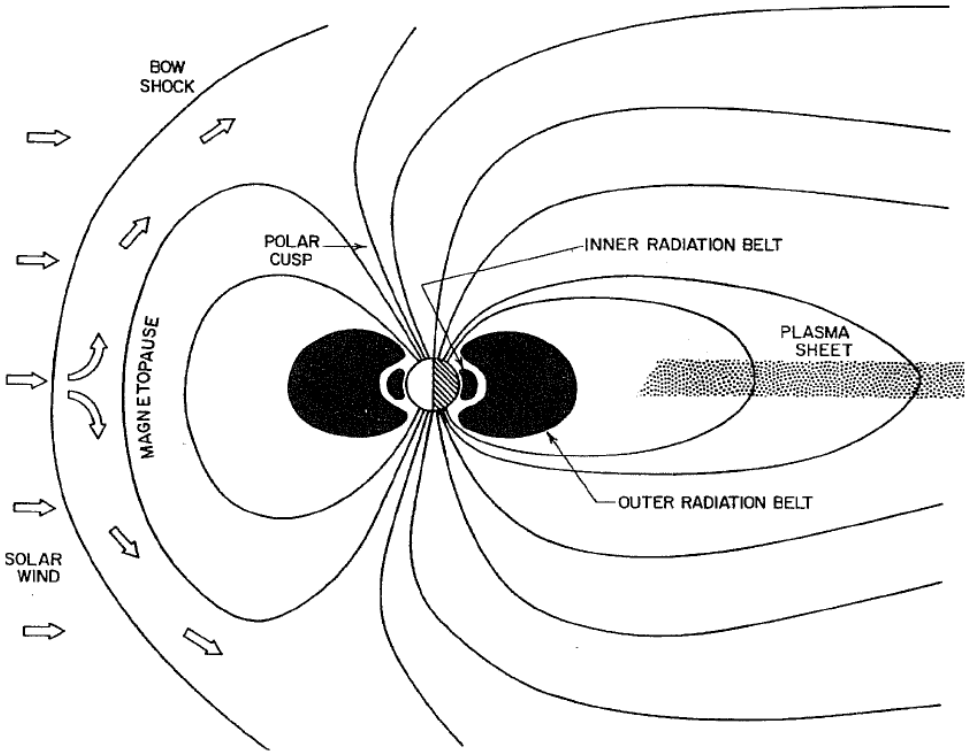

Figure 9. Principal features of the Earth's magnetosphere to approximate scale in the noon-midnight meridian plane cross section (Suess and Tsurutani, 1998).

As an alternative it could be stated that the Earth's magnetic field excludes the solar wind from the planets environment. The confinement of the Earth's magnetic field or the exclusion of the solar wind plasma is not perfect however. Due to particle gyration, the two plasma regimes overlap slightly which permits significant mutual interaction. This interaction results in the active solar process being able to affect the magnetosphere. In basic electronic terms it appears that the magnetosphere can be described as a resistive, and therefore dissipative, element in an electrical circuit that

draws its power from the kinetic energy of the streaming solar wind plasma. Any changes in boundary conditions require the circuit to adjust itself, in the same way that the constantly varying solar wind requires the magnetosphere to continuously readjust itself, sometimes almost explosively.

The magnetospheric geometry corresponding to the pressure balance configuration is a direct result of currents (Chapman-Ferraro currents) which flow on the magnetopause surface. In addition to the surface currents, a number of other currents systems are known to exist throughout the interior of the magnetosphere. The most important of these are the ring current, which flows in a circular pattern in the equatorial plane in the vicinity of 6 Re, and the tail current, which flows across the tail in the equatorial plane. The geometry of the magnetosphere and the location of the magnetopause are determined by the interaction of the Earth's dipole **magnetic field** and the solar wind. The interaction compresses the field on the dayside and creates a tail like structure on the nightside which extends in the anti-sunward direction to several tens of Earth radii. The region of closed field lines extends to the magnetopause on the dayside. At high latitudes (above $\approx 75^0$ geomagnetic latitude), the field lines extending into the magnetotail do not close back to the Earth.

The nominal magnetopause standoff distance is usually taken to be 10-11 Re at the sub-solar point, but it can range from 6 Re to 14 Re (Fairfield, 1971) depending on solar wind conditions. Simple models describing the equilibrium configuration as a dynamic pressure balance between magnetic and plasma forces within the magnetosphere and similar forces in the solar wind (Mead and Beard, 1964; Olson, 1969) predict the observed magnetopause position quite accurately on the dayside and somewhat less so in the tail region (Fairfield, 1971).

The **thermal plasma** density in the inner magnetosphere decreases with radial distance above the ionosphere, including a steep gradient known as the plasmapause where the density drops by as much as two order of magnitude in a distance of < 2 Re (Carpenter, 1963). The plasmapause location (see figure 10) varies between equatorial distance of 2 and 7 Re, depending on geomagnetic activity (Carpenter and Park, 1973). The thermal plasma consists primarily of electrons and protons in the energy range 0.1 – 1 eV which originate as upward flowing particles from the ionosphere (Lyons and Williams, 1984).

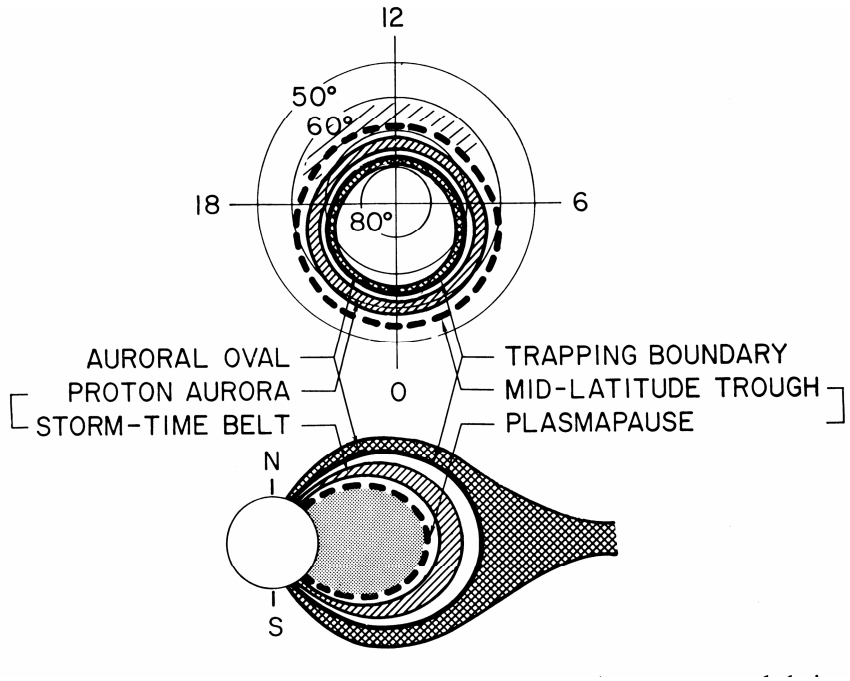

Figure 10. Schematic diagram showing the three circumpolar oval structures and their relation to the corresponding magnetospheric structures. (Akasofu, 1968)

In addition to thermal particles, the magnetosphere plasma includes a population of **energetic plasma**, of high energy (100 eV – 100 MeV) electrons and protons. The particles are trapped within the inner magnetosphere by magnetic field gradients, forming the Earth's radiation belts. Particle fluxes maximise in two regions known as the inner and outer radiation belts (Lyons and Williams, 1984). Inner belt fluxes peak

inside an equatorial distance of 2 Re and are quite stable. Outer belt fluxes peak near the plasmapause during geomagnetically quiet conditions and move inward during magnetic storms (Lyons and Thorne, 1973).

Particle-particle collisions are rare in the radiation belts; particles would remain trapped indefinitely in the absence of other scattering processes. Interactions with plasma waves thus provide an important mechanism for catering and loss of radiation belt particles. The magnetosphere supports a variety of **plasma wave** modes. Due to the spatial variations in magnetic fields strength and plasma density, the observed modes and the characteristics spectrum vary considerably with location. In the inner magnetosphere, wave activity is a function of radial position, local time and latitude. The plasmapause tends to be an important boundary dividing regions of distinctly different wave activity (Carpenter, 1968).

Within the plasmasphere, the wave spectrum consists of plasmaspheric hiss, whistlers and discrete emissions. Plasmaspheric hiss is an incoherent whistler-mode wave emission with a typical bandwidth of a few hundred Hz and a peak spectral power density near several hundred Hz. It is believed to be generated through gyroresonance interactions with radiation belt electrons (Thorne et al, 1973). Interactions between plasmaspheric hiss and radiation belt particles are thought to be an effective mechanism for continuous scattering and loss of energetic electrons from the plasmasphere into the ionosphere (Lyons and Throne, 1973). Whistlers, signals from ground-based VLF transmitters and emissions triggered by interactions of these waves with energetic particles are all known to cause significant particle scattering and loss (Rosenberg et al., 1971; Imhof et al., 1983; Voss et al., 1985). Outside the

plasmapause, plasmaspheric hiss is generally not observed and whistlers are less common.

1.8.1 Solar Wind Control of the Magnetopause

The Earth's magnetopause lies at the locus of points where magnetosheath and magnetospheric thermal and magnetic pressures balance. The solar wind dynamic and thermal pressures and the IMF control the shape and location of the Earth's magnetopause. Because the solar wind thermal and magnetic pressures are insignificant in comparison to the solar wind dynamic pressure and the magnetic pressure dominates the thermal pressure in the magnetosphere, one can predict the ***location*** of the subsolar magnetopause when only the solar wind dynamic pressure and magnetospheric magnetic fields are known (Martyn, 1951).

The solar wind thermal pressure does play a minor role in determining the ***radius*** of the near-Earth magnetotail (Spreiter and Hyett, 1963). The magnetopause moves inward when the solar wind dynamic pressure increases and outward when it decreases. This movement has been shown by Sibeck et al. (1991a) to be consistent with that predicted by the pressure balance theory (Fairfield, 1971) and empirically the position of the subsolar magnetopause is approximately given by:

$$R_{SS}(R_E) = 11.3 + (0.25 \times IMF\ B_Z)\ (nT)$$

The boundary of the Earth's magnetic field can, as a result of unusual solar events, collapse to altitudes of less than 6.6 Re where usually this boundary is located at 10-12 Re (Fairfield, 1971).

In contrast the strength and orientation of the IMF exerts an important influence on the ***shape*** of the magnetosphere. When the IMF turns southward ($B_z < 0$ nT), the dayside magnetopause moves inward and the magnetotail magnetopause moves outward (e.g. Coroniti and Kennel, 1972). The magnetospheric response to solar wind dynamic pressure and IMF variations was quantified by Sibeck et al. (1991b) who showed that the shape of the magnetopause remains self-similar for variations in the solar wind dynamic pressure, i.e., that magnetopause positions scale to solar wind dynamic pressure. A number of models predict that the magnetopause will move inward during periods of southward IMF. These models include:

i. Magnetic field superposition (Hill and Rassback, 1975; Kan and Akasofu, 1974);
ii. "Onion peel" model (Dungey, 1961);
iii. Cross-tail current fringe model (Unti and Atkinson, 1968);
iv. Birkeland current fringe model (Hill and Rassbach, 1975; Maltsev and Lyatsky, 1975).

When the solar wind dynamic pressure increases, the magnetosphere is compressed beginning at the dayside magnetopause and then continuing down the tail (see Wilken et al., 1982). If this compression occurs during a period of northward IMF we expect that the principal change in the magnetosphere will be to shrink in size and increase its magnetic field strength accompanied by rapid motion of the plasma 'tied' to those field lines. When a fast interplanetary shock or a sudden increase in the solar wind dynamic pressure makes a contact with the Earth's magnetosphere, the magnetosphere is compressed. In response to the compression, the Chapman-Ferraro current becomes enhanced and produces a sudden commencement on the ground magnetosphere.

1.9 The Radiation Belts

The "Radiation Belts" are defined as the region of magnetosphere permanently populated with energetic electrically charged particles in gradient-curvature drifting orbits encircling the Earth. They are mainly composed of protons and electrons and, in minor proportion, alpha particles, covering an energy range from tens of KeV up to hundreds of MeV. These particles are trapped in the magnetic field and would remain trapped so indefinitely if it were not for diffusion, acceleration and loss processes. Figure 11 gives an idea of where in the magnetosphere the radiation belts are located. The linear scale is given in Earth radii (1Re = 6 371 km).

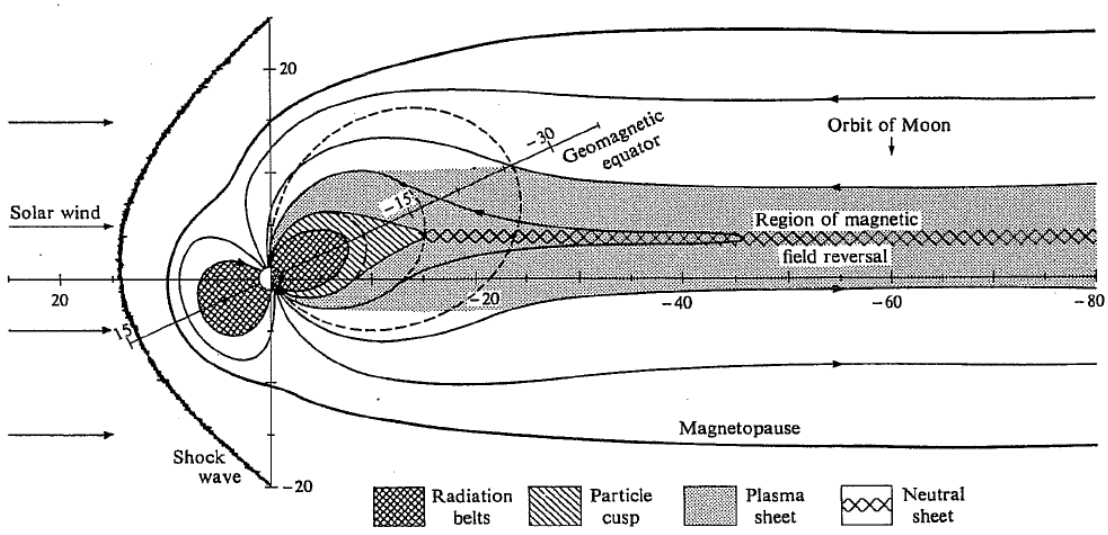

Figure 11. Schematic of the radiation belt structure within the magnetosphere (After Ness, 1969). The interior cross-hatched region contains the relatively stable radiation belts. The outer fringes of the magnetosphere are populated by large fluxes of low-energy particles.

There are various physical processes, losses and sources which modifiy the trapping mechanism. Hence the radiation belts should not be seen as a stable structure but are rather to be understood as the result of a dynamic interplay of a number of different processes. The variability of the belts is due to the temporal variations of the process involved in source and loss.

There are two main zones which are populated by trapped particles, the inner radiation belt, centred at around 1.5 Re and the outer radiation belt centred at approximately 4 Re. Whereas protons are restricted to the inner belt, electrons can be found in both regions. The region between the two belts is the so-called slot region. The trapped particle population is subject to temporal variations with a wide range of characteristic timescales, varying from solar cycle variations to changes which take place within minutes, such as Storm Sudden Commencement (SSC) events.

In addition to energetic particles, the magnetosphere contains thermal plasma and a particle population of “intermediate” energy, probably in a transitional phase from the thermal to the radiation belt category. The plasma is mainly found in two regions: the “plasma sheet” in the geomagnetic tail, probably of solar wind origin, and the “plasmasphere” which co-rotates with the Earth and is an extension of the Earth’s ionosphere. The “intermediate” energy particles can be found in the “cusp”, but also pervade the region of the radiation belts and occasionally are detected in the tail (Roederer. 1970).

Time variations of the magnetospheric field configuration, caused by changes in the solar wind plasma flow, have a considerable effect on the particles contained in this field. Slow variations induce reversible changes or “adiabatic effects”, which in

principle do not alter the dynamical balance. They do however, lead to spatial and spectral rearrangements of the particle fluxes. Sudden variations – in particular those associated with magnetic storms – have a profound and irreversible effect on the trapped particles and are believed to keep the radiation belts going by providing the main mechanisms of fresh particle injection and the first stage of their acceleration (Roederer, 1970).

In the **outer zone**, external contributions to the geomagnetic field begin to significantly alter the field configuration from that of a simple dipole, with the solar wind compressing and increasing the magnetic field on the dayside, and ring and tail currents stretching and distorting the nightside magnetic field. The "slot region" between the inner and outer zones is kept largely free of trapped electrons through wave particle interactions prevalent in this region (Kennel and Petschek, 1966). The radiation belts as a whole are largely field-aligned structures with outer zone electrons extending approximately $\pm 50^{o}$ from the geomagnetic equator.

While the physics behind the outer zone flux variations is not well understood, correlations have been noted between the solar and magnetospheric phenomena and the dynamics of the outer zone. Paulikas and Blake (1979), Baker at al (1997) and Li et al. (1993) have all noted correlations between solar wind velocity and outer zone electron fluxes. Furthermore, a strong correlation between ULF wave power in the Pc-5 frequency range (2 – 7 mHz) and outer zone fluxes has been observed (e.g. Baker et al. 1998b).

Inner zone populations are observed to be largely stable in time; however, electrons in the outer zone can show substantial variation on a variety of timescales. In particular, solar storms can have a profound effect on energetic electron fluxes observed in the outer zone. For example, in the SSC phase of a storm, induced electric fields caused by the compression of the magnetosphere can impulsively inject solar and outer zone electrons into the inner regions of the magnetosphere. This was seen in the SSC of 24 March 1991 which injected electrons inside the slot region and formed a new radiation belt over the course of a few minutes (Blake et al., 1992; Li et al., 1993).

Two useful tools in the study of radiation belt dynamics are Adiabatic Theory and Diffusion Theory. The ***Adiabatic Theory*** has been developed to simplify the study of charged particle motion in magnetic fields. The ***motion*** of charged particles in the Earth's magnetic field is complicated but is easily visualized by dividing it into three components. The trajectory of a given energetic particle in the magnetosphere can be described as a superimposition of three simple motions: a gyromotion of the particle around the field line, a bounce motion along the field line between hemispheres, and a drift motion around the Earth. Particles gyrate about magnetic field lines with a frequency that is proportional to the field strength. As they do this, they are also bouncing back and forth along the magnetic field while being reflected by the magnetic mirror force associated with the increasing strength of the magnetic field with decreasing altitude. The bounce frequency is determined by how fast the particles are moving along the magnetic field and by the length of the magnetic field line. The distance of a magnetic field line from the centre of the Earth when it crosses the Earth's magnetic equator is called its L-value. Thus, particles at low L-values, on short

field lines, bounce more rapidly than particles on long field lines at L-values in the distant magnetosphere. The third component of this motion is the circulation of particles about the dipole axis. While they are gyrating and bouncing, the particles drift. They drift all the way around the magnetic cavity until they are back where they started. This third periodic motion has a frequency determined by the gradients in the magnetic field and curvature of the field lines as well as particle energy. The drift motion usually takes from minutes to hours; the bounce motion seconds to minutes and the gyro motion milliseconds to seconds. Electric fields present in the magnetosphere can significantly distort the motions of particles at the low energies below a few keV. Distortions of the magnetic field are equally important in the distant magnetosphere.

At energies below a few tens of keV, the electric field must be taken into account in describing the motion of charged particles. The fact that this electric field has large temporal variations means that at low energies, especially in the outer magnetosphere, particle trajectories often switch from being closed and totally inside the magnetospheric cavity to being open to direct entry from (or exit to) the solar wind or, equally important, open to direct entry from the magnetotail. Thus, at the lowest energies in the distant magnetosphere the charged particle population is extremely variable.

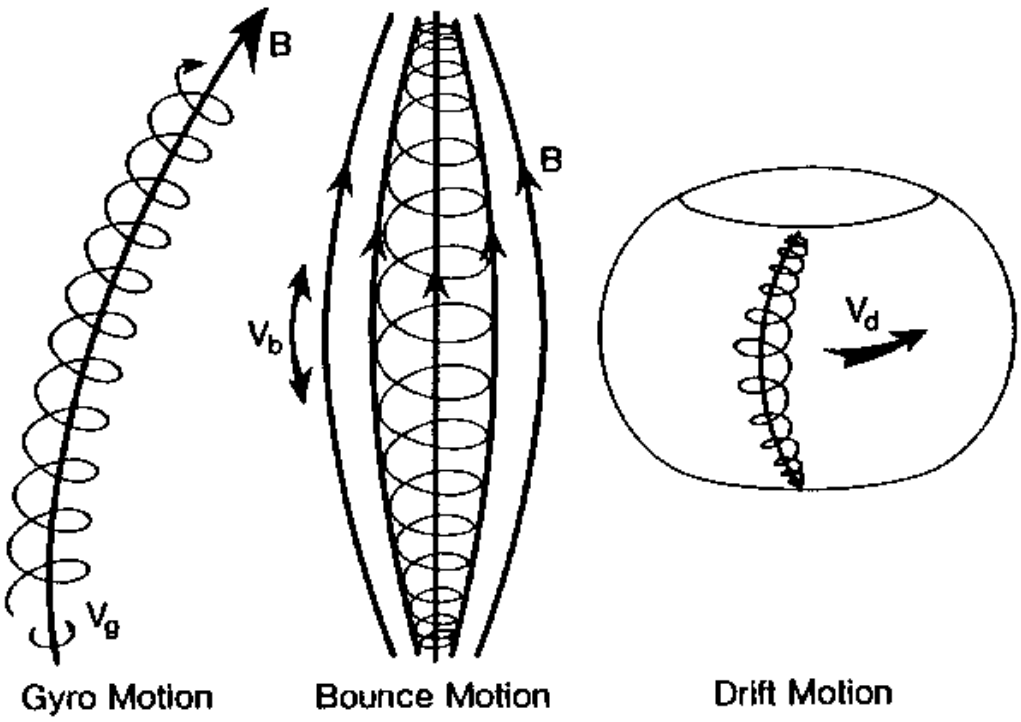

Figure 12. Three types of motion of energetic charge particles in the magnetosphere (Russell, 1987)

With reference to figure 12, Gyro motion, V_g, is the circulation of the particle about the magnetic field. Bounce motion, V_b, is the periodic motion of the particle along the field the two magnetic mirrors caused by the converging and strengthening field at low altitudes. Drift motion, V_d, is caused by the curvature of magnetic field lines and the radial decrease of the magnetic field. Each of these motions is associated with a conserved quantity called an adiabatic invariant. When these adiabatic invariants are conserved, the particles remain stably trapped. If, for example, waves cause a violation of these adiabatic invariants, the particles will diffuse in space, possibly moving closer to or further from the Earth and possibly bouncing closer to or further from the atmosphere. Resonance of a wave with the gyro motion of particles leading to pitch angle diffusion is a frequent cause of particle precipitation in the magnetosphere.

As the name Adiabatic Theory indicates it is not an exact theory – its predictions are only approximations which, however, would become exactly true when certain "smallness parameters" tend towards zero. This is the situation in most problems dealing with energetic particles trapped in the geomagnetic field. Quantitative use of Adiabatic Theory is necessary for the following (Roederer, 1970):

- to achieve physical understanding and to obtain a proper, quantitative description of the steady state configuration of geomagnetically trapped particle fluxes;
- to find the corrections that need to be applied to experimental observations in order to eliminate all effects on the particle population caused by spatial asymmetries and slow time variations of the geomagnetic field;
- to set up the proper frame, in terms of geometry, coordinates and parameters for the study of trapped particle injection, diffusion, acceleration and loss.

Diffusion theory is applied to the study of the interactions of trapped particles with the atmosphere and the ionosphere, with random field fluctuations and with electromagnetic and hydromagnetic waves. These processes control the dynamics of the radiation belts, i.e. the balance between injection and loss, their spatial distribution and their energy spectra.

A link between wave activity and particle dynamics is provided via radial diffusion theory. Here stochastic variations in the electric and magnetic fields guiding the trapped particle's drift result in diffusion of particles across drift shells though violation of the third adiabatic invariant (Cornwall, 1968; Schulz and Lanzerotti, 1974). If the first adiabatic invariant is conserved during this process, electrons will

change energy as they move into regions of differing magnetic field strength. The spatial structure and energy spectrum of the radiation belts is consistent with radial diffusion (Lyons and Thorne, 1973). However, timescales classically cited for radial diffusion processes are too slow to account for the storm time variations observed in the outer belts (Walt, 1996).

1.10 Solar Disturbances and their Effect on the High-Latitude Ionosphere.

There is a set of disturbances to the ionosphere that are associated either directly or indirectly with events that occur on the Sun. These include (Davies, 1990):

i. Sudden Ionospheric Disturbances;

ii. Ionospheric storms;

iii. Polar cap absorption (PCA) events;

iv. Travelling ionospheric disturbances;

v. Associated disturbances in the geomagnetic field leading to aurora and magnetospheric substorms.

These disturbances usually have adverse effects on the radio communications over the entire radio spectrum. While a case can be made in some circumstances that a user might be advantaged by some of these disturbances (e.g. increased D-region absorption mitigating the interference caused by sky-wave reception of MW broadcasting) in general, storms adversely affect propagation. Three examples of these adverse effects are:

- Phase changes on VLF navigation systems;

- Shortwave fadeouts;
- F_2 MUF failures.

The various effects – simultaneous and delayed – are shown in figure 13. At high latitudes these disturbances profoundly affect all three ionospheric layers in various degrees, depending on the severity of the disturbance.

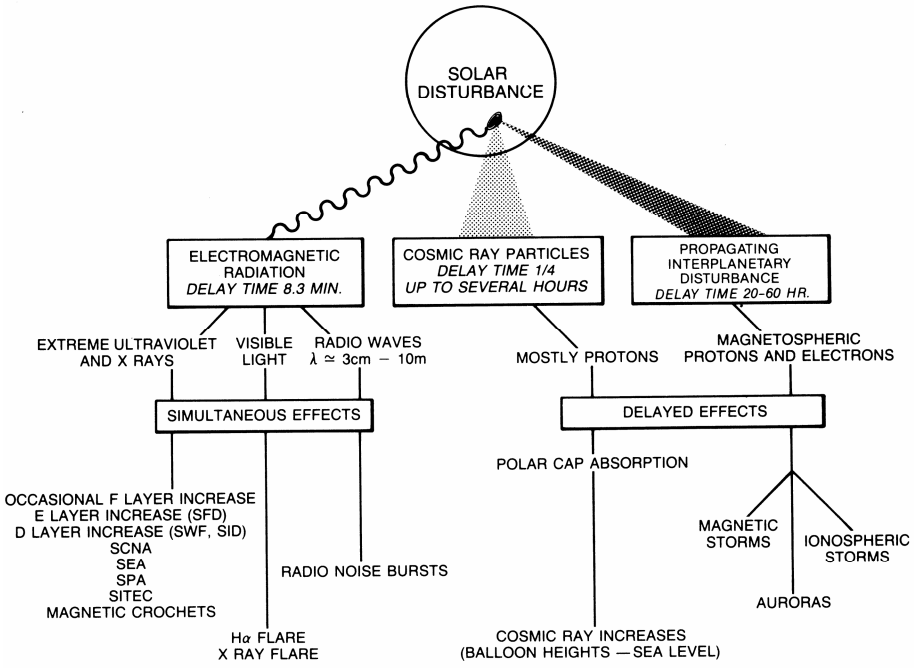

Figure 13. Terrestrial effects of solar disturbances (after Davies, 1990).

The list of solar disturbances that leads to ionospheric disturbances includes:

i. Solar Flares leading to X-ray and EUV emissions and radio bursts. X-rays flare emissions ionise the D region resulting in radio absorption. Class-X and some Class-M flares produce shortwave fadeouts which affect radiocommunications. Solar flares also cause shortwave fadeouts, sudden phase anomalies, sudden frequency deviations, etc.

ii. Coronal Holes are sources of high-speed solar wind that can cause ionospheric and geomagnetic storms by disturbing the magnetosphere.

iii. Coronal Mass Ejections (CMEs) imply a large scale disturbance propagating from the outer corona into the solar wind. The change in solar wind parameters cause ionospheric and geomagnetic storms due to magnetospheric disturbances generated by these changess.

iv. Radio bursts are associated with flares having strong microwave bursts as well as Type II and IV radio emission.

Due to the linkages between the magnetosphere and the high-latitude ionosphere there are a number of events particular to the high-latitude ionosphere:

i. Solar proton events – During some large flares, highly energetic protons are emitted, which enter and ionise the polar ionosphere. Protons with energies of about 30 MeV can penetrate to about 50 km above the Earth's surface and produce polar cap absorption (PCA).

ii. Polar cap absorption (PCA) – can last from an hour to 60 hours or more depending on the latitude and on the duration of the source of the protons on the Sun. PCAs are associated with the polar cap rather than the auroral zone and their occurrence tends to follow the sunspot cycle (Larsen, 1979). PCA appears first in high latitudes and expands equatorward. For a 10 MHz ordinary wave reflected from the F-layer it creates absorption of about 170 dB leading to transmission blackouts.

iii. Sudden Commencement Absorption - this is a strong absorption associated with the sudden commencement of the geomagnetic storm followed. Its period is short compared to PCA but it is intense enough to disrupt communications

and mislead Real Time Channels Evaluation systems. Chapter three contains a detailed analysis of this phenomenon.

iv. Storms – Ionospheric storms are an important disturbance because of their duration (several days), their adverse effects on the radio spectrum and their geographical locations. Ionospheric storms are associated with geomagnetic storms, auroral and magnetospheric storms which have been known to affect electrical power systems and atmospheric drag on satellites. Types of storms include:

   a. Magnetic storms – disturbances of the geomagnetic field lasting from a few hours to several days;

   b. D-region storms - leading to auroral absorption and sudden commencement absorption;

   c. F-region storms – the most prominent feature of an F-region storm is the reduction in F_2 critical frequency and hence the MUF. There are changes in total electron content affecting GPS signals as well as severe changes in layer heights – this is shown in the case studies in chapter 5.

v. Sporadic E-layers – due to energetic electron bombardment – the subject of chapter 4 of this thesis.

vi. Polar Radio Blackouts – a condition indicated by absorption exceeding 50 dB on frequencies near the critical frequency. It is considered that polar radio blackouts are a superposition of polar cap absorption and auroral absorption.

More details, experimental work and case studies on the effects of solar disturbances on the high-latitude ionosphere are given in the specialist publications of AGARD (1963, 1964, 1988) and in Hunsuker (1969, 1983, 1992).

1.11 Chapter Summary

This chapter has introduced the main services that use the HF bands, their requirements and the need for these services at high latitude. This reveals the importance of accurate propagation prediction methods to ensure these services reach the intended audience. Prediction and planning tools are introduced and the different approaches to prediction (statistical, deterministic, intuitive and inertial) are explained. It is noted that the prediction of perturbed conditions is a problem with few answers so far.

To make the theory practical a case study has been done of the broadcasting service and the prediction method used in it analysed. The method, P.533, has been developed to service the needs of the broadcast industry but is also used by fixed service, mobile and military system planners. It is noted that some high-latitude features (e.g. auroral absorption) have been crudely taken into account but the following effects have not been thoroughly assessed:

- Sudden ionospheric disturbances;
- Polar cap absorption (Solar proton events);
- Geomagnetic storms;
- Ionospheric Storms (effects of plasma clouds);
- Short wave fadeout;

- Blackouts.

It is shown that the high-latitude ionosphere provides a window to the outer magnetosphere, since electric fields, electric currents and energetic charged particle populations in magnetosphere readily project along magnetic-field lines down to the ionosphere (Sojka and Schunk, 1988). The main difficulty is that magnetospheric processes and solar inputs have an important effect on the morphology of the high-latitude ionosphere, and that the observational databases are still too sparse to enable the development of an empirical model which has adequate parameters to describe the dependence on the various ionospheric drivers. In a paper by Hunsucker (1992) the claim is made that HF-propagation mode structure and losses at high latitudes are impossible to describe, so predictions of paths that include ionospheric reflections and points of D-region penetration in the auroral and polar ionosphere are almost useless. While it is accepted that mode structure and losses are difficult to describe we must attempt, at least empirically, to start the analysis and see where this may lead us. So even with the most extreme simplifying assumptions, the high-latitude ionosphere cannot be treated analytically. Therefore, it is proposed that the way forward at the present time is to look at how to adapt the current propagation prediction models, which are adequate for "quiet" conditions, with empirical data based on measurements from clearly definable disturbed periods.

This chapter described the solar-terrestrial system as summarised in figure 14. Starting at the Earth's surface the ionosphere is described in terms of ionospheric regions with the focus on electron density due to ionisation. Three aspects of ionisation are discussed; production, loss and transport. The limitations and difficulties in predicting the state of the ionosphere are elaborated on. The high-

latitude ionosphere and the consequences of its direct connection to the outer magnetosphere are reviewed.

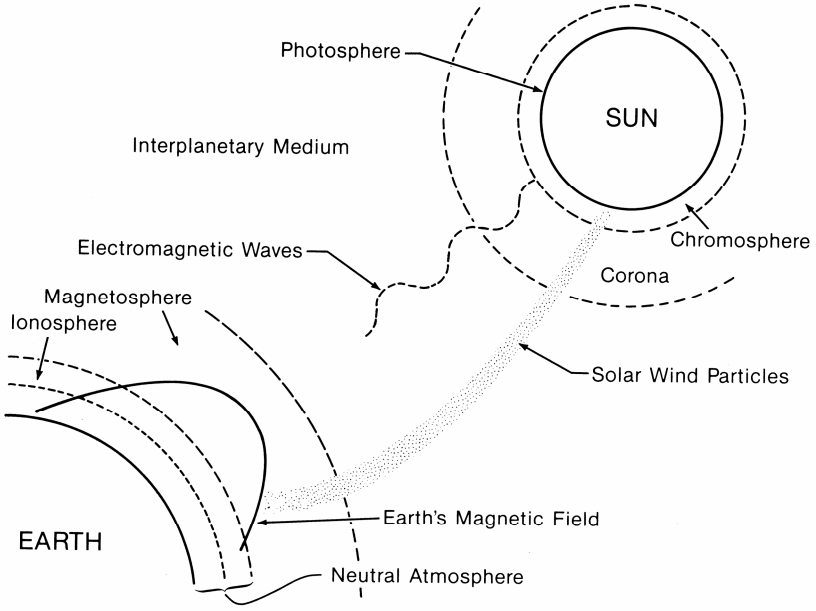

Figure 14. Solar-terrestrial system and solar ionising radiations (Davies, 1990)

Considering our move sunwards, with reference to figure 14, the magnetosphere is described in terms of its interface role between the ionosphere and the solar wind. As this thesis deals with the consequences of particle precipitation on HF communications, introductory material on the magnetosphere location, radius and shape as well as the radiation belts is included. The solar wind is treated as the transport mechanism between solar disturbances and the ionosphere, via the magnetosphere. Events that are particular to the high-latitude ionosphere are briefly discussed.

CHAPTER 2

Case Studies: SSC and its Effect on High-Latitude HF Communications

2.0 Objectives of this Chapter

The use of HF radiocommunications at high latitudes still forms the backbone of many communications systems. At high latitudes there are few alternatives to HF radio for the Merchant and Fishing fleets, the military forces (land, sea and air) and for the civil aviation industry. This chapter undertakes three case studies of how enhanced E-region electron density affects a high-latitude HF Communications circuit using data gathered from ionosondes, incoherent scatter radar and oblique sounders which show the physical changes taking place in the ionosphere.

The objectives of this chapter are to:

1. Show the typical characteristics of the effects experienced following an SSC on propagation conditions;
2. Investigate the significant propagation mode changes that occur immediately following SSC events;
3. Demonstrate the reforming of the E-layer is due to enhanced and sustained particle precipitation;

4. Discuss the importance of the E-layer for HF communication circuits at high latitudes.

2.1 Introduction

This chapter contains three case studies that examine the significant propagation mode changes that occur immediately following Storm Sudden Commencement events. The studies demonstrate the effect of these changes on propagation links operating in and through the auroral zone. The key changes in the ionosphere following the onset of a disturbed ionosphere is the rapidly dwindling influence of the F-layer as a viable reflecting layer and the rise of the E_s-layer as the primary, and in many cases, the only available reflecting layer. This change in propagation mode has implications for system design when reliable HF communications must be ensured and focuses attention on the importance of understanding the E_s-layer so that corrective action can be taken.

Sporadic-E (E_s) is characterised by little or no retardation at its critical frequency when viewed on an oblique ionogram, and may be either blanketing (totally reflecting) or semitransparent (partly reflecting), up to very high frequencies. It is understood that energetic particles play a vital role in the production of E_s and that at high latitudes the precipitation of energetic charged particles into the upper atmosphere is a regular occurrence. Most of the time at high latitudes the ionisation is dominated by energetic charged particles and only rarely is the ionosphere "quiet", i.e. varying only with solar zenith angle and solar activity (Friedrich, 2002). These precipitating particles, primarily kilovolt electrons, produce most of their ionisation in

the E- region (Rees, 1963; Walker, 1972). The maximum density in the disturbed dark ionosphere near 65^0 latitude usually occurs in the auroral E-layer, a thick layer (relative to HF radio wave lengths) with typical electron number densities of 2 to 5 × 10^{11m-3} extending for several degrees of latitude. i.e. a dense, thick and widespread in latitude reflecting layer. The density of the auroral E-layer is primarily a function of the rate at which energy is deposited in the E-region by particle precipitation, and has been shown to be a highly variable phenomenon (Baron, 1974).

The precipitation of energetic particles is modulated considerably by geomagnetic storms and substorms. In the course of a substorm, the precipitation of the charged particles from the magnetosphere into the ionosphere takes place, the electrojet is increased, the substorm current wedge system is formed and the electron density and composition of the ionosphere is changed (Buonsanto, 1999). It is known that during the substorm growth phase, accelerated particles from the solar wind can penetrate through the entry layer of the magnetosphere into the auroral ionosphere (Blagoveshchensky et al., 2005), causing E_s layers.

There have been numerous studies of the high-latitude ionosphere and the response of the HF communication channel to space weather effects. A review of both effects and problems, with many references, is provided in Leid (1967), Goodman (1991), Davies (1990), Hunsucker and Bates (1969) and Hunsucker and Hargreaves (2003). More recently, Blagoveshchensky (2008) examined the impact of 14 geomagnetic storms, which occurred during 1997-1999, on radio propagation conditions. In this study variation in the delta between the monthly median values and actual maximum

operation frequency (MOF) and lowest operational frequency (LOF) before, during and after a storm was characterised.

Several measurement campaigns covering the Arctic and relying on the oblique sounder as the key tool have been undertaken. Jull (1964) combined oblique-sounder data and riometers absorption data with a view to improving the reliability of HF communications channels over and through the auroral zone during PCA events and geomagnetic storms. Owren et al. (1963) reported on a three-year campaign into HF propagation over arctic paths with the behaviour of multiple circuits studied in detail during disturbed periods with respect to absorption measurements and Magnetic K – indices. (This detailed study is also summarised in Hunsucker and Hargreaves (2003)). Goodman and Ballard (2004) reported on a two-year campaign examining the nonclimatological patterns of signals associated with an elevated maximum observed frequency (EMOF). They describe the diurnal and seasonal behaviours of EMOF signals, the association of these observations with polar patches and blobs and the significant impact these have on over-the-pole air transport operations.

Goodman et al. (1997) examined 28 middle- and high-latitude paths over an 18 month period to evaluate the value of path and frequency diversity on overcoming various deleterious effects and a practical engineering solution was offered to effect a near 100% channel availability. Bröms et al. (1994) and Lundborg et al. (1995) reported on oblique sounding campaigns. The first campaign examined the variation of F2MOF, 2-hop F2MOF and LOF on short timescales from day to day, outside disturbed conditions noting the good agreement between oblique and vertical sounder data, and the linear relationship between variations in F2MOF and 2-hop F2MOF.

The later campaign, covering the maximum of solar cycle 22, assessed the accuracy of prediction methods during regular and disturbed periods and the possibilities of exploiting any additional propagation modes such as backscatter, spread-F and sporadic-E.

While the influence of E_s on high-latitude propagation has been published before e.g Blagoveshchensky (2008), Jull (1964), Goodman et al. (1997) this paper presents a comprehensive assessment of two specific links with a variety of sensors and techniques, some of which were not available until recent years. The two case studies presented in this chapter use Storm Sudden Commencements as the starting point for analysis. Disturbances in the solar wind such as shock waves and dynamic pressure pulses (Wilken et al., 1982; Tsurutani et al., 1995; Takeuchi et al., 2002a), when impinging on the Earth's magnetosphere, compresses it and increases the magnetopause current. This leads to a change in the low-latitude ground-based geomagnetic field intensity, lasting typically for some tens of minutes. These signatures in the geomagnetic H-field, seen suddenly and simultaneously at ground magnetic observatories (Rastogi, et al. 2001) are called Storm Sudden Commencements (SSC) and mark the beginning of a geomagnetic storm or an increase in activity lasting at least one hour. These SSC are understood to be the magnetic signature of an interplanetary shockwave, for example, Burlaga and Ogilvie (1969) report that all seven SSC events in their study were caused by hydromagnetic shocks in the solar wind. The SSC generated by these hydromagnetic shock waves transform the magnetosphere into a new compressed steady state configuration which is in balance with the increased solar wind pressure (Wilken et al. 1982, 1986 and

Tamao, 1975). In achieving the new steady state configuration a substantial flux of energetic particles are caused to precipitate into the high-latitude ionosphere.

The advantages of using SSC events as the point of origin of both case studies is twofold. Firstly, the SSC identifies the start of the change of composition of the ionosphere with associated energetic particle precipitation. Secondly, the occurrence and timing of an SSC is internationally agreed (ISGI, 2008) and is therefore a very useful reference point when comparing results from a number of different instruments in different locations.

2.2 The Importance of the E_s-Layer at High Latitudes

HF propagation at high latitudes during magnetic disturbances has been an enigma, in part because ionograms do not always provide analysable data due to absorption, blanketing and spread-F. Following disturbances rapid large changes in ionospheric parameters occur apparently so randomly that little sense can be made of them. The behaviour of the ionosphere at high latitudes differs from that at lower latitudes, mainly because it is exposed to the influence of disturbances on interplanetary space and in the magnetosphere.

At low latitudes, a magnetic field line followed upward, passes horizontally over the magnetic equator not far from the Earth and returns to the Earth in the opposite hemisphere, remaining everywhere deep within the magnetosphere. At high latitudes on the other hand, field lines lead far from the Earth, either to the outer magnetosphere or to interplanetary space. Since electrically charged particles can move easily along

magnetic field lines, but across them only with difficulty, the low-latitude ionosphere is protected from events far from the Earth, which the polar ionosphere is not.

Even when the interplanetary medium is in a steady state, the outer magnetosphere draws energy from the solar wind to create substorms which then perturb the high-latitude ionosphere. There are two major types of influence in question:

1. Energetic particles (electron and protons) from the Sun, the outer magnetosphere and the radiation belts can penetrate to the atmosphere and create ionisation at various altitudes, depending on the penetrating power or energy of the particles;
2. The solar wind blowing past the magnetic field of the Earth creates a dynamo which besides accelerating some of the charged particles to high energy, induces an electric field perpendicular to the magnetic field, which causes ionisation to drift horizontally and contributes to the formation of irregularities.

Table 3 lists for each band the auroral ionospheric effects that are known to occur and the most probable cause of the effect. In the majority of bands the E-region is involved. This highlights the importance of understanding the E-layer irregularities.

Crucial to the importance of the E_s-layer, is that at high latitudes the critical frequency of the F_2 layer (f_0F_2) is not much greater than the critical frequency of the E_s-layer (f_0E_s) and therefore most rays are cut off by the E_s-layer, showing up as one or two hop E_s-layer reflections instead of the expected one hop F_2 reflection. However, these E_s modes have different frequency/ground range dependencies than the F_2 mode. This phenomena known as “E-layer cut off” (Davies, 1965) is significant in high-latitude

regions because any frequency which penetrates the E_s-layer at a given point to reach the F-layer is also close to the maximum useable frequency (MUF) of the F_2 layer at its point of incidence with that layer.

Freq. Band	Effects	Most Probable Cause	Reference
ELF	Rapid changes in signal amplitude and phase	Changes in height and conductivity of D-region and sporadic-E	Davies, 1990 (Section 10.1 – 10.4)
VLF	As above	As above	Davies, 1990 (Section 10.5)
LF	Rapid changes in signal amplitude	D-region absorption and E-region irregularities	Davies, 1990 (Section 10.6)
MF	Radical Changes in signal strength	Auroral absorption, auroral E-region ionisation	Davies, 1990 (Chpt. 11)
HF	Radical Changes in signal strength, Doppler shift, off-great circle propagation	Auroral absorption, auroral E-region ionisation, F-region irregularities	Hunsucker, 1983 Hunsucker and Bates, 1969
VHF/ UHF	Amplitude and phase variations, bending of raypath (refraction)	Scatter and refraction from auroral E and F region irregularities	Davies, 1990 (Chpt. 13)
EHF	Ray bending, scintillation	Scatter and refraction	

Table 3. Auroral Ionospheric Effects as a Function of Operating Frequency (Based on Hunsucker, 1992)

The dimensionless value of x given by: $x = \frac{f_o F_2}{f_o E}$ determines the extent of E layer cutoff of F_2 modes. Another way of saying this is that at high latitudes only a limited range of takeoff angles, and hence a small span of ground ranges, is accessible to F_2 propagation modes at a given frequency compared to that normally accessible at mid-latitudes via this mode. The implications for HF communication are that although the F_2 mode results in good signal strength (being a one hop mode) it has severely limited

availability on account of E-layer blanketing. This phenomena is rarely present at lower latitudes because the ratio x is always significantly higher at lower latitudes.

Another factor detracting from the availability of the F_2 layer mode at high latitudes is the large variability on the timescale of fractions of an hour of the layer in these regions. The F_2 layer is known to have significant variability at mid-latitudes, often exhibiting variations of 1 – 2 MHz in the MUF(3000) over less than 1 hour (Paul, 1985). Although data on MUF(3000) variability at high latitudes is scarce, there are reasons to believe that the temporal variability in propagated frequencies for this mode would be even greater at high latitudes than at mid-latitudes. This variability can cause the real-time position of the peak frequency side of the one-hop F_2 propagation region to differ significantly from its median value given by propagation prediction algorithms.

If an F_2 mode MUF is estimated from median values of ionospheric parameters and an FOT[5] factor is applied to assure that the frequency of transmission will with reasonable certainty be below the real-time MUF, then there will also be a strong possibility that the chosen frequency will fall below the minimum frequency of the mode, thus preventing the intended one-hop F_2 propagation. In such a case, the only HF modes available for propagation to the desired ground range would be the one-hop E mode for ground ranges less than 1 800 km, or two-hop E layer modes for ground ranges between 1 800 and 3 000 km. Use of the two-hops E layer mode would incur

[5] FOT is in the transmission of radio waves via ionospheric reflection, the highest effective, i.e., working, frequency that is predicted to be usable for a specified path and time for 90% of the days of the month. The FOT is normally just below the value of the maximum usable frequency (MUF). In the prediction of usable frequencies, the FOT is commonly taken as 15% below the monthly median value of the MUF for the specified time and path.

about 10-20 dB more loss for such modes compared to one-hop F_2 modes due to the mode having to suffer two reflections and twice as many passes through absorbing layers as one-hop modes, but would be desirable from the standpoint of availability and bandwidth for a given ground range.

A further reason for unreliable F_2 mode propagation at high latitudes is the possibility of complete blockage (or screening) of the F layer by E_s. This occurs when the electron density in the E-region is sufficiently enhanced so that penetration of the layer is not possible and E_s blocks propagation via higher altitude layers. Such a layer of E_s would augment the power in a signal propagated at a frequency below the E layer MUF. For example, a highly ionised patch of E_s may make F_2 layer propagation impossible but may also contribute to a low-loss reflection point on an E mode propagation path thus enhancing that mode's signal quality.

While these characteristics can be helpful or harmful to radio communications, either type of E_s (i.e. partially blanketing and full blanketing) may extend the useful frequency range and its presence can be effectively used in system design and operations if it is understood (Lane, 2001). Hunsucker and Bates (1969) report that E_s is most important for communications at sunspot minimum, when E_s modes can occur more than 50% of the time on paths between Alaska and Greenland and Norway, with typical MUF's of 16 to 18 MHz. Jull et al. (1962) presented the results of an investigation of systematic HF channel sampling at oblique incidence and concluded that auroral E_s is a very important propagation mode over paths up to 2 300 km in the 3 – 30 MHz range.

The conclusion for high-latitude HF propagation to which one is led, based on the above discussion, is that since E-layer modes are not subject to blanketing by a lower layer, they therefore represent a wider band and hence are more reliable modes of propagation than the F_2 mode, which does suffer significant blanketing due to the E-layer and to sporadic E, and are consequently limited in bandwidth, or may even be completely absent. Of course, for the E_s mode path to be successfully used, the antenna at both the receiver and transmitter must have a suitable radiation pattern with sufficient gain to take advantage of the different range of transmission angles required to achieve the same ground-range as an F-layer using an E_s-layer reflection path.

2.3 Simple Case Study: Solar Disturbance on High-Latitude Propagation

This section is an investigation into the effect of delayed solar disturbances on a short (440 km) high-latitude propagation link. Measurements of signal-to-noise ratio, ionospheric absorption and angle of arrival data is used to demonstrate the variability of the high-latitude ionosphere and the gross effects of this variability on a HF link. This study lead to the conclusion that in addition to ionospheric absorption, propagation mode changes have a significant effect on the link path, which in turn leads to the work undertaken in Chapter 3 and 4.

2.3.1 Equipment Details and Set-up

Data from a high-latitude HF link experiment was sourced from Dr. Alan Stocker of the Engineering Department of Leicester University (Stocker, 2005a). In figure 15 the

link receiver and transmitter sites are plotted on an azimuthal equidistant projection[6]. The receiver station is located in Kiruna (67.84^0N/20.42^0E), Sweden's most northerly municipality. The six receivers and vertical monopole antennas are arranged in a circle and the system can provide an estimation of elevation with a resolution of $\pm 5^0$ and an estimation of azimuth with a resolution of $\pm\ 1^0$ to 2^0. The 100 watt transmitter (T) is located 440 km away, near Kirkenes in Northern Norway (69.717N/30.05E). The transmitter antenna, similar to those in use at the receiver site, is a vertical monopole, which is usable over the range 3 – 18 MHz. The system switches between two spot frequencies - 4.455 MHz and 6.780 MHz, and each frequency is sampled 15 times per hour.

Figure 15. Plot of the link receiver (R) and transmitter sites (T) on an azimuthal equidistant projection.

The system measured, amongst a number of parameters, the signal-to-noise ratio (SNR) in a 3 kHz channel which for this analysis is averaged over each hour. In addition the peak-to-mean values of the SNR is measured as a proxy for SNR quality. A peak-to-mean threshold of 3 – 3.5 dB was used to ensure that the SNR value used

[6] More commonly called a great circle map. This projection is unique for each place on Earth and produces a map in which points on the same bearing lie along straight lines. Distance along those straight lines is proportional to distance along the great circle with that bearing.

was measured from a usable signal. The last parameter used from this experiment is the peak elevation angle of arrival of the strongest signal measured during the sample period.

Data from the IRIS Riometer at Kilpisjärvi (69.10N, 20.80E, L=6.06) was used to measure the ionospheric absorption resulting from particle precipitation. The RIOMETER (Relative Ionospheric Opacity Meter using Extra Terrestrial Electromagnetic Radiation) is a simple instrument developed in the 1950s (e.g. Little and Leinbach, 1959) that makes medium scale measurements of ionospheric absorption of cosmic noise at a frequency in the order of 30 MHz. Operation is passive and the background cosmic radio noise from the sky is constantly monitored. By comparing the background cosmic radio noise from the sky against the received signal for an undisturbed day it is possible to determine the variation of ionospheric absorption.

In essence a riometer observes temporal variations in ionisation in the D and E-regions caused by charged particle precipitation (Hargreaves, 1969), by electrons in the energy range of ~ 10 to 100 keV (Wilson and Stoker, 2002). Figure 16 shows the location of the IRIS riometer and its theoretical antenna patterns in relation to the ideal path of the HF link. While the most common form of riometer uses a wide beam antenna with bandwidths in the order of 60^0, the IRIS has 49 narrow beams of beamwidth between 130 and 160 (Browne at al., 1995) and operates as a fast-scan multiple beam instrument which examines the whole ionospheric sky to 450 from zenith.

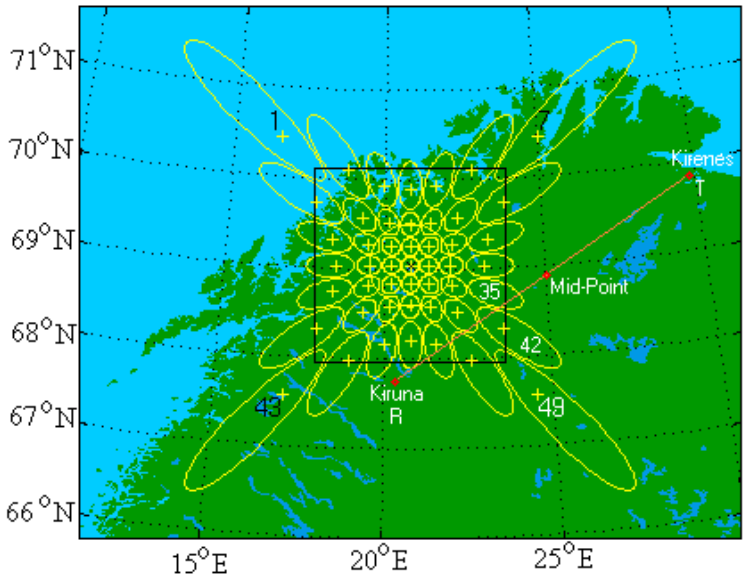

Figure 16. Location of Transmitter paths through the IRIS Riometer field of view.

The HF radio path from Kirkenes to Kiruna has a mid point just east of riometer beams 28 and 35.

2.3.2 Ray Tracing the Path.

In order to reduce complexity many of the operational aspects of HF propagation are studied using simple ray concepts. This assists in evaluating the point where an HF ray launched upwards towards the ionosphere returns again to the ground and the procedure is also used to determine the control points of the propagation path. The simplest ray tracing technique is known as virtual ray tracing and it assumes that the actual propagation can be approximated by reflection from a single horizontal mirror at an approximate height using the secant law, Breit and Tuve's theorem and Martyn's equivalent path theorem (e.g. Mc Namara, 1991).

This approach is implemented in most HF prediction decision aids as the major advantage of this approach is that it is computationally efficient. Its major disadvantage is that it cannot deal with a horizontally non-stratified ionosphere. It may, therefore, be considered an approximate method and more complicated ray tracing methods are necessary in certain situations. Virtual techniques are, however, well matched to a median ionospheric database and simple ionospheric profiles. Indeed, in most circumstances, the use of a more complicated model is not justified given the available ionospheric model (Cannon, 1994).

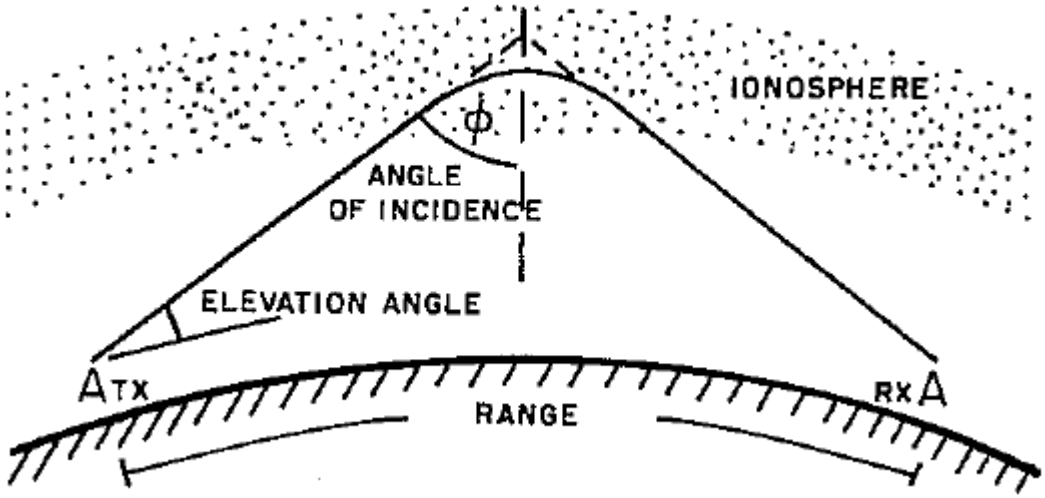

Figure 17. Simple geometry of an HF oblique circuit, illustrating the essential elements of the circuit (after Jursa, 1985)

Figure 17 illustrates the basic geometry of a one-hop HF circuit, note that the diagram ignores the ground wave as the focus of this report is solely on the sky-wave. The reflected ray is continuously refracted as it passes through the ionosphere and if sufficient refraction occurs the ray will bend down sufficiently to reach the receiver. In order to understand the maximum range that can be achieved and how the frequency in use affects this range requires an understanding of the secant factor. The

maximum oblique frequency, f, which can be supported by an ionospheric layer of critical frequency (f_c) can be approximated by:

$$f = f_c \, k \sec j$$

Where φ is the angle of incidence of the equivalent ray path to the normal to the ionosphere at the reflection point as shown in figure 17 and k is a factor that accounts for the curvature of the Earth; k ≈ 1.0 for short ground ranges and for extreme ground ranges. At ranges of 1 500 km Goodman (1992) has shown that k ≈ 1.4. The ratio f/f_c is known as the secant factor. The angle of incidence, φ, can be determined from the ground range of the propagation, D, and the virtual height of reflection, h', by first calculating the elevation angle Δ from

$$h' = R_e \left\{ \tan(\Delta + a) \sin a + \cos a - 1 \right\}$$

Where R_e is the radius of the Earth and α is half the angle subtended at the Earth's centre by the transmitter and receiver, divided by the number of hops n:

$$a = \frac{D}{2nR_e}$$

Then φ is given by:

$$\tan j = \frac{1}{\tan(\Delta + a)}$$

These equations can be used to determine the maximum frequency that will propagate along a path of given ground range and reflection height ($h' \approx 100$ km for E-region modes and $h' \approx 250$ – 350 km for day and night F region modes respectively), as a function of the layer critical frequencies f_0E and f_0F2 determined from ionosonde observations.

Figure 18 reflects the mode geometry of the link and is a basic ray trace of the possible 1E, 2E, 1F and 2F propagation modes through the ionosphere. The vertical axis is altitude above the Earth's surface in km. The curved horizontal axis is distance along a great circle path between transmitter and receiver along the Earth's surface, assuming a perfectly spherical surface[7] and symmetrical ray paths around a centre reflection point(s).

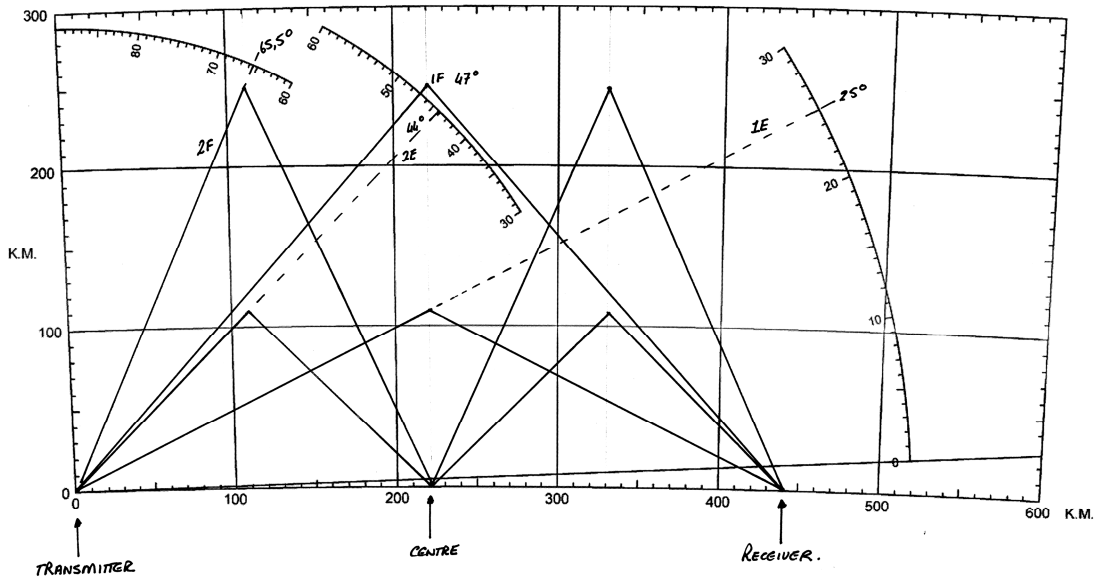

Figure 18. Kirkenes to Kiruna Mode Geometry.

Figure 18 shows the typical angle of received signal that is expected for each propagation mode on the path assuming a constant E-layer virtual height of 110 km and a constant F-layer virtual height of 250 km. One principal difficultly is that the 1F and 2E paths have similar arrival angles and it may be difficult to tell them apart.

[7] This assumption over a 440 km distance is not unreasonable.

2.3.3 Measurements: Day 81 of 2004 (21st March 2004)

Solar activity leading up to the 21 March 2004 was at low levels[8]. On the 21 March, sunspot region 576, while transiting the west limb of the Sun, produced the largest flare of the day, a C6 flare at about 10:00Z. The daily smoothed sunspot number for this day was 48. The geomagnetic field was quiet, solar activity was low and there were no active sunspot regions on the sun to produce PCA in this 24 hour period and there were no proton events during the day. Ionospheric disturbances that occur on this day are due to the delayed effects of an earlier solar disturbance.

Figure 19 captures a number of parameters for the 24-hours of day 81. The hourly average absorption seen in beam 35 of the IRIS riometer, scaled to the frequency in use on the path (6.780 MHz), is represented in blue. The left hand vertical axis represents the SNR in dB (red) and the left hand vertical axis represents the absorption data in dB. The offset right hand vertical axis represents the elevation angle of the strongest received signal (black). The x-axis gives the time (UTC) where 81.5 represents noon on day 81.

Signals are received in the early morning (81.0 to 81.1) and from 7:00 (81.3) to 14:30 (81.6). There was sporadic reception between 81.6 and 81.8 and constant reception from then until midnight. A large increase in absorption during the early morning (e.g. the period 01:30 (81.05) to 07:00 (81.3)) results in a complete loss of signal. This is not particularly surprising as there is a direct connection between high levels of absorption in the D-layer through which the ray path travels that results in a reduction of the received signal strength, to the point of complete absorption in some cases.

[8] The solar and geomagnetic activity information used is gleaned from the daily joint USAF/NOAA reports of solar and geophysical activity (NOAA 2005).

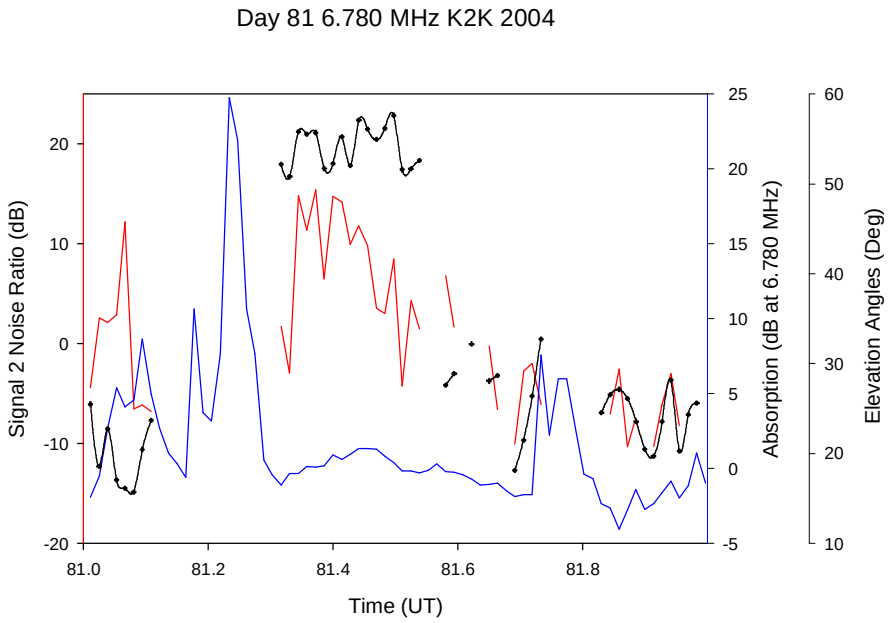

Figure 19. Day 81 of 2004: Measurements of SNR, Absorption and received signal Elevation Angles on the Kirkenes to Kiruna (6.780 MHz).

Of greater interest in this case study is the change in received signal elevation angle which needs far more detailed analysis. During periods of absorption the elevation angle is of the order of ($20^0 \pm 5^0$) which with reference to figure 18 implies a 1E mode is active. For example, for the period 81.0 to 81.1 absorption reached values of 8 $dB_{6.780MHz}$ and the elevation angle spanned 15^0 to 25^0. During periods of low absorption the elevation angle was in the range of 50^0 to 58^0 which implies either a 1F or a 2E mode was active. For example, for the period 81.3 to 81.55 absorption was less than 1.5 $dB_{6.780MHz}$ and measured elevation angles were above 50^0.

However, as further analysis will show these assumptions are simplistic as the change in virtual height of the E and F–layers, as well as the critical frequencies of each layer, have not been considered. Figures 20 and 21 have been calculated using the formulae given in section 2.5.2.

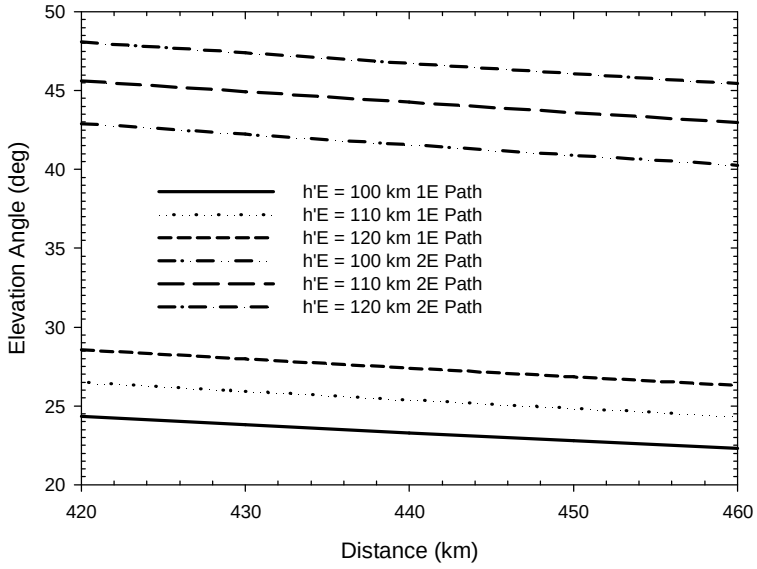

Figure 20. Range of elevation angles for 1E and 2E ray paths due to a changing E-layer virtual height.

Figure 20 shows the range of elevation angles that can be expected on 1E and 2E ray paths as the virtual height of the layer (h'E) changes from 100 km to 120 km. For a ground range of 440 km the elevation angles vary for a 1E path from 23^0 to 28^0 and for a 2E path from 41.5^0 to 47^0.

Figure 21 shows the same detail for the F-layer for h'F of 200 to 300 km. For a ground range of 440 km the range of elevation angles for a 1F ray path vary from 40.5^0 to 52^0 and for a 2F path from 60^0 to 69^0. Furthermore, the effect of varying critical frequencies needs to be examined to see if these variances are limiting the possible mode of propagation. The minimum critical frequency required at the mid-path reflection point for a variety of virtual E and F layer heights for two different ground ranges are shown in figure 22. The top curve (blue) is calculated for a ground range of 220 km which is the first reflection point for a 2E or 2F ray. The lower trace

(black) is calculated for a ground range of 440km which is the mid-path reflection point.

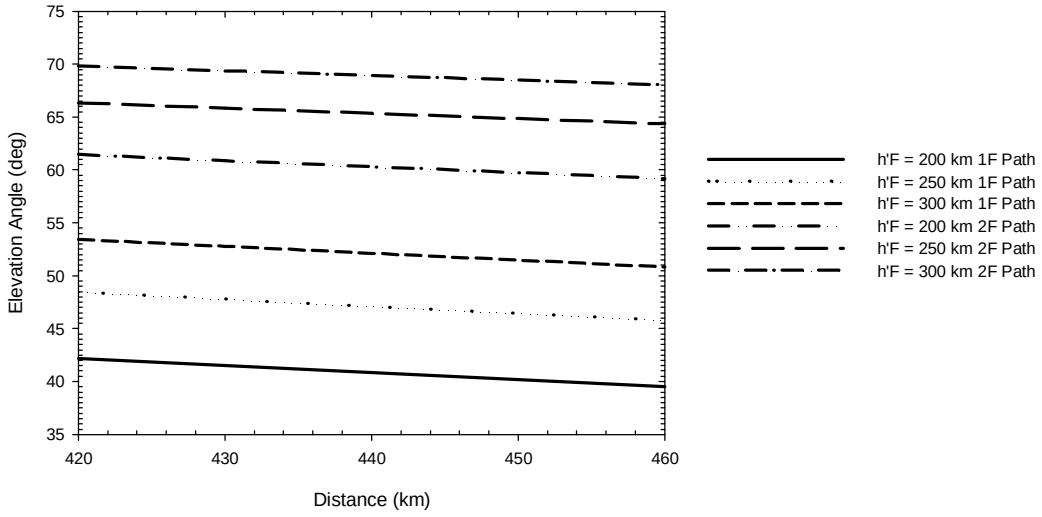

Figure 21. Range of elevation angles for 1F and 2F ray paths due to a changing F-layer virtual height.

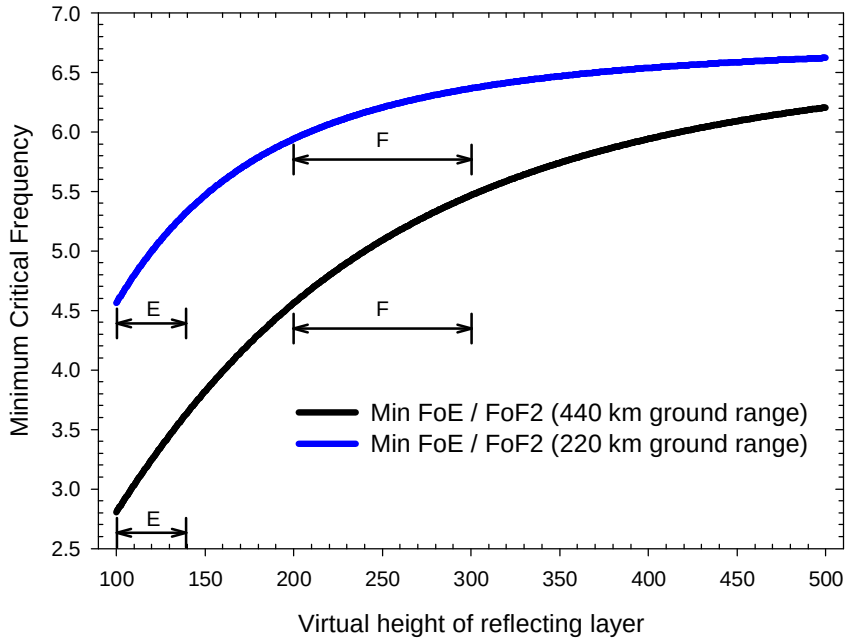

Figure 22. Minimum critical frequency required for changing virtual heights of the reflecting layer for ground ranges of 440 km and 220 km.

For a ground range of 440 km and a 1E mode where h'E ranges from 100 to 150 km a minimum f_0E of 2.8 to 3.6 MHz is required. For a 1F mode where h'F ranges from 200 to 300 km a minimum f_0F of 4.6 to 5.5 MHz is required. For a ground range of 220 km and a 2E mode where h'E ranges from 100 to 150 km a minimum f_0E of 4.5 to 5.3 MHz is required. For a 2F mode where h'F ranges from 200 to 300 km a minimum f_0F of 5.9 to 6.4 MHz is required. It can be seen that the values of E and F layer critical frequencies are significantly increased as the radio wave impinging on the layer moves closer to the perpendicular.

With these two additional pieces of knowledge, i.e. the variation of elevation angle with a varying reflection layer height and the minimum critical frequency needed for a fixed ground range, a further analysis is now possible.

Figure 23 is a modification of figure 19. While the x-axis is time (UT) the right hand y-axis is now the elevation angle of the received signal. The right hand y-axis is the critical frequency of the F-layer (f_0F) and the off-set right hand y-axis is the critical frequency of the E-layer (f_0E). These hourly values are taken from the daily f-plot[9] produced by the Sodankylä observatory as determined from their ionosonde data. Figure 24 is in turn similar to figure 19 except that the right hand y-axis now shows the virtual height of the E & F layers instead of critical frequency. These values are also extracted from the daily ionospheric virtual height plot from the Sodankylä observatory.

[9] See chapter 4, section 4.2.2 for an explanation of the f-plot.

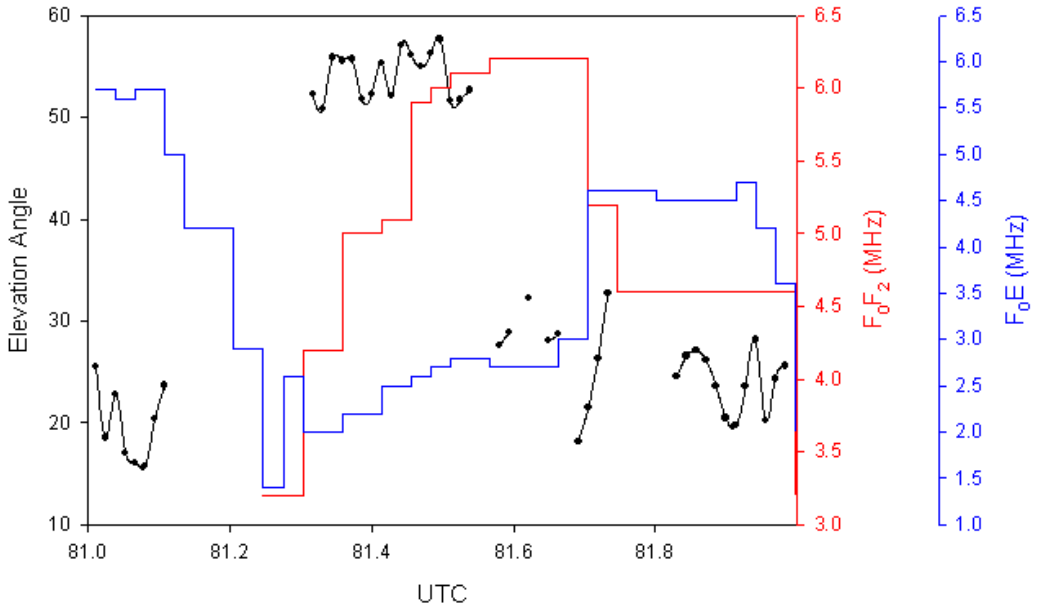

Figure 23. Range of elevation angles, F_0F_2 and F_0E measured over day 81 of 2004.

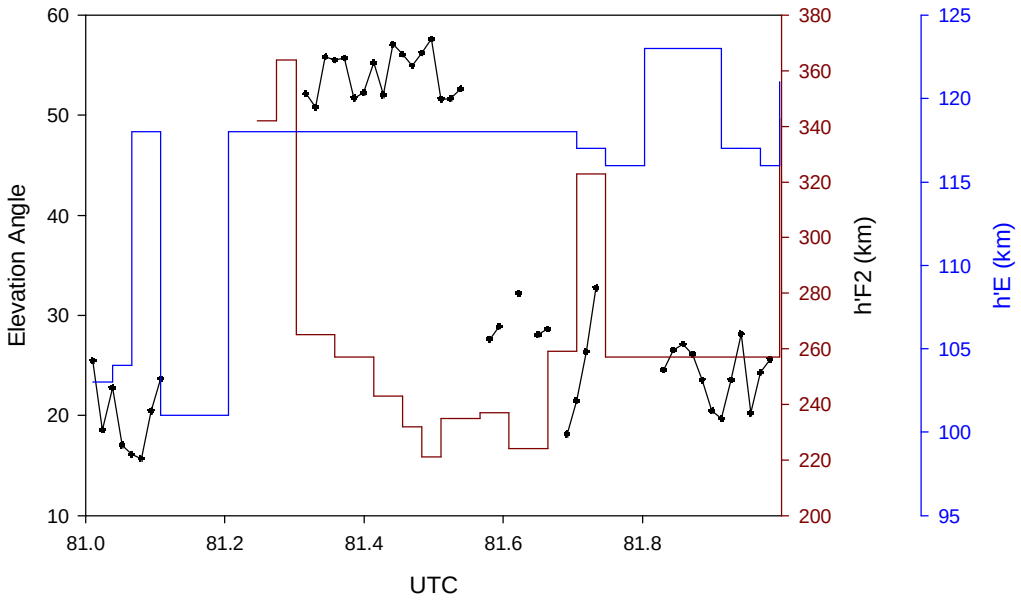

Figure 24. Range of elevation angles, h'F_2 and h'E measured over day 81 of 2004.

With reference to figures 23 and 24 we first examine the period from **81.0 to 81.2** – the ionosonde cannot penetrate the E-layer which has a relatively high $f_0E \approx 5.5$ MHz. As evidenced earlier in figure 19, there are sporadic bursts of absorption, in some

cases as high as 25 $dB_{6.780MHz}$. The occurrence of absorption indicates that particle precipitation is taking place and this precipitation affects the D-layer (absorption due to ionisation) as well as the E-layer (enhanced f_0E due to increased ionisation). During this period h'E changes from 105 km to 120 km and then returns to 105 km. Examining figure 23 shows that an f_0E of 5.5 to 3 MHz was measured and taking into account the range of elevation angles measured, only a 1E path is achievable. This removes any doubt left by the initial analysis that a 2E or 2F mode might also be active during this period.

Between **81.0 to 81.2** D-layer absorption caused the link budget margin to be exceeded and no measurements were made on the HF link. After 81.3 there is very little absorption measured until 81.8 which implies that during his time there was a reduction in particle precipitation.

Between **81.3 to 81.6** the elevation angle of the received signal increased to between 50^0 and 60^0. F_0E has fallen to 2 MHz rising to no more than 2.8 MHz over this period. h'E is constant at 117 km for this entire period. f_0F increases from less than 3 MHz to its highest value on this day of 6.2 MHz and h'F falls from 340 km to 220 km. This shows the limit in using only ray tracing as per figure 18 that does not take the constant modulation in layer heights into account. The increase in h'F and the consequential change in elevation angles are consistent with a 1F mode of propagation for this entire period.

For the period **81.6 to 81.8** a number of simultaneous changes complicate the analysis somewhat. The elevation angle of the received signal reduces to between 20^0 and 32^0. F_0E increases from 2.8 MHz to 4.5 MHz, well within the minimum critical frequency

required for a 1E mode to be active. h'E is steady in the range 120 to 115 km. F_oF_n reduces from 6.2 MHz to 5.2 MHz within the minimum critical frequency required for a 1F mode to be active and h'F increases from 220 km to 320 km before settling at 260 km. Between 81.6 and 81.7 f_0E is constant, h'E changes by only 5 km and the elevation angle varies slightly around 30^0. From 81.7 to 81.8 the elevation angle increases almost linearly from 18^0 to 32^0 which correlates to a similar increase in h'E values from 110 km to 115 km, and a simultaneous increase in f_oE from 2.5 MHz to 4.5 MHz. This period coincides with renewed absorption activity and the associated enhancement of E-layer ionisation. On this evidence it is concluded that during this period the E-layer is in control and that a 1E mode is again active.

For the period **81.8 to 82.0** the range of elevation angles, if the increase in h'E is taken into account, are very similar to the period 81.0 to 81.2. F_0E is constant for most of the period at 4.5 MHz and falls to 3.4 MHz at the end of the period but at both extremes is still within the range of minimum critical frequencies required for a 1E mode to be active. h'E is fixed at 122 km for most of the period and falls slightly to 117 km towards the end. F_0F is constant at 4.5 MHz and h'F is constant at 260 km. With the low elevation angles measured and the low F_0F it is not possible for any F mode to be active and it is concluded that a 1E mode is active during this period.

2.4 Detailed Case Studies: SSC and its Effects

The two case studies presented in this section examine two north-south auroral propagation paths following the onset of a geomagnetic disturbance. The key difference in the two case studies is the great circle path length between the transmitter and the receiver. In the first case study with a path length of 1 807 km the

1E mode of propagation dominates following the SSC. In the second case study, with a path length of nearly 3 000 km, the 2E mode of propagation dominates.

2.4.1 Data and Instrumentation

The primary instrument used in the following two case studies to demonstrate the effect of E_s-layers on HF communications immediately following an SSC event is an oblique sounder. The University of Leicester oblique sounder system consisted of a swept frequency HF transmitter at Isfjord, Svalbard and a receiving system set up initially at the Collaborative UK Twin Located Auroral Sounding System (CUTLASS) radar site in Hankasalmi, Finland and then at Malvern, UK. The transmitter was operated by the Defence Evaluation and Research Agency (DERA), Malvern, and consists of an exciter unit developed and built by the Radio and Space Plamsa Physics Group at Leicester University and a transmitter built by DERA. The unit transmits a chirp signal ranging in frequency from 2 to 30 MHz into a broadband antenna. The transmitter power is approx 10W and the sweep time is approx 5 minutes. The receiver consists of the DERA Iris receiving system supplemented by a communication system developed at Leicester to provide real-time control and data recovery (University of Leicester, 2007).

Oblique ionograms obtained from the system indicate the modal structure of signals propagating between Svalbard and Hankasalmi and Svalbard and Malvern at frequencies up to 30 MHz. Soundings were carried out at 15 minute intervals and the results are shown as oblique ionograms. An example of an oblique ionogram captured by the system during a quiet period is shown in figure 25. The abscissa is sounding frequency in MHz and the ordinate axis is group delay in milliseconds.

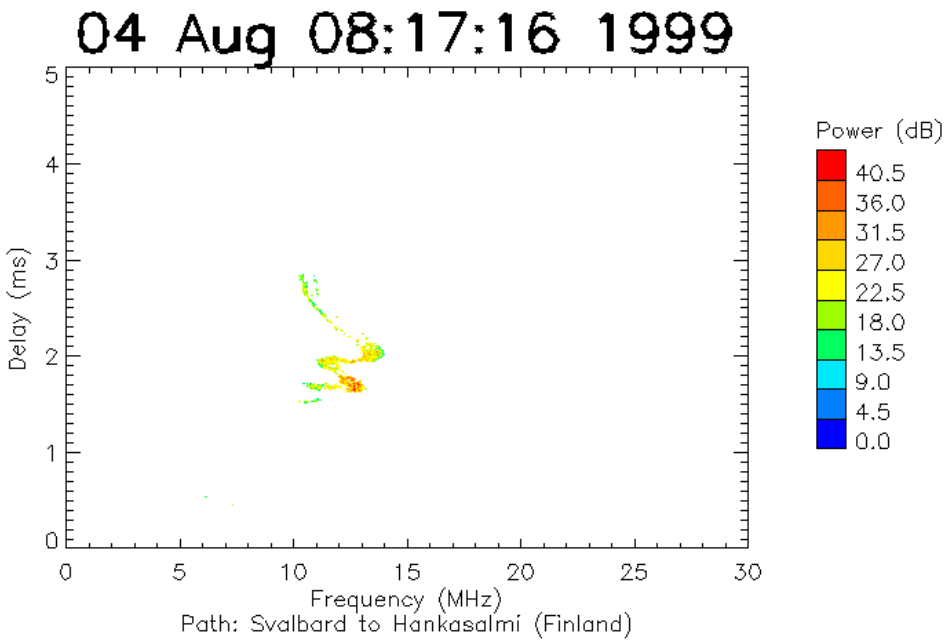

Figure 25. Example of an Oblique Ionogram during a quiet period.

The delay indicated on the oblique data used in this report is a relative delay rather than an absolute delay. The receiver locks onto the earliest arriving signal and uses that to set the axis. It is easy to see the difference in delay times between the single hop F_1 reflection and F_2 reflections (Stocker, 2007).

Supporting data is obtained from vertical sounders, more commonly known as ionosondes, located at Tromsø and Gakona. The basic principle of vertical incidence ionospheric sounding is that HF radio waves are reflected at the cut-off frequencies of the ionospheric magnetoplasma. To probe the E- and F-regions of the ionosphere, a vertical sounder scans from 1 to 20 MHz, transmitting modulated radio waves and receiving and analysing the reflected echo signals form the ionosphere (Wright et al., 1957; Piggott and Rawer, 1972). Conventionally the ionosonde presents the demodulated echo signals as time of flight (range) versus sounding frequency in the

form of ionograms. Extensive details on ionosondes and their applications are given in Ivanov et al. (2003) and Reinisch (1996).

Electron densities in the E- and F-regions are obtained from incoherent scatter radars (ISR), namely the European Incoherent Scatter (EISCAT) UHF radar near Longyearbyen and the Incoherent Scatter Radar (ISR) at Sondrestrom, Greenland. In the ISR method, incoherent scatter is produced by backscatter from the thermal irregularities in the ionization in the upper atmosphere. The signal amplitude and spectral shape yield the electron density and electron and ion temperature, while the spectral shift yields the average velocity of the ions (Bates et al., 1974).

Solar Wind and IMF data is obtained from measurements taken by the Advanced Composition Explorer (ACE) spacecraft. The ACE satellite carries high-resolution sensors and monitoring instruments that sample the parameters of low energy particles of solar origin and high-energy galactic particles. See Stone et al. (1998) for comprehensive details of the satellite and instrumentation.

Magnetometer data was collected from the Glenmore Lodge magnetometer which is part of SAMNET, the UK Sub-Auroral Magnetometer Network which continuously records natural variations in the Earth's magnetic field giving information about the complex interactions within the coupled Solar Wind-Magnetosphere-Ionosphere system. Each station records the magnetic field in three orthogonal components: H, D and Z, these being horizontal magnetic northwards, horizontal magnetic eastwards and vertically downwards.

Riometer data was obtained from the Imaging Riometer for Ionospheric Studies (IRIS) located at Kilpisjärvi, Finland. Table 4 details the location of all instruments used in these studies which are shown in figure 26, on a great circle map centred on the oblique sounder transmitter at Svalbard.

Code	Instrument - Location	Location	
		Latitude	Longitude
A	Oblique Sounder Transmitter – Svalbard	78.21 N	15.63 E
B	Oblique Sounder Receiver – Hankasalmi	62.32 N	26.61 E
C	Oblique Sounder Receiver – Malvern	52.10 N	2.32 W
D	Vertical Ionosonde - Tromsø	69.60 N	19.20 E
E	Vertical Ionosonde - Chilton	51.60 N	358.7 E
F	Vertical Ionosonde - Gakona	62.12 N	214.86 E
G	ISR – Eiscat Svalbard Radar	78.20 N	15.82 E
H	ISR – Sondrestrom, Greenland	66.99 N	309.05 E
I	Magnetometer – Glenmore Lodge	57.16 N	3.68 W
J	Riometer – Kilpisjärvi	69.10 N	20.80 E
	Advanced Composition Explorer Satellite	L1 Libration Point	

Table 4. Instrument location Details

Table 5 details the bearing and range of the great circle propagation path between the oblique sounder transmitter and both oblique sounder receiver sites shown in figure 26.

Path	Bearing (Deg.)	Distance (km)
Great circle propagation path from A to B	161.6	1807
Great circle propagation path from A to C	204.7	2990

Table 5. Bearing and distance information for both great circle propagation paths.

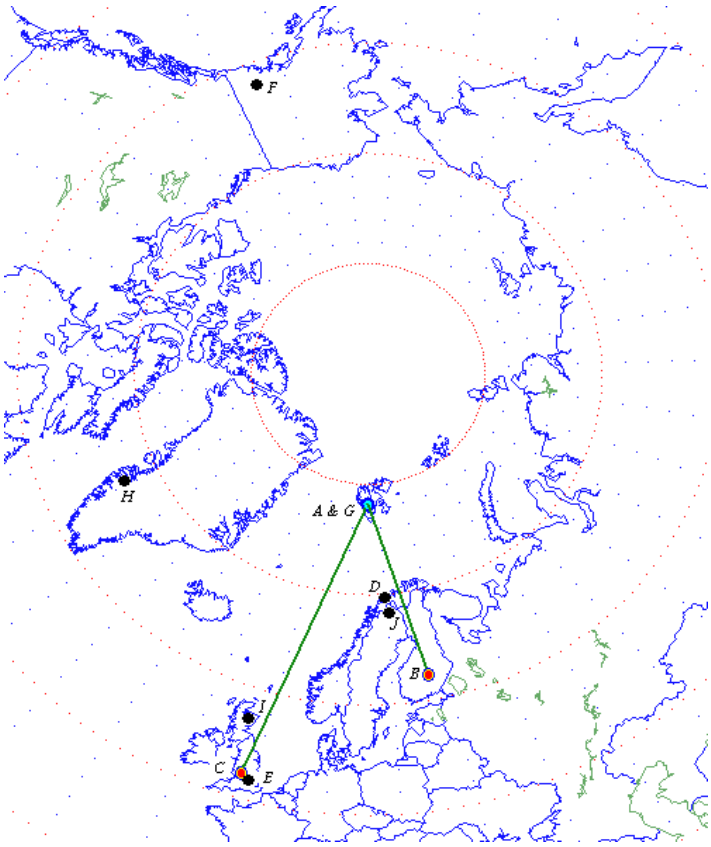

Figure 26. Great circle map centred on the oblique sounder transmitter at Svalbard showing the locations of all the instruments mentioned. Alphabetic codes indicate the instrument as listed in table 4.

2.4.2 The SSC of 31 July 1999

This case study examines the propagation path between Isfjord, Svalbard and Hankasalmi, Finland a distance of 1 807 km following an SSC at 18:27 UT on 31 July 1999.

In the period preceding 31 July 1999 solar activity ranged from low to high levels (NOAA, 1999a). Solar activity increased to high levels on 29 July by virtue of an impulsive M5 flare on 29 July at 19:34UT from Region 8651 which was accompanied

by minor discrete radio emissions. Activity returned to moderate levels on 30 July with another isolated, low-level M-class flare from Region 8649. A coronal mass ejection signature was evident on 30 July with a velocity increase from 380 - 680 $km.s^{-1}$, increased densities, and a period of sustained southward IMF B_z with deflections to minus 12 nT (GSM). Activity decreased to low levels on the day following the SSC with occasional C-class flares from Regions 8645 and 8651. No proton events were detected at geo-synchronous orbit during the period. The solar wind and IMF data for the immediate period of the SSC is shown in the top four panels of figure 27.

The top panel of figure 27 represents the solar wind particle density (cm^{-3}) against time. At 17:40 UT following seven hours of low activity and low density (1.37 cm^{-3}) the density increases very quickly to 11.4 cm^{-3}. The density remains at elevated levels for more than one hour before moderating. The third panel of figure 27 represents B_z, the north - south component of the IMF. B_z is positive when, in parallel with the Earth's field, the northward direction of the magnetic field points upwards. At the magnetopause the Earth's magnetic field and the IMF come into contact. If the IMF points southwards (i.e. B_z is negative) then the IMF can partially cancel the Earth's magnetic field at the point of contact, make direct connection with field lines and allow the injection of energy into the magnetosphere. Southward turning of the IMF initiates changes in the configuration of the magnetosphere, earthward displacement of the magnetopause and tailward stretching of the field lines, where energetic particles are more subject to precipitation due to changes in drift shells (Ranta and Ranta, 1990)

From 10:00UT to 15:30 UT, B_z is mainly northwards with a few short excursions southward. Just before 15:30UT, B_z becomes predominantly southward with an excursion northwards around 16:00UT. Coinciding with the sudden increase in density (panel 1) at 17:40 UT is a sudden change in the direction of B_z from south to north. B_z turns southwards again after two hours of maintaining its northwards direction. Panel 2 of figure 27 represents the solar wind particle velocity ($km.s^{-1}$) and shows an increasing velocity coinciding with the increase in particle density, IMF field strength and the change in B_z. The values of solar wind particle density and velocity have a direct and strong correlation to the amplitude of the IMF which in turn influences the location of the magnetopause (Fairfield, 1971).

These sudden enhancements in the solar wind dynamic pressure are known to compress the magnetosphere and enhance the magnetopause current (Kauffman and Konradi, 1969), as well as the tail currents (Russell et al., 1994). Zesta et al. (2000) noted in a study of 10 January 1977 disturbance that the response of the magnetosphere to a pressure front was practically instantaneous, global and directly driven by the propagation of the solar wind density enhancement region through the magnetosphere. The disturbance is transmitted throughout the magnetosphere in the form of hydromagnetic waves and has been observed both at satellite altitudes and on the ground as a sudden increase or decrease in the geomagnetic field strength. Corresponding to the changes in geomagnetic field strength are changes in the magnetic field geometry, the electric field configuration as well as changes in thermal and energetic particle distributions.

The geomagnetic field was at quiet to unsettled levels until 31 July when a sudden storm commencement occurred at 18:27 UT followed by active to major storm levels with brief severe storm periods at high latitudes. The disturbance continued until 1 August (not shown here). Magnetometer data for the immediate period of the SSC is shown in the bottom panel of figure 27. It can be seen that the disturbance in the solar wind measured at the ACE satellite at 17:40 UT took circa 45 minutes to reach the magnetosphere and for the effect to be measured by the Glenmore Lodge magnetometer at 18:25 UT where the H-component increased from 1171 nT to a peak of 1249 nT over a period of 6 minutes.

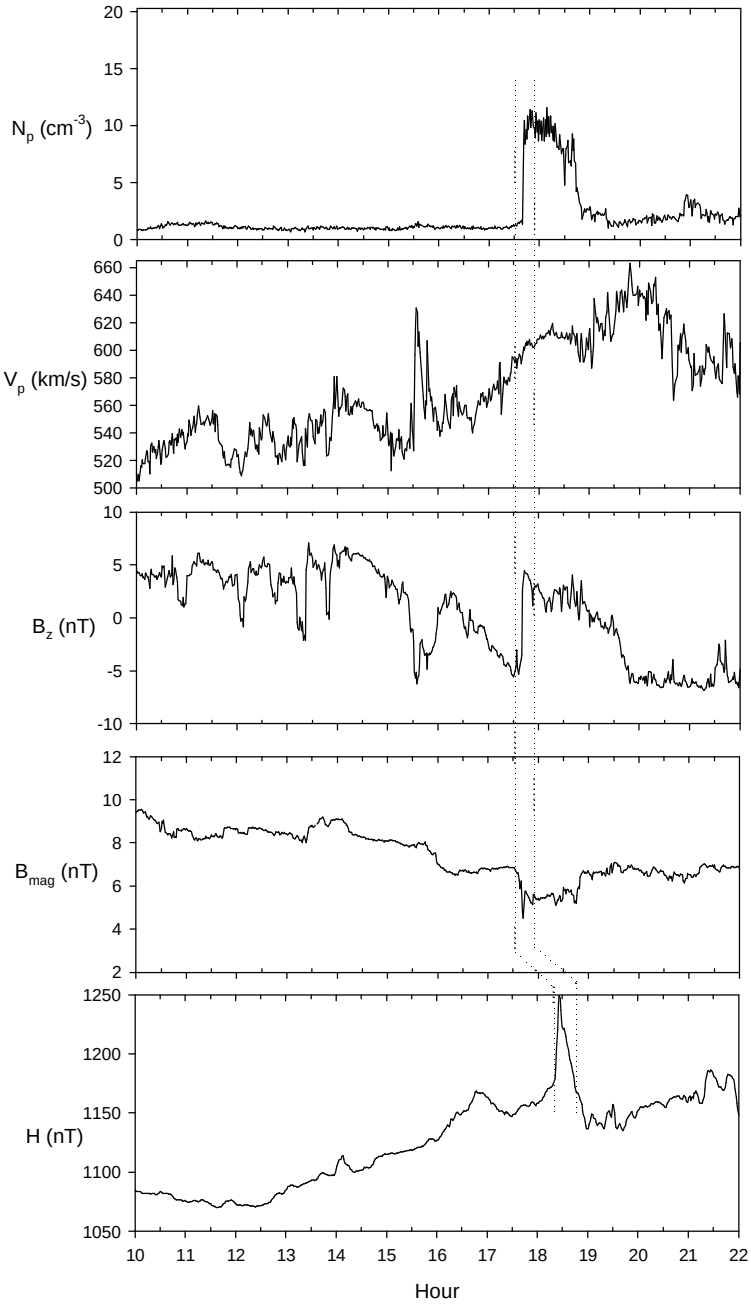

Figure 27. Solar Wind / IMF data from the ACE Satellite for the first case study is shown in the top four panels, namely; plasma density, speed, the B_z magnetic component and total field strength. Magnetometer data (the horizontal intensity (H) component) is shown in the bottom panel. Dashed lines indicate the period of disturbance.

Figure 28 is a selection of oblique sounder ionograms covering the period from 25 minutes before to 60 minutes after the SSC occurred. Twenty-five minutes before the SSC occurred the ionosphere is fairly quiet as the oblique ionogram in panel A of figure 28 reflects. Panel A shows reflections from 8 to 11 MHz from the F-layer and at the incident angle required to achieve a one hop F-layer path between transmitter and receiver the F-layer oblique critical frequency is approximately 11 MHz. At lower take-off angles the E_s-layer becomes usable for signals between 11 and 15 MHz along this path.

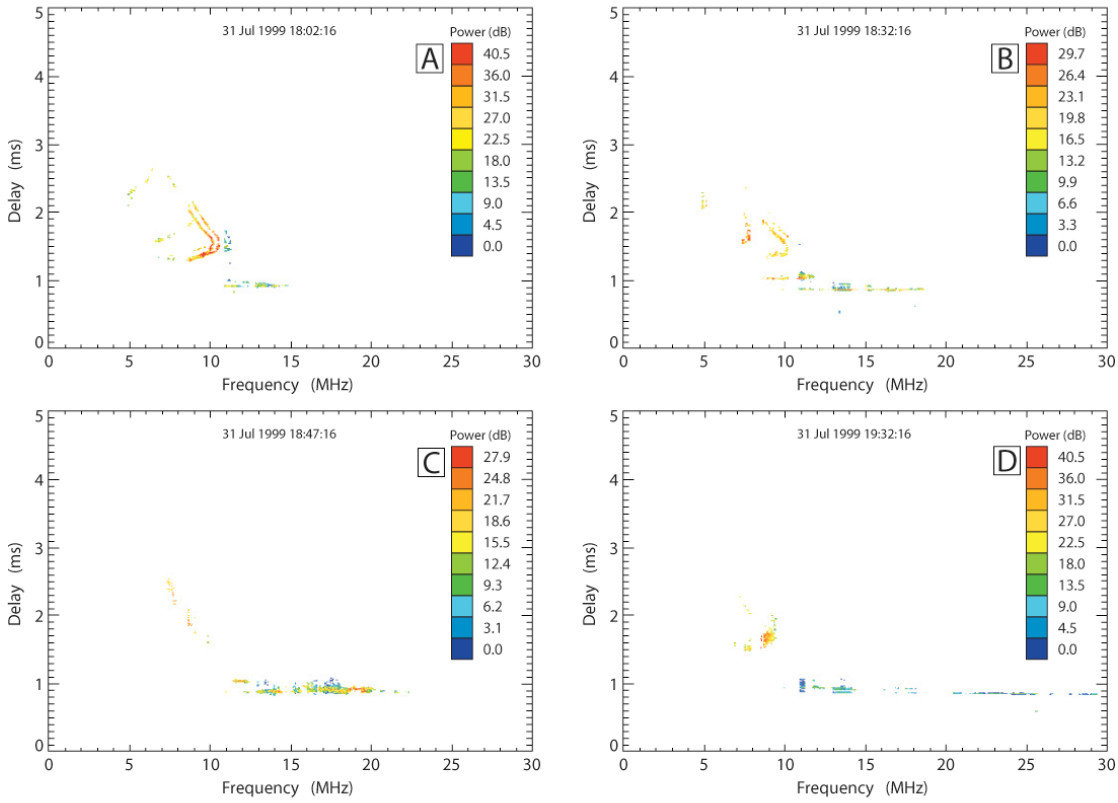

Figure 28. Selection of oblique ionograms from the Svalbard to Hankasalmi Path.

Panel B of figure 28 captures the situation five minutes after the SSC occurs when particle precipitation and the resultant enhanced E-layer ionisation has set in. While

the F-layer still provides a valid path the enhanced electron density due to precipitation has increased the usable frequency of the E-layer well above the initial value to 15 MHz. Between 9 and 10 MHz there are now two ray paths in existence, one from the F-layer and a new path from the E_s-layer.

Panel C of Figure 28 - Twenty minutes after the SSC when the E_s-layer is enhanced further as evidenced by the higher power returns, the useful frequency of the E_s-layer is further extended to more than 20 MHz. The F-layer path has degraded due to intense D-region absorption attenuating the lower frequencies, as will be seen in figure 29.

Panel D of Figure 28 - One hour after the SSC occurs, the F-layer is starting to recover with a critical frequency of 9 MHz and the E-layer enhancement, while patchy and a much weaker path than the F-layer path, can now support frequencies up to 30 MHz.

Figure 28 captures the absorption measured by beam nine of the Kilpisjärvi riometer. For this study the riometer is not ideally located to measure absorption at the exact point where the ray penetrates the D-layer and is only used to illustrate the general pattern of D-layer absorption in the area.

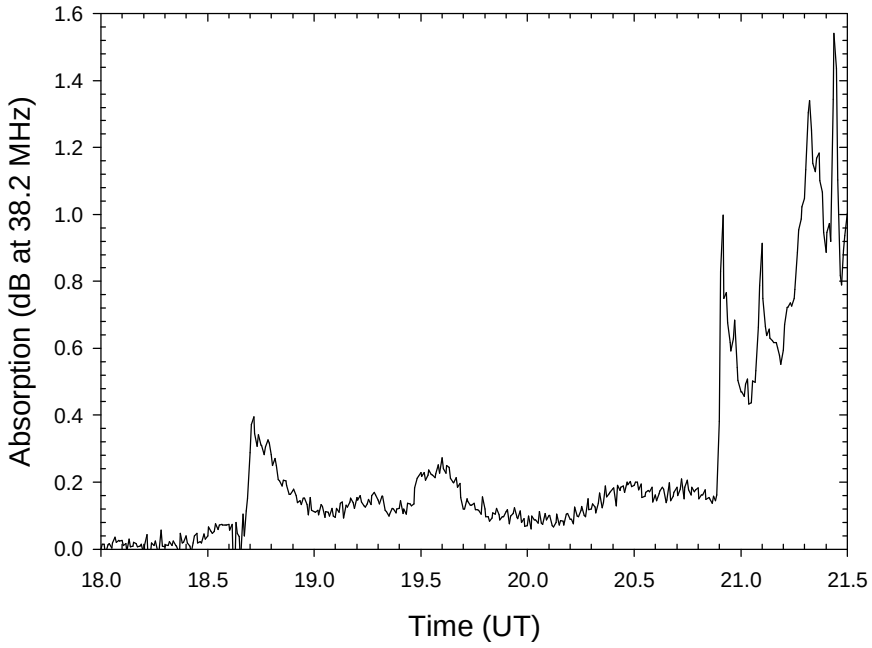

Figure 29. Riometer data from the Kilpisjärvi riometer – absorption data is from beam 9

Before the SSC at 18:27UT the absorption measured at 38.2 MHz is less than 0.1 dB. Following the SSC the absorption increases and at 18:47UT (figure 28, panel C) the absorption has increased to 0.4 dB. Neglecting the effects of the Earth's magnetic field, auroral absorption can be shown to be inversely proportional to the square of the operating frequency (Browne, et al., 1995), therefore 0.4 dB of absorption measured on the riometer at 38.2 MHz equates to 23 dB absorption at 5 MHz and to 6 dB at 10 MHz. Of course, any ray reflecting in the ionosphere at the mid point would suffer twice this absorption as the ray penetrates the D-layer twice. At 19:32UT (figure 28, panel D) the absorption has reduced slightly to 0.3 dB and continues to fall until 20:02 UT (figure 30, panel A) before increasing again (as reflected in figure 30 panel B) at 20:32 UT to values in excess of 1 dB absorption (measured at 38.2 MHz) which equates to 58 dB absorption at 5 MHz and 15 dB at 10 MHz.

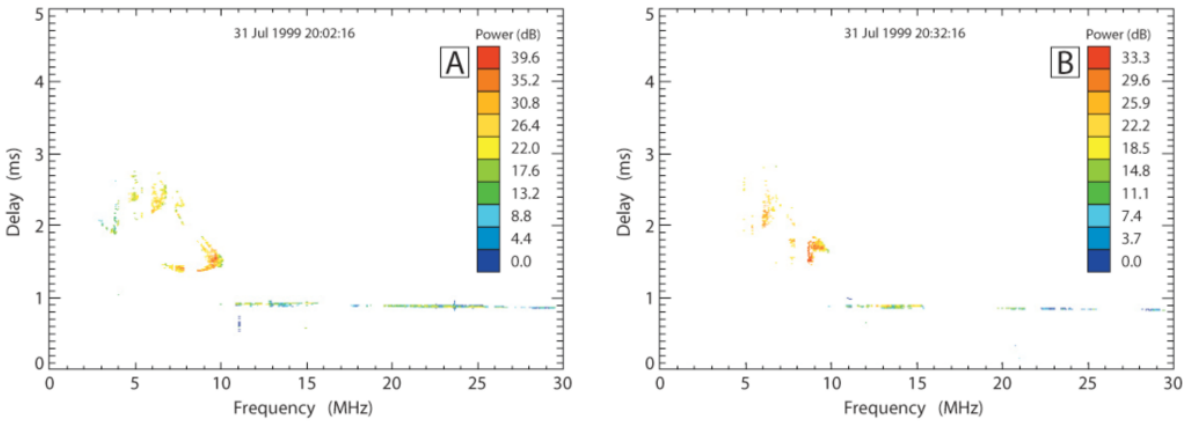

Figure 30. A further selection of oblique ionograms from the Svalbard to Hankasalmi Path

Figure 30 is a further selection of post-SSC oblique ionograms. Figure 30, Panel A - 90 Minutes after the SSC the F-layer has recovered and assuming more of an early evening structure. D-layer absorption has reduced sufficiently (as shown in figure 32) so that frequencies as low as 3 MHz can be seen reflecting from the F-layer. The E_s-layer continues to be enhanced by precipitation and maintains an oblique top frequency near 30 MHz. Figure 30 Panel B - 120 Minutes after the SSC the E-layer enhancement, while still significant, has begun to wane and has become patchy in places. Reflections from the F-layer are again affected by D-Layer absorption which as shown in figure 30 has increased at this time.

Figure 31 is a selection of ionograms from the Tromsø Ionosonde located approximately at the mid-point of the propagation path.

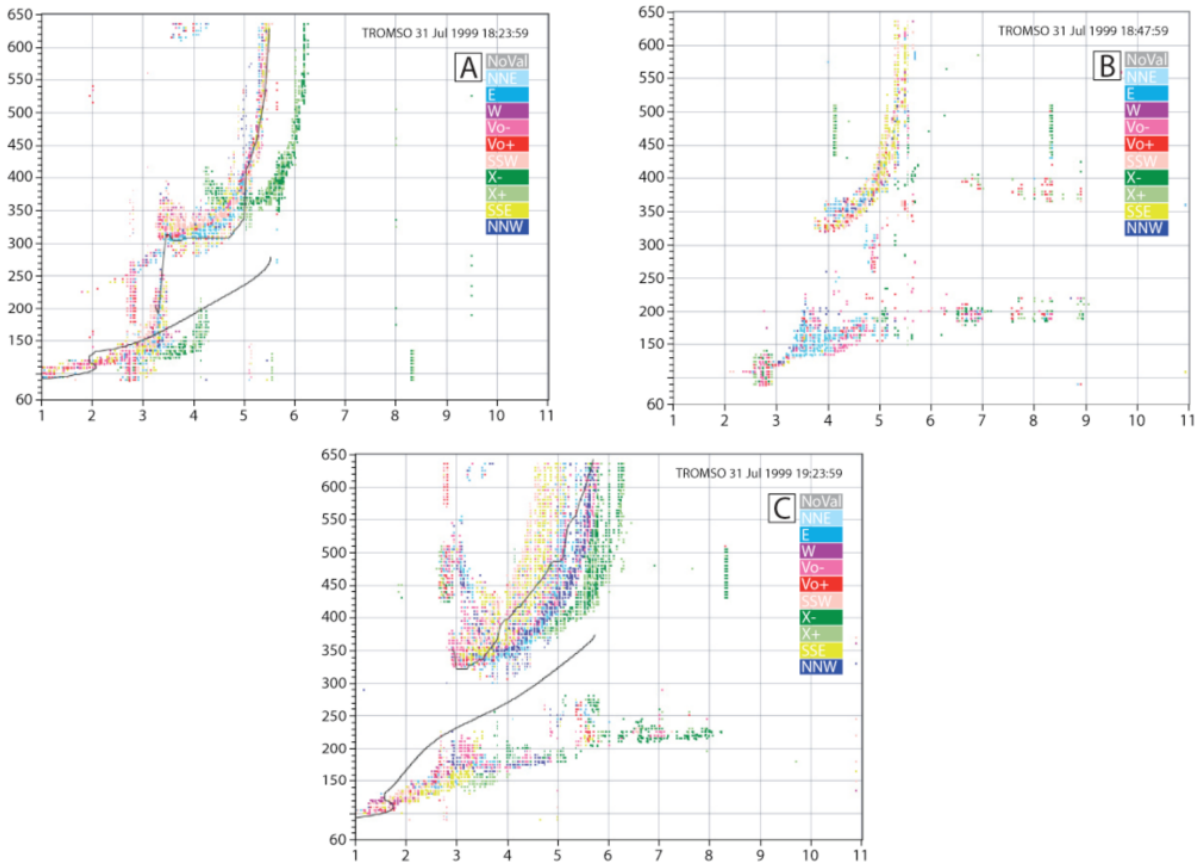

Figure 31. Selection of vertical ionograms from the Tromsø ionosonde

Figure 31 Panel A - Four minutes before the SSC occurs the ionosphere is quiet and a fairly typical early evening ionogram is displayed. The F_2-layer vertical critical frequency (f_oF_2) is 5.5 MHz and the virtual height of the F_2 layer (h'f) is 300 km. The E-layer vertical critical frequency (f_oE) is 2.85 MHz and the virtual height of the E layer (h'E) is 105 km.

Figure 31 Panel B: Twenty minutes after the SSC f_oF_2 remains at 5.5 MHz but h'f has increased to 385 km. The F-layer has increased considerably in height due to electron density depletion at lower altitudes. There is some trace spread (typical of precipitation events) which makes the virtual heights difficult to determine accurately. The E_s-layer has formed and f_oE_s is 4.9 MHz. The absence of any reflections below

2.5 MHz in panel B is most likely due to the spike of absorption seen in figure 29 at this time. The 0.37 dB of absorption at 38.2 MHz equates to a total absorption of 260 dB at 2 MHz for a ray passing twice through the D-region.

Figure 31 Panel C - Sixty minutes after the SSC particle precipitation continues to be in evidence as shown by the widespread occurrence of spread-E and spread-F. The E-layer has taken on a slant characteristic rising from 90 km to 220 km as the frequency increases. The F_2 critical frequency (f_oF_2) is now 5.7 MHz and f_oE_s is 7 MHz (ignore the extra-ordinary wave reflection (green trace)). This ionogram falls just before the third absorption spike seen in figure 29 and reflections are visible down to the lowest usable ionosonde frequency.

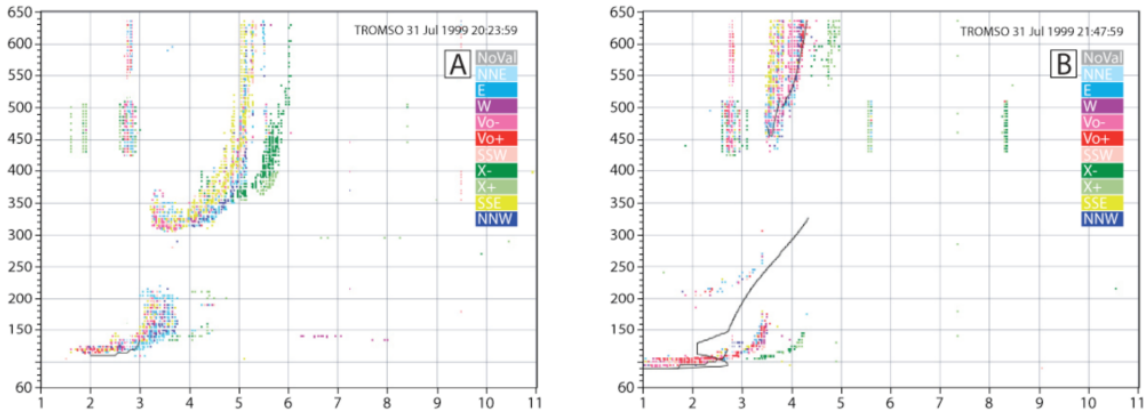

Figure 32. A further selection of vertical ionograms from the Tromsø Ionosonde.

Figure 32 Panel A - Two hours after the SSC the ionosphere has recovered with a blanketing E_s-layer up to 3.3 MHz. The virtual height of the F-layer has reduced slightly. Figure 32 Panel B - Three hours and twenty minutes after the SSC the ionosphere is further disturbed by substorms (as evident in figure 32) which provides

further precipitation of high energy particles resulting in the E-layer reforming with f_oE_s approaching 3.5 MHz and the F-layer virtual height rising to 450 km.

To assist in demonstrating the problem, a simple ray trace analysis of the path between Svalbard and Hankasalmi has been undertaken. The geometry of conventional mode configurations is shown in figure 33. Symmetrical mode geometry is assumed and the location of the Tromsø ionosonde and the Kilpisjärvi riometer is indicated in relation to the distances from the transmitter.

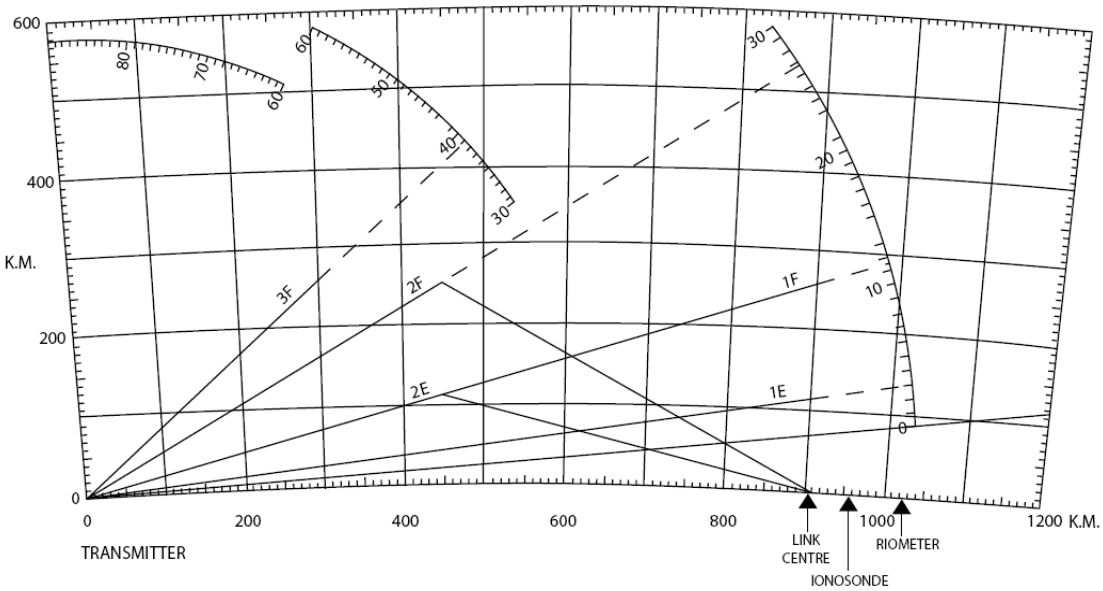

Figure 33. Geometry of conventional mode configurations.

In the conventional mode and assuming an E-layer height of 110 km a 1E ray path is possible with a take-off angle of 2.8^0. A 2E is also possible with a take-off angle of 11^0. Three F-layer modes are possible with a 1F at 11^0, a 2F at 26.5^0 and a 3F at 38.5^0. The 1E and 1F control points and the second 3F control point is very nearly directly above the Tromsø ionosonde. Figure 33 shows the option for two E-layer

paths and three F-layer paths. Evident on the oblique sounder is, however, only the 1E and 1F ray paths which according to figure 33 have a reflection point in the centre of the great circle path. The reflection point for any other ray paths would require similar ionospheric characteristics at each of the reflection points. For the 2E and 2F paths similar ionospheric characteristics are needed at the 450 km and 1 350 km reflection points. For the 3E and 3F paths, similar ionospheric characteristics would be required at the 300 km, 900 km and 1 500 km reflection points. In highly variable high-latitude ionosphere, it is not surprising that the conditions for any path other than the single ionospheric reflection paths (the 1E and 1F paths) is achievable.

With the availability of the Tromsø ionosonde close to the centre of the link path, the actual virtual heights of the E and F layers can be incorporated into the geometry of the mode configurations. This is done in figure 34.

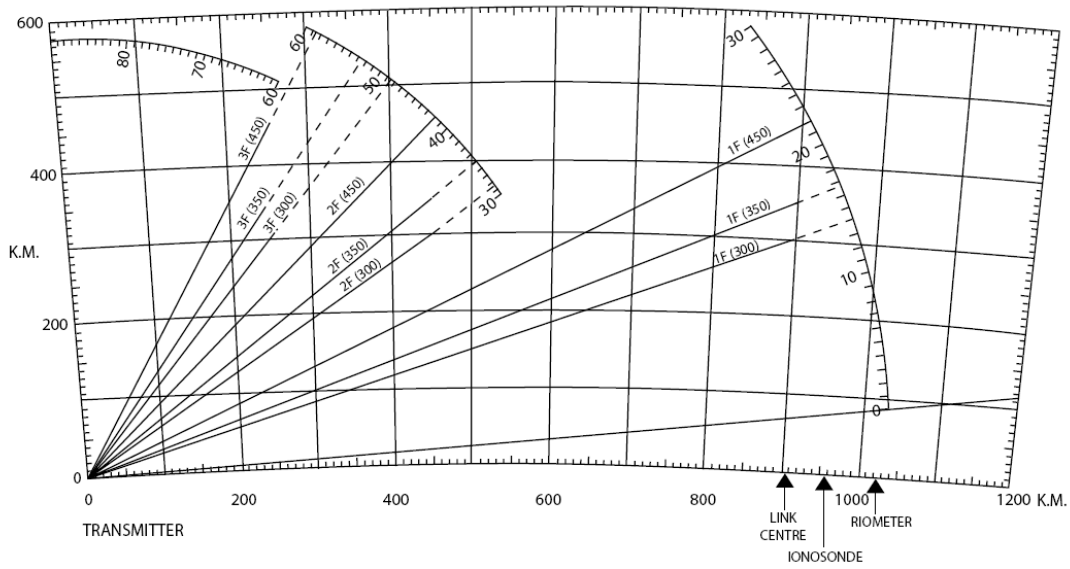

Figure 34. Modified geometry of conventional mode configurations.

As shown in figure 34, while the E_s-layer modes of operation continue to operate around the 110 – 120 km altitude mark the convention of ray tracing the F-layer at 250 km is not valid and a virtual height of 350 km is for this situation a more accurate parameter. At an F-layer height of 350 km the 1F ray angle changes from 11^0 to 14^0, the 2F changes from 26^0 to 35^0 and the 3F ray from 38^0 to 47^0. Figure 32 panel B shows that the virtual height of the F-layer can be as high as 450 km. With reference to figure 34, this would require a 1F ray take-off angle of 22^0, a 2F take-off angle of 42^0 and a 3F take-off angle of 59^0. In the 450 km case, and in some of the 350km cases, taking the secant rule into account, it is very likely that the 2F and 3F rays are penetrating through the ionosphere and hence not reflecting in any manner.

Using the modified geometry, the F-layer path and the Es-layer path were modelled using the well known HF propagation planning tool, VOACAP (Lane, 2001) in the point-to-point configuration. The validity of using HF propagation prediction programs has been addressed by Bröms et al. (1994) who found good agreement with median measurements during quiet conditions and Hunsucker (1999) (as summarised in Hunsucker and Hargreaves (2003)) who noted the aggregate correct prediction of these programs was only ~ 45% under disturbed conditions. However, using the actual layer height info from the vertical sounder allows some limited but relevant modelling to be undertaken even after the onset of disturbed conditions. The modelling shows that the increase in virtual height of the F-layer from 250 km to 450 km results in an increase in transmission loss of 6 dB and an additional spreading-loss of 4 dB. As the E_s-layer maintains its virtual height it does not suffer the same degradation. The result, for this case study, is a 10 dB increase in losses when using the partially blocked F-layer during the disturbed period. In terms of signal-to-noise

ratio (SNR) this results in the SNR of the Es-layer path exceeding the F-layer SNR by 3-5 dB.

Using 10 MHz as the default frequency of operation, the median SNR of a blanketing E_s-layer increased by 3 dB over the normal (non-disturbed) F-layer and increasing the frequency of operation by 3 MHz increased the median SNR achievable on the link by 8 dB overall and the increase in SNR has a direct effect on the reliability of the link. The principle being demonstrated is that a small increase in operating frequency during the disturbed period can assist in maximum utilisation of a blanketing E_s-layer.

The apparent increase in received field strength is not clearly shown in the oblique ionograms. This is most likely as a result of the antenna used at both the transmitter and receiver sites. The radiation angle of the vertical antenna varies considerably as operating frequency varies (McNamara, 1991) and with the wide operating range of the oblique sounder (2 – 30 MHz) it is very difficult to achieve sufficient gain at low elevation angles, less than 3^0 in this case study. As a result the oblique ionograms do not reflect the increase in SNR in the E_s-layer returns when compared to F-layer returns for which the vertical dipole antenna is better matched. The principle that must be taken into account if the E_s-layer is to be used as a replacement for the F-layer during disturbed periods is that an antenna capable of fully utilising the very-low elevation angles must be used. A further practical consideration in very-low angle operations is the need to clear any obstruction at the receiver and transmitter site to maximise this mode of operation. The very-low angles in use do, however, restrict the lengths of any $1E_s$ path to an absolute maximum of 2000 km after which the take-off angle is reduced to nearly 0^0.

2.4.3 The SSC of 15 September 1999

This further example examines the propagation path between Isfjord, Svalbard and Malvern, UK a distance of 2 990 km. This case study is different from the previous in a number of ways. Firstly the great circle path length is long enough to preclude a 1E mode of propagation and the receiver is well out of the auroral zone. The B_z component of the solar wind does not change direction following the evening SSC, being northward before the SSC at 20:19 UT and moving further northwards in the five hours following the SSC. There is a greater change in f_oE immediately following the SSC followed by similar subsequent changes to the value of f_oE. Finally, ISR data is available from two spatially well separated instruments showing the changes in electron density in the ionosphere before and after the SSC occurs.

Solar activity was predominately low before and after 15 September dominated by events in Region 8700 which developed a mixed polarity sunspot group and produced numerous c-class flares (NOAA, 1999b). The period before and after 15 September was dominated by high-speed coronal hole conditions. Wind speeds were high, ranging from 550 to 650 $km.s^{-1}$ and the IMF B_z fluctuated between northward and southward for most of the time with prolonged periods of predominately southward conditions. No proton events were detected at geo-synchronous orbit during the period. The solar wind data for the immediate period of the SSC is shown in the top 4 panels of figure 35.

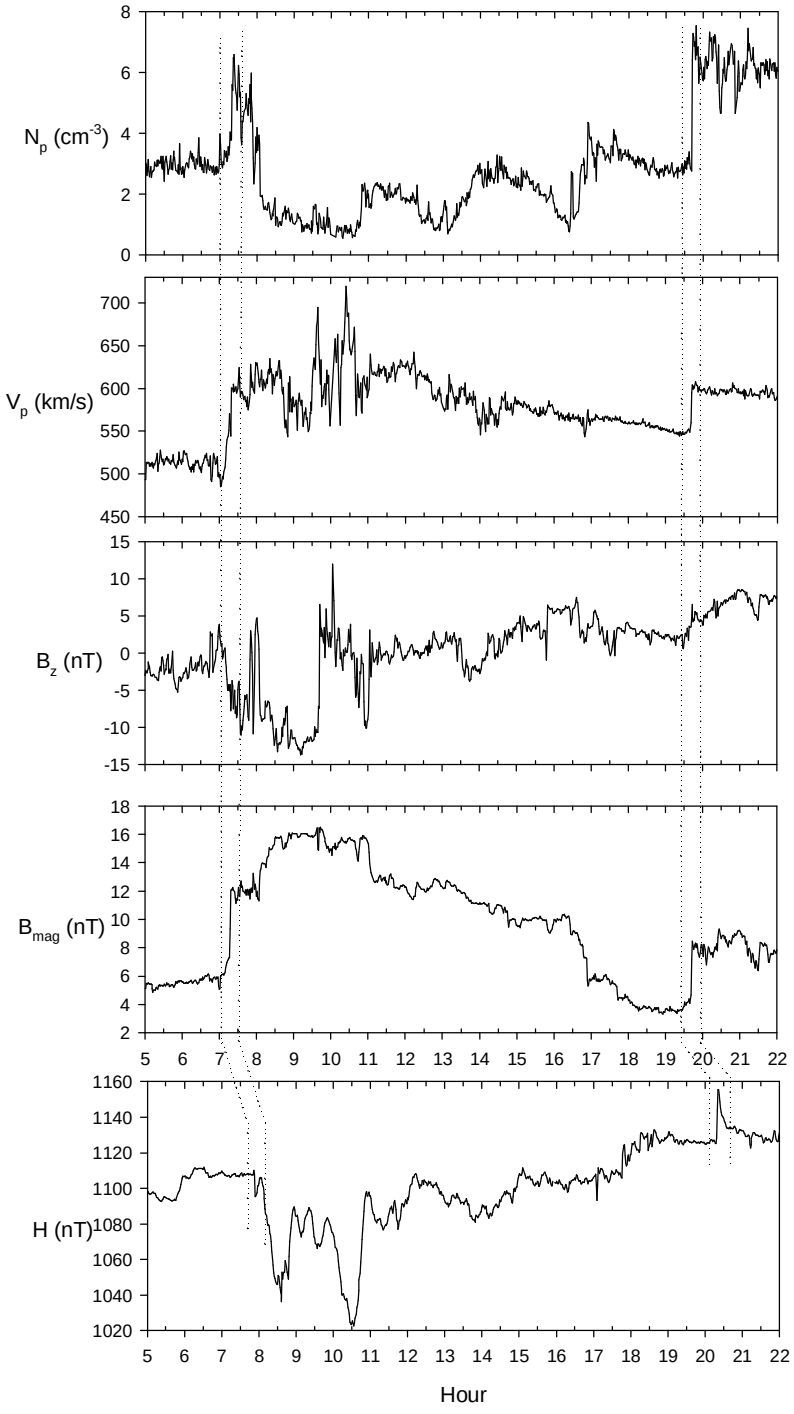

Figure 35. Solar Wind data from the ACE Satellite for the second case study is shown in the top four panels, namely; plasma density, speed, B_z and total magnetic field. Magnetometer data (horizontal intensity (H) component) is shown in the bottom panel. The dashed lines delineate the two periods of SSC disturbance.

The top panel of figure 35 shows solar wind particle density (cm^{-3}) against time. The first disturbance occurred at 07:03 UT when the density increased from 2.9 cm^{-3} to a peak of 6.6 cm^{-3}. The second clearer step change occurred at 19:41UT when the density suddenly increased from 2.8 cm^{-3} to 7.5 cm^{-3}. In both cases there was more than a doubling of density. Panel 2 of figure 35 shows the solar wind particle velocity; at the first disturbance the velocity increased from 486 $km.s^{-1}$ to 605 $km.s^{-1}$, a substantial change of more than 100 $km.s^{-1}$. At the second disturbance, the velocity increased from 560 $km.s^{-1}$ to 608 $km.s^{-1}$, an increase of 48 $km.s^{-1}$.

The third panel of figure 35 shows the magnitude and direction of B_z, B_z is slightly southwards and moves slightly northward just before the first disturbance and becomes stronger southwards following the disturbance. The situation is different for the second disturbance as B_z has been northwards for a number of hours before the disturbance and becomes even stronger northwards following the disturbance. The fourth panel of figure 35 shows the interplanetary magnetic field strength (nT). The magnetic field strength jumps from 6 nT to 12.1 nT during the first disturbance and from 4.7 nT to 8.3 nT during the second disturbance.

The geomagnetic field experienced minor to major disturbances at high latitudes associated with a high-speed coronal hole stream over the week 13 – 19 September 1999. On September 15 mid-latitudes experienced minor storm level and high latitudes experienced severe storming in conjunction with the high-speed shock mentioned above. The effects of the high-speed stream began to diminish only four days later. Magnetometer data for the immediate period of the SSC is shown in the bottom panel of figure 35. The first disturbance in the solar wind at 07:03UT was

measured on the Earth's surface at 07:55UT. The magnetometer displayed a small reduction in the H component, a recovery and then a step decline from 1108 nT to 1045 nT. The second disturbance in the solar wind at 19:41UT was measured by a change in the magnetometer from 1128 nT to a peak of 1156 nT at 20:20 UT. Both magnetometer signatures are typical mid- to high-latitude magnetometer SSC indicators with preliminary and main impulses as explained by Ferraro et al. (1951) and Araki (1977).

The EISCAT ISR was in operation from 15:08 on 15 September 1999 to 13:00 the following day. Figure 36 shows the electron density versus altitude data from 15:08 UT on the 15 September until noon on the next day. When the ISR begins measurements the E-region electron density above 100 km altitude is already enhanced due to magnetic activity during the day following the 07:53 UT SSC.

At the time of the second SSC (20:19 UT) the ISR shows a sudden enhancement in electron density at altitudes around 150 km and as low as 100 km. The electron density increases from about 2.5×10^{10} m^{-3} to 6.3×10^{10} m^{-3}, more than a doubling of electron density which lasts for more than three hours. It should be noted that the electron density values quoted should not be seen as absolute values but rather as an indication of the scale of change that occurs during this period and the subsequent effect on ionospheric propagation. The electron density between 100 km and 150 km altitude decreases after midnight but just after 01:00 UT the following day the electron density undergoes frequent and intense enhancements until at least 11:00 UT. This is a result of ongoing precipitation due to substorms that followed the SSC.

Figure 37 covering the same period as figure 36 is taken from the ISR at Sondrestrom which was in operation from 22:41 UT on 14 Sept to 24:00 UT on 17 September 1999. The E-region enhancement (circled in figure 37) begins near 20:20UT and lasts for about 2 hours, very similar to what has been seen in the EISCAT data even though the two ISR's are spatially well separated (figure 26 refers). Following a three hour period of relative quiet the Sondrestrom ISR shows a 2 hours sudden enhancement in electron density reaching peaks of 13×10^{10} m^{-3}. Again the electron density values quoted should not be seen as absolute values but rather a reflection of the scale of change that is possible and the consequences these changes have on ionospheric propagation.

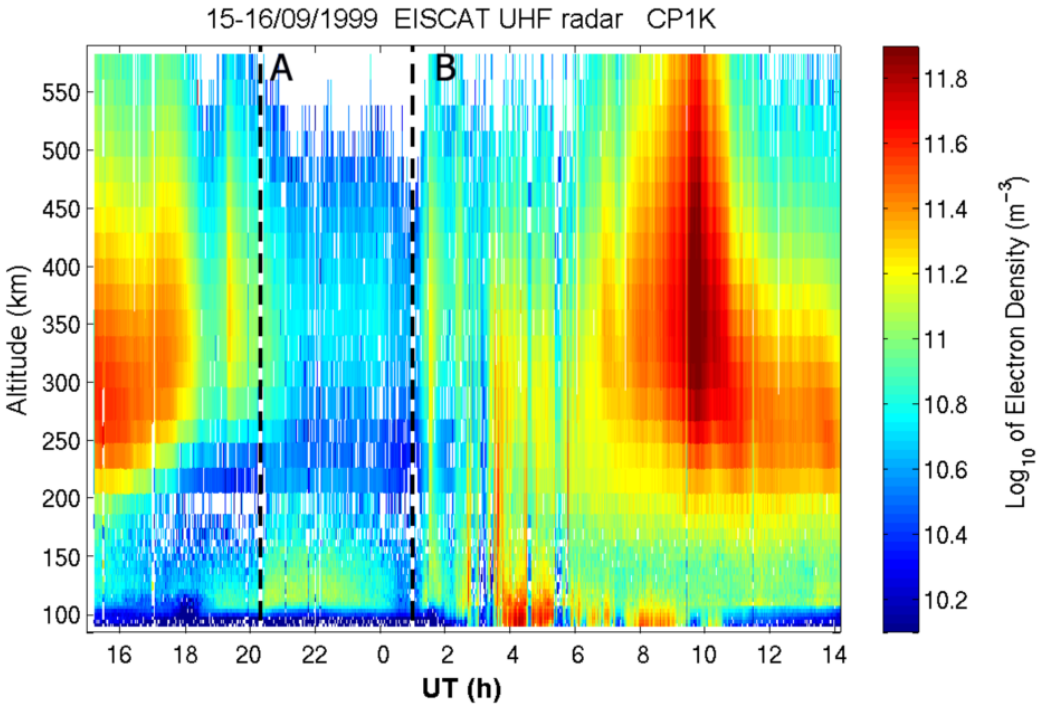

Figure 36. EISCAT UHF IS Radar captures the changes in electron density from 15:08 UT on 15 September 1999 till after noon the following day. From left to right, the first dotted line marks the moment of SSC and the second marks the onset of frequent and intense substorms

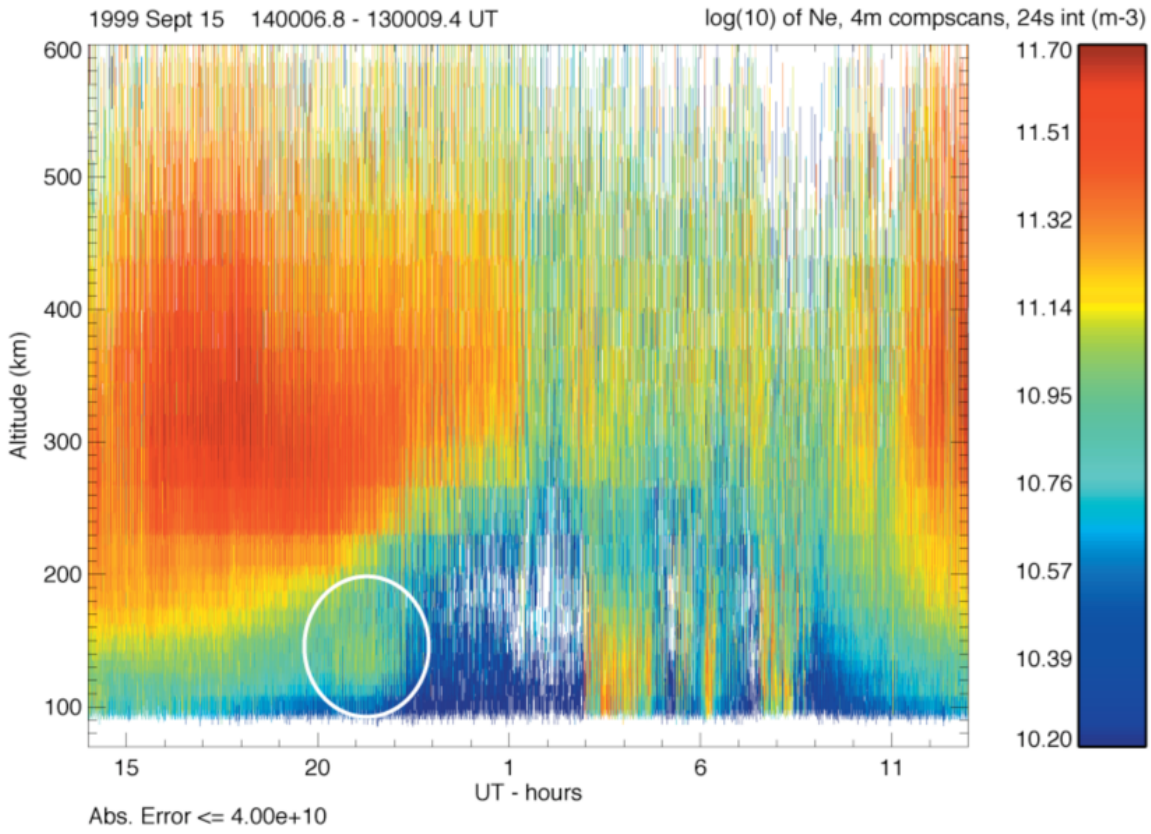

Figure 37. Sondrestrom IS Radar captures the changes in electron density from 14:00 on the 15 September 1999 to 13:00 the following day. The white circle indicates the moment of Ne enhancement at E-layer altitudes at the time of SSC. Note the onset of substorm activity from 03:00 the following morning causing further electron density enhancements.

A selection of oblique sounder ionograms from the Svalbard to Malvern propagation path are shown in figure 38. Figure 38 Panel A - Seventeen minutes before the SSC occurs the F-region is disturbed with only a small window of reflection between 2.5 – 4 MHz. There is a slight return from the E-layer around 11 MHz. Figure 38 Panel B - Thirteen minutes after the SSC occurs the high-latitude E-region is strongly enhanced

forming an E_s-layer reflection path between 10 - 18 MHz. At this point there is virtually no F-layer path visible.

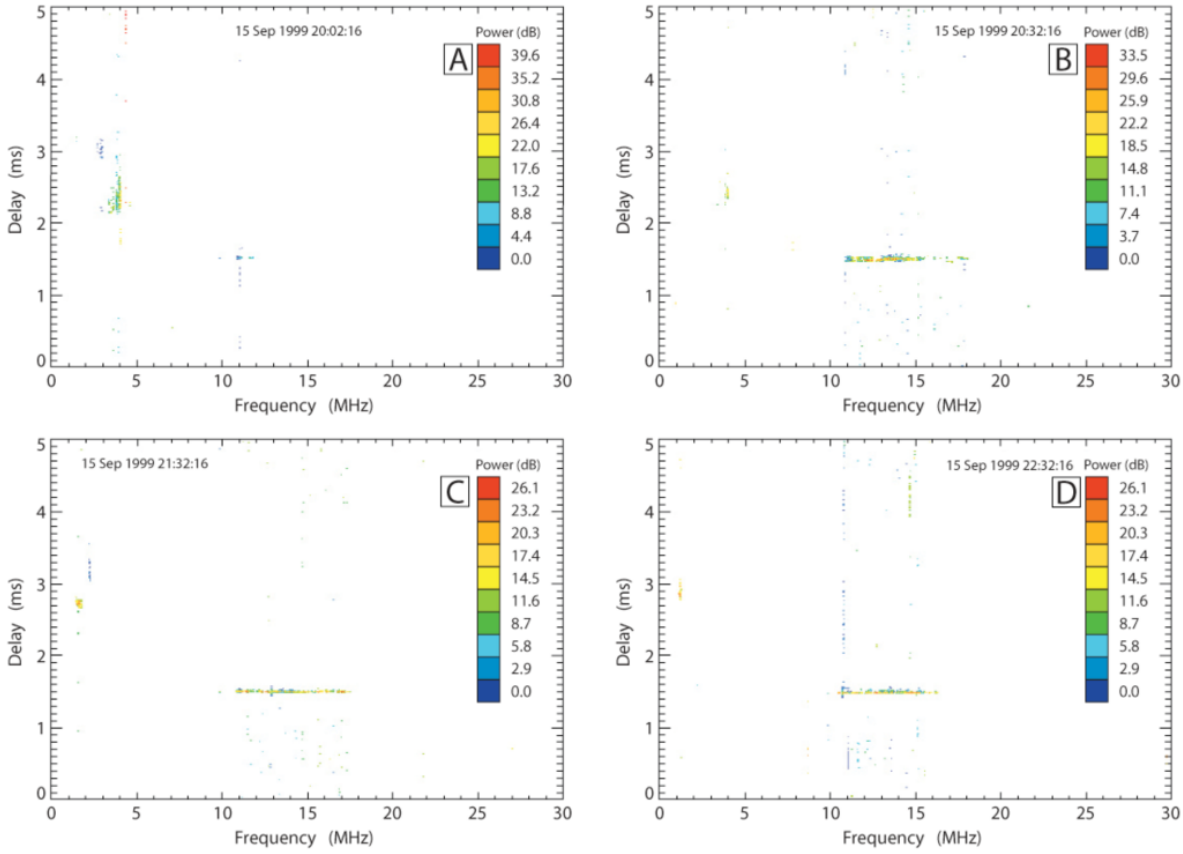

Figure 38. Selection of oblique ionograms from the Svalbard to Malvern path.

Figure 38 Panel C: A further sixty minutes on and the situation remains unchanged. Standard predictions of this propagation path are useless as the enhanced E-region dominates and no F-layer path is available. Figure 38 Panel D: A further sixty minutes on, now 2 hours and 15 minutes after the SSC occurs and the situation remains virtually unchanged. The E-region window has reduced slightly to cover 10.8 – 17.5 MHz. There is a slight return from the F-layer around 2 MHz. It is likely that any return of signals below 10 MHz is either suffering extensive D-region absorption

or there is simply no suitable reflecting F-layer available due to ionisation depletion at these altitudes.

Figure 39 is a selection of ionograms from the Tromsø Ionosonde showing similar characteristics to that seen in the first case study. Figure 39 Panel A - Seven minutes before the SSC occurs. The F-region is disturbed and h'F has already increased to 405 km. This change in reflection height would adversely affect HF links and HF broadcasting services which usually assume an h'F of around 250 km in the planning process which in turn determines the amount of power and type of antenna to be used. The antenna type is most often dependent on the take-off angle required. F_oE_s is already above the norm at 3 MHz at this stage.

Figure 39 Panel B - Eleven minutes after the SSC occurs the E_s-layer is dramatically enhanced and almost completely blankets the F-region. F_oE_s is 2.9 MHz with a F-region window of only 0.5 MHz between 3 – 3.5 MHz. Figure 39 Panel C - The situation continues and more than one hour later, in the 21:24UT ionogram, a similar situation exists with F_oE_s = 3.1 MHz which is sufficient to completely blanket the F-region. Interestingly in this case we do not see the large increases in virtual F-layer heights as seen in the first case study.

The virtual height of the F-layer (> 400 km, figure 39) before and after the SSC, the low frequencies seen on the oblique high ray path (>2ms, figure 38) and the 28^0 take-off angle required fits in well with the considered view that a 2F mode occurs normally instead of a 1F mode on this path. As the length of the path prohibits a 1E

mode of propagation, a 2E mode with a take-off angle of 5^0 dominates following the SSC.

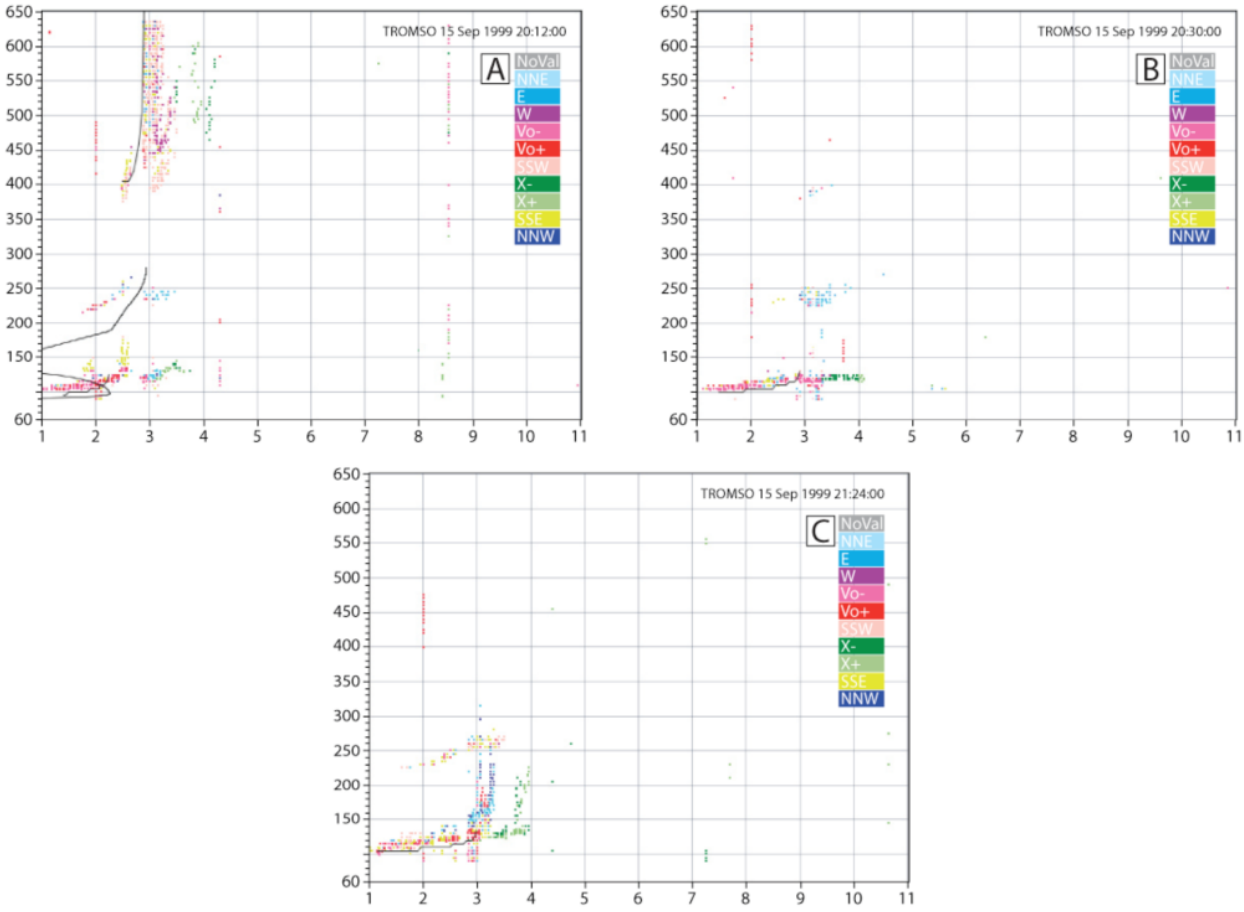

Figure 39. Selection of vertical ionograms from the Tromsø ionosonde.

Figure 39 is a selection of ionograms from the Gakona Ionosonde which captured events around the SSC that occurred at 7:53 UT. This ionosonde, located on the other side of the polar cap from the link transmitter is included to show the extent of the ionospheric disturbance following the SSC.

Figure 40 Panel A - A fairly disturbed early morning ionogram where trace spread makes it difficult to extract any accurate parameters, however f_oF is approximately 3.2

MHz and f_oE_s is approximately 2.8 MHz. It is difficult to determine h'f from the ionogram. Figure 40 Panel B - Thirty seven minutes after the SSC a dense sporadic E-layer has formed which almost completely blankets the F-region, f_oE_s has extended to 5.5 MHz. The second reflection from the E-layer is visible at a height of 220 km and a small reflection is visible from the F-layer at a height of 280 km. Figure 40 Panel C - The now fully blanketing E_s-layer continues for at least another two hours after SSC, albeit slightly patchy at the top end.

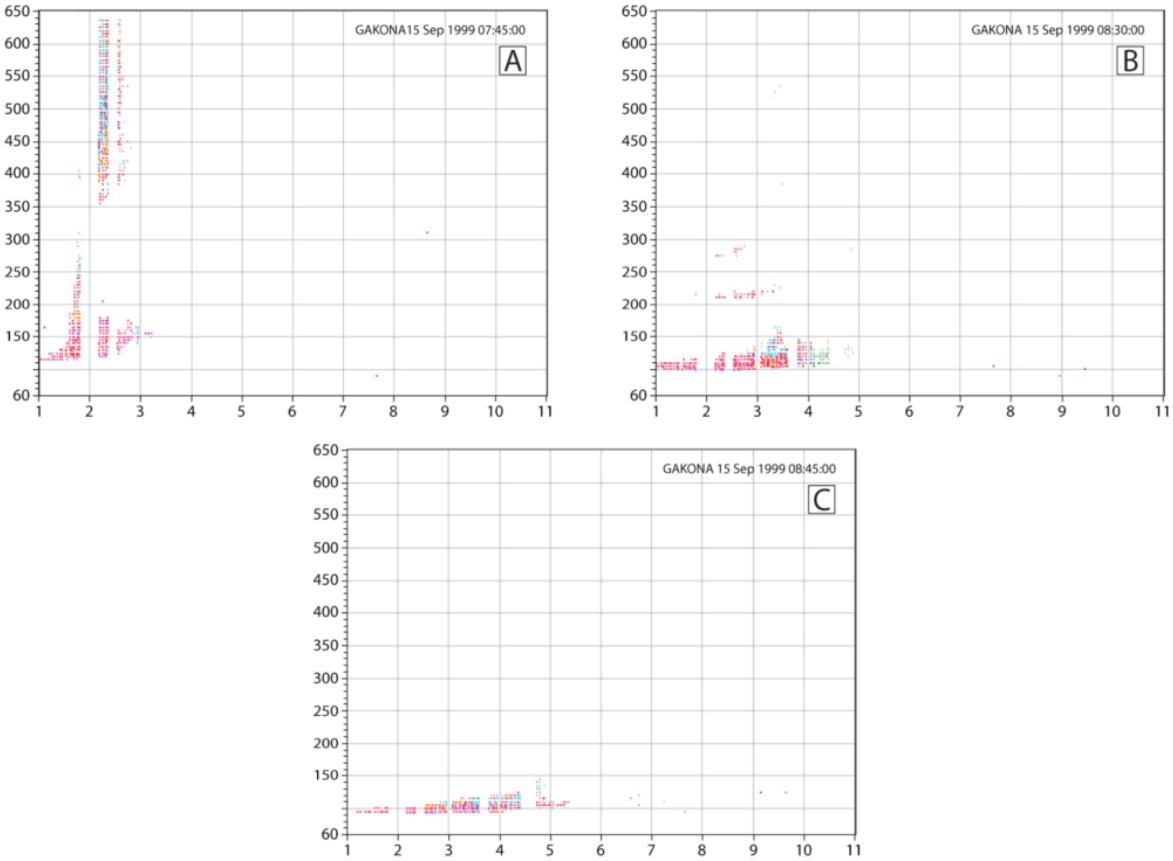

Figure 40. Selection of vertical ionograms from the Gakona ionosonde.

2.5 Conclusions

Seven different instruments have been utilised in these case studies to show the cause and effect of enhanced E_s-layers immediately following an SSC. These studies demonstrate the profound effects these sporadic layers have on high latitude HF circuits by dramatically extending the E-layer maximum usable frequency (MUF) and/or "shielding" any F-layer ray paths.

The first simple case study of a high-latitude link showed the correlation between ionospheric absorption and SNR on a high-latitude HF link. But, more importantly, the case study shows the dominance of the E-layer in the high-latitude region during particle precipitation and the effect of the dominant E-layer (which dominates due to enhanced ionisation caused by precipitating particles) on the link. This case study demonstrates many of the problems in predicting the state of the ionosphere, especially at high latitudes: for example, rapidly varying virtual heights of reflection layers, D-layer absorption and frequent propagation mode changes. As shown in the case study of chapter 1 many propagation methods use simplistic ray tracing concepts and the case study demonstrates how the rapidly changing ionospheric parameters reduce the usefulness of these models and the factors that need to be considered.

Data from the ACE satellite is used to show the magnitude of changes that occur in the solar wind due to disturbances in the solar wind, such as when shock waves and dynamic pressure pulses move past the satellite on their way to impinging on the Earth's magnetosphere. The step changes in total magnetic field strength, particle density and velocity as well as changes in direction of the B_z component are shown. The direction of B_z changes from south to north in the first case study but starts northwards and becomes progressively more northwards in the second case study.

Changes in the ground based geomagnetic field intensity due to an increase in magnetopause current, as a result of magnetospheric compression caused by solar wind disturbances, are seen in the magnetometer data.

The observation of sudden changes in the solar wind which are the cause of SSC is well understood as is the prediction of the time delay between observation by the ACE satellite platform and the arrival of the disturbance at the Earth's surface. The SSC event is used as a proxy to herald the change between a "quiet" and a "disturbed" high-latitude ionosphere and the subsequent onset of an enhanced E-layer. However, for the first time the linkage between SSC and the enhanced E-layer ionisation is exposed in both case studies detailed in this paper.

Ionosonde records show how the usefulness of the F-layer is reduced as its electron density decreases and its virtual height increases following disturbances initiated by the SSC. The records further show the enhancement of the E_s-layer for extended periods, in both cases for at least two hours and in one case as long as three hours. The enhancement is so great in some cases that the F-layer is completely screened off from the ground. The Tromsø ionosonde, close to the centre of the first case study link path demonstrates the change that occurs in the height of the F-layer around the single reflecting control point. This knowledge allows a more realistic ray tracing geometry to be used when attempting to model and predict propagation during such disturbances.

The ISR records reveal the sudden enhancement of electron density in the E-region coincident with the SSC as well as the scale of the increase in electron density that can

be expected. The effect of storms and sub-storms on the significant modulation of electron density at E_s altitudes is clearly demonstrated. The ISR records support the longevity of enhancement of the E_s-layer electron density that is seen in the ionosonde and oblique sounder records.

The change in cosmic radio noise absorption as measured by a riometer reflects the effect of particle precipitation on the D-layer and supports the interpretation of the ionosonde and oblique sounder data. There is good correlation of the effect of absorption, as expected, between the oblique sounder, the Tromsø ionosonde and the riometer measuring the absorption. The characteristics of absorption observed following SSC events have recently been empirically formulated by Ritchie and Honary (2009).

Key to both detailed case studies are records from the oblique sounder which reveals the practical effects of an enhanced E_s-layer. The majority of all HF communication links are planned assuming the use of the F_2 layer as the refracting layer as well as assuming a fixed reflection height (normally 250 km). An HF system designed to reach a particular point or area such as point-to-point links and targeted broadcasting use complex antennas that concentrate the radiated power in both azimuth and elevation. These two assumptions are perfectly valid when dealing with a quiet ionosphere. However, the variations in the height of the F-layer, the reduction of the height of the expected reflecting layer from 250 km to 100 km as well as the phenomena of the E_s-layer screening the F-layer, has severe implications. This can be seen when examining figures 33 and 34. Figure 34 shows the modified geometry for a number of different modes at three different fixed heights (300 km, 350 km and

450 km). The change in reflection layer from the F- to the E_s-layer has the most drastic effect as the elevation angle changes from a maximum peak of 22^0 at h'F of 450 km to a low of 3^0 at h'E of 110 km. For many types of specialist antenna this change is greater than the available elevation beamwidth. The change in h'F from 250 to 450 km and the corresponding elevation angle modification from 11^0 to 22^0 has similar antenna issues.

Following an SSC event or during magnetic storms, one rational approach toward using the ionosphere for HF communications in high-latitude regions is to rely solely on E-layer modes and to provide higher power or increased antenna gain in bands appropriate for E_s-layer propagation. Overcoming these problems may prove to be economically challenging for operators of fixed-links and broadcasting services. However, with relevance to tactical links and safety of life transmissions, the oblique sounder reveals, counter-intuitively perhaps, that instead of reducing the frequency of operation to re-establish disrupted links, it would be better to increase the frequency of operation to fully utilise the enhanced E-layer while overcoming some of the effects of absorption. In the second case study, before the SSC occurs the F-layer can support reflections from 6 to 11 MHz over this link while the E_s-layer is supporting reflections between 10 and 15 MHz after the SSC. Twenty minutes after the SSC there are sporadic reflections from the F-layer but the E_s-layer is now capable of supporting a number of paths using frequencies between 12 and 20 MHz. During this period of approximately one hour, any attempt to re-establish a link by reducing the operating frequency would be futile. The oblique ionogram shows no link paths are available on this circuit if the frequency is reduced. The only solution is to increase the operating frequency, by more than 5 MHz, in order to re-establish the link. The same principle

is clearly shown in the third case study where the only manner in which a link can be established in the two hours following the SSC event is for the operator to increase frequency by more that 7 MHz to be able to utilise the E_s-layer for communications. As explained, in order to implement this mitigation technique, equipment at both ends of the link will need to be sufficiently frequency agile and have access to antenna with take-off angles appropriate for E_s -layer operation.

The case studies demonstrate that the effect of the ionospheric disturbance is an enhanced E_s-layer that dominates the mode of propagation, the durability of the enhanced E_s-layer allowing the re-establishment of a reliable reflecting layer following the demise of the F-layer and the viability of using the E_s-layer in supporting HF communications at high latitudes. Following up on the last point, the extent of the enhanced E_s-layer is evident in the second case study. A 2E mode of propagation is relied on over the 3 000 km path which requires two E_s-layer reflections spaced 1 500 km apart; this is confirmed by ISR data showing similar enhancements in different sectors.

Previous work in this area has been done by Hunsucker and Bates (1969) who reported that E_s is most important for communications at sunspot minimum, when E_s modes can occur more than 50% of the time on paths between Alaska and Greenland and Norway, with typical MUF's of 16 to 18 MHz. Jull et al. (1962) presented the results of an investigation of systematic HF channel sampling at oblique incidence and concluded that auroral E_s is a very important propagation mode over paths up to 2 300 km in the 3–30 MHz range. For both of these studies the occurrence of E_s was noted but no attempt was made to predict the occurrence and severity of E_s. To the author's

knowledge there has not been any published work that quantifies the expected changes in the lower ionosphere (the D and E-regions) due to particle precipitation.

A primary part of the problem is establishing when the transition from a 'quiet' high-latitude ionosphere to a 'disturbed' high-latitude ionosphere starts. A 'quiet' high-latitude ionosphere for the purposes of his research is one that behaves like a mid-latitude ionosphere in the absence of solar and geophysical activity. A 'disturbed' high-latitude ionosphere is one under the influence of particle precipitation. As shown in these case studies, even during low solar and geophysical activity, particle precipitation has a significant effect. Some effort is required to predict the variances in E-layer critical frequency in order to better plan high-latitude communications particularly when ionospheric reflection points occur within the disturbed high-latitude ionosphere. This effort is made in chapter 4 of this thesis.

Although modelling of the high-latitude ionosphere has improved in recent years, most of the modelling attempts are only case studies (e.g. Sojka and Schunk, 1988). The main difficulty is that magnetospheric processes and solar inputs have an important effect on the morphology of the high-latitude ionosphere, and that the observational databases are still too sparse to enable the development of an empirical model which has adequate parameters to describe the dependence on the various ionospheric drivers. Also, even with the most extreme simplifying assumptions, the high-latitude ionosphere cannot be treated analytically (Cander et al., 1998) and hence we continue to rely on empirical data and statistical analysis.

CHAPTER 3

Characterisation and Prediction of SCA

3.0 Objectives

The objectives of this chapter are to:

1. Introduce and define Storm Sudden Commencements (SSC) including the source and cause of SSC particle precipitation known as Sudden Commencement Absorption (SCA);
2. Investigate the characteristics of SCA, caused by the precipitation of energetic particles, as a result of the physical effects of an SSC event;
3. Analyse and determine what parameters of the solar wind and Interplanetary Magnetic Field (IMF) correlate strongly against SCA in order to determine what solar wind parameter(s) are most efficient in predicting SCA;
4. Empirically model the expected amplitude of SCA following a shock/discontinuity in the solar wind.

3.1 Storm Sudden Commencements

Experimental and theoretical investigations more than two decades ago have led to our initial understanding of the principal nature of SSC. Burlaga and Ogilvie (1969), Gosling et al. (1967) and Ogilvie et al. (1968) have shown the correlation between

impulsive changes in solar wind parameters and SSC signatures in the magnetosphere or on the ground. Nishida (1964) studied the coupling of compression waves to the ionosphere current system. A hydromagnetic description of SSC events has been given by Wilson and Suguira (1961) and Tamao (1964b, 1975). Araki (1977) investigated details of the global onset time distribution for SSC events and their relationship to the magnetosphere-ionosphere coupling.

The spatial and temporal structure of SSC associated magnetohydrodynamic (MHD) waves propagating within the magnetospheric cavity remained a matter for speculation until the work of Wilken et al. (1982). They observed that rapid variations of particle fluxes and magnetic fields occurred at different universal times depending on the local time of observation. They interpreted the onset times as the times when the SSC-associated MHD wave front passed the various spacecraft used.

More than 30 years of study has shown that SSC are caused by the global compression of the magnetosphere as a result of interplanetary disturbances such as shock waves and dynamic pressure pulses. Great storms are preceded by impressive SSC events. The great storm of 24 March 1991 started with an SSC compressional pulse that resulted in a magnetic pulse observed on the ground that increased more than 200 nT in less than one minute. (Araki et al., 1997).

Interplanetary shock waves are observed in the solar wind, usually associated with the interplanetary remnants of coronal mass ejections (Gosling et al., 1990). Shocks are generated when the relative velocity between the interplanetary structure and the slow solar wind is higher than the magnetosonic velocity. The most usual type of shock,

the fast forward, shows a simultaneous jump in plasma parameters (speed, density and temperature) and in magnetic field strength. Usually a very disturbed B_z component is seen after the shock (Gonzalez et al., 1999).

Impulsive or step-like changes in the magnitude of the geomagnetic field which are observed on a global scale are known as Sudden Impulses (SI). These changes may be either positive or negative and represent a rapid expansion or compression of the entire geomagnetic field. In many cases, these sudden impulses are followed by geomagnetic storms and then are designated Storm Sudden Commencements (SSC). The distinction between SI and SSC is somewhat arbitrary, and many authors have suggested that there is no difference between the initial disturbance associated with SI and SSC (Matsushita, 1962). Joselyn and Tsurutani (1990) note that the term SCC is a traditional one, and there is no distinction between SI+ and SSC, because the physics during a sudden compression of the magnetosphere is independent of whether the impulse is followed by a storm main phase or not. However, we use the term SSC exclusively as all the events examined and the focus of this work are classified officially as SSC events.

An SSC is an increase in the low-latitude ground based magnetic intensity which typically lasts for tens of minutes and then is followed by a magnetic storm or by an increase in geomagnetic activity lasting at least one hour. SSCs preceding geomagnetic storms are caused by the global compressions of the magnetosphere as a result of interplanetary (IP) disturbances such as shock waves and dynamic pressure pulses (Wilken et al., 1982; Tsurutani et al., 1995; Takeuchi et al., 2002a). The SCC is a transition between two equilibrium configurations characterised by different

multiples of Earth radius (Re). In the equatorial region between Re ≈ 4 to 9 the magnetic effects of an SSC can be described by a simple magnetic compression accompanied by a displacement of the field lines (Perona, 1972). The SCC magnetic field compression at the equator and in the nearby region along a field line can be described by the following empirical equation:

$$B = B_0(1+dt)$$

Where: B_0 is the initial value of the magnetic field

δ is chosen in such a way that, at the end of the phenomena, namely at t = T, B reaches its final value. Ondoh (1963) assumed values of T = 100 sec in the noon sector and T = 200 sec in the midnight sector.

Impulsive global magnetic events were of great interest to the pioneers of magnetospheric research. Chapman and Ferraro (1931) suggested early on that they could result from disturbances of the geomagnetic field by interplanetary phenomena. It is now well accepted that sudden changes in the momentum of the solar wind associated with shocks and discontinuities can produce the compression of the magnetosphere that is manifested as a sudden impulse (Nishida, 1978). Observations have shown that such solar wind disturbances are indeed associated with SI / SSC (Burlaga and Ogilvie, 1969; Patel and Coleman, 1970).

To interpret the SSC rise time, Takeuchi et al. (2002b) introduced the concept of a 'geoeffective magnetopause' and conjectured that the geoeffective magnetopause would be confined within ≈ 30 Re, since the effect of a compression of the distant tail magnetopause would not be detected on the Earth's surface. The time for an

interplanetary (IP) shock to sweep by the geoeffective magnetopause predominantly determines the SSC rise time (Wang et al., 2006).

The SSC is not a simple increase in the H component of the geomagnetic field. Extensive studies with ground level magnetic field measurements have revealed that the SSC waveform is quite complex with a strong dependence on latitude and local time (see review by Araki, 1977). The rise time of a SSC generally ranges from 2 to 10 min centred around 4 min (Maeda et al., 1962). The SSC as observed at any point on the surface of the Earth is a superimposition of the arrival of compressional waves generated over the broad extent of the magnetopause during the passage of a shock. Nishida (1966) suggested that the rise time is principally determined by the time required for interplanetary shocks to sweep by the magnetosphere on the basis of an inverse relationship between the rise time and the mean transmission speed of the interplanetary disturbances from the Sun as found by Nishida (1964). Another mechanism suggested in the past was that the SSC rise time was simply the time constant of the magnetosphere against a sudden compression (Baumjohann et al., 1983). Although numerous explanations have been suggested for the SSC rise time as cited above, there does not yet appear to be any consensus.

SSC compressions of the dayside magnetosphere have been shown to produce radiation belt electron and proton flux enhancements which can be very long lived inside of L=3, as for the March 24 1991 geomagnetic storm near the solar maximum (Vampola and Korth, 1993; Looper et al., 1994) and also for the February 1986 storm near solar minimum (Gussenhoven et al., 1989). The enhancement of radiation belts

have been interpreted in terms of radial acceleration of solar protons inward by the induction electric field associated with the SSC (Hudson et al., 1997).

An SSC accompanied by solar protons produces a trapped population from those protons which experience significant inward radial transport and perpendicular acceleration due to the induction electric field associated with the SSC magnetic field compression (Araki et al., 1997). The March 24 1991 SSC demonstrated that new radiation belts can form on the MeV particle drift timescale, which coincides with the SSC timescale, of tens to a few hundred seconds, in contrast to the hours to days of the geomagnetic storm. The induction electric field which accompanies magnetopause compression transports particles radially inward, increasing energy with conservation of the first adiabatic invariant. This mechanism is resonant over a range of initial energies, or equivalent magnetic moments, such that protons (or electrons) gradient-drift either too slowly or too fast relative to the azimuthal spreading of the pulse and do not spend an optimum amount of time in the region of maximum pulse amplitude (Hudson et al., 1997).

Having examined data from the CRRES satellite, Hudson et al. (1998) determined that the solar wind dynamic pressure determines the effectiveness of penetration in L and corresponding energisation. Quantitative studies have revealed a good correlation between the SSC amplitude at low latitudes and the change in the square root of the solar wind dynamic pressure at the shock/discontinuity (e.g. Russell et al., 1992, 1994a, 1994b). Shinbori et al. (2003) conclude that SSC disturbances in the polar region first propagate into the dayside polar ionosphere along the magnetic field line with shear Alfvén waves. After the Alfvén waves are converted into the fast-mode

MHD waves near the polar ionosphere, it expands from the dayside to nightside polar ionosphere regions with a mean speed of about 47 km/s.

3.1.1 Physical Processes at SSC Events

Recently, Wang et al. (2005) conducted a global MHD simulation of the interaction between the magnetosphere and IP shocks with different orientations. The model results show that a highly oblique shock requires more time (in the order of minutes) to compress the forward part of the magnetosphere. Thus the IP shock orientation plays an important role in determining the SSC rise time. Shock orientation is taken as the angle between the shock normal and the GSE X-axis which points towards the Sun. In the work by Wang et al. (2006) most of the shock orientations were in the range of 135^0 – 180^0; an angle of 180^0 indicates that the shock front is perpendicular to the solar wind flow and thus hits the magnetosphere head on. For IP shocks with similar orientations, when IP shock speeds are higher, the shock sweeps by the geoeffective magnetopause in less time and thus SSC rise times are shorter. For IP shocks with similar speeds, the bigger the angle between the IP shock normal and the Sun-Earth line, the shorter the rise time.

A hydromagnetic description of SSC events has been given by Wilson and Sugiura (1961) and Tamao (1964, 1975). According to the results of Wilken et al. (1982, 1986) and Tamao (1964, 1975), a SSC generates hydromagnetic waves which transform the magnetosphere into a new compressed steady state configuration which is in balance with the increased solar wind pressure. The associated compression of the Earth's magnetosphere induces electric fields which substantially alter both particle energies and drift motions. The SSC-generated step-like waves were

measured to transverse the magnetosphere within 2 min. The radial propagation time of the wave from the frontside magnetosphere down to the equatorial ionosphere was found to be about 1 min and the azimuthal delay from day to night side at geostationary altitude was about 2 min correspondingly. The particle precipitation into the ionosphere due to those transitional waves have been observed by several researchers e.g. Ortner et al. (1962).

Ultra Low Frequency (ULF) and Very Low Frequency (VLF) waves have been noted in association with SSC on the ground and aboard satellites (Kokubun and Oguti 1968; Hayashi et al. 1968; Olsen and Lee 1983). The stimulation of these waves has been interpreted as evidence of increased anisotropy of pitch angle distribution and enhanced precipitation. During stressed conditions, especially at night side, particles are generally considered to be subject to scatter into a loss cone due to the increased curvature of the magnetic field lines (e.g. Pytte and West 1978). This may explain to some extend the increase in precipitation at night side.

Perona (1972) reported that at the time of a SSC, VLF waves can be excited. In turn the wave turbulence drives the pitch-angle diffusion of energetic electrons trapped in the magnetosphere, causing them to be precipitated into the lower ionosphere. In addition Perona found it reasonable to assume that at the peak of an SSC absorption event, the number of electrons precipitating per second is as much as 0.01 – 0.001 of the total electron content of the tube of flux. Hence their lifetime is 100 – 1000 seconds, which is comparable to the lifetimes expected during strong pitch-angle diffusion (Kennel and Petschek, 1966).

The SSC of a magnetic storm is interpreted as an effect of the impact of a solar gas stream on the geomagnetic field, as was originally proposed by Chapman and Ferraro

(1931, 1932, 1940) and discussed in detail by Ferraro (1952, 1960b). The impact is transmitted to the Earth by hydromagnetic waves (Dressler, 1958; Piddington, 1959; Dressler and Parker, 1959). Shinbori et al. (2003) analysed plasma wave phenomena associated with SSC using the database of the Akebono satellite observations. They showed that plasma wave enhancement correlates to SSC.

Wilson and Sudgiura (1961) show that the perturbation generated by the impact of the solar stream is propagated to the Earth primarily by longitudinal hydromagnetic waves in low latitudes and by transverse hydromagnetic waves in high latitudes. These propagation modes were convincingly deduced from the study of the characteristics of the polarisation of the SSC magnetic field. In high latitudes the SSC magnetic field is essentially elliptically polarised, whereas in low latitudes the polarisation is linear. Wilson and Sugiura (1961) also showed that at geomagnetic latitudes above about 40^0 the SSC magnetic field has characteristics of elliptical polarisation and that at the geomagnetic latitude of Honolulu, namely 21^0, the polarisation of the SSC field is linear. The elliptical nature of the polarisation is most pronounced at high latitudes. They interpreted these gross features of the SSC's in the following manner: as the front of a solar gas stream advances into the geomagnetic field, it creates a shock, because the speed of the stream surface is greater that the local Alfvén wave velocity in the region of the impact. The longitudinal hydromagnetic shock wave propagates to the Earth and is observed as a sudden increase in the magnetic field in low latitudes.

Sugiura (1961a, 1961b) has shown examples of transverse waves generated at a distance of several Earth radii and transmitted along the magnetic field lines to the northern and southern auroral zones. This suggests that the compression wave created

by the impact of the solar gas might generate transverse hydromagnetic waves that will propagate along the magnetic field lines to high latitudes.

Tamao (1975) contends that a transient state of compression or rarefaction in the outermost magnetosphere, caused by the interaction with the solar wind disturbance, is transmitted into the inner magnetosphere by the magnetosonic waves. In examining transient effects on the magnetosphere, Tamao draws a distinction between fast and slow magnetosonic waves, the fast magnetosonic wave as result of an SCC event and the slow magnetosonic wave as a part of the growth phase of substorms. The SSC is a transient phenomenon with a short timescale of less than 1 minute, whereas the southward turning of the solar wind magnetic field, which would cause the growth phase disturbance of substorms, occurs with a much longer timescale of 10 min or more. Enhanced solar wind pressure behind a shock front tends to compress the outermost part of the day side magnetosphere. The resulting enhancement of the Chapman-Ferraro current at the magnetopause attains its saturation level when there is a total pressure balance between the solar wind and the magnetosphere. During the transient stage before this saturation the state of compression will be transmitted into the inner magnetosphere by the magnetosonic wave. Since a traversing time of the fast shock front over the day side magnetopause is rather short, less than 100 seconds, the fast magnetosonic mode plays the dominant role in this transmitting process.

Ullalan et al. (1970) carried out balloon observations of X-rays produced by precipitating electrons in the morning sector of the auroral zone at the time of an SSC event. The researchers were able to distinguish between an X-ray burst associated with the SSC and the weak slowly varying X-ray event upon which it was

superimposed. The energy spectrum of the weak X-ray event is rather hard with an e-folding energy of about 50 keV, whereas the SSC associated X-rays were found to have an e-folding energy of 18-22 keV. In addition, they concluded that an important feature of an SSC precipitation event appears to be their soft energy spectrum, which is atypical for the times of day when the measurements were made (Brown, 1967; Barcus, 1968). They found an e-folding energy of 18-22keV for the bremsstrahlung X-rays, whereas a simultaneously occurring background X-ray event had an e-folding energy of 40-50 keV, the latter being typical for the morning sector.

Barcus (1968) concluded that the local release of quasi-trapped electrons through the impulsive disturbance of the field could not be responsible for the observed soft electron precipitation. This is a most important result since SSC-associated precipitation events observed in the morning and day sectors occur on closed field lines, and as Brown et al. (1961) have shown, that the supply of electrons trapped on such field lines would be sufficient to produce the observed X-ray events. The assumption of a wave-particle association mechanism is further strengthened as Kokubun and Oguti (1968) found that the same event as was reported on by Ullalan et al. (1970) was accompanied by VLF emission in the 2 kHz band. Several more recent studies confirm a connection of VLF emission enhancements with the precipitating energetic particles at high latitudes during SCC events (Saito et al., 1974; Gail et al., 1990) and with periodic solar wind pressure variations (Sibeck et al., 1989).

SSC phenomena include tailward propagating compressional waves which can produce precipitation of energetic particles and VLF waves (Yahnin et al., 1995). In their research which used an extensive chain of riometers, the energetic electron

precipitation spikes were limited in a zone ranging from 72^{o} to 66^{o} corrected latitude. The EISCAT radar at Tromsø identified the presence of a significant fraction of 40 keV electrons in the precipitating electron population. The precipitations reflected simultaneously at numerous riometers at different longitudes and latitudes indicate that the precipitation is not related to some local mechanism but rather is of a global nature. Association of SCA with VLF waves in the 1.2 – 2.5 kHz range suggests that 10-40keV electrons were precipitated by the electron cyclotron instability developing in the equatorial plane. This mechanism has been studied in detail and is believed to be responsible for the precipitation of the energetic electrons observed during SSC events (Yahnin et al., 1995).

Farrugia et al. (1989) presented a study of magnetopause motion and associated ground magnetic field oscillations which appear to be caused by changes in the pressure of the solar wind. Their analysis of an event shows that the changes are caused in the main by both increases and decreases in the solar wind dynamic pressure and, in particular, by changes in the solar wind density. They further show that changes in the solar wind dynamic pressure can be large enough to give rise to boundary velocities of many tens of kilometres per second and directly confirmed the occurrence of such velocities using a number of spaced satellites in geostationary orbit.

Nishida (1978) showed that variations in solar wind dynamic pressure alter the magnitude and distribution of currents around and within the magnetospheric cavity. This feature manifests itself by strong variations of the magnetic field at the Earth's surface within 1 min after the shock on the magnetosphere. Using riometers and balloon-borne X-ray detectors, Brown et al. (1961), Matsushita (1961), Ortner et al.

(1962), Ullaland et al. (1970), and Vorob'yev (1974) detected an immediate response to shock impacts in the form of increased energetic (tens of keV) electron precipitation and enhanced auroral luminosities along the auroral oval. The enhancements observed by these authors lasted ~ 3 to 10 min.

3.1.2 Observational Characteristics of the Initial SSC Perturbation

The response of the magnetic field to the SSC both on the ground and at satellite altitudes has been documented and forms the basis for most of the current knowledge of SSC mechanisms. SSC are usually identified in ground magnetometers by a sudden change in the H component (Horizontal, Geomagnetic North) of the magnetic field (e.g. Wilson and Sugiura, 1961; Matshushita, 1962). Linear polarisation of the disturbance vector predominates near the equator (Wilson and Sugiura, 1961) while elliptic polarisation is common at high latitudes (Wilson and Sugiura, 1961; Patel and Cahill, 1974) although there appears to be some disagreement about the latter conclusion (Matshushita, 1962; Araki and Allen, 1982). In most events, a negative pulse known as a preliminary reverse pulse (PRI) precedes the main impulse (MI) at high and low latitudes, but is not observed at middle latitudes (Araki, 1977). The combination of this delay with the polarisation relations led early workers to conclude that the PRI is the signature of the Alfvén wave arriving in the auroral region.

Figure 41 shows the characteristic signature in the horizontal component of the Earth's mantic field left by a magnetic storm. The SSC is associated with the initial compression of the magnetosphere, whereas the main phase results from the build-up of the storm-time ring current in the magnetosphere.

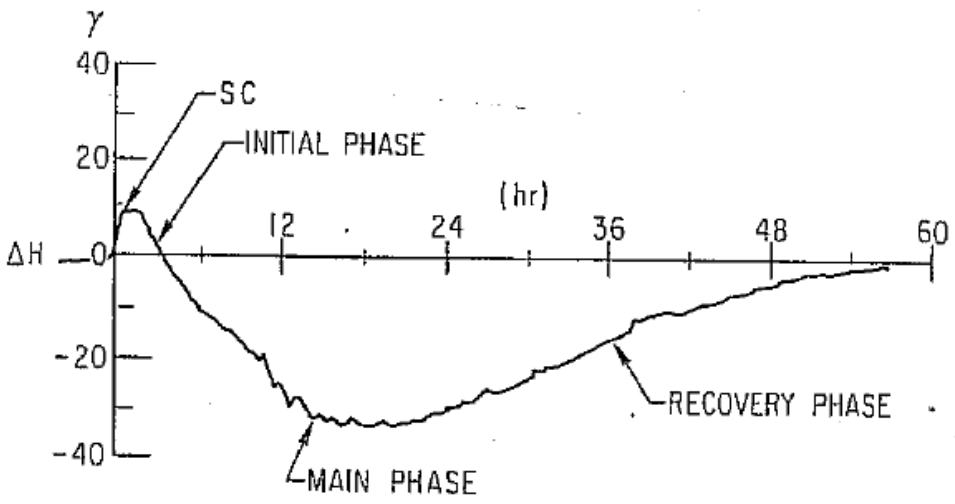

Figure 41. Characteristic signature left by a magnetic storm leaves in the horizontal component of the Earth's magnetic field. (Paulikas, 1972)

The onset of SSC is nearly simultaneous around the world, but the amplitude varies with latitude and local time. A statistical study of SSC (Mayaud, 1975) showed a mean rise time, defined as the time interval between the onset of the disturbance and the first extreme in the H component, of 4 minutes and a typical H component amplitude of 10 – 30 γ.

The magnetic signature observed at satellite altitudes is distinctly different from that seen on the ground, due in large part to the absence of ionospheric current effects. The nearly simultaneous onset of the initial magnetic perturbation seen at ground stations is not observed at satellite altitudes. Wilken et al. (1982) and Kuwashima and Fukunishi (1985) measured the relative onset time of SSC using geostationary satellites separated in local time and found differences of up to 3 minutes between the onset time at local noon and midnight. Wilken et al. (1982) calculated the azimuthal

propagation velocity of the disturbance in one case to be 910 km/sec, consistent with the expected value for a magnetosonic wave. Kokubun (1993) and Kuwashima and Fukunishi (1985) showed that SSC amplitude is highly dependent on local time at geostationary altitude, the maximum amplitude occurring near local noon and very small amplitudes occurring near midnight.

Several authors have measured energetic particles during SSC and in all cases, simultaneous flux changes were observed at all energies for both ions and electrons at the time of the magnetic perturbation (Arnoldy et al., 1982; Wilken et al., 1982, Tsunomura and Kuwashima, 1984; Korth et al., 1986; Wilken et al., 1986). Arnoldy et al. (1982) found that plasma injections associated with SSC were similar to those observed during substorms with the exception that SSC plasma injection occurs at all local times. Two competing mechanisms are thought to account for the initial flux variations observed by satellites (Paulikas and Blake, 1970; Wilken et al., 1982; Tsunomura and Kuwashima, 1984). Betatron acceleration due to the increased magnetic field causes a flux enhancement for any given energy. The earthward plasma drift behind the wave front causes a flux decrease for any radial position, since particle flux generally decreases with radial distance. Following the initial effects, plasma convected from the tail may account for additional flux variations (Arnoldy et al., 1982).

Observations have shown that sudden changes in wave activity in the ULF, ELF and VLF bands occur during SCC. The changes indicate that wave-particle interaction properties are significantly affected by the magnetic perturbation and associated plasma variations. It is commonly believed that the interactions leading to the observed wave activity involve ion gyroresonance in the ULF band and electron

gyroresonance in the ELF and VLF bands. Morozumi (1965) was the first to recognise that changes in ELF/VLF wave activity in the inner magnetosphere are associated with SSC events. Hayashi et al. (1968) also noted that the VLF noise was always seen about 30 seconds prior to the magnetic perturbation at high latitudes and that the centre frequency of chorus bands increased during positive SI's. The results lead them to suggest that VLF wave growth rates along the dayside equator increase/decrease as a result of the magnetic compression/expansion. In their model, based on the theory of Kennel and Petschek (1966), the magnetic field change preferentially affects the perpendicular energy of the gyrating electrons through betatron acceleration, changing the pitch angle anisotropy and thus modifying the growth rate.

Kokubun (1977) invoked the model of betatron acceleration to qualitatively explain observations of VLF intensity enhancements simultaneous with magnetic field changes over one several hour period. Korth et al. (1986) used a refinement of the Kennel-Petschek theory by Cornilleau-Wehrlin et al. (1985) to explain wave activity observed during an SSC. In their theory, wave growth is only possible when betatron acceleration increases the anisotropy beyond a level which will support path-integrated amplitude gain.

3.1.3 Morphology of the Initial SSC Perturbation

The pressure equilibrium condition which determines the magnetopause standoff distance may be upset by changes in the solar wind momentum associated with shocks and discontinuities, and the magnetopause position must be adjusted to maintain the dynamic pressure balance. Satellite observations show that the geocentric distance of

the magnetopause at the subsolar point can change as much as 2 – 3 R_e from an initial radius of 8 – 12 R_e (Nishida and Cahill, 1964; Kaufmann and Walker, 1974; Knott et al., 1982) in a period of 2-6 minutes. The adjustment is thought to occur adiabatically (Baumjohann et al., 1983).

The response of the geomagnetic field to such disturbances is complex but reasonably well understood (Nishida, 1978 or Wilken et al., 1982). Compressional hydromagnetic waves are generated along the magnetopause as a result of the solar wind disturbance and propagate isotropically inward (Tamao, 1975). These are fast magnetosonic waves with a propagation speed slightly higher than the local Alfvén speed. Both field line curvature and non-uniformities couple the magnetosonic mode to the transverse Alfvén mode (Tamao, 1969; Chen and Hasegawa, 1974), generating field-aligned hydromagnetic waves that propagate at the local Alfvén speed.

The initial magnetic signal observed on the ground is generated from currents in the ionosphere driven by the electric field of the hydromagnetic wave (Nishida, 1964; Schutz et al., 1974; Newton et al., 1978). Observations of a well-defined minimum in the amplitude of SI/SSC magnetic perturbations at magnetic latitudes near 200-300 (Wilson and Sugiura, 1961) are in general agreement with the fact that the Hall conductivity at high latitudes and the Cowling conductivity near the equator are much larger than conductivities at middle latitudes (Araki, 1977). The electric field generated in the ionosphere couples to the Earth-ionosphere waveguide where it propagates at nearly the free-space speed of light (Kikuchi et al., 1978; Kikuchi and Araki, 1979a; Kikuchi and Araki, 1979b; Kikuchi, 1986), explaining the observed nearly simultaneous onset of the initial magnetic perturbation at all latitudes and local

times (Matsushita, 1962). These currents decay with the disappearance of the original hydromagnetic disturbance, but longer term modifications to the geomagnetic field may continue as a result of enhanced convection in the outer magnetosphere and modification of the Chapman-Ferraro current on the magnetopause as well as subsequent development of the ring and tail currents (Araki, 1977).

Events associated with the SSC of magnetic storms have been measured by balloon instruments on at least three occasions (Anderson, 1958; Brown et al., 1961). The increase in cosmic noise absorption during these events appears to be due to high-energy electrons and/or X-rays produced by bremsstrahlung from them which penetrate into the lower ionosphere from outside the Earth's atmosphere (Matsushita, 1962). The duration of the X-ray burst and the riometer absorption signature is usually only in the order of a few minutes and the energies of the photons are clearly below those of nuclear gamma-rays (Hoffman and Winckler, 1963). These features, with the exception of the energy range, are very different from the common auroral X-ray bursts and indicate that the processes producing the precipitation are quite different and it has been noted (Pfotzer, 1965) that the hydromagnetic shock due to the arrival of the plasma cloud at the boundary of the magnetosphere will initiate a precipitation of an obviously distinctly limited flux.

3.1.4 The Physical Process of the Initial SSC Perturbation

The environmental changes observed during an SSC are driven by a number of physical processes which act over different timescales. During the early part of the SSC, the dominant processes are directly linked to the original magnetic disturbance. As the SSC progresses, secondary effects such as ionospheric modification, ring

current development and particle injection from the magnetotail play increasingly significant roles. The compression of the magnetosphere during an SCC causes the field lines to move earthward, as shown schematically in figure 42.

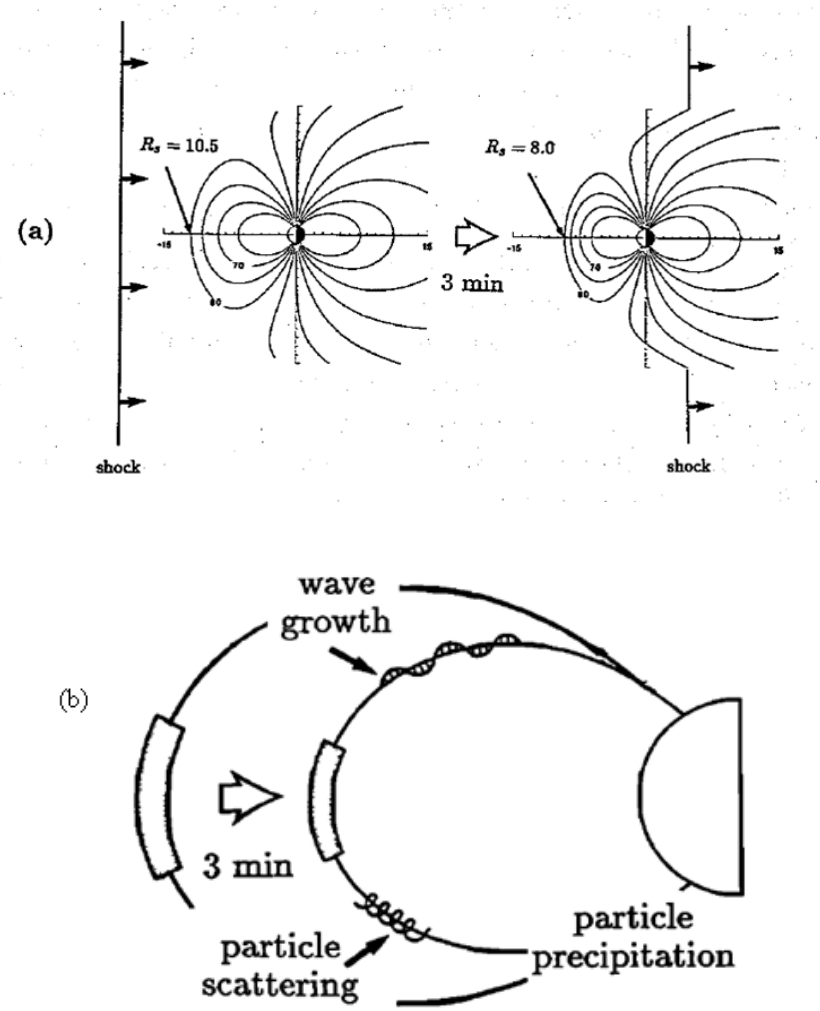

Figure 42. Schematic Diagram showing magnetospheric changes associated with SSC. (a) the compression of the magnetosphere caused by the passage of the solar wind shock. The two magnetospheric configurations shown correspond to standoff distances of 10.5 R_e and 8.0 R_e. (b) the displacement of a magnetic field line, the motion of the interaction region and the corresponding consequences for the wave and particle populations (Gail et al., 1990b)

The thermal plasma is "tied" to magnetic lines as a result of the frozen-in condition of MHD theory. A duct thus remains collocated with a given field line throughout the SSC compression and the waves and particles associated with a particular duct prior to the SSC will be associated with that duct throughout the SSC event. For the particle energies of interest, drift velocities are sufficiently small that energetic particles may also be considered "tied" to field lines for most purposes.

The current understanding is that the changes in thermal and energetic plasma populations resulting from an SSC include changes in flux density, velocity space distribution and drift properties. It is understood that non-adiabatic modifications of the energetic plasma also occur as a result of wave-particle interactions.

3.2 Energisation/Precipitation Models

Previous work (Ortner et al., 1962; Hartz, 1963) has shown that riometer absorption is associated with SSC at all local times and is generally linked to the geomagnetic latitude zone between 57^0 and 75^0. Wave-induced particle precipitation is often assumed to be the cause of the absorption (Leinbach et al., 1970; Perona, 1972), implying that changes in wave activity are triggered by the SSC throughout a large portion of the inner magnetosphere. The effect of other mechanisms can be minimised by analysing absorption effects that occur during the initial perturbation. Since the adiabatic changes in particle trajectories can only increase the pitch angle, adiabatic effects alone can not increase the particle flux within the loss cone and thus can not account for all the absorption seen. With the assumed absence of other scattering mechanisms during the initial perturbation, the increase absorption seen must result from wave-induced precipitation (Gail, 1990).

Tsurutani et al. (2001) showed that there is significant solar wind energy transfer to the magnetosphere – ionosphere system during and after interplanetary shock impingement at the Earth's magnetosphere. They further outlined three solar wind energy transfer mechanisms that may be responsible for the energetic particle precipitation. It is of course possible that several different mechanisms might be taking place at the same time.

3.2.1 Adiabatic Compression

A schematic representation of an adiabatic compression model is given in figure 43. The ram pressure increase across the shock compresses the frontside magnetosphere. Pre-existing plasma on outer zone magnetospheric field lines becomes betatron accelerated/energized from the absorption of solar wind ram energy. By conservation of the first adiabatic invariant, $E\perp/|B|$, where $E\perp$ is the particle perpendicular kinetic energy, magnetospheric compression leads to an increase in $E\perp$. Because $E\|$ remains nearly constant, $E\perp/E\|>1$. This latter effect leads to loss-cone instabilities with the growth of plasma waves and concomitant electron and proton pitch angle scattering. The particles that get scattered into the loss cone have collisions with upper ionosphere atoms and molecules and lose most of their energy by electron excitation. The subsequent atomic and molecular decays lead to increased ionisation in the ionosphere.

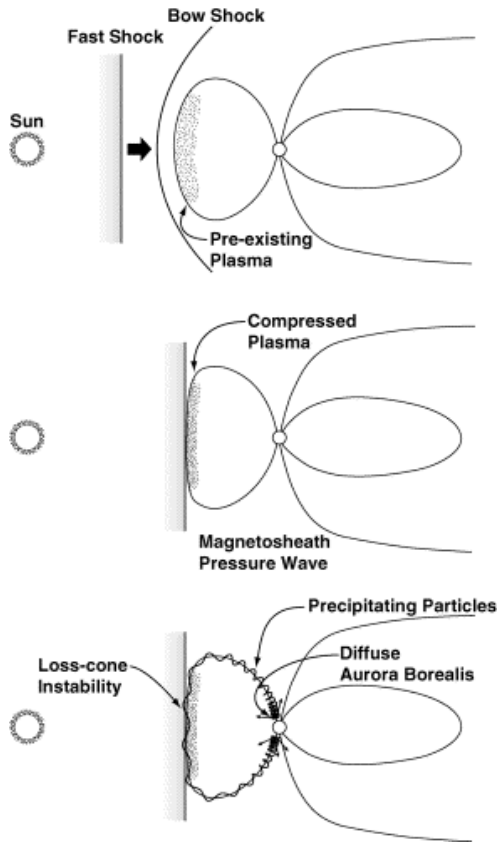

Figure 43. A schematic representation of adiabatic compression of dayside magnetospheric plasma. Zhou and Tsurutani (1999)

Olsen and Lee (1983) and Anderson and Hamilton (1993) have noted enhanced electromagnetic ion–cyclotron waves and Lauben et al. (1998) enhanced electromagnetic whistler mode chorus emissions during magnetospheric compression events. These results support the above scenario for the onset of dayside proton and electron loss-cone instabilities during shock compression events, respectively. This is a good model to explain what occurs at SSC events. Although Zhou and Tsurutani (1999) focus on the dayside magnetosphere, it is clear from other observations using networks of geosynchronous satellites that the night-time magnetosphere also undergoes compression as the shock waves pass the Earth (see Baker et al.., 1978 for a review), resulting in loss-cone instability in the night-time magnetosphere.

One expects that the most dramatic changes in the global drift of energetic particles due to the IMF shock might be expected to occur at the front side of the magnetosphere (Wilken et al. 1982) where one could expect most of the precipitation to occur but that is not the case and precipitation occurs on both night and day side. It was found by Ranta and Ranta (1990) that at L>5 the precipitation events are more numerous at night than during the day.

3.2.2 Field-aligned Current Intensifications

Shock compression of the magnetosphere may also lead to intensification of field-aligned currents (Araki, 1994; Lysak et al., 1995). A schematic representation is shown in figure 44. If current-driven instabilities (Lakhina et al., 1999) are caused by this mechanism, depending upon the ion to electron temperature ratio, T_i/T_e, either electrostatic ion acoustic waves or lower hybrid waves are expected to have strong growth rates. The turbulence due to current-driven instabilities could enhance anomalous resistivity, which could then support large parallel electric fields along auroral zone field lines. These parallel electric fields can accelerate charged particles, and downward accelerated electrons can produce intense aurora. Alternatively, the nonlinear development of these waves may lead to the generation of double-layers and the acceleration of auroral particles close to the ionosphere. Once again this model applies equally to the night-time and day-time magnetosphere as the compression creating shock-wave passes the Earth.

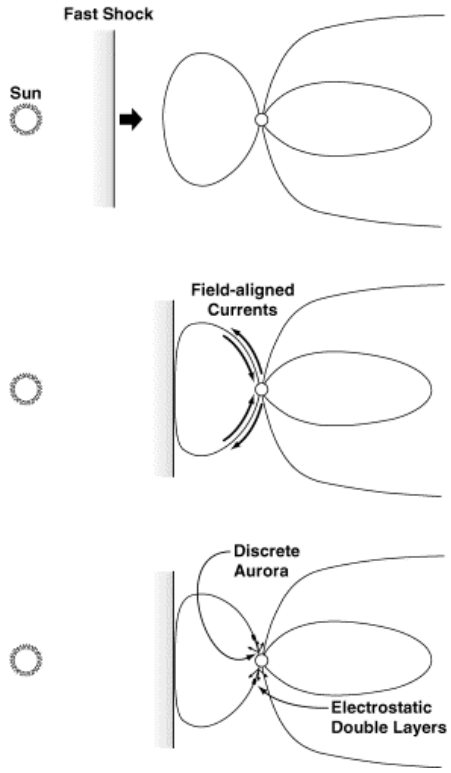

Figure 44. A schematic representation of dayside field-line current intensification.

Zhou and Tsurutani (1999)

How can one distinguish between these two models? It is clear that both plasma compression and field-aligned current intensification can be associated with shock compression events. Clearly, field and plasma compressions take place, but whether or not the loss-cone instabilities are sufficiently strong to lead to significant particle losses to explain all the ionisation effects seen is not known at this time.

3.2.3 Viscous Interaction

It was noted that the E-layer phenomena can be present many hours after shock passage, well into the initial phase of a magnetic storm. It is doubtful that either of the two shock-related mechanisms discussed previously could account for these displays. The bounce times of energetic ~1–10 keV electrons and ions are seconds and minutes,

respectively, so compressed, pre-existing particles should be lost after ~10 s or minutes and this corresponds to the short sharp bursts of SCA. For field-aligned current enhancements, this would be expected just at the time of shock passage and the effects would be maximum at noon rather than at dawn or dusk. Thus, this latter mechanism seems unlikely to explain auroras near dawn and dusk hours after shock passage. A more likely scenario is the development of a Kelvin–Helmholtz instability (Rostoker et al., 1992). This instability growth rate maximizes when the field lines of the magnetosheath and the magnetotail are orthogonal to the solar wind fields. A schematic representation of this mechanism is given in figure 45.

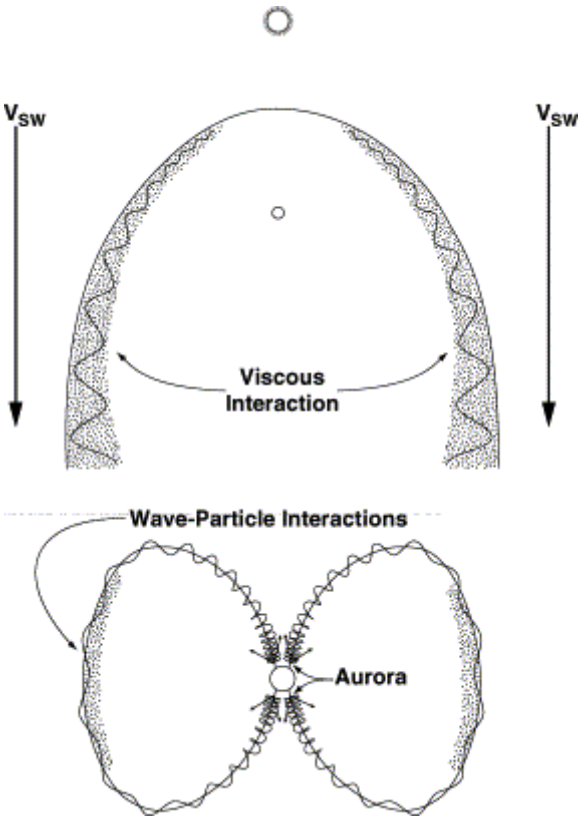

Figure 45. A schematic representation of viscous interaction. Zhou and Tsurutani (1999)

In this model there is a constant triggering of wave particle interactions until the solar wind returns to its quiet state and the magnetosphere returns to its pre-shock state. Of course the solar wind, even in its quiet state is subject to these viscous interactions which result in the continuous low level precipitation experienced at high latitudes. However, it is the enhanced viscous interaction, due to solar wind pressure enhancements following SSC events, which it is postulated leads to intense E-layer formations that occur during the initial storm phase. This model appears most applicable when explaining the work covered in chapter 4 on partial and full blanketing E-layers where particle precipitation following an SSC event creates intense, long-term E-layer formations.

3.2.4 Particle Penetration

Figure 46 shows the penetration depths of electrons and protons in the Earth's atmosphere. The quantity plotted against altitude is the approximate height where the particles are stopped if their path is vertical. Polar absorption is caused by protons in the energy range 1 to 20 MeV and possibly to some extent by α-particles in the same energy range. Absorption due to the increased D region ionisation is usually called auroral absorption. It is caused mainly by electrons in the energy range 50 to 500 keV. The sporadic E-ionisation occurs in the same height range as the visual aurora. Both effects are probably caused by protons in the energy range 50 to 200 keV and electrons in the range 5 to 30 keV (Eriksen et al., 1967).

Wilson and Stoker (2002) noted that the differences in morphologies of optical emissions and absorption regions, together with temporal differences, imply that there are two categories of energetic auroral electrons: the softer electrons (<10keV)

causing optical emissions in the E and F regions of the ionosphere and the harder (>10keV) electrons ionising down into the D region for cosmic radio noise absorption.

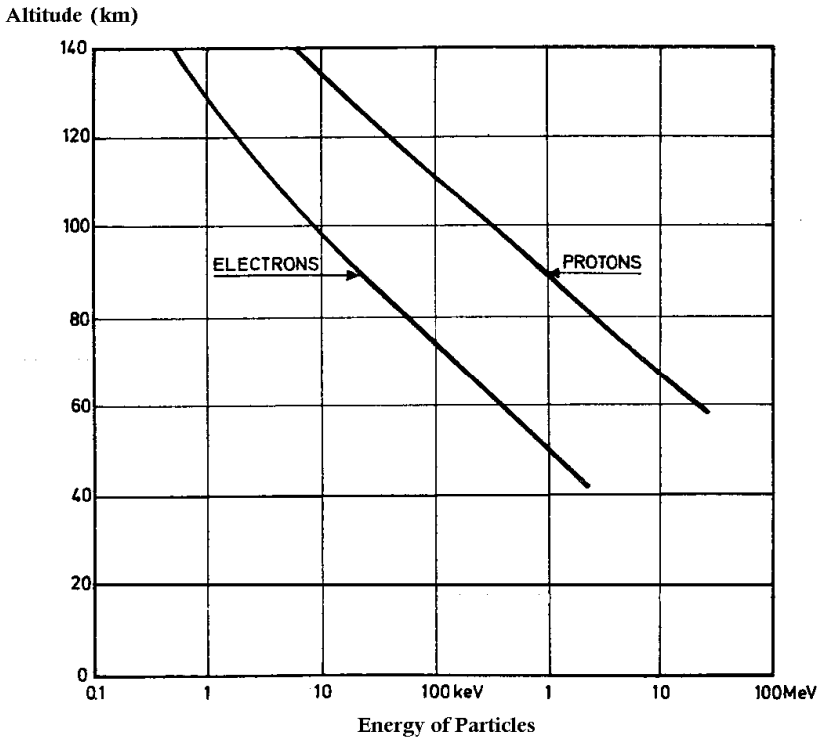

Figure 46. Penetration depth of electrons and protons in the Earth's atmosphere (Eriksen et al., 1967).

These observations suggest that the softer electrons, causing E and F region optical emissions, may be injected onto drift paths closer to Earth than the more energetic electrons, ionising down into the D region for cosmic radio noise absorption. Wilson and Stoker (2002) postulate that the harder electrons could have been accelerated by, for instance, an increasing dawn-to-dusk electric field.

Hartz and Brice (1967) studied the latitudinal and diurnal variations of 10 years of auroral data and concluded that there were two basic categories into which observations fell, implying electron precipitations into two different energy ranges.

The first category included the discrete or localised events, which are rapid-changing events associated with heights generally in excess of 100 km, where the electron collisional frequency is sufficiently low to expect magnetic field-aligned ionisation structures. The second category contained the slowly varying auroral events, which appear to be associated with heights of the order of 80 km, where the electron collisional frequency is great enough for significant radio wave absorption and where field aligned ionisation irregularities are not expected. Both categories appear to be always present (Hartz and Brice, 1967). The harder precipitation (>10keV) tended to occur at a slightly lower latitude than the softer precipitation (<10keV).

Energetic particles can influence the ionosphere in a variety of ways, both directly and indirectly. While work continues on the influence of energetic particle bombardment on the low- and middle-latitude ionosphere, there is no doubt that bombardment by energetic particles plays a very important role and lies at the root of most of the distinct features of this region. Particle bombardment influences the high-latitude ionosphere very directly at times by increasing the free electron density and rather more indirectly through its heating effects.

Historically, probably the first realisation of the importance of particle bombardment effects in the high-latitude ionosphere came about through the work carried out during the Second International Polar Year at Tromsø, Norway (See refs in Reid, 1965). These observations showed clearly that an enhancement of the ionisation in the ionosphere due to precipitating particles commonly accompanied aurora and geomagnetic activity.

3.3 Short Case Study: Particle Precipitation at SSC.

This case study examines the precipitation of particles that occurred during the SSC event at 20:25 UT on 25 September 2001 as captured by Incoherent Scatter Radar. In this case the event was captured on the Sondrestrom IS radar using a scanning mode that is well suited for F region measurements where the scale height is large. This mode uses dual frequency 320 microsecond pulses, resulting in 48 km range resolution. However, in the E-region where the scale height is small, this greatly smears the returns from those altitudes, and consequently the E-region data can only be used qualitatively and not for quantitative studies: however, this does show the relative change that occurs in electron density before, during and after the SSC occurs.

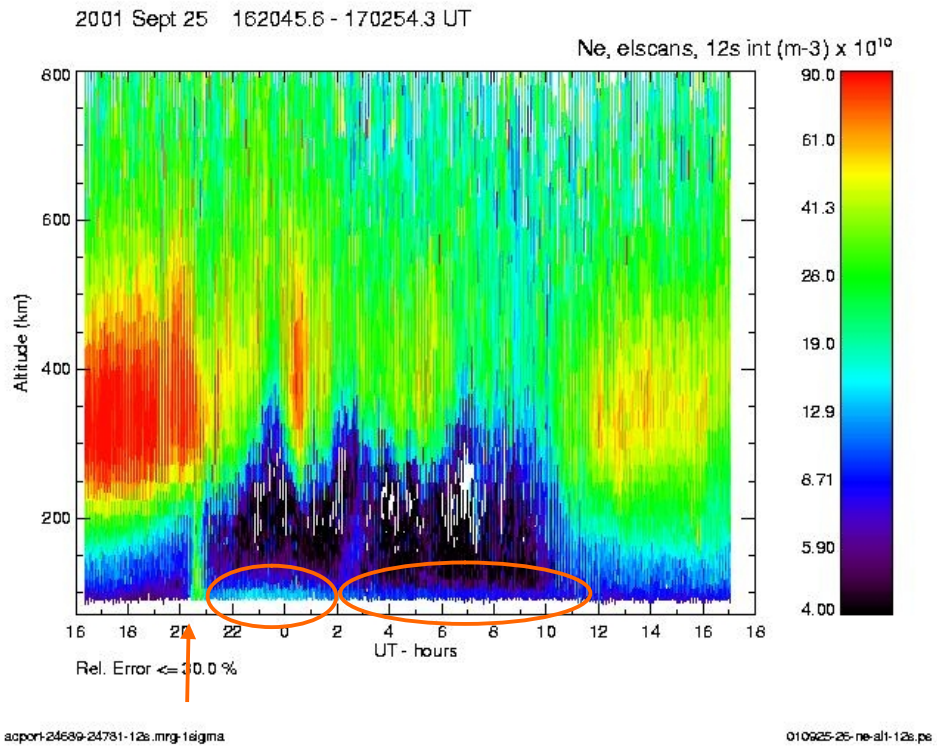

Figure 47. Electron Density Measurements from the Sondrestrom ISR, the arrow indicates the moment of SSC.

As shown in figure 47, in the four hours before the SSC the electron density is reducing in line with the reduction in solar energy as night sets in. At the moment of SSC there is a clear band of enhanced electron density for just over half an hour starting at 20:25 and ending just after 21:00 covering the altitude 90 – 200 km. During this 35 minute period the electron density is at least quadrupled as particle precipitation penetrates to at least 90 km (the lowest measured altitude on this scan) causing significant enhanced electron density values.

Further disturbances occur and just visible after 21:00 at 100 km altitude and continuing until 01:00 the following day are patches of enhanced electron density at, and even below, 100 km altitude. Interestingly, after 02:00 the zone between 100 km and 120 km altitude has a higher electron density than the area above 120 km.

3.4 Sudden Commencement Absorption

Sudden enhancements in the solar wind dynamic pressure are known to compress the magnetosphere and enhance the magnetopause current (Kauffman and Konradi, 1969), as well as the tail currents (Russell et al., 1994a). Zesta et al. (2000) noted in their study of the 10 January 1977 disturbance that the response of the magnetosphere to a pressure front was practically instantaneous, global and directly driven by the propagation of the solar wind density enhancement region through the magnetosphere.

A SSC, heralding the arrival of the shock wave, creates hydromagnetic waves which spread out through the magnetosphere and transform the magnetosphere everywhere into a new compressed steady state configuration which is in balance with the increased solar wind pressure. This requires a restructuring of pitch angle

distributions and the precipitation of excess particles to rebalance the magnetosphere under this new compressed state. However, one factor that has been suggested as a cause of geomagnetic activity is the solar wind dynamic pressure p_s (Rostocker and Falthammar, 1967). An increase in this quantity implies an increase in either the solar wind velocity v_s, the number density of particles in the solar wind, n_s, or some combination of variations in these two parameters to produce an increase in p_s.

Sudden Commencement Absorption (SCA) occurs simultaneously with the sudden commencement of a world-wide geomagnetic storm. The arrival at the front of the magnetosphere of shock fronts travelling in the solar wind or other sudden changes in the solar wind plasma pressure may cause sudden compressions or inflations of the magnetosphere. Such strong disturbances may cause impulsive precipitation of the otherwise trapped high energy electron population. The precipitation of typically 30 – 300 keV electrons (Stauning, 1996) may create considerable – but short lived – ionisation enhancements in the D-region (60 - 90 km). These enhanced ionisation events may have durations of typically a few minutes.

The character of SCA is very similar to that of the SCNA (Sudden Cosmic Noise Absorption). The sudden onset of the absorption to sometimes high values within a minute and its short duration are common characteristics. SCA differs from SCNA mainly by virtue of the very different diurnal and latitudinal patterns. Not only can SCA be simultaneously registered at riometers both on the day side and the night side, but it seems to be limited to stations near the auroral zone maximum, whereas SCNA is observed over the entire sunlit hemisphere. Furthermore, SCA is not accompanied by solar noise bursts as is SCNA (Ortner et al., 1962).

The first record of an SCA event of this kind appears to be the one described by Brown et al. (1961) and was associated with the SSC of 27 June 1960 at 0146UT. During this same event an X-ray burst was measured by balloon-borne cosmic ray detectors over College, Alaska (Brown, 1961). The assumption from this and other studies is that the ionisation in the lower ionosphere that occurs at the time of an SSC is due to X-rays, presumably originating at a greater height from electrons entering the upper atmosphere.

Previous studies (Brown et al., 1961) have shown that on occasion, brief ionospheric absorption events occur promptly with the onset of sudden commencements of geomagnetic storms. This is confirmed as often a particle precipitation event, observed as ionospheric absorption, occurring simultaneously with a SSC (Ranta et al., 1990). These SCA events occur most often at auroral latitudes (Ortner et al., 1962). However, it is clear that the sudden compression of the magnetosphere that occurs with an SCC can also give rise to SCA events at auroral latitudes in the night time hours (Brown, 1973). In their paper, Ranta and Ranta (1990) compared the magnitude of the absorption seen at Kevo (L=6) and the magnitude of negative B_z. From this they clearly showed that there is no dependence between the magnitude of the absorption and the magnitude of negative B_z.

It is noted by Ortner et al. (1962) that when taking readings on a co-located vertical and oblique riometer, most SSC absorption events were strongest on the oblique riometer than on the vertical riometer. This is consistent with the concept of a uniform absorbing layer, increasing absorption being due to the obliquity factor for

the oblique antenna. The fact that SCA effects have been found to be concentrated in the auroral zone clearly implies that the ionising electrons are precipitating into the Earth's atmosphere along the geomagnetic field lines.

The consequences of precipitation on HF circuits at high latitudes, within the aurora1 zone and polar cap ionosphere, are less well known. Physical models have been employed to investigate the interplay between storm-time processes: for instance Sojka and Schunk (1983) predicted a near 10-fold increase in the polar cap F-region electron density as a consequence of enhanced precipitation in the aurora1 oval and convection of enhanced electron densities into the polar cap. Enhanced convection velocities can also result in a deepening and enlarging of the mid-latitude trough (St. Maurice and Torr, 1978), a region of depleted F-region electron densities in the night-side sub-aurora1 ionosphere (Muldrew, 1965). Competition between the storm-time processes results in highly complex behaviour that is difficult to predict. The effect of a storm at a given location is dependent on local time, season, latitude and the time elapsed since the storm commencement. Consequently, the influence of the ionospheric perturbation on HF propagation is dependent on the positions of the transmitter and receiver relative to the various high latitude regions (e.g. the aurora1 oval, polar cap, and mid latitude trough) (Davies, 1990).

3.4.1 Source of Energetic Particles Causing SCA

Figure 48 shows the various particle source regions that have been identified in the magnetosphere.

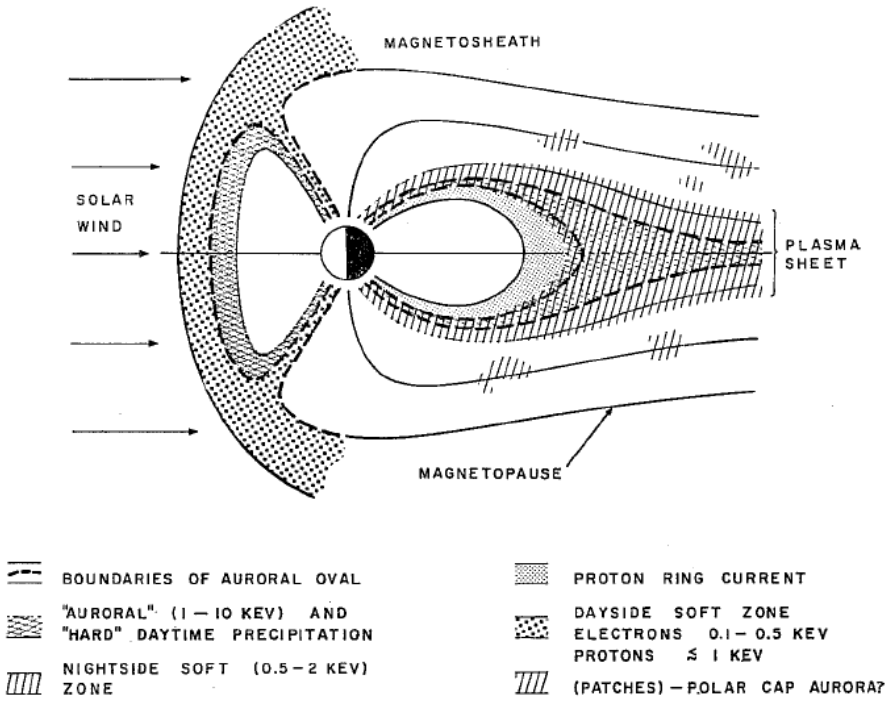

Figure 48. Source regions in the magnetosphere (Eather and Mende, 1972).

Kikuchi and Yamagishi (1989) present compelling results that clearly indicate that the energetic electrons associated with an SSC originate in the trapped radiation belt. Using a scanning beam riometer at Syowa Station (Antarctica, L=6.1) the authors observed distinct differences in the latitudinal features of energetic electron precipitation and the time delay of precipitation associated with an SSC, and precipitation associated with substorms.

The observations show SSC-associated CNA moving equatorward at a speed of 500 m/s, while the subsequent substorm-associated CNA was displaced poleward at a speed of 5.8 km/s. The equatorward displacement of the SSC-associated CNA observed in the midnight sector coincides with the propagation of hydromagnetic waves in the nightside magnetosphere (Wilken et al., 1982). The poleward movement

of the substorm associated CNA corresponds to the poleward expansion of auroras at the time of auroral break up (Kikuchi and Yamagishi, 1989). With reference to figure 49, this result strongly suggests that the SSC-associated energetic electrons originate in the trapped radiation belt within the plasmasphere where the closed field lines are limited in latitude. While substorm associated energetic electrons must come from outside the plasmasphere, mostly likely from the plasmasheet where access to higher latitudes is possible.

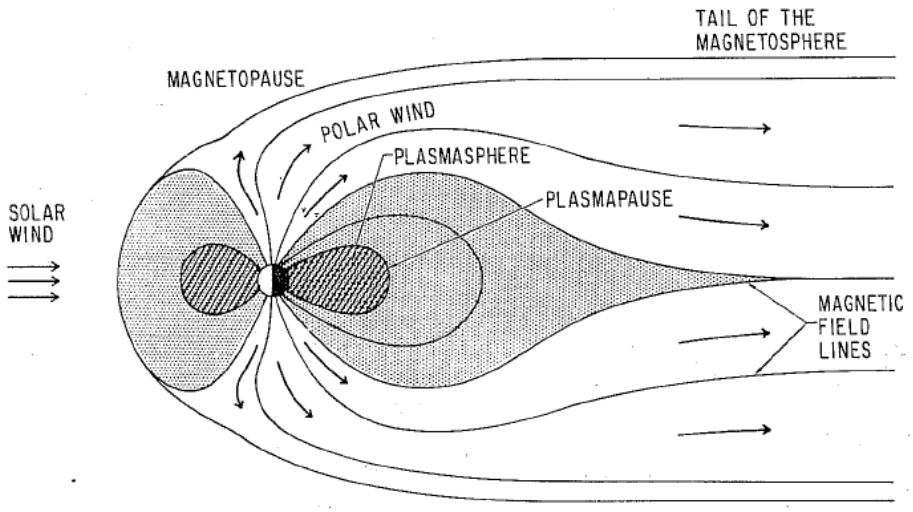

Figure 49. The different source regions of the magnetosphere. In the plasmasphere field lines are closed and, to a large extent, co-rotate with the Earth. At very high latitudes the field lines are open to the tail of the magnetosphere. Between the plasmapause and open regions field lines are closed, but convect around the Earth (Banks, 1972).

3.5 Characteristics of SCA: Data and Analysis

From the IAGA (IAGA, 2009) list of officially recognised SSC events, events spread across the years 2000 to 2006 were selected for analysis. This period encompasses more than half a solar cycle, from the sunspot maximum in 2000 to the near sunspot minimum in 2006 and allows any dependency on solar activity to be evaluated. During this period a total of 201 SSC events occurred of which 26 were categorised in the IAGA list as possible SI events by one or more participating observatories. To ensure only unambiguous SSC events were examined, these 26 events were discounted, leaving 175 events that form the basis of the findings in this thesis.

3.5.1 Riometer Data

For each of the 175 SSC events examined, data from the IRIS Riometer at Kilpisjärvi (69.10N, 20.80E, L=6.06) was used to measure the peak absorption resulting from particle precipitation caused by SSC shocks. An example of such an absorption signature, from the 3 April 2004 SSC event, which occurred at 14:10 UT, is shown in figure 50. Before the SSC the absorption was negligible. At the start of the SSC the absorption increases within 5 minutes to 0.8 dB, peaking at 0.85 dB ten minutes after the SSC event commences. Fifteen minutes after the peak the absorption falls to less than 0.2 dB with some variability thereafter due to subsequent magnetospheric activity.

Excluded from the dataset, by visual examination of each riometer record, are cases where absorption cannot be clearly attributed to the corresponding SSC events or where observations occurred against a background of solar proton precipitation. This ensures that absorption phenomena other than SCA is excluded from the dataset.

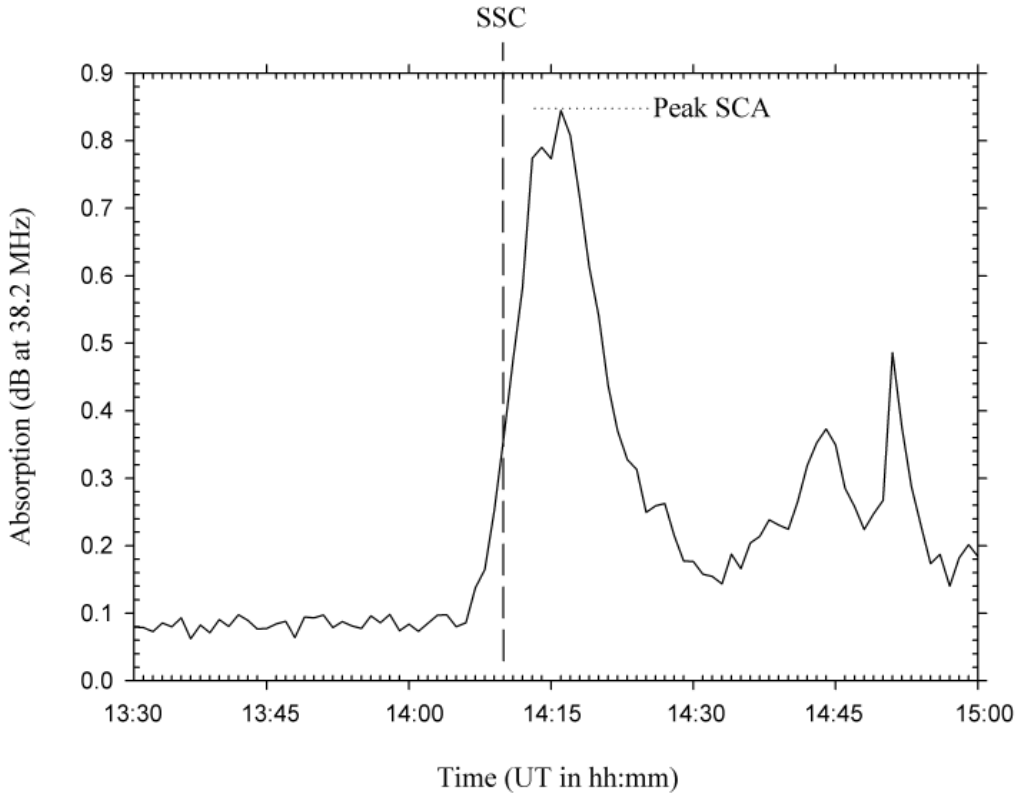

Figure 50. Riometer measurement from the central beam of the IRIS riometer at Kilpisjärvi (69.050N, 20.790E) on 3 April 2004, 1 minute resolution sampling. The SSC occurred at 14:10 UT which is indicated by the long-dashed line. The peak SCA measured in this example is indicated by the dotted line.

3.5.2 IMF Data

IMF Data for this study was sourced from measurements taken by the ACE spacecraft. See Stone et al. (1998) for details of the satellite and instrumentation. Figure 51 is a typical example of the data collected for each SSC event. This particular event occurred at 10:52 UT corresponding to an SSC observed at the Earth's surface at 11:37 UT. The window of measurement is marked between long dashed lines.

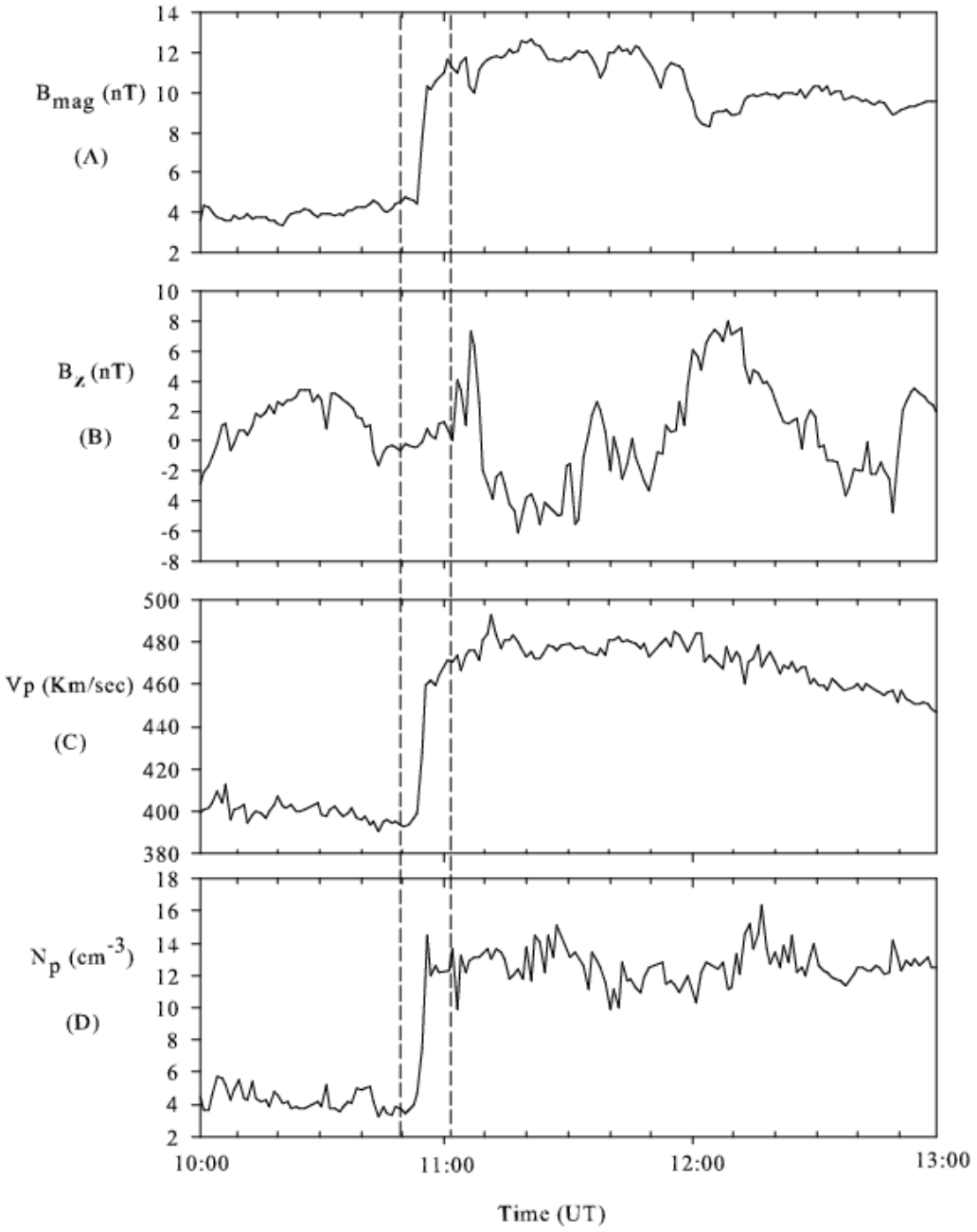

Figure 51. Example of IMF data collected showing the sudden increase in the solar wind pressure, corresponding increase in plasma speed, density and changes in the magnetic components. Data from 23 March 2002, 64 seconds averages used.

Figure 51 panel A captures the magnitude of the solar wind. Before the shock the solar wind was quiet for more than 12 hours. Following the shock the amplitude more than doubles and remains at this elevated level for at least another 12 hours.

Figure 51 panel B indicates the magnitude and direction of the B_z component. B_z oscillates between slightly positive and slightly negative before and during the window of measurement, after which B_z undergoes first a stronger positive (movement north) then negative (movement south) before continuing with larger oscillations for a number of hours.

Figure 51 Panel C captures the proton velocity (V_p) which is fairly steady around 400 km/sec for 12 hours before the shock. Following the shock the velocity increases to nearly 480 km/sec before slowly tailing off over the next 8 hours. Figure 51 Panel D shows the proton density (Np) which is steady below 5 cm^{-3} for 12 hours preceding the shock after which it increases to a peak of 14 cm^{-3} where it remains for at least 6 hours.

Using the event shown in figure 51 as an example, the data in table 6 was gathered or calculated for each of the 175 SSC events.

	Description	Value from figure 51
ΔB	The change in IMF magnitude. (Fig 44, A)	6 nT
B_z	The change in direction of the B_z, component. (Fig 2, B)	South to North
ΔVp	The change in proton velocity. (Fig 44, C)	75 $km.sec^{-1}$
ΔNp	The change in proton density. (Fig 44, D)	10.5$.cm^{-3}$
P_{Ram}	The change in ram pressure[1].	4.2 nPa
$\Delta_R B$	The relative change[2] in IMF magnitude	0.18
$\Delta_R Vp$	The relative change in proton velocity	2.63
$\Delta_R P_{Ram}$	The relative change in ram pressure	4.03

Table 6. Description of solar wind data gathered for each SSC event.

[1]Ram pressure is also known as dynamic pressure and is a function of solar wind speed and density. The recommended formula when using ACE data is (SEC 07):

$$P = 1.6726 \times 10^{-6} . n_p . V_p^2 \quad \text{(nPa)}$$

where Pressure P is in nPa, n_p is the density (particles.cm^{-3}) and V_p is the velocity (km.s^{-1}) of the solar wind.

[2]The concept of relative change can be used to normalise any parameter by reflecting the relative change in the parameter and not the absolute value of the change. It is calculated as follows, using pressure as an example:

$$\frac{\text{Change in Pressure}}{\text{Initial Pressure}} = \frac{\Delta P\,[\text{nPa}]}{P_i\ [\text{nPa}]}$$

$$= \text{unitless relative change in solar wind pressure}$$

3.5.3 Data Analysis: Effect of Solar Activity on SCA

As the data spans more than half a solar cycle it can be used to determine if solar activity influences the data set. This was done by evaluating the link between SCA and the change in IMF magnitude against solar activity as reflected by the value of the relevant monthly sunspot number.

Figure 52 (top panel) shows a general spread of low, medium and high values of SCA at all levels of sunspot activity. Figure 52 (bottom panel) shows a similar pattern in ΔB (the change in IMF magnitude) at all levels of sunspot activity. It is concluded that there is no causal link between SCA and sunspot number or between IMF magnitude and SCA, other than in the frequency of occurrence of SSC events.

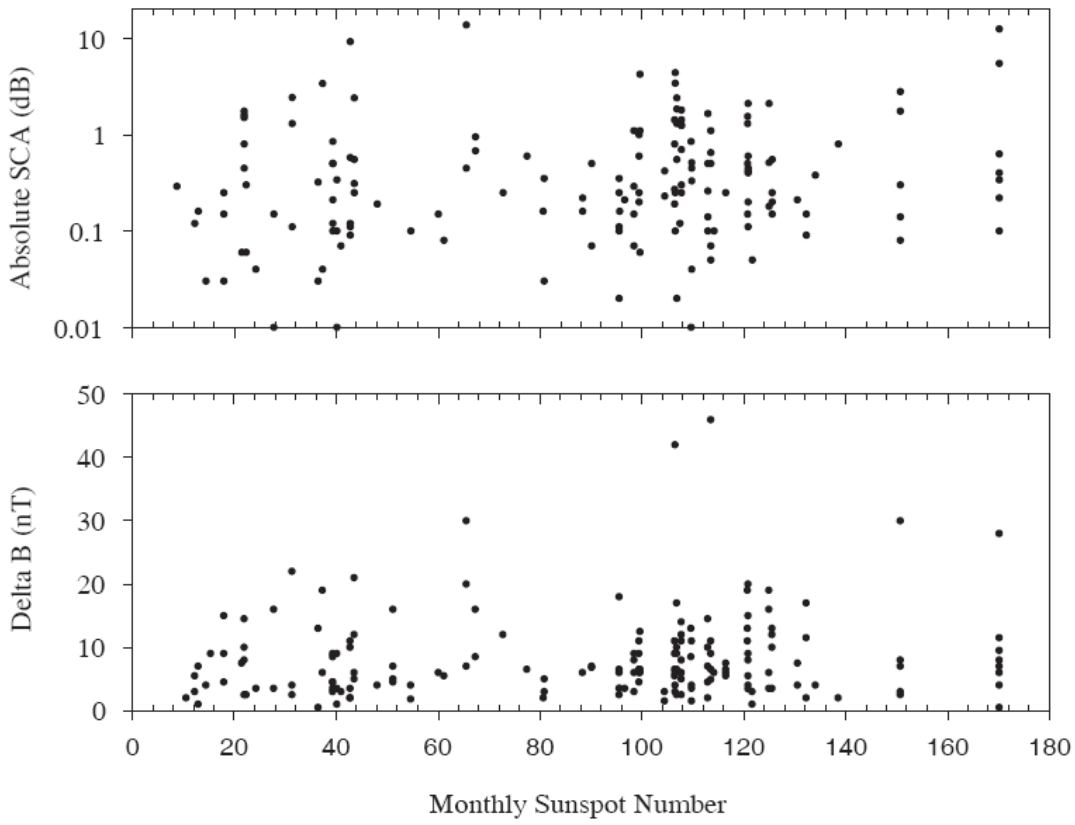

Figure 52. Scatter plot of the absolute values of SCA vs. Sunspot Number (top panel) and Change in IMF Strength (bottom panel)

3.5.4 Basic SCA Statistics

An examination of the basic statistics of all SCA measured is presented to give some idea of the typical SCA levels that can be expected. Figure 53 is a graph of SCA measured at each SSC event, sorted left to right by ascending SCA amplitude. A logarithmic vertical axis is used in this graph in order to reveal the range of SCA values measured. The following SCA statistics are revealed in the database:

- Maximum SCA value measured - 13.8 dB
- Mean of SCA values calculated - 0.84 dB
- Median of SCA values calculated - 0.29 dB

- Mode SCA value observed - 0.25 dB
- Standard Deviation of SCA calculated - 1.47 dB

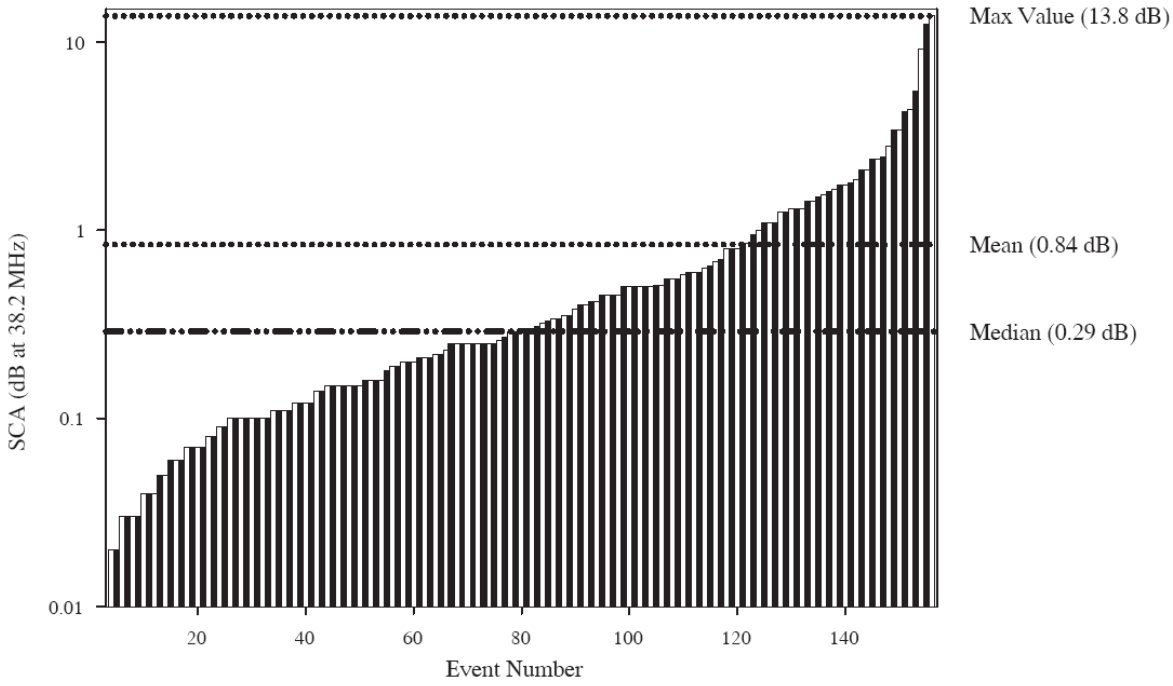

Figure 53. Basic SCA Statistics – Sorted events

Over the six year period of measurements there is a wide variation in the amplitude of SCA measurements.

3.5.5 Influence of Local Time on SCA

This section examines if there is any dependency between SCA (SSC events) and the time of their occurrence. This is done to ensure that there are no local influences on the data as is often seen in absorption caused by substorm effects. As shown in the left-hand side graph of figure 54, there is clearly no grouping of SSC events in any particular MLT hour. This confirms that there is a random occurrence of SSC events across all local times. The right-hand side figure of figure 54 indicates the spread of

the occurrence of the 175 SSC events examined in this study. The radial axis has no unit and is arbitrarily selected. In general there is an even spread across all sectors with some small gaps around 7, 13, 17 and 20-21 MLT. There is no apparent reason for these gaps and they appear to be random.

Table 7 gives a breakdown of SCA statistics divided into day events (6 – 18 MLT) and night events (18 – 6 MLT). While the occurrence of SCA is slightly greater during the day there is no significant difference in the mean or median values of SCA between the two sectors. This illustrates that SCA occurs with similar characteristics during both the day and night. The response of the magnetosphere to abrupt solar wind enhancements is a global disturbance directly driven by the solar wind, and we believe that the response is typically not that of a substorm. This confirms similar findings by Zesta et al. (2000) and Boudouridis et al. (2004).

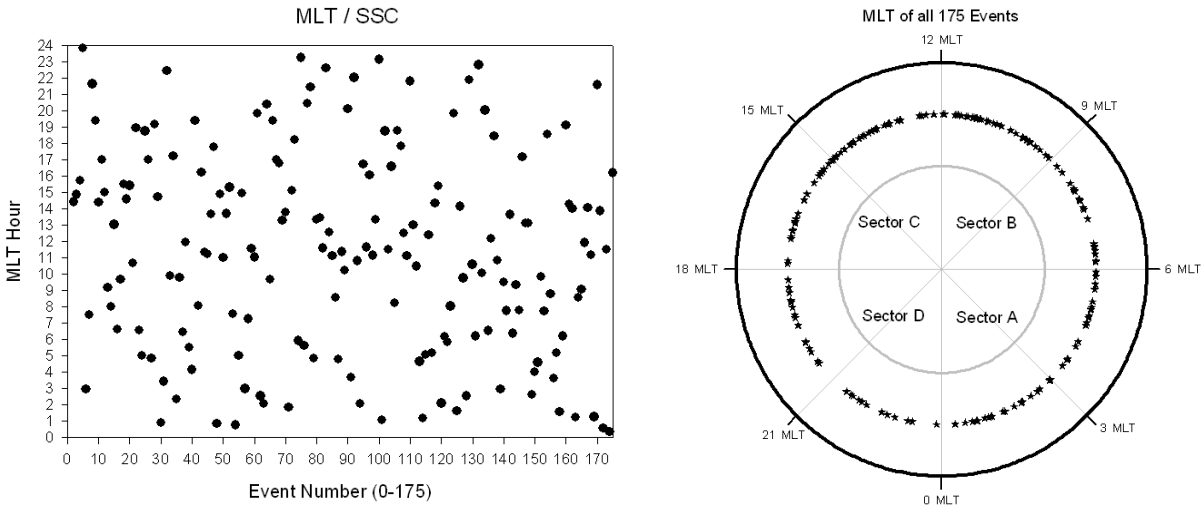

Figure 54. LHS- scatter plot of SSC event vs. MLT hour of occurrence; RHS - indication of MLT occurrence of all 175 SSC events analysed.

	No. events (% of 175 Events)	Mean SCA (dB)	Median SCA (dB)	Standard Deviation (dB)
Period				
Day (6 – 18 MLT)	104 (59%)	0.85	0.29	1.93
Night (18 – 6 MLT)	71 (41%)	0.83	0.26	1.57

Table 7. Statistics of Riometer Absorption during SSC events.

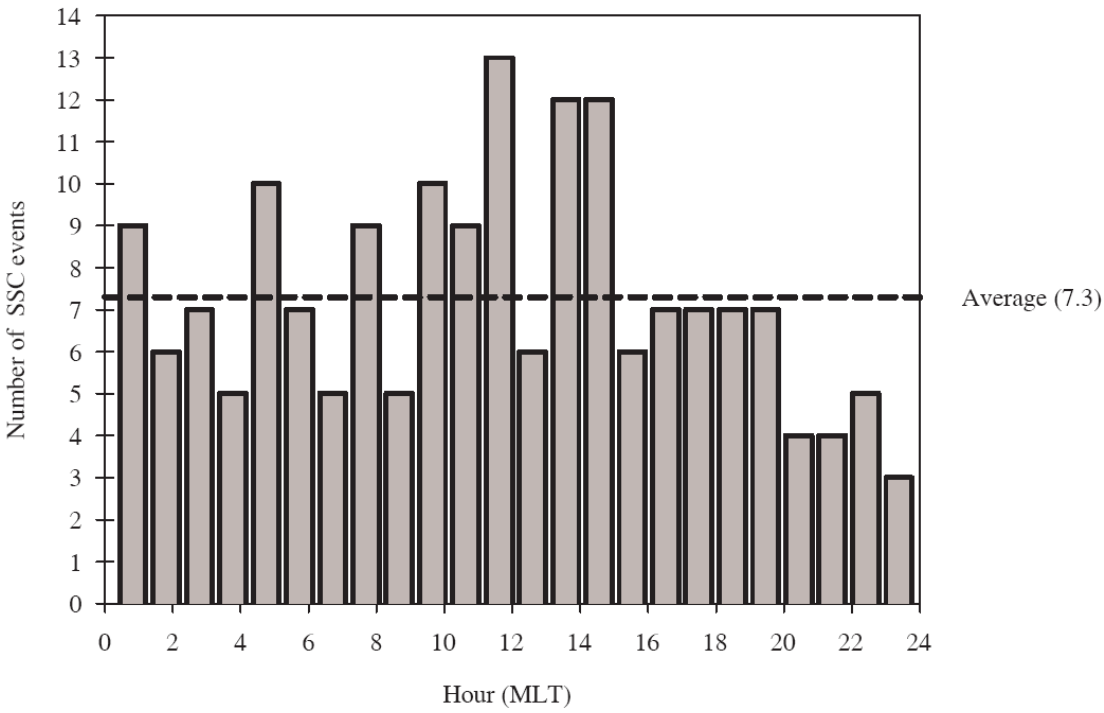

Figure 55. Histogram of the number of SSC events that occur in each MLT hour

Figure 55 presents a histogram indicating the number of SSC that occurred in each MLT hour over the six year period. The average number of SSC that occur in each hour is 7.3. Using a Chi-squared test the number of events occurring within each hour was evaluated against the expected value, assuming no change over time. The test was also repeated after grouping the data into eight three-hour periods and assuming no change in the expected value, in this case between adjacent three-hour time

periods. Both tests were not significant at the 5% level indicting a random occurrence in the number of events that occurred both within each hour and within the three-hour groupings. This is in line with findings by Lee et al. (2004) that the solar wind pulse leads to a near simultaneous enhancement of the energetic flux at all MLT sectors at the geosynchronous orbit.

3.5.6 Direction of B_z and SCA

Of the 175 SSC events selected for this study it was not possible to ascertain the direction of B_z in 23 of the events due to data unavailability. The movement of B_z during the shock was classified into four possible types as shown in table 8. The absorption statistics for each of the 4 categories of B_z direction described in table 8 follows in table 9.

	Description
Designator	
NN	B_z is positive before and after the shock, i.e. it remains northward pointing
SS	B_z is negative before and after the shock, i.e. it remains southward pointing
NS	B_z is positive before and changes to become negative after the shock
SN	B_z is negative before and changes to become positive after the shock

Table 8. Breakdown of B_z information into four categories according to direction of B_z before and after the SSC event.

The standard deviation in the North and South events is skewed significantly by the presence of very large outliers. Rather than remove the outliers which are valid measurements, it was decided to leave them in so that the standard deviation can reflect the variance expected over a solar cycle. In 75% of the events, B_z does not

change direction during the shock and there is an almost equal split between north and south maintaining B_z.

	Type of event (see table 8. for description of type designator)				
	All events (dB)	**NN (dB)**	**SS (dB)**	**NS (dB)**	**SN (dB)**
Mean	0.81	0.8	0.73	0.56	0.54
Median	0.3	0.31	0.34	0.27	0.36
Std. Deviation	1.77	1.9	1.1	0.64	0.53
% of total events	100% (152)	36%	39%	15%	10%

Table 9. Absorption Statistics for the four categories of B_z movement.

The similarity in statistics between all four types of event indicates that the direction of B_z has little impact on the typical values of SCA. This supports an assertion that SCA is not caused by particles from the solar wind gaining access to the high-latitude zone but rather from particles already captured in the magnetosphere. This confirms the same conclusion made by Paulikas and Blake (1970) in their paper examining proton flux both outside and inside the magnetosphere during the occurrence of SCC events.

Sudden Commencement Absorption is therefore not caused by southward turning B_z events as more than half of the selected SCA events occurred during northward B_z movements, which in some cases continued even more strongly northward after the SSC event. The examination of these 152 events shows that similar precipitation events occur independently of the direction of B_z immediately before or after the SSC event.

3.5.7 The Link Between the Solar Wind, IMF and SCA

Perreault and Akasofu (1978) studied how the solar wind energy is dissipated inside the magnetosphere during stormtime periods. They defined empirically an "energy coupling" function (ε) as the fraction of the solar wind Poynting flux entering the magnetosphere. While ε is proven to correlate well to stormtime periods it is compiled using hourly average values of variables and is not useful when studying short period (typically less than 15 minute) SSC events.

There are other forms of expression based on different combinations of solar wind parameters which also correlate with substorm occurrence. There are many instances of substorms when B_z is southward, when B_z turns southward, but also when the IMF turns northward having been southward for a few hours before. In particular it has been shown that geomagnetic activity is principally controlled by the solar wind velocity and the IMF field strength and direction (Burton et al., 1975; Maezawa 1979). Other parameters such as density may play some role but are generally thought to be less important. With the exception of the occurrence of shock waves, the velocity and magnetic field strength are slowly changing parameters when compared with the magnetic field direction. Thus, while the strength of the IMF (ΔB) and the solar wind velocity (V_p) may be very important parameters in controlling geomagnetic activity, it is the changes in field direction which correlate well with geomagnetic events in the magnetosphere.

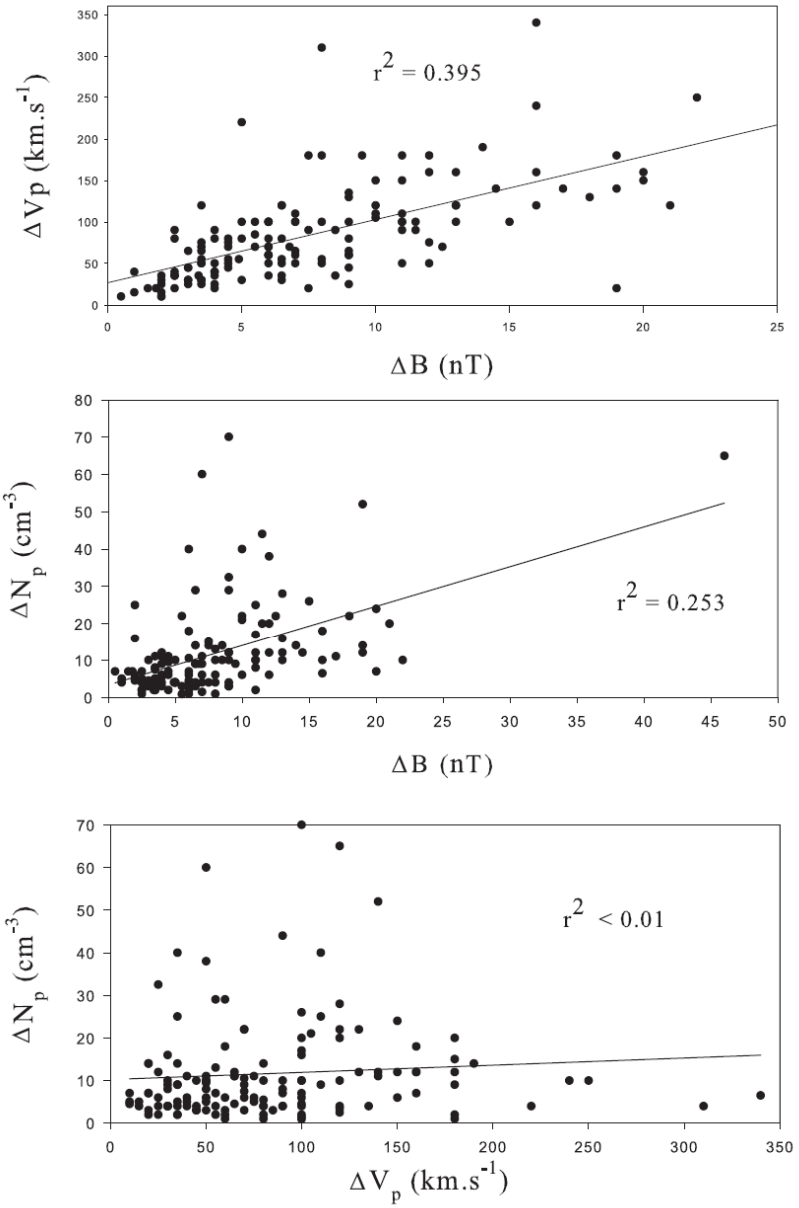

Figure 56. Scatter plot and first order regression of ΔVp vs. ΔB (top panel), ΔNp vs. ΔB (middle panel) and ΔNp vs. ΔVp (bottom panel).

Figure 56 examines the interdependency between the IMF and the solar wind. The top panel shows the correlation between the change in solar wind velocity and the IMF at the time of the shock. Although fairly weak, this is by far the best correlation

as evidenced by the very weak correlation between particle density and IMF (middle panel) as well as between particle density and velocity (bottom panel). The correlation between velocity and IMF (figure 56 top panel) could be explained by remembering that the solar wind is magnetised plasma and that the faster, travelling shock wave will overtake the slower, preceding solar wind in front of the shock. This causes the magnetic flux to be compressed at the front of the shock with some proportionality to solar wind velocity.

3.5.8 Dependency of MLT, SCA and Solar Wind Parameters

In order to check if the SCA measured in IRIS has a relationship with MLT the graph in figure 57 was prepared. The scale is limited to SCA <3 dB absorption in order to scale the graph so that it can be interpreted.

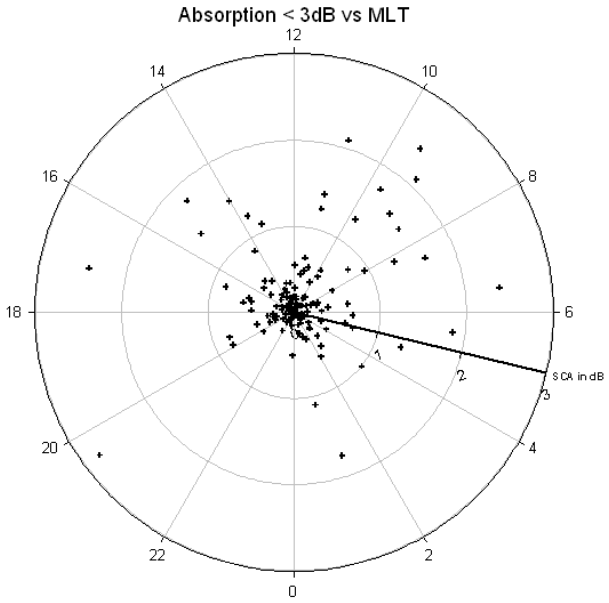

Figure 57. Polar scatter plot of absorption less than 3dB against MLT.

There appears to be SCA of similar amplitude at all MLT except perhaps between 21 MLT and midnight where there is a slight reduction in values greater than 0.5dB. In

order to zoom into the sector between 21 MLT and midnight the graph is duplicated in figure 58 using only SCA < 1.5 dB.

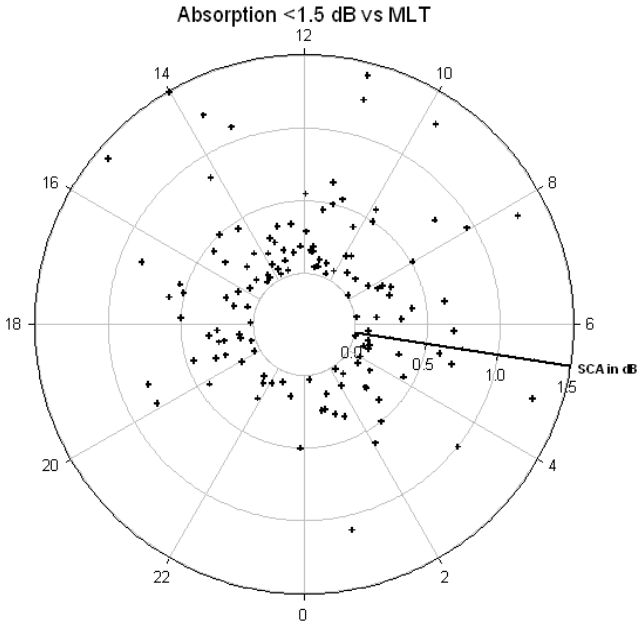

Figure 58. Polar scatter plot of absorption less than 1.5 dB against MLT.

While there are numerous SCA events that occur between 21MLT and midnight this sector has no SCA greater than 0.5 dB. This is fairly suspicious and may lead us to speculate that all else being equal, the flux of precipitating particles that occur as a direct result of the SSC is significantly reduced in the 21MLT to midnight sector, due to some local effect. However, it will be shown in the following two graphs that this is not the case. In examining figure 59 a scatter plot Δ|B| plotted against MLT, it can be seen that there is a fairly symmetrical distribution of Δ|B| values in all MLT sectors.

In examining figure 60 a scatter plot of Vp plotted against MLT it can be seen that there is a fairly symmetrical distribution of ΔVp values in most MLT sectors. There are, however, no ΔVp values above 150 km.s-1 in the 21 MLT to midnight sector.

This clearly reflects the high correlation between SCA and ΔVp that we have seen in results already presented and why no SCA value greater than 0.5 dB occurs in this sector.

There is no local effect coming into play; the lack of higher values of SCA is simply due to the lack of solar wind shocks that occurred in this sector with a ΔVp above 150 $km.s^{-1}$. It can be seen that there is a fairly symmetrical distribution of Δ|B| values in all MLT sectors.

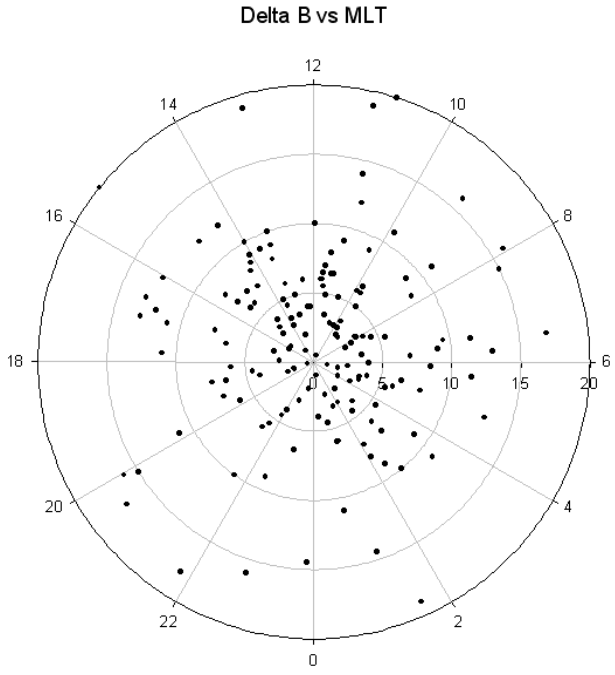

Figure 59. Polar scatter plot of Δ|B| against MLT.

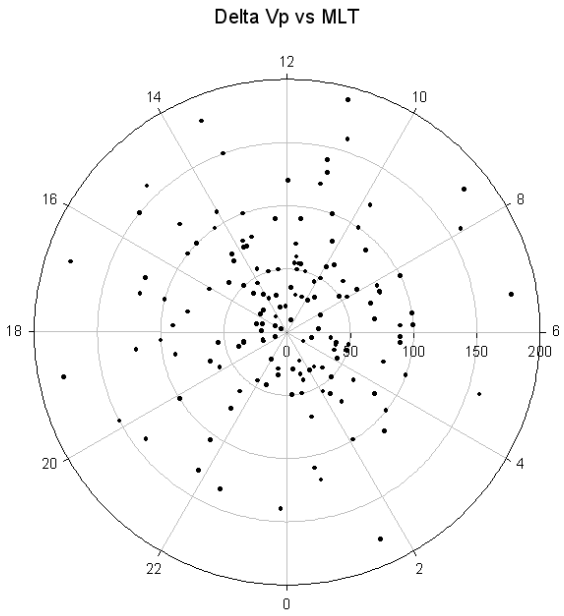

Figure 60. Polar scatter plot of ΔVp against MLT

3.5.9 Solar Wind Long Term Values: Any effect?

This data has been gathered to show that the variations in solar wind parameters pre-shock compare favourably with the long-term values of solar wind values. This serves to show that there are no unexplained variations in the pre-shock solar wind values which will need to be taken into account. Figure 61 is a histogram of the solar wind velocity derived from 18 months of measurements from the ISEE-3 satellite platform. Figure 62 is two histograms representing the solar wind velocity measured immediately before the shock occurred and the velocity immediately following the shock.

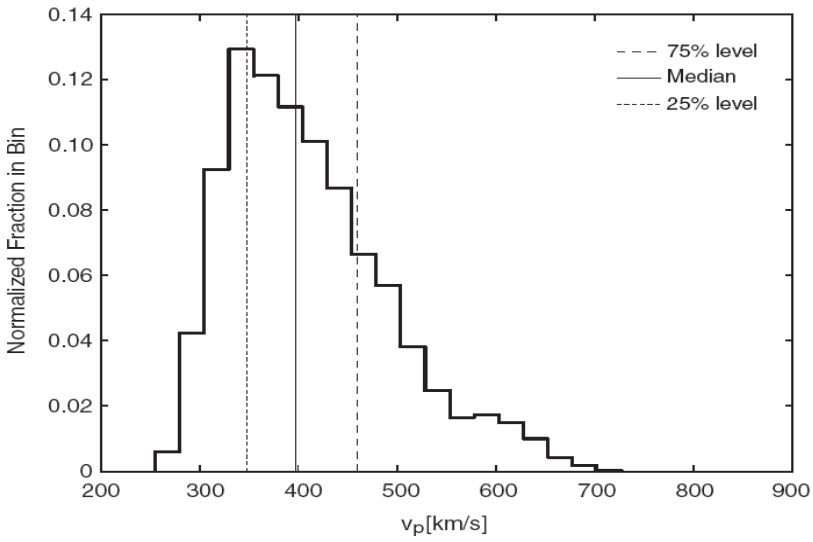

Figure 61. Histogram of the solar wind long-term velocity (From Russell et al., 2001).

Quartiles of the velocity are: 348, 397 and 459 km.s^{-1}

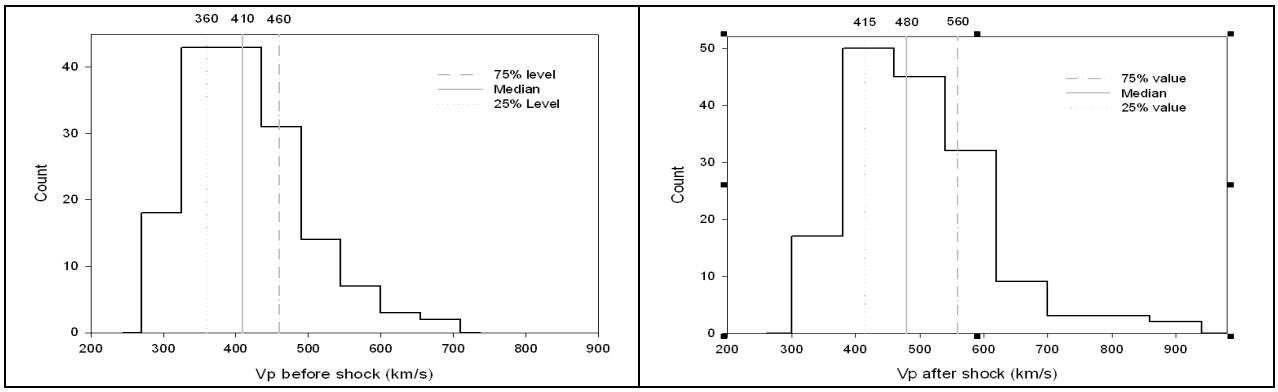

Figure 62. Vp measured pre-shock (LHS) and post-shock (RHS) (km/s)

The values of solar wind velocity are summarised in table 10.

Km/s	Long term statistic	Vp Before shock	Vp after shock
25% Level	348	360	415
Median Value	397	410	480
75% Level	459	460	560

Table 10. Comparison of the long-term value of Vp with Vp before and after each shock occurrence.

The values of Vp before the shock occurs match closely the long-term statistics presented by Russell (2001). This indicates that there are no unexplained variations in the pre-shock solar wind values of Vp which need to be taken into account.

Figure 63 is a histogram of the solar wind density derived from 18 months of measurements from the ISEE-3 satellite platform. Figure 64 is two histograms representing the solar wind density measured immediately before the shock occurred and the density measured immediately following the shock.

The values of solar wind density are summarised in table 11.

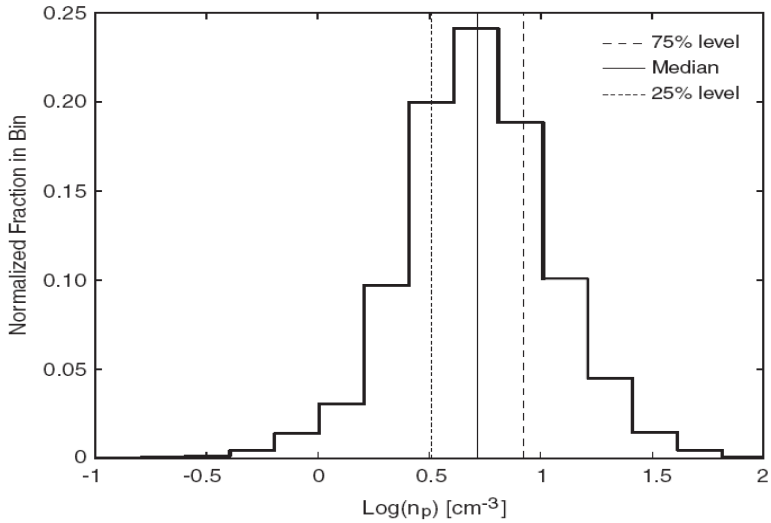

Figure 63. Histogram of the logarithm of the long-term solar wind density. Quartiles of the density are: 3.2, 5.2 and 8.4 cm^{-3}. (From Russell, 2001)

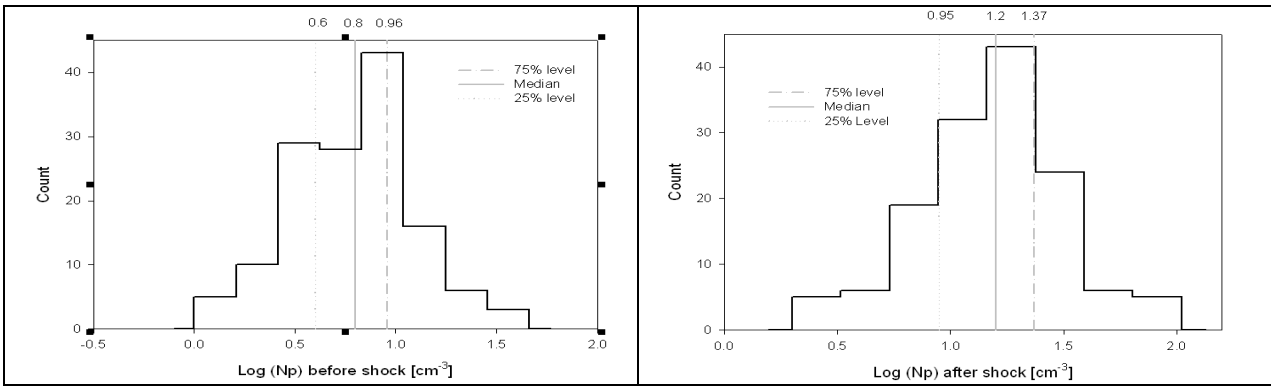

Figure 64. Np measured pre-shock (LHS) and post-shock (RHS) (cm^{-3})

***cm*$^{-3}$**	Long term statistic	Np Before shock	Np after shock
25% Level	3.2	4	9
Median Value	5.2	6.25	16
75% Level	8.4	9.1	23.3

Table 11. Comparison of the long-term value of Np with Np before and after each shock occurrence.

The values of Np before the shock occurs match closely the long term statistics presented by Russell (2001). This indicates that there are no unexplained variations in the pre-shock solar wind values of Np which need to be taken into account. The post-shock values clearly show the effect of the shock on the parameter Np.

Figure 65 is three histograms of the occurrence of IMF magnitude |B| in the IMP-8 5-minute data, separated by solar activity level. (Luhmann et al., 1993). Figure 66 contains two histograms representing |B| measured immediately before the shock occurred and |B| measured immediately following the shock. The values of |B| are summarised in the table 12.

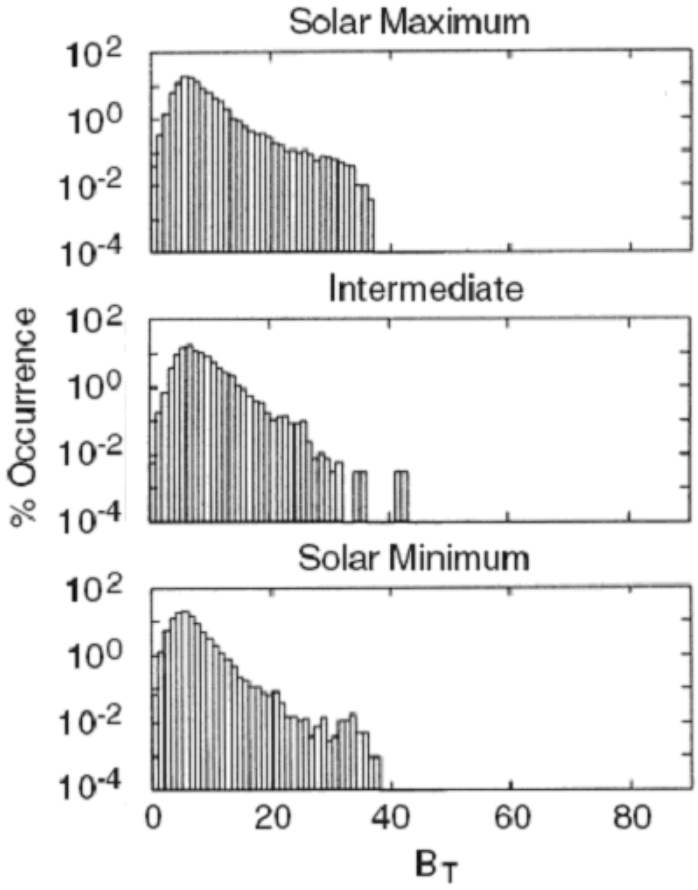

Figure 65. Histograms of the occurrence of field magnitudes in the IMP-8 5-minute data, separated by solar activity level. (Luhmann et al., 1993)

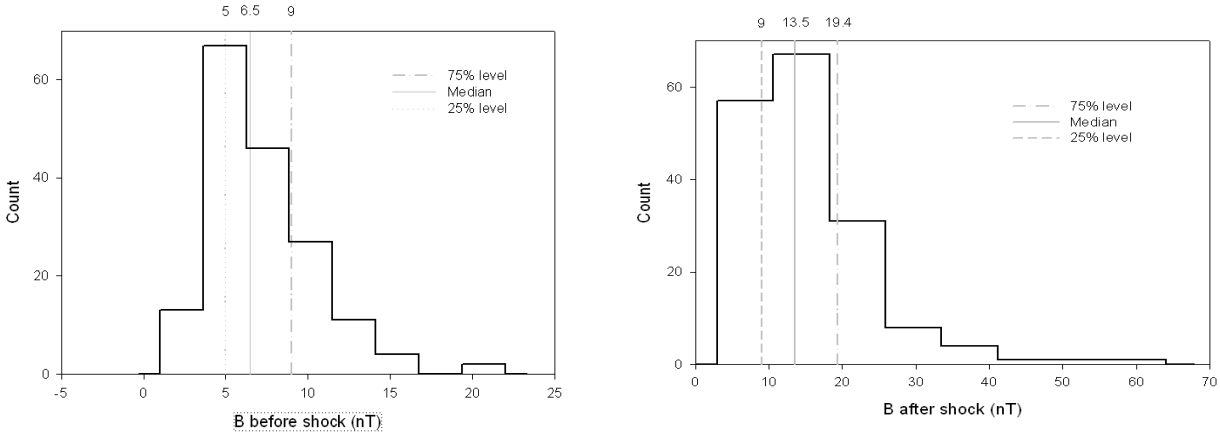

Figure 66. Histograms of |B| measured pre-shock (LHS) and B measured post-shock (RHS) (nT).

	Long term statistic	B Before shock	B after shock
	% of occurrence	***nT***	***nT***
25% Level	10 %	5	9
Median Value	10 %	6.5	13.5
75% Level	5 %	9	19.4

Table 12. Comparison of the long-term value of B with B before and after each shock occurrence.

The information gathered by Luhmann et al., (1993) is not in a format that allows direct comparisons to be made. Some inference can be made however that the long term statistics show at least a similar range of values as |B| measured before the shock. This indicates that there are no unexplained variations in the pre-shock solar wind values of |B| which need to be taken into account. The post-shock values clearly show how the parameter |B| is modified during the shock.

3.5.10 Finding the Best Predictor of SCA

As shown in figure 51, the velocity and magnetic field strength undergo rapid change (as do other parameters such as density) during the shock and we need to test if there is any direct connection between any of these quickly changing parameters and the SCA measured. One method to do this is to find the best predictor of SCA based on one or more solar wind parameters in order to clarify the effect of solar wind and IMF shocks on SCA. In order to do this a substantial body of work was undertaken to correlate each parameter shown in table 6, with the absolute, average and median values of SCA measured at the moment of SSC. This methodology results in an evidence-based assessment of what the best parameter is to use when attempting to predict the value of SCA expected following an SSC event, based only on observations of the solar wind. Table 13 is a collation of all the analysis undertaken.

Absolute value of SCA vs	Correlation Coefficient R2
Δ|B|	0.245
ΔVp	0.213
ΔNp	0.002
ΔRam Pressure	0.07
Relative change in Δ|B|	0.08
Relative change in ΔVp	0.12
Relative change in ΔNp	0.02
Relative change in ΔRam Pressure	0.06
Average value of SCA vs	**Correlation Coefficient R2**
Δ|B|	0.5
ΔVp	0.7
ΔNp	0.05
ΔRam Pressure	0.2
Relative change in Δ|B|	0.34
Relative change in ΔVp	0.23
Relative change in ΔNp	0.2
Relative change in ΔRam Pressure	0.153
Median value of SCA vs	**Correlation Coefficient R2**
Δ|B|	0.85
ΔVp	0.78
ΔNp	0.24
ΔRam Pressure	0.22
Relative change in Δ|B|	0.37
Relative change in ΔVp	0.27
Relative change in ΔNp	0.2
Relative change in ΔRam Pressure	0.16

Table 13. The correlation of absolute, average and median values of SCA and each solar wind parameter.

The strongest correlation occurred when comparing the median values of SCA to solar wind and IMF values. The median value is a measure of central tendency that provides us with a description of the entire data set and is especially useful when data sets contain a few extremely high values that can skew the distribution, as is the case

here. The median is less sensitive to extreme values than the mean and, therefore, it is a very good summary statistic to use when the data contains outliers and is an appropriate measure when dealing with the highly variable ionosphere and magnetosphere. It is for similar reasons, and also convenience, that hourly median values are the standard output from HF propagation prediction programmes and using median values of SCA allows comparisons to be made.

Figure 67 consists of four panels showing the median value of SCA compared against the step change in IMF (ΔB) (top panel), solar wind velocity (ΔV_p) (second panel), solar wind particle density (ΔN_p) (third panel) and solar wind ram velocity (ΔRam Pressure) (bottom panel). A first order regression is applied to the last two scatter plots and a second order regression is applied to the first two scatter plots. The choice of only a first order regression for the last two plots was determined by the wide spread of values in the data. Figure 67 demonstrates the strong correlation between solar wind velocity and SCA but also the even stronger correlation between the IMF and SCA.

By a wide margin, the strongest correlation was found between the median value of SCA measured and ΔB, the step change in IMF magnitude that occurred during the shock. The fitted curve in the top panel of figure 67, with a correlation coefficient (R^2) of 0.852, is a second order equation of the form:

$$A_m = 0.32 - 0.07\Delta B + 0.0077\Delta B^2$$

Where: Am = the median value of SCA expected
ΔB = the change in IMF due to the shock

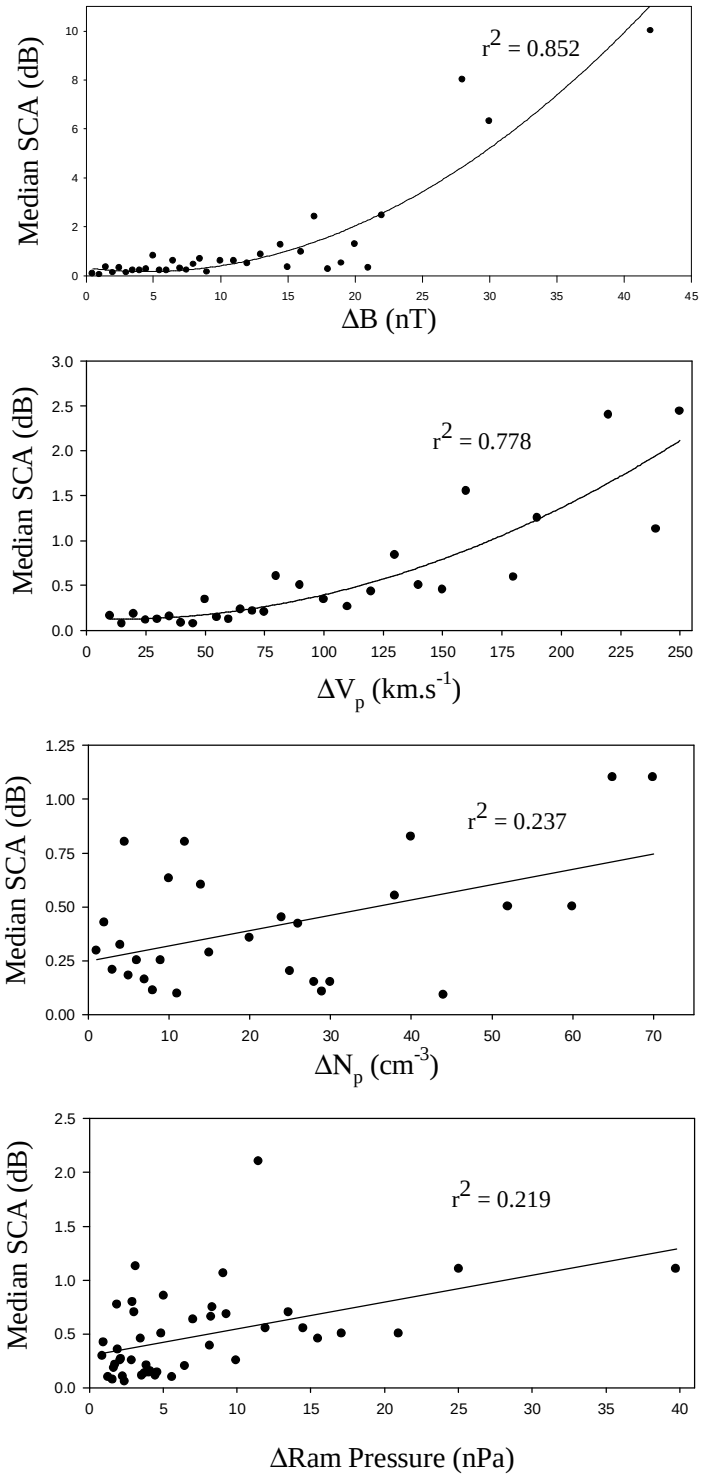

Figure 67. Scatter plot and regression of median SCA vs. (from top to bottom) ΔB, ΔV_p, ΔN_p and ΔRam Pressure.

The fit for ΔB against median SCA is very good at values of ΔB < 25 nT, reducing somewhat at values of ΔB > 25 nT. One explanation of this apparent phenomenon is that there may be some form of non-linear effect in the magnetosphere that only becomes evident as ΔB exceeds 25 nT. While this does bear further investigation, less than 3% of SSC shocks in the data set generated a Δ|B| > 25 nT, that is ~ 5 events in a six year period.

A further consideration in using ΔB as a predictor becomes evident when examining the differences in the y-axis of each panel in figure 67. When examining the solar wind velocity, particle density and ram pressure, the maximum median SCA does not exceed 2.5 dB. Compare this to the top panel where SCA values in excess of 10 dB can be predicted when the IMF is used as the predictor. The reason for this anomaly is that the ACE SWEPAM data becomes unreliable in the presence of proton contamination and solar wind parameters are not reported (see for example NOAA, 2001a). These protons are invariably present following solar energetic particle events (see for example NOAA, 2001b) which are often responsible for the disturbance in the solar wind originally initiating the SSC event.

3.5.11 Relationship of |B| with Vp and Np

The solar wind impinges upon an Earth which is "protected" by its magnetic field. The charged particles of the solar wind are deflected by this magnetic field, so that the Earth's field effectively forms a barrier. The outer limit of the Earth's field influence is known as the "magnetopause". The volume within, where the Earth's field dominates, is the "magnetosphere".

We can calculate the stand-off distance of the sun-side magnetopause by considering the balance of forces there. Note that it is generally true that the "stand-off" point which is the nearest point the solar wind and IMF get to a planet, will in general be determined by the balance of forces between the solar wind environment and the planet's environment. Thus, if the planet has no atmosphere and no magnetic field, the balance will just be that the solar wind is stopped by the planet's surface. If it has either a magnetic field or an atmosphere, however, there will be a balance where the pressures in the two environments cancel each other out.

Both solar wind and planet in general will have a particle pressure (atmospheric pressure or momentum pressure in the case of the solar wind) and a "magnetic pressure". Thus for any planet we find the balance point or stand-off point by calculating the point where the magnetic pressure and the momentum pressure from the two environments balance. If we calculate the momentum pressure and magnetic pressure in the solar wind we find that, at 1AU from the Sun, the particle pressure dominates. Thus, to find the stand-off point for the Earth we equate particle momentum "pressure" due to the solar wind, with magnetic field pressure due to the Earth. Thus we can treat this by looking at a particle "reflected" off the magnetopause as illustrated in figure 68:

The change of momentum of a single particle will be given by $2.m.v.\cos j$, and the number of reflections per unit surface ions per unit surface area of solar wind particles will be $\frac{v.N}{\sec j}$ or $v.N.\cos j$ (m is the mass of a solar wind particle and v is the velocity of the solar wind particle, N the particle density (number per cubic meter) -

and j the angle shown in figure 68). This gives an equation from which we can find the magnetic field strength at the boundary:

$$\frac{B^2}{8.p} = 2.m.v^2.N.\cos^2 j$$

j = 0 at the subsolar point, hence $B^2 = 16.p.m.v^2.N$

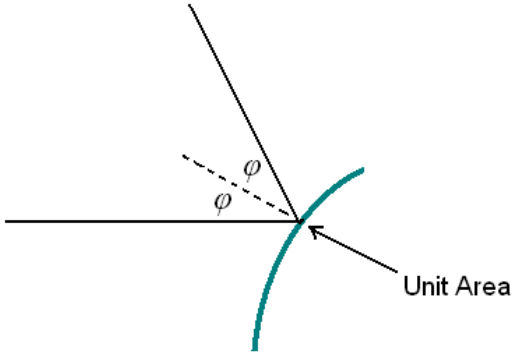

Figure 68. Reflection of a particle off the magnetopause.

For the purposes of this work, to examine the effect of the solar wind variables on SCA, we can for the purposes of examination remove all the effective constants.

$$B = v.\sqrt{N}$$

This simple equation reflects the contribution of the solar wind particle velocity and particle density to the total magnetic field strength |B|. It is now clear why |B| is such a good predictor of SCA as it reflects the relative contributions of all relevant contributory parameters in the right relative proportions. The simple equation also demonstrates why ΔVp is also a strong predictor.

3.5.12 Typical SSC Event compression

The location of the magnetopause can be determined from (Fairfield, 1971):

$$B_S = 2\left(\frac{B_e}{r^3}\right)$$

B_S = magnetic field at the magentopause subsolar point
B_e = magnetic field at the Earth's surface at the equator
r = distance in km.

For a quiet solar wind, B_s = 50 nT and $B_e = 0.32\times10^5$ nT sec j , r = 11.R_e and the literature indicates that is roughly where the magnetopause is found on a quiet day.

As $r^3 = \frac{2.B_e}{B_S}$ we can test the sensitivity of r to the parameters involved by testing

$r^6 = \left(\frac{2.B_e}{B_S}\right)^2$ where $B_S = 16.p.m.N.v^2$ producing $r^6 = \frac{{B_e}^2}{4.p.N.m.v^2}$.

To compress the boundary from $11R_e$ to $8R_e$, where it has been found, requires an increase in the solar wind energy density $\frac{N.m.v^2}{2}$ by a factor of 7. Let us examine if this is a typical compression of the magnetopause by considering the following two SSC events, selected as they both occur around noon (MLT).

The first event occurred on 8 June 2000 at 09:10 UTC and resulted in a peak SCA of 2.1dB. The solar wind velocity jumped from 520 to 760 km.s^{-1} and the density jumped from 4 to 14 particles.cm^{-3}. As a result of the shock the solar wind energy density increased by a factor of 7.5.

The second event occurred on 13 July 2000 at 09:32 UTC and resulted in a peak SCA of 0.4dB. The solar wind velocity jumped from 510 to 610 km.s^{-1} and the density

jumped from 5 to 12 particles.cm^{-3}. As a result of the shock the solar wind energy density increased by a factor of 3.4.

Clearly there are a large range of changes in solar wind energy density values that results in significant compression of the magnetopause and that a compression of the magnetopause boundary from $11R_e$ to $8R_e$ is well within the scope of typical SSC events.

3.6 Chapter Summary

1st Objective

A geomagnetic SSC is caused by a solar wind shock or impulse. The shock or impulse excites an MHD disturbance in the magnetosphere. This disturbance propagates toward the Earth to be detected as an SSC signature on the ground.

Energetic electrons associated with SSC originate in the trapped radiation belt within the plasmasphere where the closed field lines are limited in latitude. This was conclusively demonstrated by Kikuchi and Yamagishi (1989).

During the impact of a pressure pulse on the magnetosphere, the outer magnetosphere is compressed. The breaking of the first adiabatic invariant by the compression increases the perpendicular-to-parallel ratio of particle energy and promotes the growth of loss-cone instability. This in turn increases the amount of particles that are scattered into the loss cone by wave-particle interactions (Zhou and Tsurutani, 1999). Any violation of the first two invariants causes changes of the pitch angle (pitch angle scattering). This can lead to losses of particles when the pitch angle becomes so

small, that the corresponding mirror points move down into the atmosphere where the particles can be scattered and absorbed. As the periods of the first two invariants are short their violation is mainly caused by particle and particle-wave interactions.

Violation of the adiabatic invariants appear to be responsible for some of the precipitation but since the adiabatic changes in particle trajectories can only increase the pitch angle, adiabatic effects alone cannot increase the particle flux within the loss cone and thus cannot account for all the absorption seen. With the assumed absence of other scattering mechanisms during the initial perturbation, the increase absorption seen must result from wave-induced precipitation (Gail et al., 1990a).

2nd Objective

SCA is caused by the precipitation of high energy electrons and protons into the atmosphere where they generate excess ionization at low altitudes. Typically the processes causing ionospheric absorption of radio waves take place at altitudes in the range of 60 to 100 km (Stauning 1996). The precipitation of energetic particles, and thus the associated radio wave absorption processes, is most intense in the auroral and polar regions.

3rd Objective

A detailed examination of sudden commencement absorption, the absorption that occurs simultaneously with storm sudden commencements, has been undertaken in this chapter. To the author's knowledge this is the first time that a statistical analysis of the characteristics of sudden commencement absorption has been published. The results in this chapter have a direct application to real-time and near-time ionospheric

propagation prediction in respect of the prediction of the occurrence and expected amplitude of sudden commencement absorption.

By design the dataset used spans more than half a solar cycle and this was used to determine if solar activity, using the relevant sunspot count as a proxy, influences the value of SCA. By evaluating the link between SCA and solar activity, and the link between the change in IMF magnitude and solar activity, it is concluded that in both cases there is no causal link, other than in the number of SSC events that occur. This last point is not unexpected as higher sunspot levels reflect the increase in the number of active regions on the Sun that are the source of shocks leading to SSC events.

Following the presentation of the basic database statistic, the influence of local time on SCA amplitude was investigated by dividing the dataset into day events (6 – 18 MLT) and night events (18 – 6 MLT). While the number of SSC events is slightly greater during the day, there is no significant difference in the mean or median SCA values between the two sectors. This confirms that the immediate response of the magnetosphere to the shock is a global disturbance directly driven by the solar wind.

In considering all the possible combinations of how the direction of B_z might change during the shock, the similarity between the statistics calculated for each of the four possible combinations leads to the conclusion that the change in the direction of B_z in whatever combination has very little impact on the value of SCA. This supports an assertion that SCA is caused by particles already captured in the magnetosphere. If it was the alternative option that solar wind carried particles were gaining direct access

to high latitude zones then the change in solar wind – magnetosphere coupling, caused by changes in B_z direction, would be clearly evident, which is not the case.

4th Objective

In an attempt to model the expected SCA values after a shock has occurred, solar wind and IMF parameters were correlated in turn against the absolute, mean and median values of SCA. A strong correlation (R^2=0.852) was found between the median value of SCA measured and the step change in IMF magnitude that occurred during the shock. In some ways this is not surprising as ΔB is fundamentally an indirect measure of the changes in solar wind proton velocity (V_p). The fit is particularly good at ΔB values less than 25 nT which accounts for 97% of the SSC events in the database. In addition, due to proton contamination of the ACE SWEPAM instrument during large events, solar wind data is not reported, leaving the use of ΔB as the only reliable predictor of SCA during these times.

In summary the key findings of this chapter are as follows:

i. There is no causal link between the amplitude of SCA and solar activity;
ii. There is no causal link between the change of IMF magnitude, caused by the passage of the shock wave past the ACE satellite, and solar activity.

These first two points are very relevant to radio engineers in that most propagation prediction programs only use a solar activity index to predict performance: the implication is that some other method is required, which this thesis presents, namely an empirical relationship based on the change in IMF.

iii. SCA occurs with similar statistical characteristics during both the day and night.

iv. The direction of B_z before and after the shock has little impact on the expected value of SCA.

The implication of these two points is that both of these variables can be ignored when predicting SCA.

v. The change in the strength of the IMF is the best predictor for small to medium shocks and the only predictor that can be used during large shocks.

CHAPTER 4

The Variability and Screening Effects of the Sporadic-E Layer

4.0 Objectives of this Chapter

The typical features of HF radio communications following an SSC event are:

- A large absorption spike;
- The range of operational frequencies is significantly reduced as electron density in the various reflective layers changes;
- A change in the propagation mechanism;
- A growth in auroral absorption due to precipitation as storms and substorms start within the hour following an SSC.

At high latitudes most of the time the ionisation is dominated by energetic charged particles (electrons or protons) and only rarely is the ionosphere "quiet", i.e. it varies with solar zenith angle and solar activity (Friedrich, 2002). At high latitudes, as elsewhere, the Sun is able to produce an E-layer when is it above the horizon, but ionisation can also be produced in the same altitude range by the precipitation of energetic particles, principally electrons, which then dominates and controls the characteristics of the E-layer. For example, in the course of a substorm, the precipitation of the charged particles from the magnetosphere into the ionosphere

takes place, the electrojet is increased, the substorm current wedge system is formed and the electron density and composition of the ionosphere is changed (Buonsanto, 1999). It is known that during the substorm growth phase, accelerated particles from the solar wind can penetrate through the entry layer of the magnetosphere into the auroral ionosphere (Blagoveshchensky and Borisova, 2000), causing sporadic-E layers.

Taking the above into account the five objectives of this chapter are to:

1. Review current knowledge on Sporadic-E layers at high latitudes;
2. Introduce the ionosonde as a measurement tool of Sporadic-E characteristics and the f-plot as a presentation tool of ionosonde results;
3. Characterise the change in the E-layer critical frequency that occurs in the six hours following an SSC event and to check for any diurnal, seasonal or solar activity dependency in the data;
4. Determine the occurrence of full blanketing E-layer formation at high latitudes as seen on vertical ionosondes in Northern Finland (67^0 Latitude);
5. Determine the appropriate value of f_oE that should be used as a threshold of blanketing, which defines a good probability of blanketing occurring following the commencement of ionospheric storms.

4.1 Introduction to Sporadic-E

The term Sporadic-E or E_s is used to refer to certain abnormal phenomena in the E-region of the ionosphere. Sporadic-E is the name given to all the ionogram traces that are clearly not due to the regular E-layer. As researchers began to study ionogram

traces in different parts of the world it became clear that there are at least three distinct phenomena (Smith, 1967).

1. A type of sporadic-E peculiar to the magnetic equator (Matsushita, 1953) which is largely limited to a belt centred on the equator and approximately 700 km in width (Knecht and McDuffie, 1962). This type of sporadic-E appears to have its source in the equatorial electrojet current and has been explained in terms of a two-stream plasma instability mechanism (Bowles et al., 1960). It is also known as low-latitude sporadic-E.
2. In the auroral zone and polar cap, on the other hand, a second type of sporadic E occurs which appears to be due to the precipitation of charged particles. It is the prediction and characterisation of blanketing sporadic E in this zone that is the focus of this chapter. This form of sporadic-E is also known as high-latitude sporadic-E and in some literature as Auroral Sporadic-E.
3. The type of sporadic E which occurs over the largest portion of the Earth's surface is called the temperate-latitude sporadic-E. This area has been the focus of much of the research work reported to date in the literature. This type of sporadic-E is also known as mid-latitude sporadic-E.

The different zones, using the ITU standard definitions, (ITU 1970) are:

- Temperate zone Sporadic E;
- Equatorial Sporadic E; and
- Auroral Sporadic E (the focus of the work here).

High latitude Sporadic-E ionisation is situated in the height range 100 – 150 km, and is also referred to in the literature as the Sporadic E-layer, the E_s layer and even the night E-layer.

It is understood that energetic particles play a vital role in the production of Es and that at high latitudes the precipitation of energetic charged particles into the upper atmosphere is a regular occurrence. The precipitating particles, primarily kilovolt electrons, produce most of their ionisation in the E-region (Rees, 1963; Walker, 1972). The maximum density in the disturbed dark ionosphere near 65^0 latitude usually occurs in the auroral E-layer, a thick layer (relative to HF radio wave lengths) with typical densities of 2 to $5 \times 10^{11} e.m^{-3}$ extending for several degrees of latitude i.e. a dense, thick and widespread in latitude reflecting layer. The density of the auroral E-layer is primarily a function of the rate at which energy is deposited in the E-region by the auroral precipitation, and it is has been shown that this is a highly variable phenomenon.

High-latitude E_s can have a much higher critical frequency than the regular E-layer. Sometimes the ionogram indicates that the E_s is thick and opaque with a well-defined maximum, at other times the layer may be thin, patchy and partly transparent, so that higher layers are observed through the E_s. At night the auroral precipitation ionises the E-regions, producing the thick auroral E layer – even on magnetically quiet days.

E_s has different characteristics in different latitudinal zones and there may be several mechanisms governing the behaviour of these layers. Sporadic-E as studied in this report is caused by the enhanced precipitation of particles. These sporadic layers have

been shown to have a “first-order effect” on HF circuits at high latitudes (e.g. Hunsucker and Bates, 1969; Davé 1990), by dramatically extending the E-layer maximum usable frequency (MUF) and/or “shielding” the ray paths from the F-layers.

Sporadic-E layers are important to consider as they are almost always present at high latitudes, and frequently the sporadic E ionisation is strong enough to totally reflect radio waves in the 3 - 10 MHz range at vertical incidence. Thus the mode of propagation for a short range HF link will be a one or two hop sporadic-E path. The mode of propagation during quiet ionospheric conditions for short ranges is often dominantly determined by one-hop sporadic-E Layer reflections and one-hop reflections from the ordinary E and F1 layers (Ostergaard, 1988). For the longer distances, four paths, i.e. low and high ray E and low and high ray F1 paths are possible.

The starting point for this study is the SSC index and the choice of this reference is not random. An SSC is an increase in the low-latitude ground-based magnetic intensity which typically lasts for tens of minutes and then is followed by a magnetic storm or by an increase in geomagnetic activity lasting at least one hour. A link to SSC has been noted by Collis and Haggstrom (1991) who observed a rapid depletion of F-region electron density by the EISCAT ISR, following a geomagnetic SSC. They observed, following the SSC, a more than halving of electron density compared as well as an abrupt enhancement of E-region electron density within one hour of the SSC occurring. Building on this observation is the focus of this chapter. Using the SSC as the starting point is convenient as the SSC marks the beginning of a storm period i.e. a period of ionospheric disturbances and corresponding variability in

ionospheric communications. In using the official list of SSC events, the link to magnetospheric changes and modifications to the ionosphere is unequivocal and internationally recognised. This is done in preference, for example, to the use of the Kp value which, as a three hourly index, does not provide the resolution required for this investigation.

In the seminal paper by Hartz and Brice (1967) on the general pattern of auroral particle precipitation, reference is made to the occurrence of intense sporadic-E echoes. As a reference point in their paper, intense sporadic-E is taken to mean an echo that extends beyond 7 MHz on the ionograms. It will be shown in this chapter that the choice of 7 MHz is inappropriate as full blanketing of the F-layers occurs frequently when ionograms echoes are substantially less than 7 MHz.

4.1.1 Production and Recombination[10] Rates in the E-region

In the E layer the chemical reactions are fast compared to the F region as there is a far high density of major species (e.g. O_2, N_2, O, A_r, H_e, H, O_3) than in higher altitudes. For example, the number density of oxygen (O) at 400 km altitude is in the order of $10^{11}m^{-3}$ while at 120 km the number density of oxygen (O) is 10^{19} m^{-3}. Almost all the ions are molecular in the E-region and hence the rate of recombination of electrons equals the rate of combination of the molecular ions (i.e. $a.N_e^2$, where a is the mean dissociative recombination coefficient for the molecular ions (Davies, 1990).

The rate of increase of electron density N_e is given by the simplified continuity equation:

[10] Recombination is the term applied to the formation of neutral particles when ions and electrons reform.

$$\frac{dN_e}{dt} = q - a.N_e^2$$

Where q is the rate of production of ions pairs.

Measured and calculated recombination coefficients derived at 100 – 120 km, given in the literature are summarised in table 14.

Recombination Coefficient (cm3. sec-1)	Measurement Method	Reference
10^{-8}	Ionospheric Sluggishness	Appleton (1953)
10^{-8}	Solar Eclipse Observations	Ratcliffe (1956)
2×10^{-6}	Auroral Luminosity	Gustavson (1964)
2×10^{-6}	Auroral Brightness	Omholt (1971)
3 to 5×10^{-7}	Auroral Brightness	Knecht (1956)
4 to 7×10^{-7}	Rocket	Ulwick (1967)
1×10^{-7}	Auroral intensity / Rocket	Jespersen et al. (1969)
2×10^{-7}	Auroral intensity / Rocket	Bryant et al. (1970)
3 to 6×10^{-7}	Rocket	Baker (1968)
2.5 to 5×10^{-7}	ISR	Baron (1974)
0.85 to 7.4×10^{-7}	Lab measurements	Banks and Kockarts (1973)
1.47 to 1.75×10^{-7}	ISR	Brekke, 1975

Table 14. Summary of measured and calculated recombination coefficients as given in the literature.

Brekke (1975) calculated that the ion production rate associated with SSC to be at least 4.5×10^4 el cm^{-3} sec^{-1} at 110 km. This corresponded to an enhancement above the background ionisation by more than a factor of 10. Brekke demonstrated that at the time of an SSC an additional ion production mechanism is turned on and off as rapidly as possible in the ionosphere.

Using the Chatanika radar Brekke (1975) captured a set of electron density profiles during the period of an SSC. As shown in figure 69, the period of E-layer ionisation

at the moment of an SSC to a return to normal (full recombination of ions) can be as quick as 3 minutes.

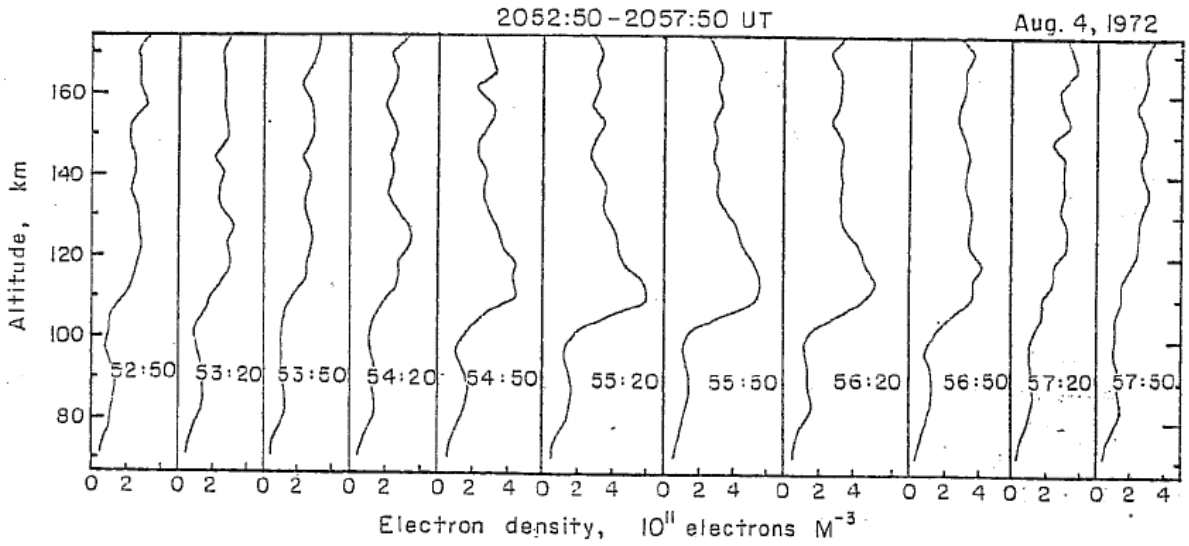

Figure 69. Electron density profiles observed every 30 seconds, by the Chatinika radar in the period of a SSC that occurred at 20:54UT on 4 August 1977 (Brekke, 1975)

Thus during intense E-layer ionisation there must be a continuous influx of high energy particles to initially form and then sustain the E-layer. If the inflow of particles was not continuous during the periods of Sporadic E, then due to the high recombination rate, the E-layer ionisation disperses very quickly.

Sporadic-E at night presents special problems. Without an ionisation source, compressed ionisation composed of NO^+ or O_2^+ ions and electrons recombines within a few hundred seconds or less (Whitehead, 1970). The ionisation produced by dumping has been the subject of several investigations. Sugiura et al. (1952) showed that 100 keV protons produce a layer ~ 15 km thick at 130 km and 1 MeV protons a

layer ~ 1 km thick at 95 km. To give the observed ionisation, the flux has to be ~ 10^{+7} to 10^{+8} protons cm^{-2} sec^{-1}, the density being 10^{-2} to 1 proton cm^{-3}. Eather (1967) considered secondary ionisation by H_α and H_β to be unimportant compared to direct ionisation by protons.

Rees (1964) and Maeda (1965) pointed out that the thickness of layers produced by electrons is at least 5 km and that a layer an altitude of 100 km, if formed by electrons 2 – 10 keV and has a minimum thickness of 20 – 30 km. Kamiyama (1967) found that a flux of $2\pi \times 107$ cm-2 sec^{-1} of 10 keV electrons gave a maximum rate of ionisation of 1.7×10^3 cm^{-3} sec^{-1} at 116 km, whereas the same flux of 100 keV electrons gave a maximum of 2.3×10^4 cm^{-3} sec^{-1} at 88 km. By comparison the rate of ionisation in the E-region by the Sun's radiation is ~ 3×10^3 cm^{-3} sec^{-1} at 116 km.

4.1.2 Sporadic-E: A Definition

Sporadic-E is defined as an altitude-thin E-region layer at an unpredictable altitude and/or an unexpected intensity (Mathews, 1998). Historically the term "Sporadic-E" derives from ionosonde observations and from the beginning has been used to describe a variety of E-region level echoes from a variety of HF sounding instruments. The term "sporadic" continues to pose semantic difficulties in that the different classifications of E_s display various levels of periodicity and thus predictability. The most common current definition of E_s is simply that of an altitude thin ionisation layer lying anywhere in the E-region.

In discussing Sporadic-E we must be very careful in the terminology used. In the literature the phrase "Sporadic-E" is applied to different types of layers that form around the 100 km altitude mark. For example, the evening E_s and midnight E_s are not

the intense, often blanketing E-layers dealt with in this report. Both of these types of E_s are thin layers and understood to be caused by vertical wind shears and ionospheric electric fields (Wan et al., 1999).

"Abnormal E" and "Nocturnal E" are perhaps the earliest chronological use of a term to describe what we know today as Sporadic-E (Ratcliffe and White, 1933; Appleton and Naismith, 1933). The term "sporadic E" is first found in Kirby and Judson (1935). Each of the terms was originally an abbreviation, e.g. "abnormal E-region ionisation", "sporadic E-region ionisation", etc. The original objections to the use of the term Sporadic E were two-fold. First it is unclear from the term whether this sporadicity is temporal or geographic. Second, if it is the temporal variation which is considered "sporadic" how can one logically then include the phenomenon observed on the magnetic equator in which a daytime transparent E-layer reflection exists which is highly regular in its time variation but is clearly not the normal E layer?

However, a survey done in the late 1950's (Smith, 1957) revealed that in literature up to that time the use of the term Sporadic E and E_s were employed extensively and were synonymous with each other. Since then the use of both of these terms has remained consistent in the literature. In keeping with this convention, for the purposes of this report, both terms are used interchangeably, having adopted the following definition:

> Sporadic E propagation – a comparatively strong and protracted transmission (several minutes to several hours) returned from the E-region of the ionosphere by some mechanism other than the normal reflection process from the regular E layer.

The word "protracted" is used to remove the effect of meteoric bursts. The word "returned" is used to include any active scattering mechanism and it implies that the return is from overhead in the vertical-incidence path and on the great circle path for oblique-incidence transmission. The following standard conventions and acronyms are used in this chapter.

- The E-region is used to define a height interval of 90 to 140 km.
- f_oE_s – The highest frequency at which ordinary wave echoes are observed from the approximate height of the E layer.
- f_bE_s – The frequency at which the E_s is first penetrated as indicated by the return of an echo from a higher layer.

4.1.3 Cause of Sporadic-E

A reflecting stratum could be produced in any of the following three ways (Layzer, 1962):

i. By greatly enhanced ionisation in a narrow region;
ii. By a near-discontinuity in the electron-density profile e.g. a ledge or a step;
iii. By turbulence, especially in a region where the electron-density gradient is large.

The first mechanism requires that the electron density in the reflecting stratum be considerably higher than the region immediately below it. Several possible causes of enhanced ionisation have been suggested – solar particles, cosmic rays, meteors and thunderstorms. That some of these play a role in the production of reflecting strata seems to be well established. In the auroral zone, auroral activity and the incidence of

E_s show a strong positive correlation. A marked rise in the incidence of sporadic-E has been found to accompany some meteor showers.

Sporadic-E arises when clouds of intense ionization form occasionally in the E-region ionosphere in low- and mid-latitudes. The most common theoretical explanation of the formation of Sporadic-E layers is the wind shear theory (e.g. Whitehead, 1961; Mathews, 1998) According to this theory, ions are accumulated into thin, patchy sheets by the action of high altitude winds in the E-region ionosphere. Wind shear occurs at the boundary between two wind currents of different speed, direction, or both. For example, two high speed winds blowing approximately in opposite directions in the E-region ionosphere create a wind shear which makes it possible to redistribute and compress ionized particles into a thin layer.

It has also been suggested that the electric field alone can produce sporadic-E layers (Nygréen et al., 1984). This theory demands an electric field pointing in a proper direction. Convincing evidence for the electric field theory has been presented by Parkinson et al. (1998) who presented the number of observed sporadic-E layers versus electric field direction at Antarctica; he confirmed that this theory is particularly effective at high latitudes where strong electric fields are encountered. This theory leads to compressive vertical plasma flow if the ionosphere electric field points in some direction between west and north in the northern hemisphere and between west and south in the southern hemisphere.

Damtie et al. (2002) found evidence in their short study of both the presence of vertical shears in the meridional E-region neutral wind and the right conditions for the

electric field theory. Using data from the SuperDARN radars they detected that the plasma flow direction in the area of observation between west and north. The conclusion was that both processes may be active simultaneously and their relative importance remains unknown.

King (1962) inclines to the view that the ionisation moves down from the F region, though as the ionisation has to be replaced at least every few hundred seconds (with the lowest recombination coefficient acceptable) the whole of the F region ionisation would be depleted in a few hours.

Whitehead (1970) suggested a three stage phenomenon. First of all, we have ionisation by incoming particles. The dumping mechanism may itself be associated with magnetic activity. Sufficient ionisation may be produced to give a plasma frequency approaching 2 MHz in a thick layer (night E). A second mechanism forms this ionisation into irregularities with a plasma frequency approaching 10 MHz (to account for the F_oE_s observed on ionograms), and possibly the same mechanism or a third one causes the smaller irregularities for the VHF reflections.

Ring currents during magnetic storms move the auroral region (at the pole ward boundary of the trapping region) toward the equator. All field lines from the auroral zone touch the outer boundary of the magnetosphere (thus allowing particle injection). Piddington (1967) showed the energisation of particles to 1 keV by the destruction of magnetic energy along the neutral sheet in the centre of the magnetospheric tail. As the field lines contract toward the Earth, the particles gain further energy, those with

small pitch angles (moving nearly parallel to the magnetic field) being dumped and the others becoming trapped and forming the outer Van Allen zone and ring currents.

The influence of geomagnetic disturbances on sporadic-E layers in general has been investigated by a number of researchers (Whitehead, 1970; Majeed, 1982; Baggaley, 1984; Whitehead, 1989), where they revealed positive and negative correlation of E_s with the geomagnetic activity and the absence of correlation. They also reported on the dependence of the E_s layer response to the geomagnetic disturbances on latitude, season, time of the day and the type of E_s layer. Thus the question of the influence of geomagnetic disturbances on the E_s layer has not yet been solved completely (Maksyutin et al., 2000). Indeed, Whitehead (1989) concluded that the nature of geomagnetic activity influence on the E_s layer is insignificant.

Maksyutin et al. (2001) performed an analysis of dependence of E_s layer response to geomagnetic disturbances on the level of solar activity and showed that during the years with a low level of solar activity, the E_s layer response to the geomagnetic disturbances was more pronounced than during the years with a high level of solar activity.

In a study conducted by Wratt (1976) it was concluded that precipitation of electrons with energy above 150 keV into the mesosphere (70 – 80 km) following the storm–time filling of the slot region between the two electron zones in the radiation belts is at times an important daytime ionisation source in the lower D-Region at middle latitudes. Electrons with energies less than 100 keV are also precipitating out of the slot region to sustain the long duration E_s layer that we see on ionograms.

The high latitude E_s layers are generally considered to be due to particle precipitation (Buchau et al., 1972; Whitehead, 1970; Whalen et al., 1971; Wagner et al., 1973). Naridner at al. (1980) found that electron precipitation usually is the major cause for the formation of the high-latitude sporadic E layer and that the modified wind shear mechanism, which takes into account the effect of electric fields, is important under low electron precipitation conditions only.

It is widely held that sporadic-E ionisation at high latitudes is created as a direct consequence of some storm-associated phenomenon, be it the precipitation of energetic charged particles (as it is most commonly assumed) or a local discharge mechanism (Odishaw, 1964).

4.1.4 Forms of Sporadic-E

There are eleven categories into which E_s traces are classified – fortunately the number seen at any one station can be far smaller. For comprehensive details, including examples of each type see Piggott and Rawer (1972) and Piggott (1975) - a summary of types is presented in table 15. The three highlighted types are commonly seen at high latitude stations and form the majority of data collected in this thesis.

No.	E_s Type	Summary of E_s type
1	**F**	A clean E_s trace which shows no appreciable increase of height with frequency. Observed at night-time only.
2	**L**	A flat E_s trace below the normal E or particle E minimum virtual height.
3	**C**	An E_s trace showing a relatively symmetrical cusp at or below the critical frequency of the normal E or particle E layer.
4	**H**	An E_s trace showing a discontinuity in height with the normal E or particle E layer trace at or above the critical frequency. The cusp is not symmetrical.

No.	E_s Type	Summary of E_s type
5	**Q**	An E_s trace which is diffuse and non-blanketing over a wide frequency range.
6	**R**	An E_s trace showing an increase in virtual height at the high frequency end but which becomes partially transparent below f_oE_s. Bailey (1968) has shown that electron precipitation, characterised by exponential energy spectra with e-folding energies between 3 and 15 keV, results in type–r E_{sa}.
7	**K**	Denotes the presence of a particle E layer, similar in appearance to normal E, which obscures higher layers up to its critical frequency.
8	**A**	Denotes all types of very spread E_s traces. The typical pattern shows a well-defined flat or gradually rising lower edge with stratified or diffuse traces present above it.
9	**S**	A diffuse E_s trace whose virtual height rises steadily with frequency.
10	**D**	A weak diffuse trace at or below 95 km associated with high absorption and consequently high fmin. The d-type E_{sa} in the 80 to 90 km height region is thought to be caused by similar electron density spectra with e-folding energies as high as 60 keV (Bailey, 1968).
11	**N**	An E_s trace which does not fall into any of the standard categories above.

Table 15. Classification of Sporadic-E

4.1.5 World Wide Distribution of E_s

A comprehensive study of the worldwide occurrence of Sporadic E was carried out by Smith (1957) on the basis of occurrence of f_oE_s (the critical frequency of the E layer) above 5 MHz. That study addressed equatorial mid-latitude and auroral sporadic-E but was unable to assess the situation in the polar cap because of the absence of suitable positioned instrumentation. The seasonal and diurnal variations in percentage occurrence of f_oE_s > 5MHz in the auroral zone is shown in figure 70.

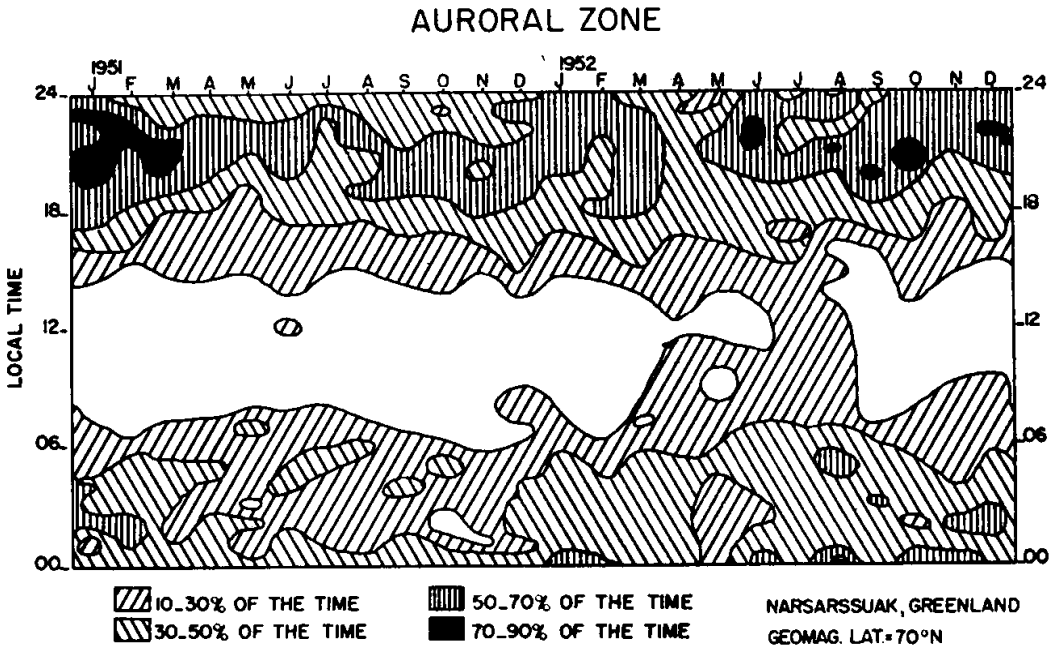

Figure 70. Seasonal and diurnal variation in percentage occurrence of $f_oE_s > 5$ MHz in the auroral zone (From Smith, 1957)

However, figure 70 was developed from three years of observations at Narsarssuak and there are normally close to only thirty observations (one for each day) for any given hour and month in a years worth of data. If a particular hour and month on the time map above has an incidence of 10%, this means that there only 10 observations of sporadic-E for that hour recorded over the three year period. This indicates the granularity in the interpretation of the data used. This is not intended as a criticism of the enormous task under taken by Smith but rather a comment on the limited use of Smith's results in attempting to interpret the data gathered for this thesis.

In the auroral region the situation is more complicated and on vertical ionosondes a number of different layer types are seen at heights around 100 km. These are reviewed by Bates and Hunsucker (1974) and the scaling of such ionogram traces is

dealt with by Piggott and Rawer (1972). According to Smith (1957), auroral sporadic-E with f_oE_s above 5 MHz is observed mainly at night.

The occurrence of sporadic-E, i.e., its variation over the Earth with time of day, season and sunspot cycle, has been studied extensively, notably by Smith (1957, 1962), Leighton et al. (1962). From Smith (1957) it becomes meaningful to talk about temperate, auroral and equatorial zones, on the understanding that the boundaries between the zones are not clearly definable and change with time. For example, Sodanklya is strongly influenced by temperate zone effects. The probability of $f_oE_s \geq$ 3 MHz behaved as at a temperate zone station, whereas the probability of $f_oE_s \geq 5$ MHz behaved as at an auroral zone station.

The sporadic-E layer ionisation at high latitudes is restricted to a certain latitude interval, which is centred at a latitude close to the maximum of visual auroral activity. This zone is at an average geographical latitude of about 70^0 over Northern Europe and at about 60^o geographic latitude over North America. A similar zone is found in the Southern Hemisphere close to the zone of maximum occurrence of Aurora Australia (AGARD 1967).

An ionospheric layer does not necessarily provide a good medium for radio communications, even if the density of free electrons within the layer is large. The presence of small irregular clouds in the electron density may cause a high degree of fading and this may cause serious problems in communications. It is therefore important to know how the ionisation varies in space before we can determine the usefulness of the layer for communications.

The E_s layer is a problem in HF communications because of its irregular and as yet unpredictable behaviour. It should be pointed out that efficient use of E_s reflections may prove useful in some instances. One of the most important effects of E_s on HF propagation is the screening effect. The sudden occurrence of an E_s layer can prevent the signal from reaching the F-layer. The patchy and irregular structure of an E_s layer may introduce rapid fading. The retardation type of sporadic-E ionisation is fairly uniform in a horizontal direction and shows regular, slow variations during the night and in this respect is good for communications as it behaves more like a regular ionospheric layer. The non-retardation E_s, on the other hand, shows a very irregular structure with large and rapid time variations during the night. Probably this layer is made up of small clouds with high electron density and radio waves reflected from this layer normally fade rapidly.

4.2 The Ionosonde: HF Radio Sounding of the Ionosphere

Radio sounding is a well established technique that was first employed in the 1920's for ionospheric sounding from the ground (Breit and Tuve, 1926). In more recent years, advanced digital sounders have been developed for ground- based observations that provide detailed information about the structure and dynamics of the bottomside ionosphere (Reinisch, 1996). These modern sounders measure more than just the time of flight and amplitude of the echoes, they also determine the arrival angle, wave polarisation and Doppler frequency. Radio sounding relies on total reflection of radio waves from plasma structures that have plasma frequencies f_n equal to the radio frequencies f for the ordinary wave mode.

Electromagnetic waves propagate through a magnetoionic medium in the so-called free-space mode as long as $n^2 > 0$ where n is the index of refraction. Reflection occurs where n = 0 and the plasma gradient is parallel to the wave normal (Budden, 1985). Solving dispersion relation for n = 0 gives the following three reflection conditions (cutoff frequencies):

X=1	ordinary (O) wave
X=1-Y	Extraordinary (X) wave
X=1+Y	Z-wave

Where:

$$X = \left(\frac{f_n}{f} \right)^2$$

$$Y = \frac{f_h}{f}$$

$$f_n = \frac{1}{2p} \sqrt{\frac{N.e^2}{m.e_0}}$$

$$f_h = \frac{e.B_0}{2.p.m}$$

$N =$ *number density*
$e =$ *charge*
$m =$ *mass of electron*
$e_0 =$ *free space permittivity*
$B_0 =$ *earth's magentic field*
f_n *=Plasma frequency*
f *=Carrier frequency*

Ionosondes typically scan through frequencies from ~ 0.5 to 30 MHz, transmitting narrow pulses in the vertical direction and measuring the echo delay time. The data is usually displayed in the form of an ionogram showing the echo delay as a function of the sounding frequency. The echo delay t_d is usually expressed in terms of the virtual height h´:

$$h' = 0.5 \times c \times t_d$$

where c is the free space speed of light.

Typical values of t_d are:

- 467μs equates to a virtual height of 70 km

- 5333μs equates to a virtual height of 800 km

Radio observations of sporadic-E layers are characterised by strong reflections from the E-region at a virtual height that is constant with frequency. The echoes from sporadic-E are often detected at frequencies much greater than the plasma frequency of the normal E-region.

A new era for ionogram analysis evolved with the introduction of digitally controlled ionosondes in the 1970's. The tedious and time-consuming effort required to manually scale ionograms was replaced with automated computer algorithms that identify the features inherent in an ionogram. The analysis of digital ionograms has been a subject of extensive research within the ionospheric physics community for at least a decade or more. One of the major challenges of digital ionogram analysis is the classification of data in order to autonomously identify the different ionised layers of the ionosphere. However, the majority of these efforts have been directed toward the extraction of F-layer parameters, to the detriment of the E-region, partly due to the complex nature of the E-region (Wilkinson, 1998). None of the algorithms that are now being employed for autonomous ionogram analysis (e.g. ARTIST or DSND) attempt to differentiate between the different forms of E_s, frequently leading to an erroneous identification of the characteristic parameters that describe the E-layer (Sikdar, 2004).

4.2.1 Interpreting E-Layer Records on the Ionosonde

The standard ionosonde produces records known as ionograms, which show the variation of the virtual height of reflection as a function of the radio frequency, h'(f).

The frequency band normally used is from about 1 MHz to about 20 MHz, although some ionosondes can be operated down to 0.2 MHz when interference allows.

An ionogram actually shows the time of travel of the pulse signal from the transmitter to the receiver, reflection in the ionosphere normally occurring at vertical incidence. As this signal always travels more slowly in the ionosphere and in the receiver than in free space, the heights observed always exceed the true heights of reflection. If the frequency of a radio signal reflected from a single thick layer is increased the virtual height increases more rapidly than the true height. When the level of maximum electron density in the layer is reached, the virtual height becomes effectively infinite (Piggot and Rawer, 1972); see figure 71 below. The frequency at which this occurs is called the critical frequency of the layer.

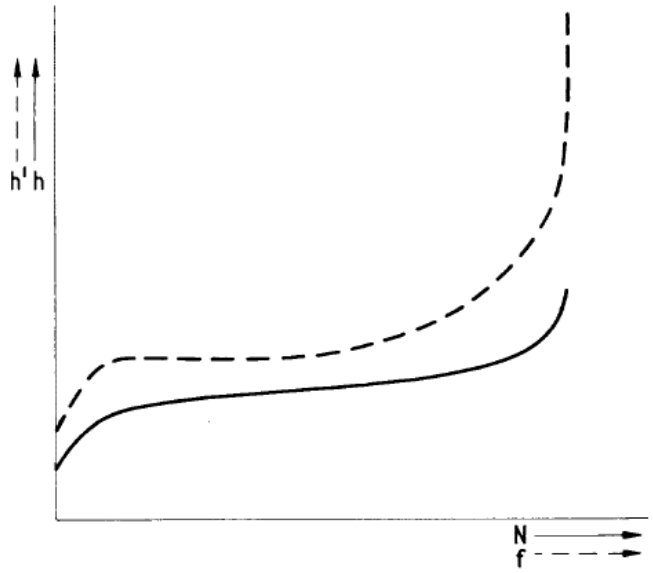

Figure 71. Relations between virtual height and true height (no magnetic field) (Piggott and Rawer 1972). ---- = h`(f), —— = ionisation distribution

If the reflecting layer is very thin, the increase in virtual height with frequency cannot be observed but the amplitude of the signal appears to decrease rapidly above a certain frequency. The highest frequency at which a clear, almost continuous, trace is obtained is called the top frequency of the trace.

Ionosonde records show two types of E_s traces, and these two types are referred to as the retardation and the non-retardation types of sporadic E ionisation, respectively. The layer that gives rise to the retardation type of E_s traces on the ionogram is fairly thick, whereas the non-retardation type of E_s trace may be referred to as a thin, blobby, ionospheric layer.

The Earth's magnetic field, in general causes a radio wave incident on the bottom of the ionosphere to be divided into two waves of different polarisation, which are reflected independently in the ionosphere. These waves are known as magneto-ionic or magneto-electronic component waves. They are due to the interaction of the electrons in the plasma with the magnetic field. One is called the ordinary wave and the other, the extraordinary wave. The following conventions are applied to interpreting the characteristics of magneto-ionic components:

- Top frequency of a layer - the highest frequency at which an echo trace is obtained from the layer at vertical incidence;
- Blanketing frequency of a layer - the lowest frequency at which the layer begins to become transparent. This is usually identified by the appearance of echoes from a layer at greater heights;

- Critical frequency of a layer - the highest frequency at which the layer reflects and transmits equally. The definition shows that the critical frequency of a layer always lies between its top frequency and its blanketing frequency.

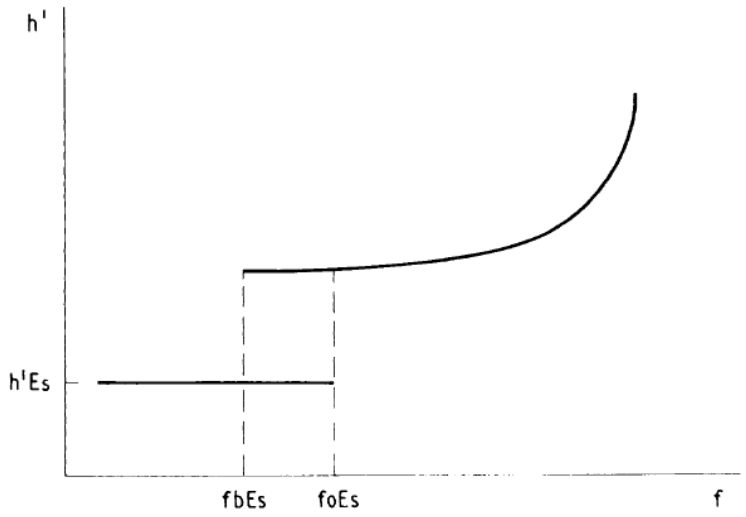

Figure 72. Idealised ordinary ray pattern where a thin layer is present. Note that the quantity corresponding to the critical frequency of a thick layer always lies between f_oE_s and f_bE_s (Piggott and Rawer 1972).

With reference to Figure 72, the following conventions are applied when identifying critical and characteristic frequencies of the E-layer[11]:

- f_oE: The ordinary wave critical frequency corresponding to the lowest thick layer stratification in the E-region which causes a discontinuity in the height of the E trace;
- f_oE_s: The ordinary wave top frequency corresponding to the highest frequency at which a continuous trace is observed;

[11] Please note this caveat: f_oE_s, f_bE_s and $h'E_s$ must all be scaled using the same E_s trace.

- f_bE_s: The blanketing frequency of a E_s layer, i.e. the lowest ordinary wave frequency at which the E_s layer begins to become transparent. This is usually determined from the minimum frequency at which ordinary wave reflections of the first order are observed from a layer at greater heights;
- $h'E_s$: The lowest virtual height of the trace used to give f_oE_s.

Particle-E has its own ionogram characteristic which is a thick layer in the E-region with a critical frequency significantly greater than that of normal E. In most cases particle-E can be attributed to direct or indirect ionisation by particle activity (Piggott and Rawer 1972). Particle-E always causes group retardation in any traces from higher layers, and this retardation near f_oE is sufficient to identify the critical frequency. Traditionally this trace was called night E as the critical frequency of the normal E was below the lowest recordable frequency at night. Fortunately, in almost all practical cases, the difference between the critical frequency of the particle-E and of normal E is large. Thus at night when f_oE for normal E is between 300 kHz and 500 kHz particle E usually has an f_oE above 1 MHz – often up to about 5 MHz and beyond.

As an example, figure 73 represents a low level particle-E event at Tromsø (High-latitude station). The E-layer is enhanced, blanketing the upper layers to 3.5 MHz and retarding up to nearly 5 MHz. This ionogram is mostly a type E_s-a with some characteristics of a type E_s-r, demonstrating the difficulty in accurately defining different types of E_s.

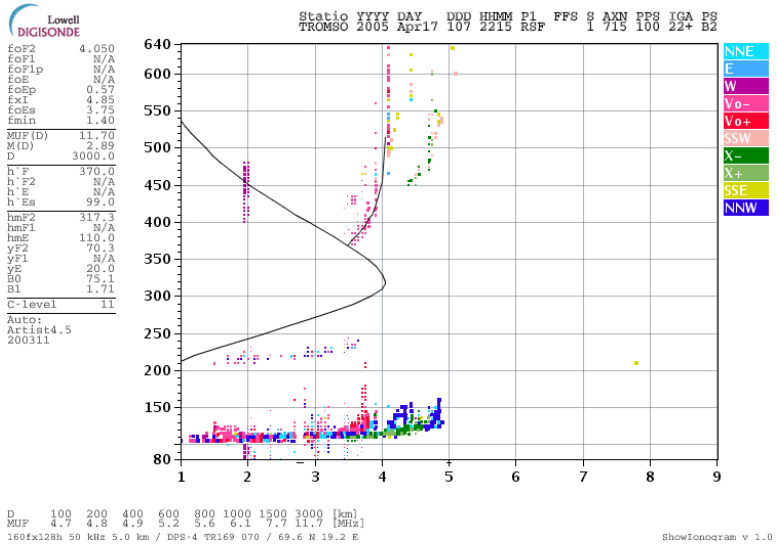

Figure 73. Example Ionogram from a Digisone located at Tromsø, Norway.

The distinction between blanketing and non-blanketing traces is very important both scientifically and operationally and statistics of the blanketing frequency can be at least as useful as those for f_oE_s. It should be noted that f_bE_s is determined at a well-defined place – where the ray path of the first F echo goes through the E_s layer. In contrast, f_oE_s corresponds to the highest ordinary wave returned from E_s by a reflection or scattering mechanism. f_oE_s corresponds roughly to the electron density at the places of highest concentration, while f_bE_s corresponds to that at the places of lowest concentration (were waves can penetrate as long as $f > f_bE_s$).

A special difficulty arises at high-latitude stations during particle precipitation. It frequently happens that, during the course of a disturbance, storm types of E_s (that is E_s-a and r) transform into a thick night E layer (E_s-k) or vice versa. Thus, f_oE_s and f_bE_s transform into f_oE values and careful analysis is required.

4.2.2 The f-Plot

The f-plot is a daily graph of the frequency characteristics of all the daily ionograms as a function of time, using an internationally agreed convention, so that detailed observations from different stations may be compared efficiently. It has been acknowledged that the f-plot is a valuable tool for identifying variations in the ionosphere and in the interpretation of complex records, particularly at high latitudes (Piggot and Rawer, 1972).

The f-plot was originally developed to enable the complicated and rapidly changing ionograms from high-latitude stations to be reduced without numerous arbitrary and difficult decisions on the interpretation of the individual ionograms (Piggott and Rawer, 1972). However, it rapidly became clear that the f-plot provided a very efficient method of recording and studying data which were too complicated or too numerous for conventional analysis, and it has become a primary tool for analysing the hour-to-hour or day-to-day changes in the ionosphere. Thus, it is the right tool for the analysis undertaken in this report. In principle, any frequency characteristic can be indicated on an f-plot. In practice, certain characteristics have found to be both valuable and easy to plot and these have been chosen for world-wide reduction. Other frequency characteristics have been added where local or regional ionospheric reasons are applicable.

The f-plot provides a summary of the original observations with the minimum of interpretation and enables difficult decisions needed for hourly tabulations to be made with due consideration of all the available data. This is particularly important at high-latitude stations where blackouts, spread echoes or rapidly changing oblique reflections frequently prevent the normal characteristics from being observed on

individual hourly ionogram records. Figure 74 is a good example of an f-plot from the Sodankyla observatory generated from the ionograms produced on the 9 November 2006. The time of sunrise at 100 km, sunrise at the Earth's surface, sunset at 100 km, sunset and SSC are marked on the plot.

As there are no fault indicators given on the original plot, it is not clear why there is only limited data before 8:00 (all times quoted in this section are MLT). The F-layer and the E-layer, between 8:00 and 17:00 follows the monthly median values closely. F_{min}, often used as an indicator of absorption, is normal around 1.4 MHz until 19:00.

An SSC occurs at 18:50 (MLT) and very little change from the expected values occurs until after 20:00 (point 2). At the measurement taken at 21:00 (point 3) the F-layer is completely blanketed by the E-layer which reaches a high critical frequency of 5 MHz. Note that f_{min} increased dramatically reflecting the increase in electron density in the D and E-regions which causes complete absorption of lower frequencies. The enhanced E-layer continues for at least another two hours reaching a peak critical frequency of 5.7 MHz (point 4) before reducing to a critical frequency of 3.8 MHz (point 5) which still blankets the F-layers.

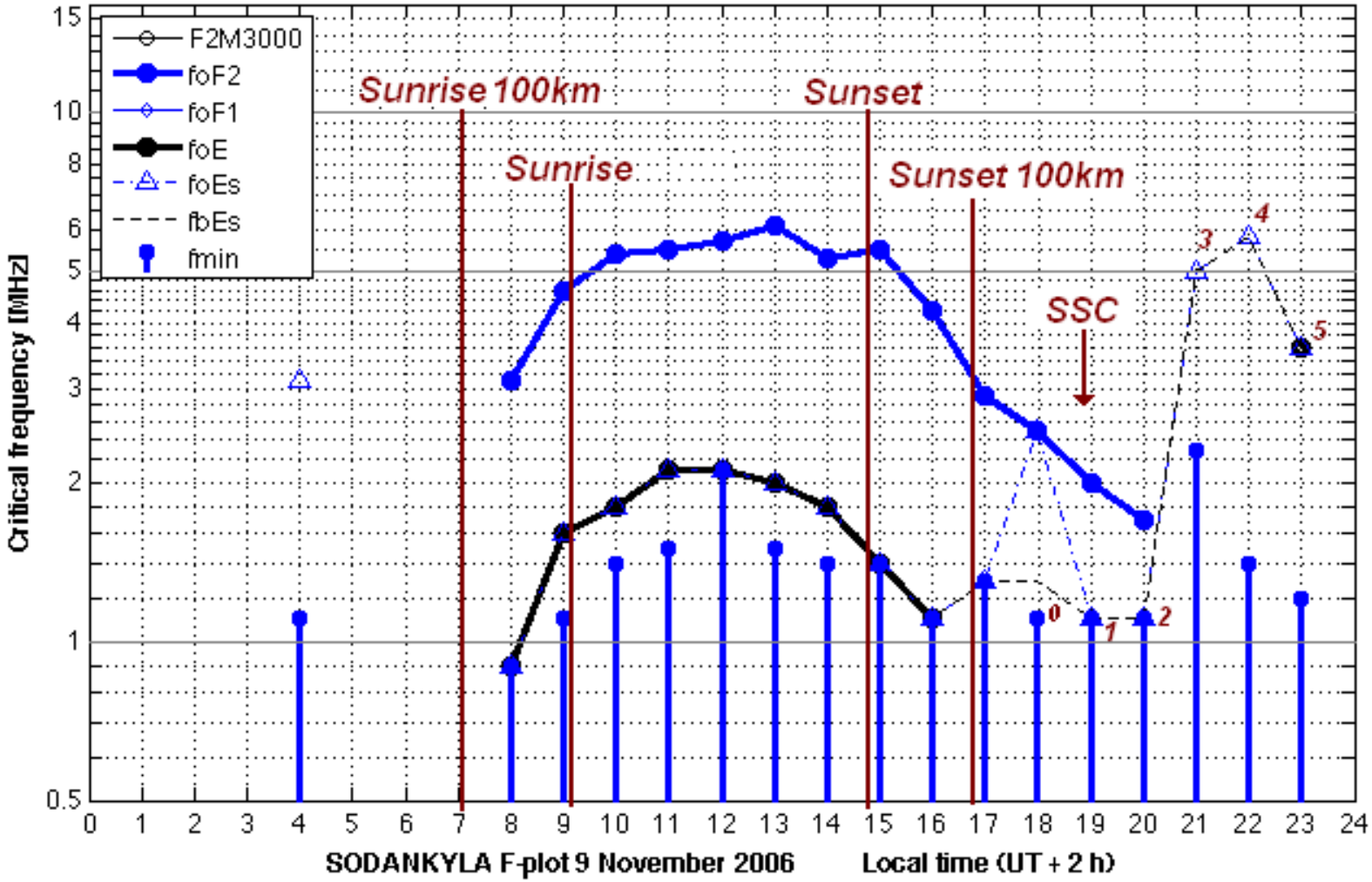

Figure 74. F-plot Example - Event 175, the arrow at 18:50 MLT indicates the occurrence time of the SSC

The data used in this report are gathered from the f-plots generated at the Sodankylä observatory which is located 120 km north of the Arctic Circle in Finland, 67° 22′ N, 26° 38′ E, L-value 5.2. Data are gathered over six years from the sunspot minimum in 2000 until the near sunspot maximum in 2006.

4.3 ISR Data: Revealing E-Layer Electron Density

In the incoherent scatter radar method, incoherent scatter is produced by backscatter from the thermal irregularities in the ionization in the upper atmosphere. The signal amplitude and spectral shape yield the electron density and electron and ion temperature, while the spectral shift yields the average velocity of the ions. Since four independent measurements are made, each of these data is independent of the rest in the sense that no one value depends entirely upon another value. Usually a co-located ionosonde is used to provide an absolute calibration for the system. The precision of individual profiles (ten to fifteen minutes of data averaged together) is estimated to be better than 10% for the electron density and 50 to 100K for the electron temperature during a period of adequate electron density ($>10^{11}$e m^{-3}) (Bates et al., 1974).

The extremely wide variations in ionospheric electron density profiles at auroral latitudes have been documented using data from the Chatanika ISR (Bates and Hunsucker, 1974). The following three figures (figures 75, 76 & 77) show ISR electron profiles with considerably increased densities in the E-layer from auroral ionisation. The ISR shows confirms that the auroral E-layer is a thick layer, i.e. it reflects HF energy and therefore has a true critical frequency, so that HF propagation through the E-region near the auroral oval can be disrupted by blanketing.

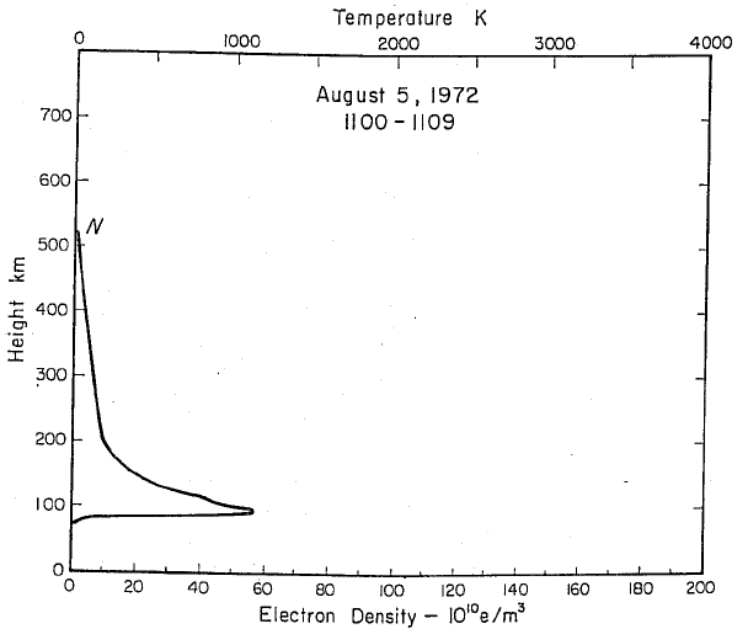

Figure 75. Day time example of the response of the high-latitude E-region to particle precipitation event during the intense solar proton event of August 1972, (System resolution is 10 km). (Bates and Hunsucker, 1974)

Figure 75 gives a very clear indication of the large increase in electron density at E-layer altitude as a result of particle precipitation. This example corresponds to previous work done in this area which also captured ISR electron density data at E-layer altitudes at the time of SSC events (Ritchie and Honary, 2006).

Figure 76 shows a fairly strong blanketing E-layer. The ionosphere shows a F_oE approaching 10 MHz which is 4 MHz higher than F_0F_2.

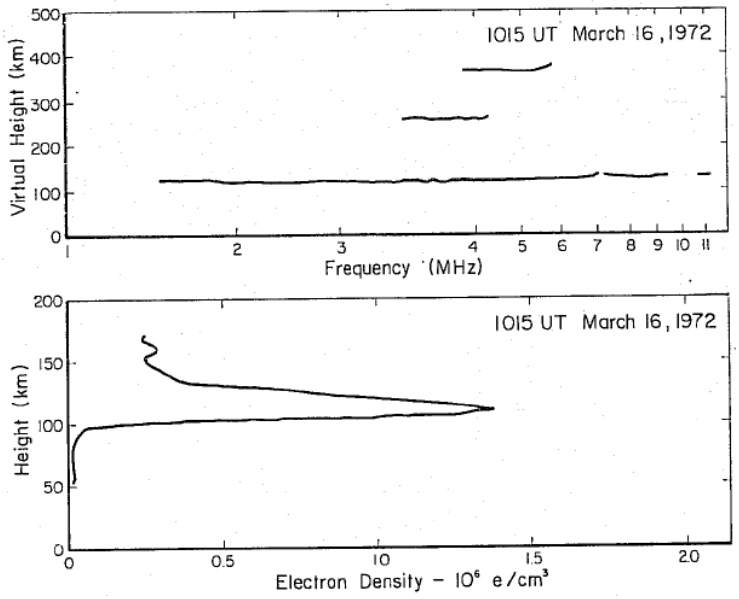

Figure 76. Response of the E-region to auroral electron precipitation as shown on simultaneous ISR and ionosonde data. (Bates and Hunsucker, 1974)

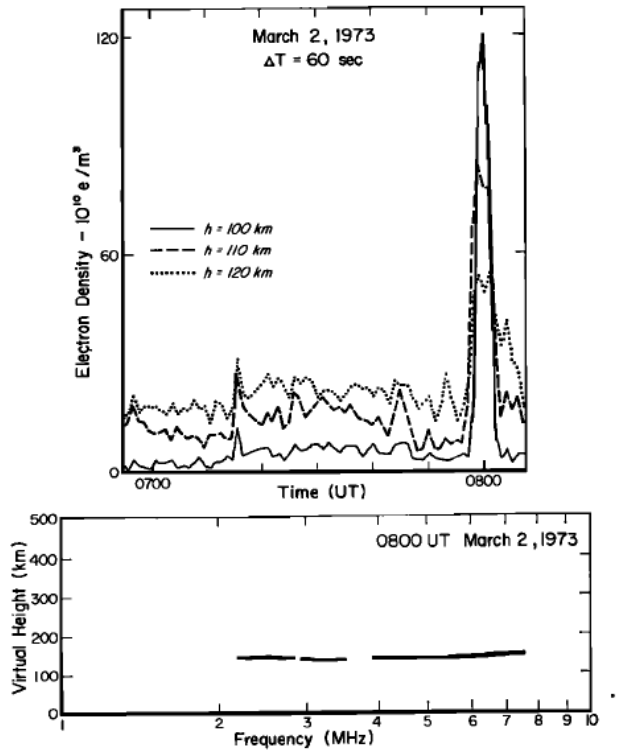

Figure 77. Response of the E-region to auroral electron precipitation as shown on ISR and ionosonde data. (Bates and Hunsucker, 1974)

Figure 77 represents the electron density at three different heights over more than a one hour period. At the time of the electron precipitation (around 08:00UT), the electron density increases massively (from 5×10^{10} e.m^{-3} to 120×10^{10} e.m^{-3}) for a ten minute period. At the moment of maximum electron density, the ionosonde captured the full blanketing E-layer ($f_oE \approx 8$ MHz) that results.

4.3.1 Variability of the E-region

Baron (1974) captured the variability of the E-region using the Chatanika radar in September 1971. As shown in figure 78 the E-region displayed shows considerable variability, in terms of electron density, between three scans only 20 seconds apart:

i. The profiles have a rather sharp lower boundary and the electron density increases dramatically in the space of a pulse width on the bottom side of the auroral E layer;
ii. The decay of the layer above the ionisation maximum is more gradual and relatively smooth;
iii. There is a rapid disappearance of ionisation in the 20 seconds between the second and the third profiles;
iv. Note also that the ionisation extends down to relatively low altitudes of approximately 80 to 85 km. This implies that the precipitating electrons that produced the ionisation were fairly energetic, having energies in the order of 20 keV.

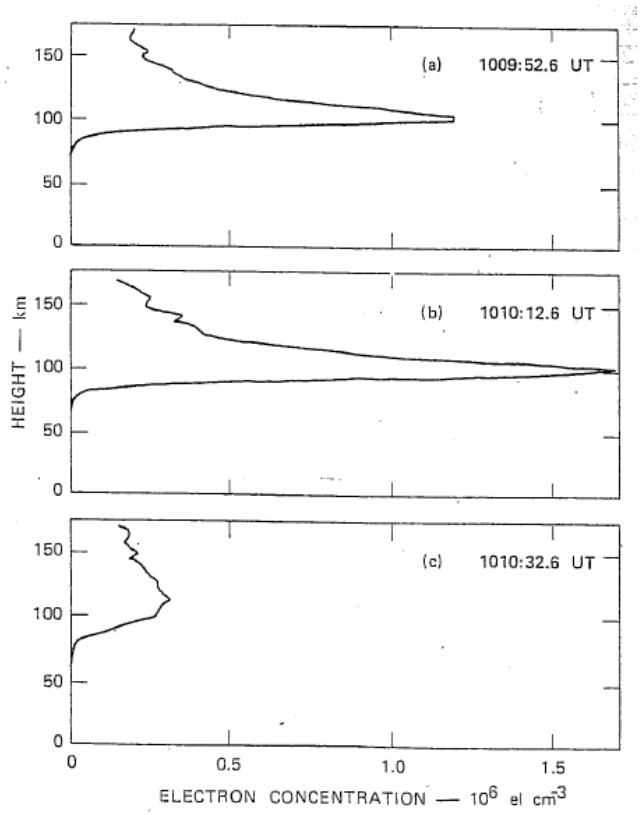

Figure 78. Sequence of E-region electron profiles using the Chatanika radar on 27 September 1971 (From Baron, 1974).

Baron (1974) also looked at the behaviour of the auroral E-layer by plotting the electron profiles at fixed heights as a function of time. An example is shown in figure 79 which shows:

i. Very rapid changes with time (5 second integration times) occur at both altitudes;

ii. The behaviour at the two altitudes is not always correlated – this implies that along a particular field line, the precipitating electrons at two different energies behave differently.

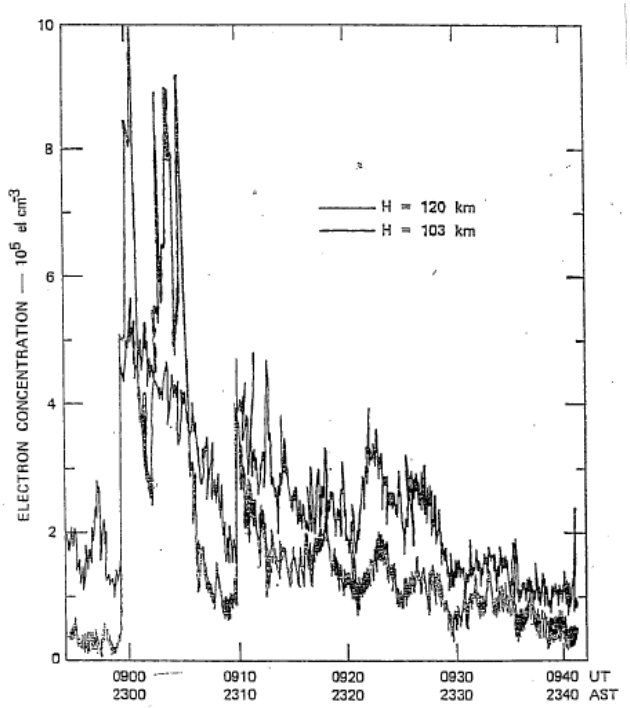

Figure 79. E-region electron concentration at 103 and 120 km altitudes as a function of time: 21 November 1971 (From Baron 1974)

Baron (1974) determined that the peak production rate for auroral ionisation produced by particle precipitation is two orders of magnitude greater than the peak photo-ionisation production rate as calculated by Hinteregger et al. (1965), showing that precipitation is often the dominant mechanism affecting the high-latitude ionosphere.

Figure 80 shows the height of the maximum ionisation rate as a function of electron energy for mono-energetic electrons with an isotropic pitch angle. Also shown are the altitudes at which the production rate is 10% of the maximum production rate. If different (more filed-aligned) pitch angle distributions are used, the altitude of the maximum remains essentially the same but the 10% curves move closer to the maximum curve.

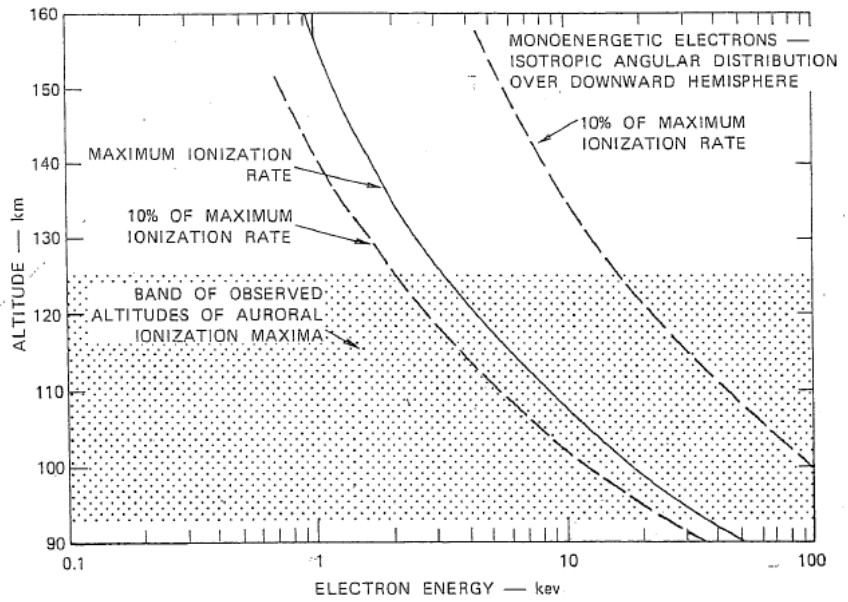

Figure 80. Altitude of maximum ionisation rate as a function of primary electron energy for mono-energetic electrons with an isotropic pitch angle distribution (After Baron, 1974). The lower the altitude of peak ionisation the harder the precipitation that causes it.

Using this curve we can estimate the particle energy from the observed altitude of electron concentration maximum. Baron (1974) noted maxima at 92 and 125 km, thus the mean energy of the primary electrons ranges between 2 and 35 keV for the events studied (using the lower dashed curve in figure 80).

4.3.2 Electron Density Profiles During Storms

In comparing satellite and ground based observations of the substorm of 2 February 1969, Larsen (1973) determined the ion production rates and electron density profile in figure 81 for a position near the mid-point of the propagation path being examined.

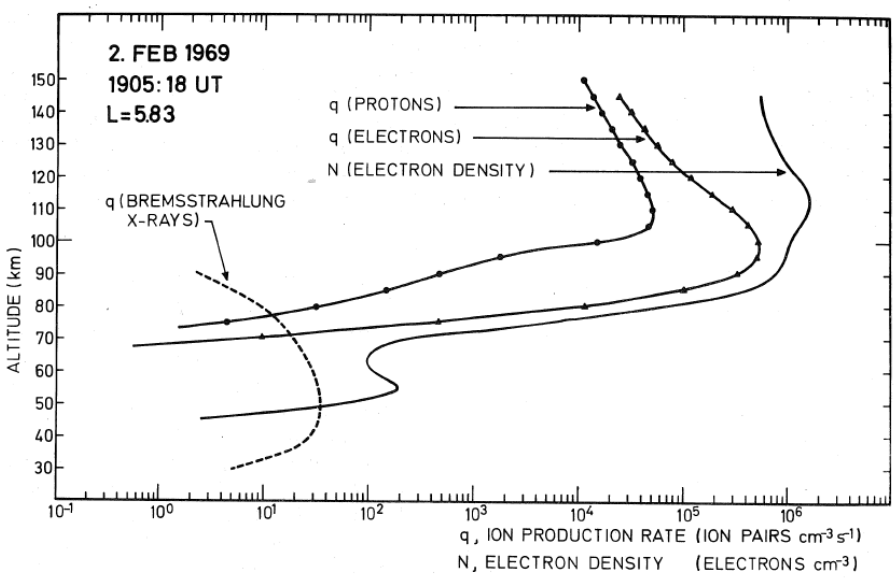

Figure 81. Ion production rates and electron density profile determined in the mid point of a high-latitude propagation path (Larsen, 1973)

For this event high fluxes of protons were observed, but the computation shows that the ion pair production due to precipitating protons is, at all heights considered, smaller than that due to electrons. Maximum total ion pair production occurs at 100 km altitude with a rate of 2.5×10^5 ion pairs $cm^{-3}.s^{-1}$. The large fluxes of high energy electrons will, however, produce a significant flux of Bremsstrahlung X-rays which in turn act as a secondary ionisation source. Note that ionisation due to Bremsstrahlung X-rays in fact dominates over the other ionisation sources below 70 km.

A rather broad maximum in N_e is found between heights of 95-125 km where the electron density exceeds 10^6 electrons/cm^{-3}. The Bremsstrahlung X-rays produce a smaller secondary maximum at 55 km with electron density of about 200 electrons/cm^{-3}. While the latter peak is important for VLF propagation, the total free electron concentration below 70 km produces no significant attenuation of cosmic noise at riometer frequencies.

Collis and Haggstrom (1991) studied the high latitude ionosphere response to an SSC. While their paper focuses on F-region electron density depletions the results also highlight a clear E-layer phenomenon which is shown in figure 82. Forty five minutes after the SSC, the E-region electron density more than doubles to ~ 2×10^{11} m^{-3} and maintains this level for more than 1 hour before slowly decreasing over the following 2 hours. The sudden increase in electron density occurs in a period of approximately 5 minutes.

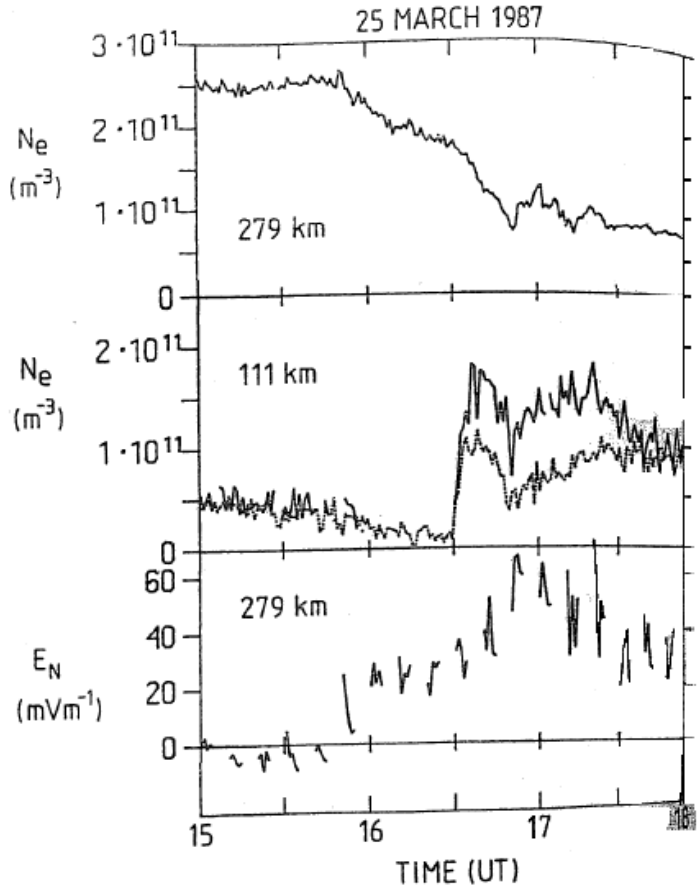

Figure 82. E-region plasma density (Ne) and F-region plasma density and northward electric field measurements by the EISCAT radar for the interval 15-18 UT, 25 March 1987 (at 111 km the upper curve is corrected density and the lower curve is raw density values) (Collis and Haggstrom, 1991)

The F region electron density declined slowly from 2.5×10^{11} m^{-3} to 1×10^{11} m^{-3} over a two hour period. As there is no correlation between the slow decline in F region plasma at 280 km and the sudden increase in E-region plasma at 111 km, it can be taken that the increase in Ne in the E-region is not due to an influx of ionisation from higher altitude layers.

Enhanced northward electric fields have been in existence since the SSC started, 45 minutes previous to the E-region N_e enhancement, and by the same argument the sudden E-region enhancement is not due to a sudden inflow of ionisation from the equator. The sudden enhancement is therefore more likely due to a sudden and sustained dumping of high energy particles causing enhanced E-layer ionisation. The dumping is perhaps due to the magnetosphere returning to normal after the sudden compression has relaxed.

The onset of intense sporadic-E following an SSC just after midnight and lasting up to 12 hours has been noted by Herman and Penndorf (1963). In this particular case F_oE reached 12 MHz and the sporadic-E layer covered most of North America above 40^0 N within two hours of the SSC. Other observations (Batista et al., 1991; Morton and Mathews, 1993) have also shown that during large geomagnetic storms, the electron density of the night lower ionosphere increased significantly compared to quiet conditions. Lyons and Richmond (1978) and Tinsley (1979) assumed that a possible cause of these density enhancements is the precipitation of energetic neutral atoms with energies of 1 – 100 keV from the ring current zone during a magnetic storm

when a considerable amount of energy comes into the ring current from the inner magnetosphere.

4.4 Methodology and Data Gathering

The SSC, by definition, guarantees that a magnetic storm or an increase in geomagnetic activity lasting at least one hour occurs. An SSC is the magnetic signature of an interplanetary shockwave most often produced by solar flares. Based on its definition, SSC is always a precursor to increased geomagnetic activity, most often followed within 3 – 8 hours by a geomagnetic storm (IAGA). Characterising the effect of magnetic storms and of geomagnetic activity on the E-layer is the goal of this research work and hence the occurrence of SSC is used as the reference point to start each six hour analysis. Using this methodology means that we have a well-defined and understood starting point from which we can:

- Undertake data gathering;
- Examine the magnitude and variance of expected disturbances to the E-layer.

Initially, the ideal was to calculate the statistics for each MLT hour of the day for each of the six hours following the 175 SSC events analysed. However, it became apparent that in many MLT hours there were too few data points available to generate adequate statistically sound results. It was therefore decided to compromise by splitting the day into the four traditional sectors as shown in table 16 below and then to gather the relevant statistics for each of the sectors.

For the six hours following the SSC the following statistics are collected for each sector, using the f-plot generated at the Sodankylä observatory:

- The percentage of blanketing that occurs in each sector;

- The critical frequency at which blanketing occurs (i.e. no F-layer reflection is visible;
- The mean, median, minimum, maximum, standard deviation, lower quartile and upper quartile of the change in critical frequency that occurs in each sector.

Sector	MLT hours included in this sector
A	0 – 6 MLT
B	6 – 12 MLT
C	12 – 18 MLT
D	18 – 24 MLT

Table 16 Definition of Sectors

Bearing in mind that the f-plot accumulates hourly data, f_oE, the critical frequency of the E-layer is noted on the hour before the SSC occurs (called F_oE_0). The same information is then gathered on the hour following the SSC (called F_oE_1) and every hour thereafter for five hours. This is illustrated in table 17 using the F-plot example in figure 74.

Designator	Meaning	Value (MHz)
foE_0	f_oE measured on the hour before the SSC occurs (Point 0)	1.1
foE_1	f_oE measured on the hour after the SSC occurs (Point 1)	1.1
foE_2	f_oE measured on the second hour after the SSC occurs (Point 2)	1.1
foE_3	f_oE measured on the third hour after the SSC occurs (Point 3)	5.0 (Full Blanketing)
foE_4	f_oE measured on the fourth hour after the SSC occurs (Point 4)	5.7 (Full Blanketing)
foE_5	f_oE measured on the fifth hour after the SSC occurs (Point 5)	3.6 (Full Blanketing)

Designator	Meaning	Value (MHz)
foE_6	f_oE measured on the sixth hour after the SSC occurs. (Appears on the f-plot of the following day)	3.2 (Full Blanketing)

Table 17 Example of Data Gathered and Calculated.

Note: in all cases the sector quoted is the sector in which the SSC occurred and not the sector in which the critical frequency is determined, other than when the measurement hours happens to correspond.

4.4.1 The Median Value of the Parameter

The median is a very commonly reported summary statistic. It is accurate whether the data set is normally distributed or if there are extreme values which skew the data. In a normal distribution, the mean, median, and mode are approximately equal to each other. In a skewed distribution, there are extreme values (outliers) at either the left or right side of the distribution. The median is less sensitive to extreme values than the mean. Therefore, it is a very good summary statistic to use when the data contains outliers.

The weakness of the median as a representative value can be caused in two ways:

i. Little numerical data used to calculate the median;

ii. Large dispersion in the distribution indicating excessive deviation.

In dealing with ionospheric data, it was the recommendation of the URSI High Latitude Scaling Group, back in 1956, that the count be included when median values are published as well as the quartile range be included as a measure of dispersion

(Knecht, 1957). This was proposed to ensure that both weaknesses mentioned above in the use of the median value, if existing, will be revealed. To ensure academic rigour, this approach is adopted, where appropriate in this chapter.

4.4.2 Discounting Solar Control

The E-layer is generally considered to be under the control of solar radiation and in many low-latitude ionograms the E-layer ritually forms as the sunrise reaches 100 km altitude and begins to fade as sunset falls below 100 km altitude. There is also a very strong correlation between sunspot number, as a measure of solar activity, and the critical frequency of the E-layer. This is illustrated using the "Edinburgh method" as an example. Developed by Muggleton (1975), the Edinburgh method produces monthly-medians of f_oE values. In this method the monthly median value of f_oE, as a function of solar activity, month, geographic position and time, is expressed in the form:

$$\left(foE \right)^4 = A.B.C.D$$

Where the terms A, B, C, D involve solar activity, season, geographic position and time, respectively.

In calculating the four terms it is required to input the sunspot number and solar zenith angle, both which are shown in the analysis of ionograms at Sodankylä to play no role in the amplitude of E_s that occurs concurrently with particle precipitation. While the Edinburgh model has only been validated up to 60^0 latitude, it has great value in determining monthly means which also has the effect of averaging out periods of disturbed ionospheric conditions. It is easy to see that such a method has very limited

applicability at high latitudes in disturbed conditions during which the E-layer is modified extensively by particle precipitation: this itself has no seasonal variations and is not under the influence of solar activity, other than in the number of disturbances that occur.

Initial thoughts in data gathering envisaged some technique of normalising the f_oE seen on the f-plot to compensate for seasonal variations and sunspot number to compensate for solar activity effects. It was not apparent how such a normalisation can be undertaken. The only accepted reliable long-term predictions of f_oE produce monthly median values which do not correlate well against f_oE measured at any random hour on any specific day when the primary source of ionisation is due to particle precipitation. The high-latitude ionosphere is fairly variable normally and highly variable during disturbances and there is no merit attempting to normalise the measured values of f_oE for any hour of any day. As shown by Baron (1974) and Hinteregger et al. (1965) the ionisation produced by particle precipitation is two orders of magnitude greater than that produced by photo-ionisation, so intense precipitation is the dominant mechanism affecting the high-latitude ionosphere. This removes most, if not all, solar and seasonal control concerns and reflects the conclusions of a number of researchers e.g. Hargreaves (1992, pg 253), McNamara (1991, pg 99), Davies (1990, pg 132), etc.

As already stated, the E-layer is generally under the strong control of solar activity and there is also a very strong correlation between sunspot number, as a measure of solar activity, and the critical frequency of the E-layer. However, the difference in electron density at altitudes less than 120 km between low sunspot numbers and very

high sunspot numbers is relatively small – on the scale of less than a doubling of electron density. This effect is clearly shown in figure 83 below (after Wright, 1962).

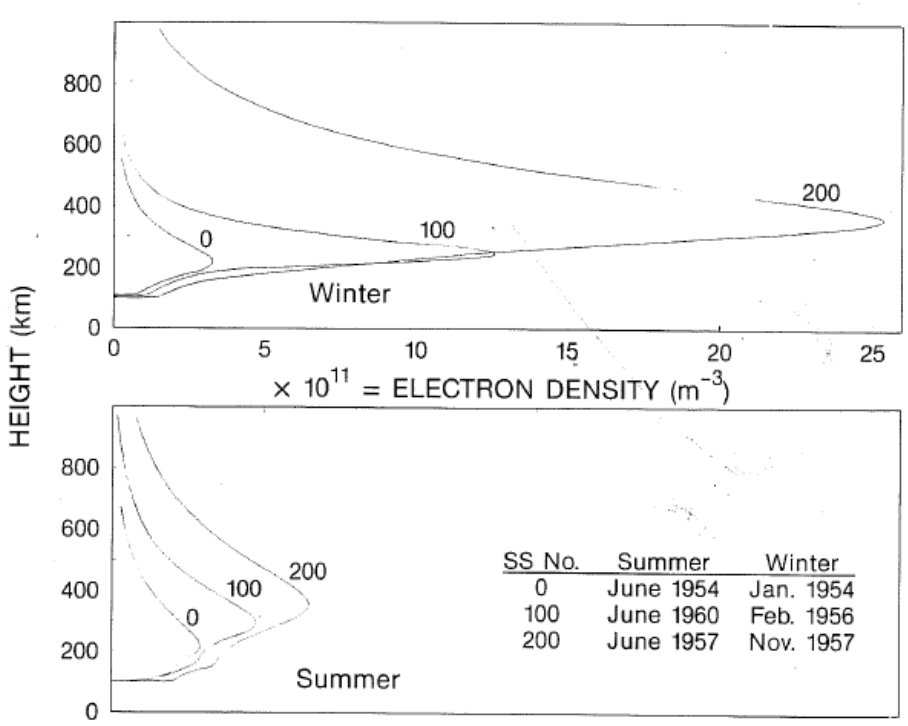

Figure 83. Typical electron density profiles at sunspot numbers 0, 100 and 200 (After Wright, 1962)

Further evidence of the limited difference in electron density is reflected in the work of Levin (1976) who presented a formula for calculating f_oE at midnight and at sunrise/sunset which only required the input of a sunspot number. The difference in f_oE at midnight varies only 0.2 MHz between a sunspot number of 0 and 150. The difference in f_oE at sunrise/sunset varies only 0.5 MHz between a sunspot number of 0 and 150.

To overcome any remaining possible problems envisaged in normalising the data it was decided to use the difference in critical frequency measured per hour (Δf_oE_{n-m}) to

determine the variability of changes that occur. These values reflect the reduction or increase in E-layer ionisation due to all applicable factors. However, as enhanced ionisation is due to particle precipitation which is by far the dominant ionisation source, Δf_oE_{n-m} captures predominantly the particle precipitation influence. It is accepted for the work in this chapter that Δf_oE_{n-m} will be equal for equivalent circumstances of particle precipitation, independent of diurnal, seasonal or solar activity variations. In other words, two identical particle precipitation events will generate an identical increase in electron density in the E-region which is represented by Δf_oE_{n-m} values, the base f_oE being equal.

As an example of the data calculated we extend further the data gathered from figure 74 and tabulated in table 17 by calculating the Δf_oE for each hour following the SSC. This is shown in table 18 which also notes if full blanketing has occurred, i.e. the F layer is not visible through the E-layer.

Designator	Meaning	Value (MHz)
foE_0	foE measured on the hour before the SSC occurs	1.1 MHz
ΔfoE_{0-1}	$foE_0 - foE_1$	0 MHz
ΔfoE_{1-2}	$foE_1 - foE_2$	0 MHz
ΔfoE_{2-3}	$foE_2 - foE_3$	3.9 MHz (Full Blanketing)
ΔfoE_{3-4}	$foE_3 - foE_4$	0.7 MHz (Full Blanketing)
ΔfoE_{4-5}	$foE_4 - foE_5$	-2.1 MHz (Full Blanketing)
ΔfoE_{5-6}	$foE_5 - foE_6$	-0.4 MHz (Full Blanketing)

Table 18 Example of Δf_oE_{n-m} Data.

4.5 Testing for Dependency on Solar Activity

This section tests for any dependency in the data on solar activity. The monthly sunspot number is used as a proxy for solar activity. While it could be argued that using the daily sunspot number would provide better resolution, it became difficult to deal with a large number of SSC events where the six hours being examined cut across two days.

4.5.1 The First Hour Following SSC (f_oE_0 to f_oE_1)

The line, scatter and range bar plot polar plot of figure 84 captures the change between f_oE measured on the hour preceding the SSC (f_oE_0) and f_oE measured on the hour immediately following the SSC (f_oE_1) binned against monthly sunspot number as a proxy for solar activity. The points joined by the solid line are the median value of all $\Delta f_oE_{0\text{-}1}$ values that fall in each sunspot number range bin. The range bars show the minimum and maximum values for each bin. Minimum and maximum values are used in preference to the 25% and 75% quartiles in order to expose the typical magnitude of variability that can be expected.

The following observations are made:

- There is no distinctive pattern of change in the median value of $\Delta f_oE_{0\text{-}1}$ as solar activity increases; there is a slight increase when the monthly sunspot number (MSN) reaches 140, but this is inconclusive as there is a similar increase at very low MSNs.
- There is a reduction in the variability of $\Delta f_oE_{0\text{-}1}$ as solar activity increases.

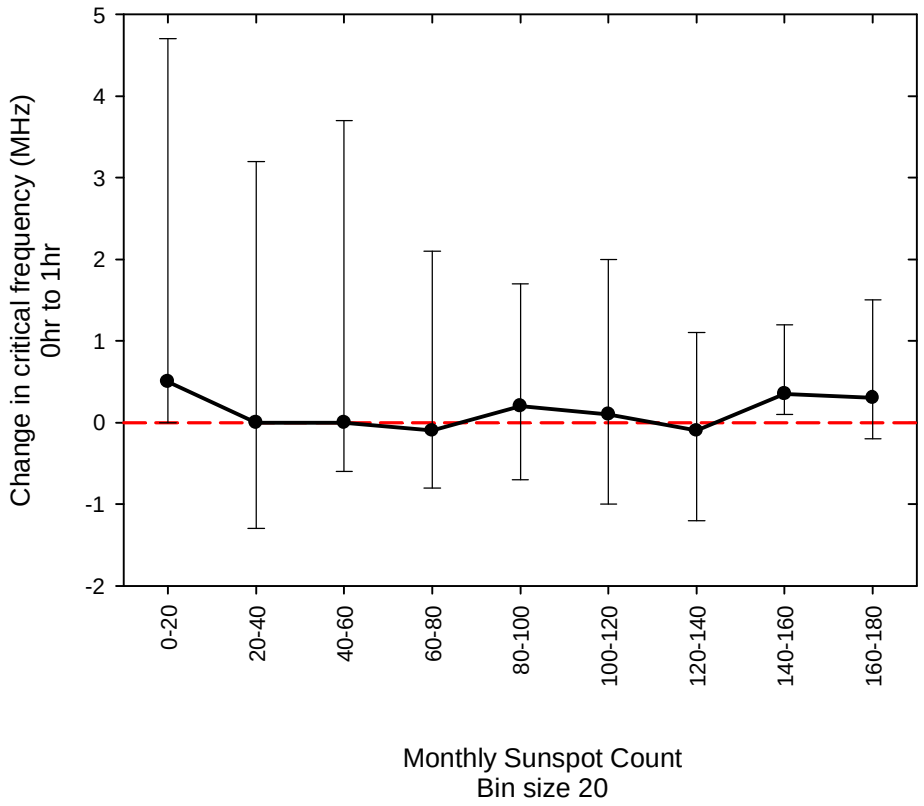

Figure 84. Line, scatter and range bar plot of the change between f_oE_0 and f_oE_1.

4.5.2 The Second Hour Following SSC (f_oE_1 to f_oE_2)

The line, scatter and range bar plot polar plot of figure 85 captures the change between foE measured on the first hour following the SSC (f_oE_1) and f_oE measured on the second hour immediately following the SSC (f_oE_2) binned against monthly sunspot number as a proxy for solar activity.

The following observations are made:

- There is no distinctive pattern in the median value of $\Delta f_oE_{1\text{-}2}$ as solar activity increases; there is again an increase in the median value at low MSN's.

§ At high values of MSN the variability is significantly reduced.

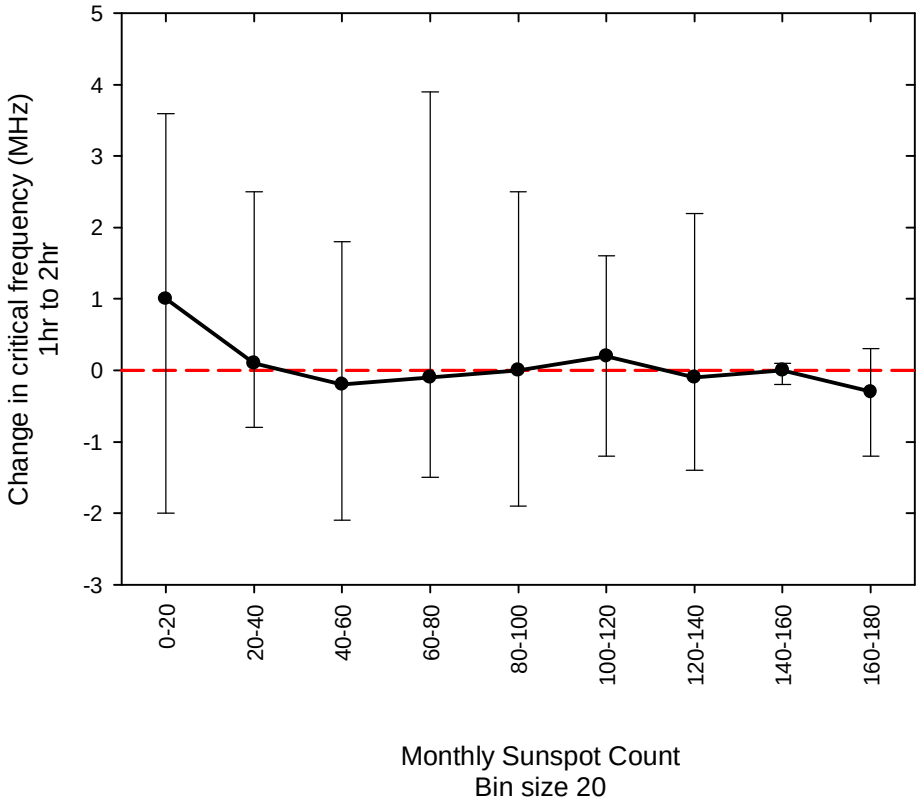

Figure 85. Line, scatter and range bar plot of the change between f_oE_1 and f_oE_2.

4.5.3 The Third Hour Following SSC (f_oE_2 to f_oE_3)

The line, scatter and range bar plot polar plot of figure 86 captures the change between f_oE measured on the second hour following the SSC (f_oE_2) and f_oE measured on the third hour immediately following the SSC (f_oE_3) binned against monthly sunspot number as a proxy for solar activity.

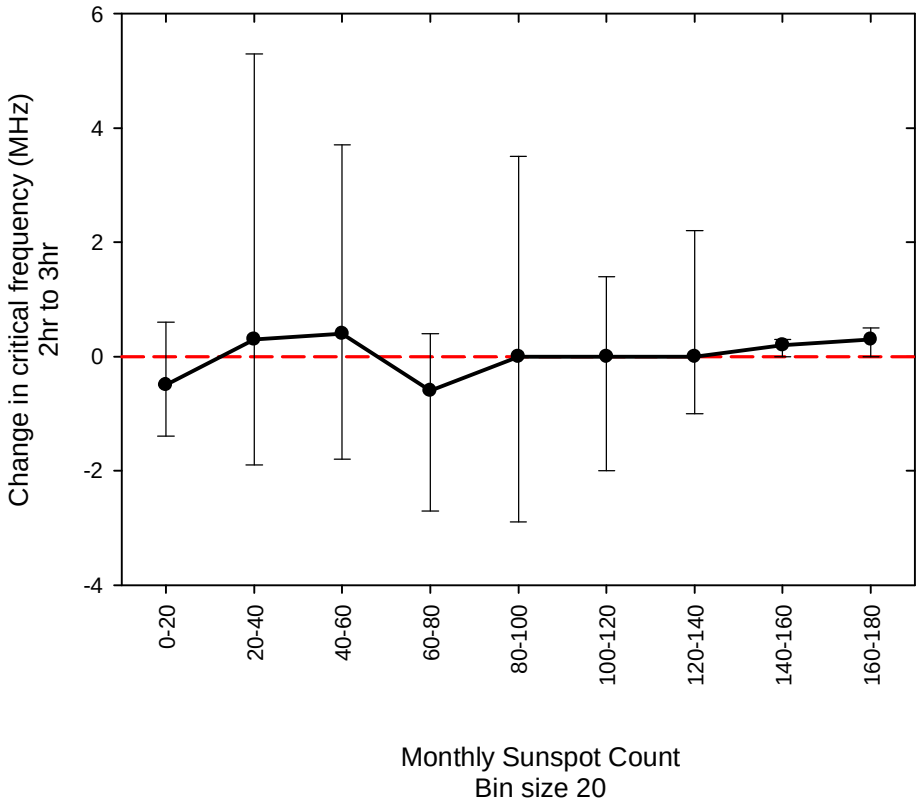

Figure 86. Line, scatter and range bar plot of the change between f_oE_2 and f_oE_3.

The following observations are made:

- There is no distinctive pattern in the median value of $\Delta f_oE_{2\text{-}3}$ as solar activity increases. The increase in median values of $\Delta f_oE_{2\text{-}3}$ at low MSN's is no longer apparent and is negative in this hour.
- At high values of MSN the variability is significantly reduced.

4.5.4 The Fourth Hour Following SSC (f_oE_3 to f_oE_4)

The line, scatter and range bar plot polar plot of figure 87 captures the change between f_oE measured on the third hour following the SSC (f_oE_3) and f_oE measured on the fourth hour following the SSC (f_oE_4) binned against monthly sunspot number as a proxy for solar activity.

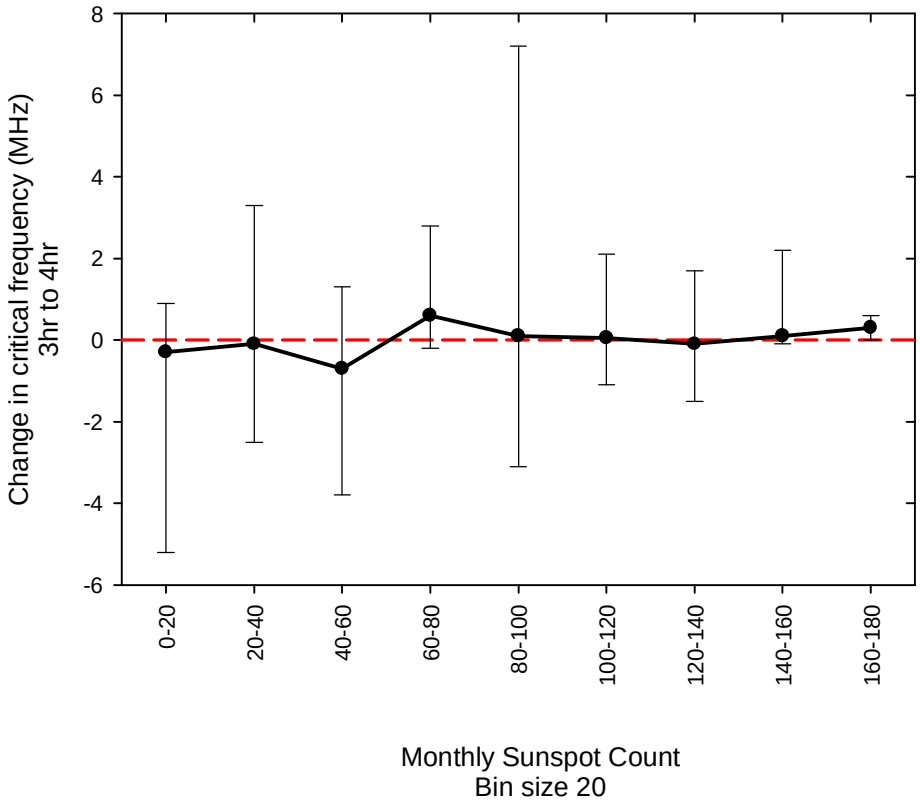

Figure 87. Line, scatter and range bar plot of the change between f_oE_3 and f_oE_4

The following observations are made:

- There is no distinctive pattern in the median value of $\Delta f_oE_{3\text{-}4}$ as solar activity increases;
- At high values of MSN > 100, the variability is again significantly reduced.

4.5.5 The Fifth Hour Following SSC (f_oE_4 to f_oE_5)

The line, scatter and range bar plot polar plot of figure 88 captures the change between f_oE measured on the fourth hour following the SSC (f_oE_4) and f_oE measured on the fifth hour following the SSC (f_oE_5) binned against monthly sunspot number as a proxy for solar activity.

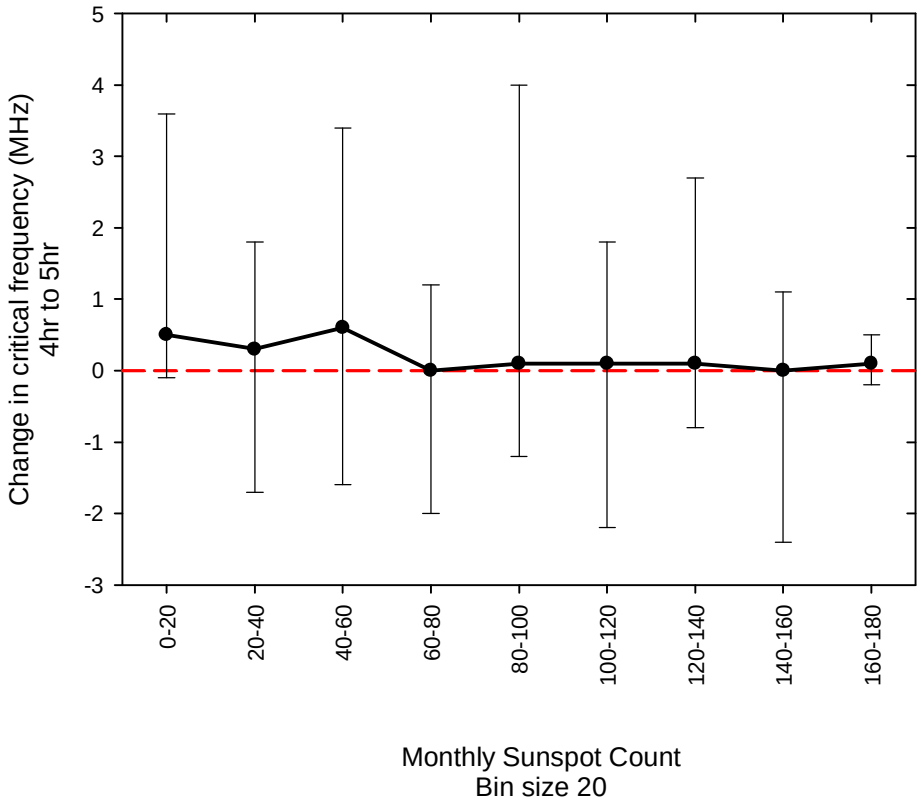

Figure 88. Line, scatter and range bar plot of the change between f_oE_4 and f_oE_5.

The following observations are made:

- In this hour a higher median value correlates with lower solar activity, when MSN< 60;
- At very high values of MSN (> 160) the variability is reduced

4.5.6 The Sixth Hour Following SSC (f_oE_5 to f_oE_6)

The line, scatter and range bar plot polar plot of figure 89 captures the change between f_oE measured on the fifth hour following the SSC (f_oE_5) and f_oE measured on the sixth hour following the SSC (f_oE_6) binned against monthly sunspot number as a proxy for solar activity.

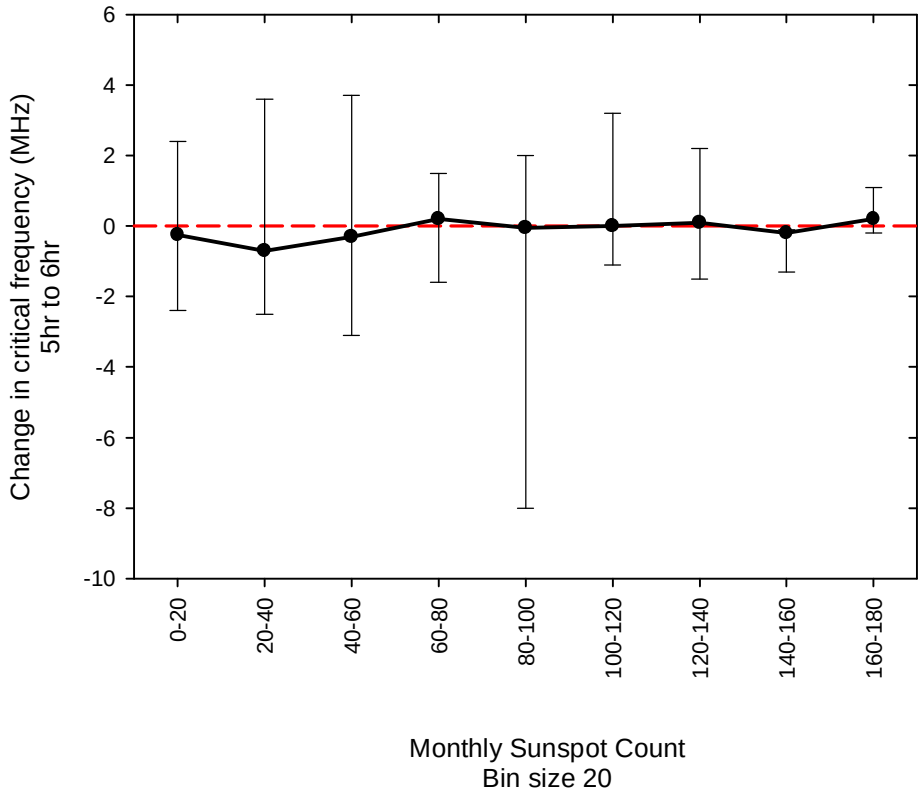

Figure 89. Line, scatter and range bar plot of the change between f_oE_5 and f_oE_6.

The following observations are made:

- In this hour a lower median value correlates with lower solar activity when MSN< 60;
- At very high values of MSN (> 140), the variability is reduced.

4.5.7 Overall – All Six Hours Combined

The line, scatter and range bar plot polar plot of figure 90 captures the change between f_oE measured across all six hours following the SSC.

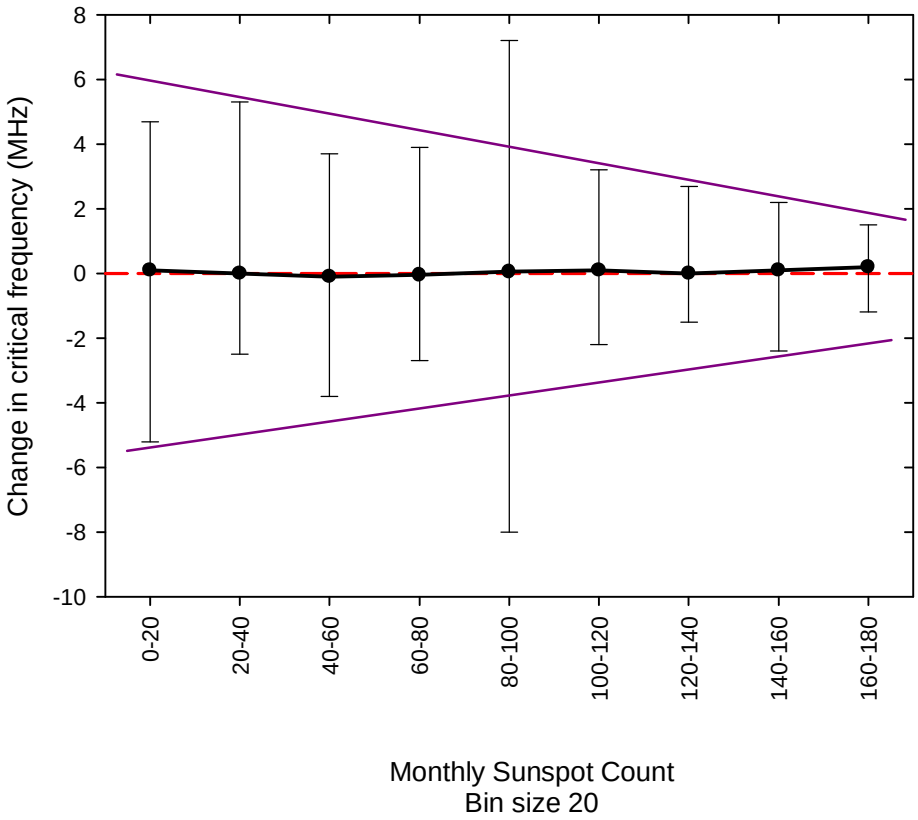

Figure 90. Line, scatter and range bar plot of all values combined.

The following observations are made:

- The median change of f_oE is very similar if all the values of f_oE_{m-n} across all 6hrs are combined;
- A decrease in the min and max values is now patently obvious and occurs earlier at MSN > 100.
- The measurement error stemming from visual interpretation is 0.05 MHz.

To zoom in on the median change of critical frequency, the graph in figure 91 was prepared. This graph is in essence the same as the graph above but with the range bars removed. While the highest change in f_oE does occur at high value of solar activity the change in critical frequency oscillates around zero. There is inconclusive evidence that solar activity affects the change in critical frequency.

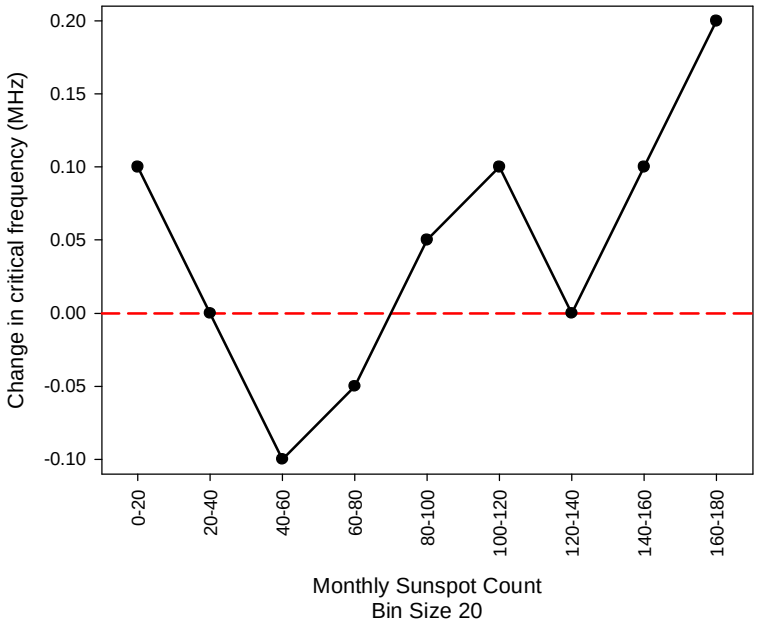

Figure 91. Zoom of line and scatter plot

4.5.8 Conclusion on Solar Activity Dependency

In the first two hours following the SSC during periods of low solar activity, there appears to be a higher median value of Δf_oE_s. The pattern repeats in the fifth hour but not in the third, fourth and sixth hours and not when considering Δf_oE_s measured across all six hours. It is concluded that the median value of Δf_oE_s has no clear solar dependency. This supports the assertion that particle precipitation is the dominant source of ionisation following the onset of a storm. Across all six hours there is a clear reduction in the variability of Δf_oE_s as solar activity increases. The reason for this reduction in variability is not clear.

4.6 Testing for Seasonal Dependency

This section tests for seasonal dependencies in the data by binning $\Delta f_o E_s$ against the month in which the SSC occurs.

4.6.1 The First Hour Following SSC (f_oE_0 to f_oE_1)

The line, scatter and range bar plot polar plot of figure 92 captures the change between f_oE measured on the hour immediately before the SSC (f_oE_0) and f_oE measured on the first hour following the SSC (f_oE_1) binned against the month in which the SSC occurred. The point joined by the solid line is the median value of all $\Delta f_oE_{0\text{-}1}$ values that fall in the month. The range bars show the minimum and maximum values for each bin. Minimum and maximum values are used in preference to the 25% and 75% quartiles in order to expose the magnitude of variability that can be expected.

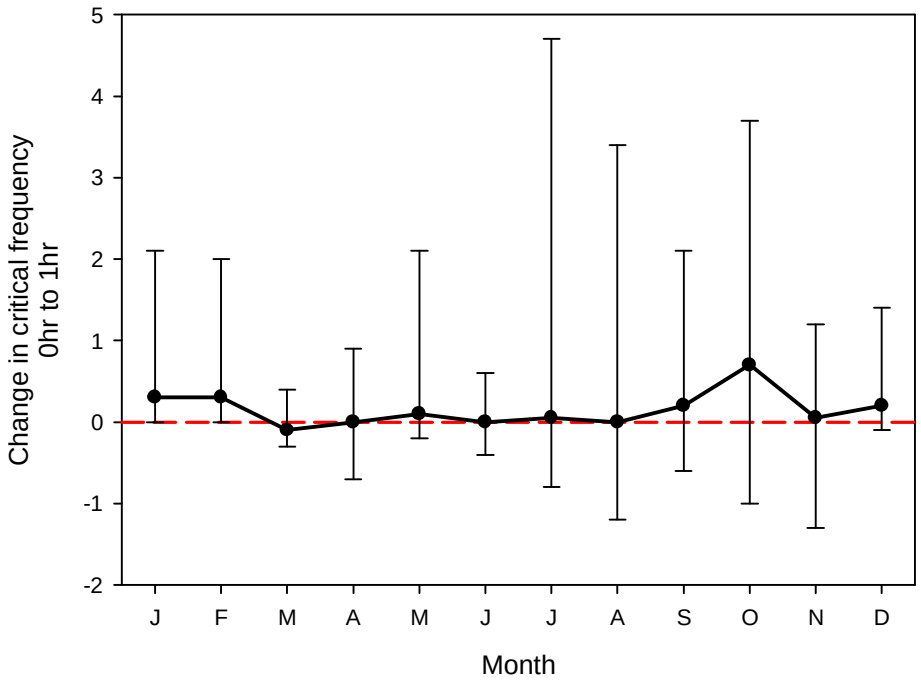

Figure 92. Line, scatter and range bar plot of the change between f_oE_0 and f_oE_1.

The following observations are made:

- Greater variability in summer and autumn months than in winter and spring months;
- Median value is elevated in winter months (October to February).

4.6.2 The Second Hour Following SSC (f_oE_1 to f_oE_2)

The line, scatter and range bar plot polar plot of figure 93 captures the change between f_oE measured on the first hour following the SSC (f_oE_1) and the f_oE measured on the second hour following the SSC occurring (f_oE_2) binned against the month in which the SSC occurred.

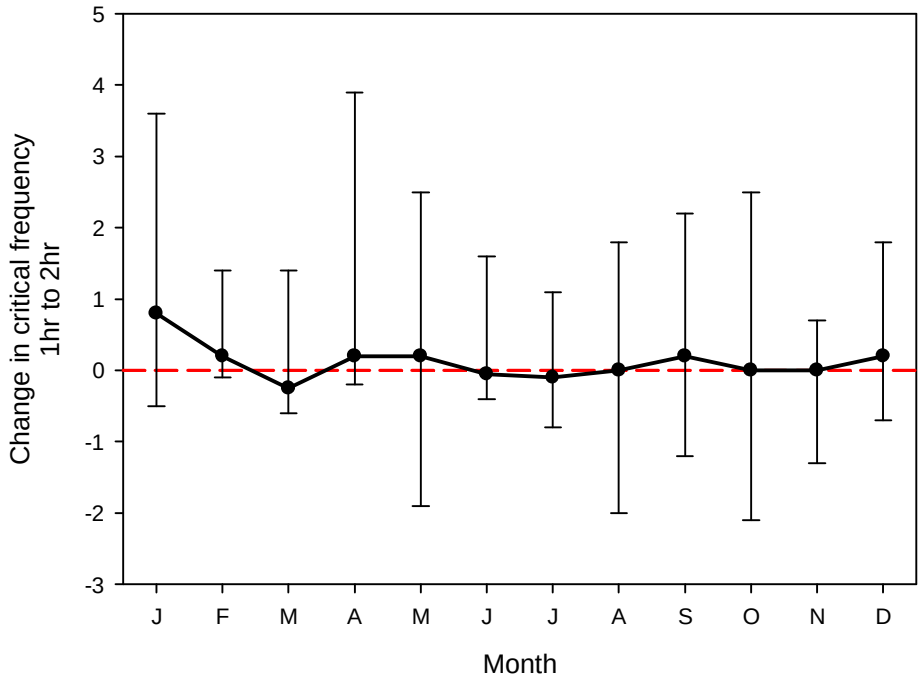

Figure 93. Line, scatter and range bar plot of the change between f_oE_1 and f_oE_2.

The following observations are made:

- No particular pattern in variability with fairly similar minimum and maximum values seen in both summer and winter months, except for a maximum in January.
- Slightly elevated median values in winter – not as pronounced as in the first hour.

4.6.3 The Third Hour Following SSC (f_oE_2 to f_oE_3)

The line, scatter and range bar plot polar plot of figure 94 captures the change between f_oE measured on the second hour following the SSC (f_oE_2) and the f_oE measured on the third hour following the SSC occurring (f_oE_3) binned against the month in which the SSC occurred.

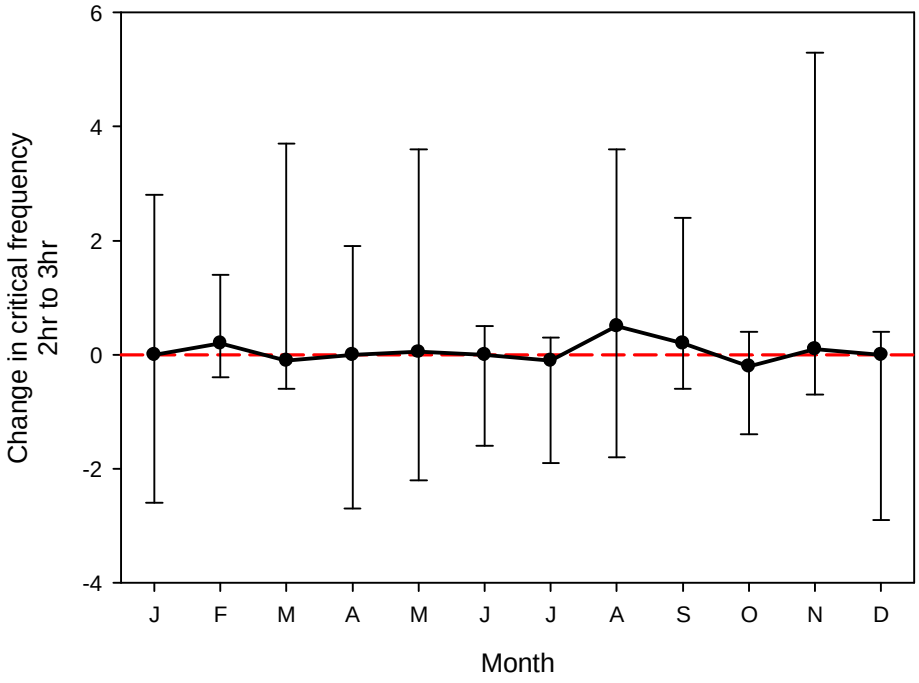

Figure 94. Line, scatter and range bar plot of the change between f_oE_2 and f_oE_3.

The following observations are made:

- No particular pattern in variability with similar minimum and maximum values seen in both summer and winter months;
- The median values show no particular pattern in any season.

4.6.4 The Fourth Hour Following SSC (f_oE_3 to f_oE_4)

The line, scatter and range bar plot polar plot of figure 95 captures the change between f_oE measured on the third hour following the SSC (f_oE_3) and the f_oE measured on the fourth hour following the SSC occurring (f_oE_4) binned against the month in which the SSC occurred.

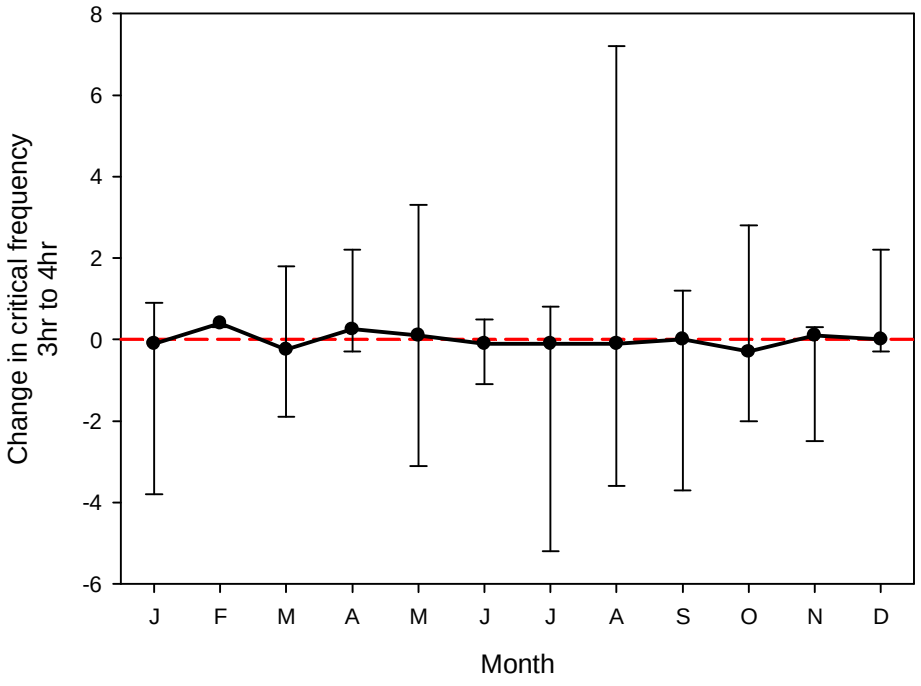

Figure 95. Line, scatter and range bar plot of the change between f_oE_3 and f_oE_4.

The following observations are made:

- No particular pattern in variability with similar minimum and maximum values seen in both summer and winter months;

§ The median values show no particular pattern in any season.

4.6.5 The Fifth Hour Following SSC (f_oE_4 to f_oE_5)

The line, scatter and range bar plot polar plot of figure 96 captures the change between f_oE measured on the fourth hour following the SSC (f_oE_4) and the f_oE measured on the fifth hour following the SSC occurring (f_oE_5) binned against the month in which the SSC occurred.

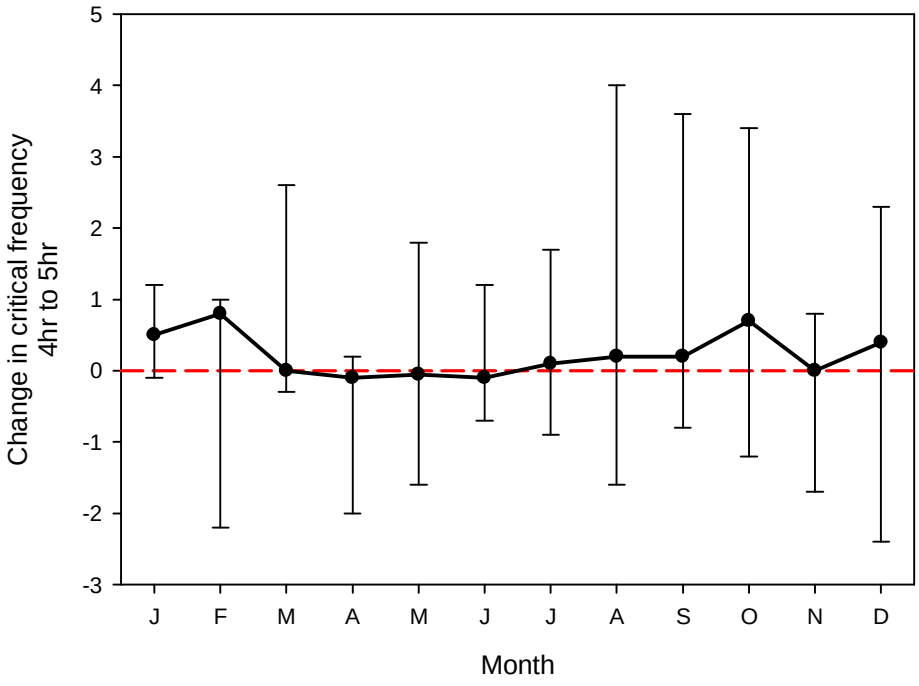

Figure 96. Line, scatter and range bar plot of the change between f_oE_4 and f_oE_5.

The following observations are made:

§ No particular pattern in variability with similar minimum and maximum values seen in both summer and winter months;

§ The median values is elevated in most winter months (October to February).

4.6.6 The Sixth Hour Following SSC (f_oE_5 to f_oE_6)

The line, scatter and range bar plot polar plot of figure 97 captures the change between f_oE measured on the fifth hour following the SSC (f_oE_5) and the f_oE measured on the sixth hour following the SSC occurring (f_oE_6) binned against the month in which the SSC occurred.

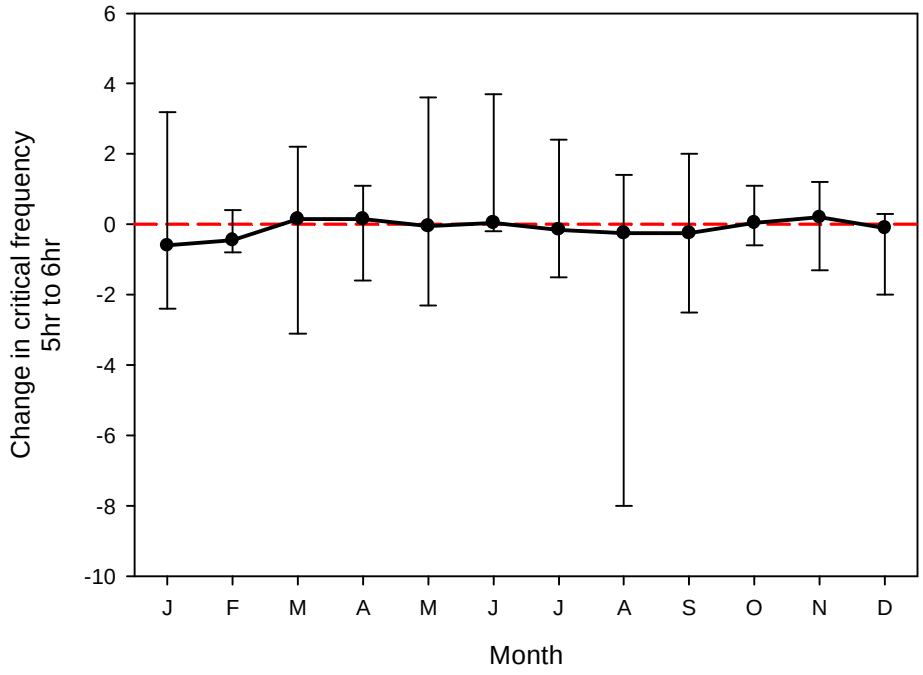

Figure 97. Line, scatter and range bar plot of the change between f_oE_5 and f_oE_6.

The following observations are made:

- No particular pattern in variability with similar minimum and maximum values seen in both summer and winter months, except for august which has a very large negative variability;
- The is no pattern in the median values other than a sight decrease in the winter months.

4.6.7 Overall – All Six Hours Combined

The line, scatter and range bar plot polar plot of figure 98 captures the change between f_oE measured across all six hours following the SSC binned against the month in which the SSC occurred.

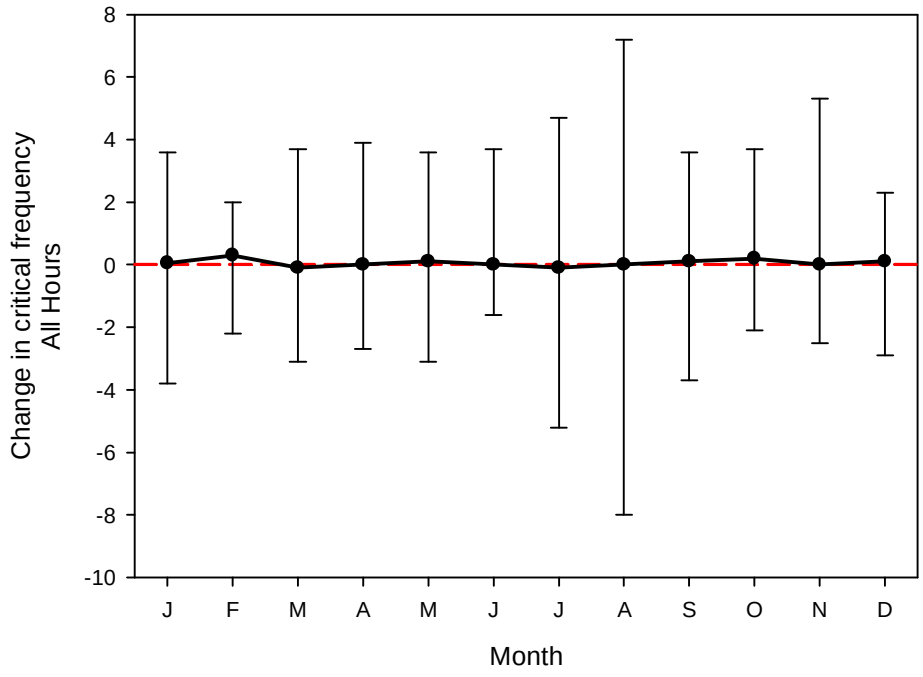

Figure 98. Line, scatter and range bar plot of all values combined.

The graph in figure 99 below shows the seasonal dependency of the median Δf_oE_s. There are generally higher values of median values in the winter months than in the summer months.

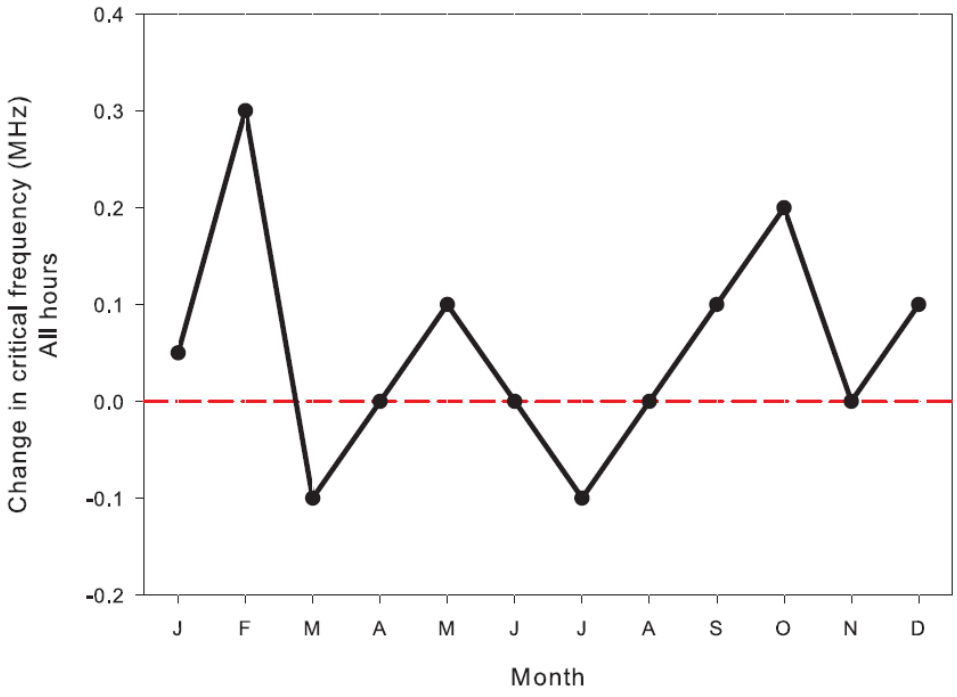

Figure 99. Zoom of line and scatter plot

The following observations are made:

- There appears to be a general increase in the median value of $\Delta f_o E_s$ in winter months;
- No particular pattern in variability with a fairly comparable variability across all seasons, except August which has a very large positive and negative variability.

4.6.8 Conclusion on Seasonal Dependency

While during the first hour following an SSC there is a greater variability of $\Delta f_o E_s$ in summer and autumn than in winter and spring, overall the variability of $\Delta f_o E_s$ does not appear to have any seasonal dependency.

In the first, second and fifth hour the median value is elevated but this is not the case in the third, fourth and fifth hour and even a decrease occurs in the sixth hour. Overall there appears to be a propensity for higher median values of Δf_oE_s in the winter months.

4.7 The Variability of Particle Sporadic-E

This section examines, in some detail, the variability of E_s in the six hours following an SSC. Particular attention is given to the occurrence of blanketing.

4.7.1 The First Hour Following SSC (f_oE_0 to f_oE_1)

The polar plot in figure 100 captures the difference between f_oE measured on the hour preceding the SSC (f_oE_0) and the f_oE measured on the hour immediately following the SSC occurring. The radial is Δf_oE and the clock hours indicate local time. The red dots indicate where full blanketing of the F layers occurred. Table 19 captures the statistics of the polar plot sector by sector.

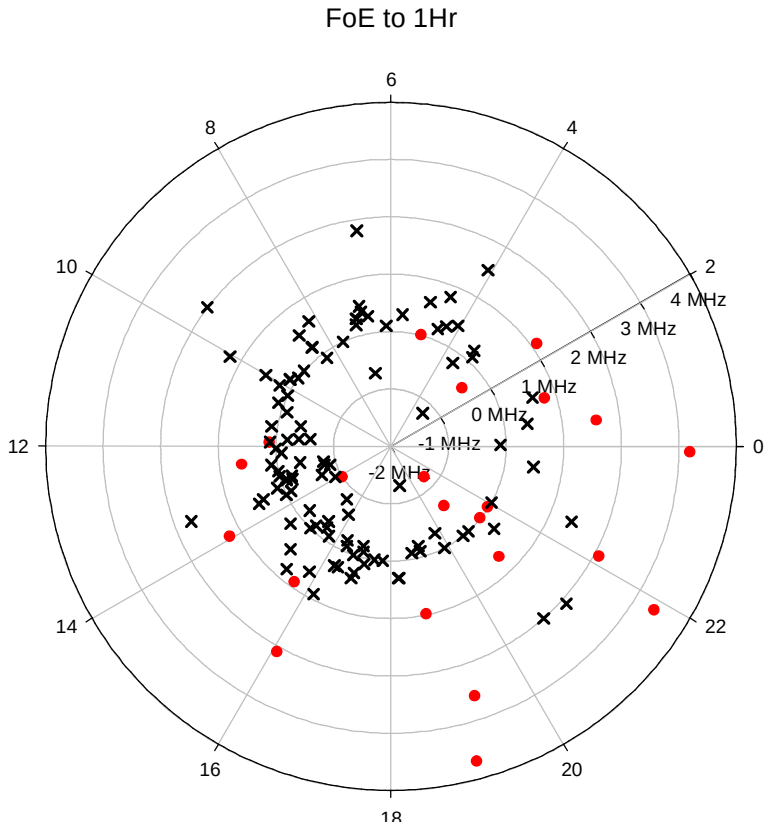

Figure 100. Polar Diagram of the difference between E_s measured on the hour before the SSC occurs (FoE_0) and on the hour following the SSC (FoE_1). The red dots indicate where full blanketing has occurred.

Sector	No. events	Blanketing	Min. Change	Max. Change	Mean Change	Median Change	Std. Dev.	25% Quart	75% Quart
		%	*MHz*	*MHz*	*MHz*	*MHz*	*MHz*	*MHz*	*MHz*
A	19	26	-1.2	1.6	0.37	0.3	0.65	0.05	0.7
B	33	3	-0.7	2	0.22	0.1	0.56	0	0.3
C	51	10	-1	2.1	0.1	0	0.61	-0.2	0.3
D	28	43	-1.3	4.7	0.9	0.3	1.53	-0.03	2.03

Table 19. Statistics capturing the change in E_s from the hour before the SSC (foE_0) to the first hour after the SSC occurs (foE_1).

Figure 101 illustrates the statistics given in table 19 and shows the high variability that occurs in sector D. The vertical bars encompass the 25% and 75% quartiles, the diamond symbol indicates mean values and the circle symbol indicates median values. All of this type of graph presented in this report use the same identical axis scaling so that visual comparisons can be made.

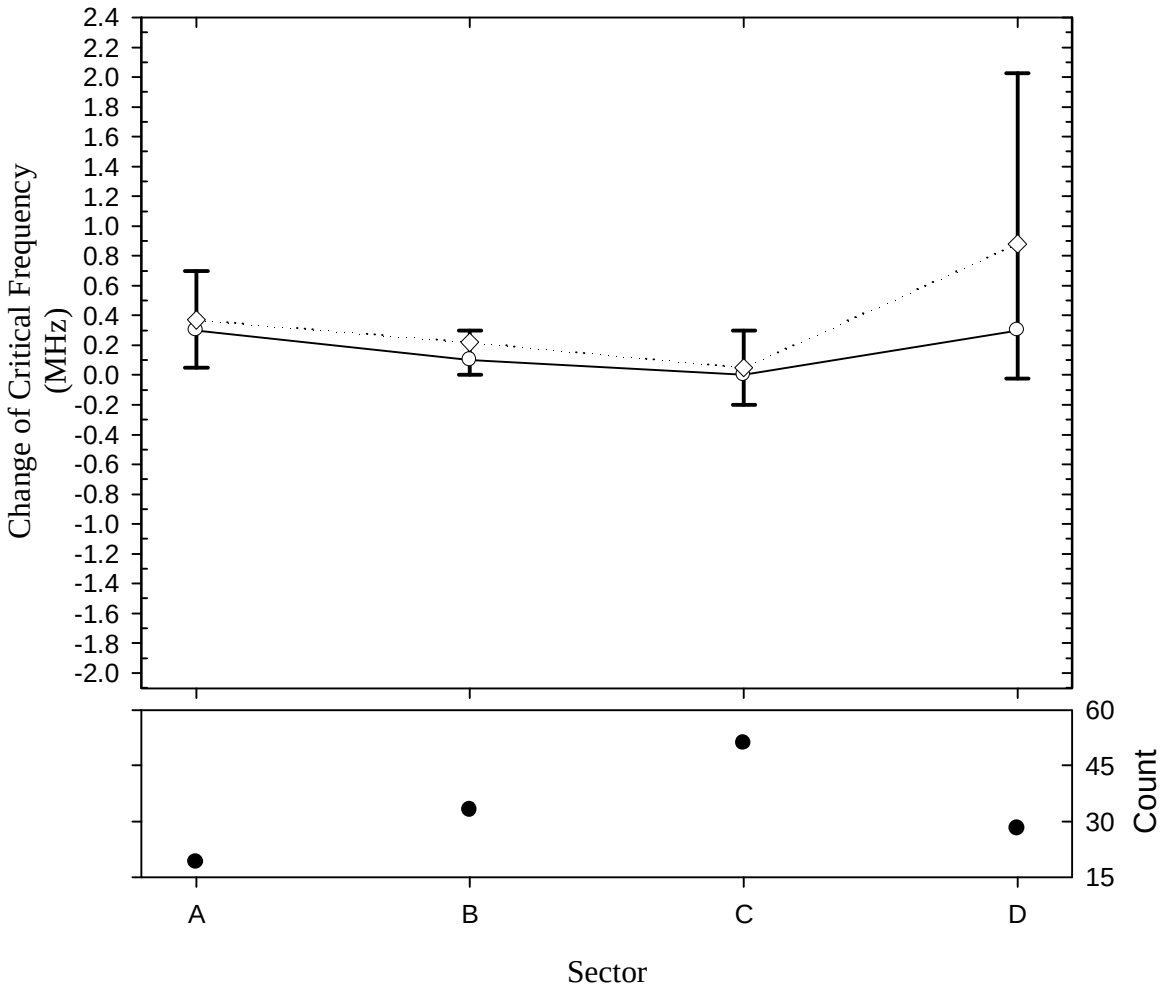

Figure 101. Line, scatter and range bar plot of mean (diamond) and median (circles) values of $\Delta foE_{0\text{-}1}$ per sector, the 25% and 75% percentiles between vertical range bars and the count of events in the lower panel. A familiar pattern will be seen of highest variability occurring in sector D, followed by sector A, then sector C and minimum variability in sector B.

The statistics show considerable variation, as is expected when working with the ionosphere in general and which is amplified when dealing with the high-latitude ionosphere. Of significance is:

- $\Delta f_o E_{0-1}$ can be positive and negative, this depends on whether or not storm induced precipitation has commenced in this hour.
- Full blanketing can occur even when $\Delta f_o E_{0-1}$ is negative (4 examples shown in figure 100). This implies that the F-layer ionisation has dramatically reduced so even though the E-layer is penetrated, no F-layer reflecting plane exists.
- Full blanketing can occur when $\Delta f_o E_{0-1}$is zero (4 examples in figure 100) implying a F-layer disappearance or particle precipitation maintaining what would otherwise be a decrease in critical frequency.
- Blanketing is guaranteed in the first hour following SSC when $\Delta f_o E_{0-1}$exceeds 2.1 MHz. (6 examples in figure 100).
- Blanketing occurs in all sectors $\Delta f_o E_{0-1}$except between 6 – 12 MLT (Sector B) where only one out of 33 events over a six year period caused blanketing in the first hour.

The results in figure 100 justifies the individual treatment of each sector. The highest $\Delta f_o E_{0-1}$ values occur in sector D (18-24MLT). This will become a familiar pattern as we move through the six hours following the onset of disturbance. This is not surprising as sector D is when the field lines are open to direct particle injection, directly opposite to sector B (9-12 MLT). Sector A and Sector C have similar

statistics and variance reflecting their intermediate postion between sector D and sector B.

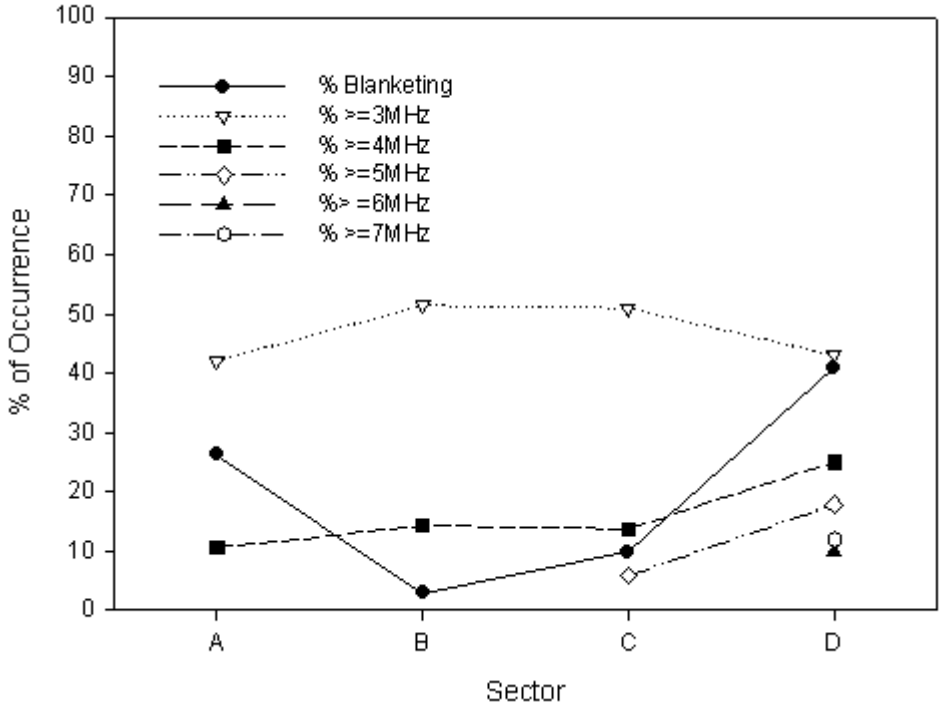

Figure 102. Percentage occurrence of incrementing levels of critical frequency and the percentage occurrence of blanketing that occurs. Occurrence

Figure 102 shows the occurrence of certain thresholds of critical frequency that occur in each sector as well as the occurrence of blanketing. A familiar pattern will be seen of higher values in sector A and D, very low values in sector B and an intermediate value in sector C.

4.7.2 The Second Hour Following SSC (foE1 to foE2)

The polar plot in figure 103 captures the difference between f_oE measured on the first hour following the SSC (f_oE_1) and the f_oE measured on the second hour following the

SSC occurring (f_oE_2). The red dots indicate where full blanketing of the F layers occurred. Table 20 captures the statistics of the polar plot sector by sector.

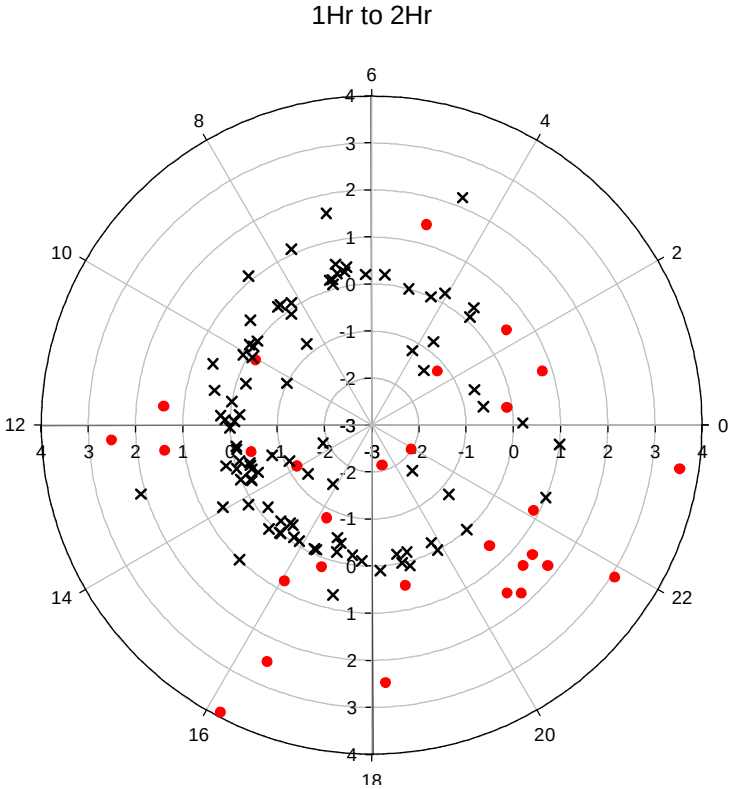

Figure 103. Polar Diagram of the difference between E_s measured on the hour following the SSC occurrence (foE_1) and on the second hour following the SSC (foE_2). The red dots indicate where full blanketing has occurred.

Sector	No. events	Blanketing	Min. Change	Max. Change	Mean Change	Median Change	Std. Dev.	25% Quart	75% Quart
		%	*MHz*	*MHz*	*MHz*	*MHz*	*MHz*	*MHz*	*MHz*
A	18	27.8	-1.4	2.2	-0.01	0.05	0.92	-0.68	0.28
B	33	6	-1	1.6	0.22	0.2	0.52	0	0.4
C	48	19	-1.9	3.9	0.05	-0.1	1.03	-0.3	0.1
D	25	60	-2.1	3.6	0.57	0.5	1.43	-0.2	1.4

Table 20. Statistics capturing the change in E_s from the first hour after the SSC (foE_1) to the second hour after the SSC (foE_2) occurs.

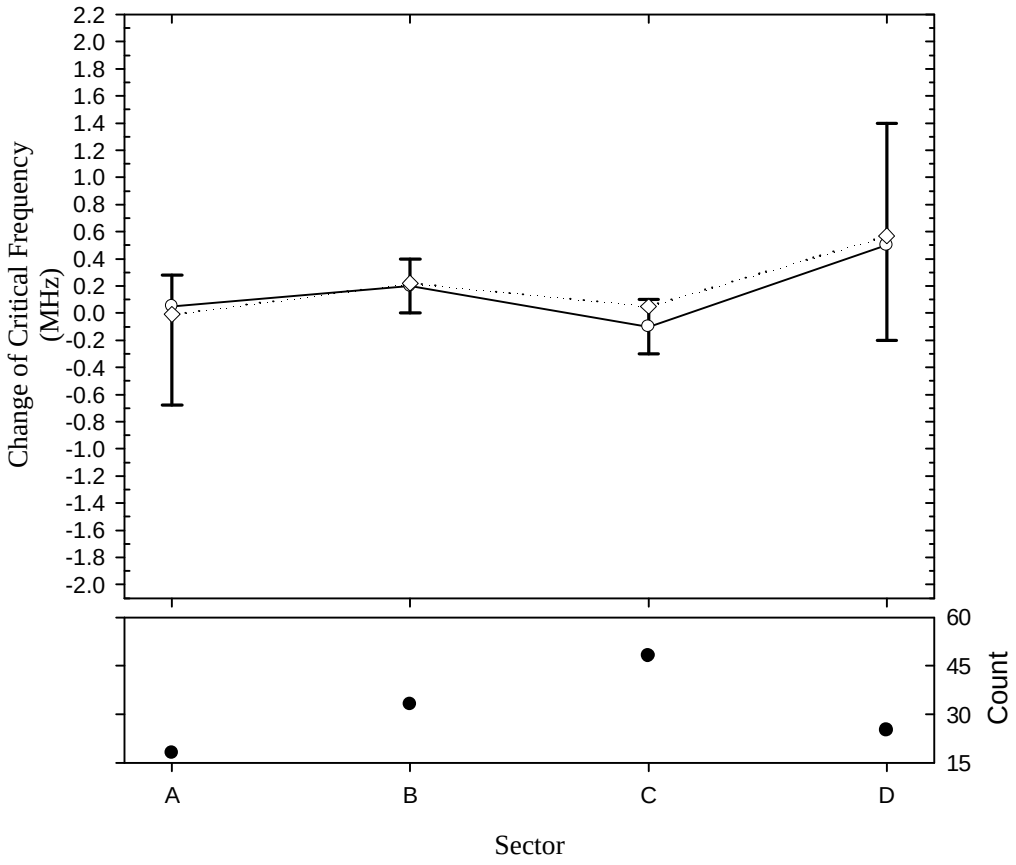

Figure 104. Line, scatter and range bar plot of mean (diamond) and median (circles) values of $\Delta foE_{1\text{-}2}$ per sector, the 25% and 75% percentiles between vertical range bars and the count of events in the lower panel.

Of significance in this hour is:

- The percentage blanketing in each sector is comparable to those occurring in the previous hour;

- Blanketing occurs extensively when $\Delta f_o E_{1\text{-}2}$ exceeds 1 MHz and exclusively when $\Delta f_o E_{1\text{-}2}$ exceeds 2.1 MHz. This last value is identical to the previous hour;
- Once again limited blanketing occurs in sector B and reaches a maximum (60% of events) in sector D;
- There is a slightly greater variability in Sector A and similar variations in the three other sectors.

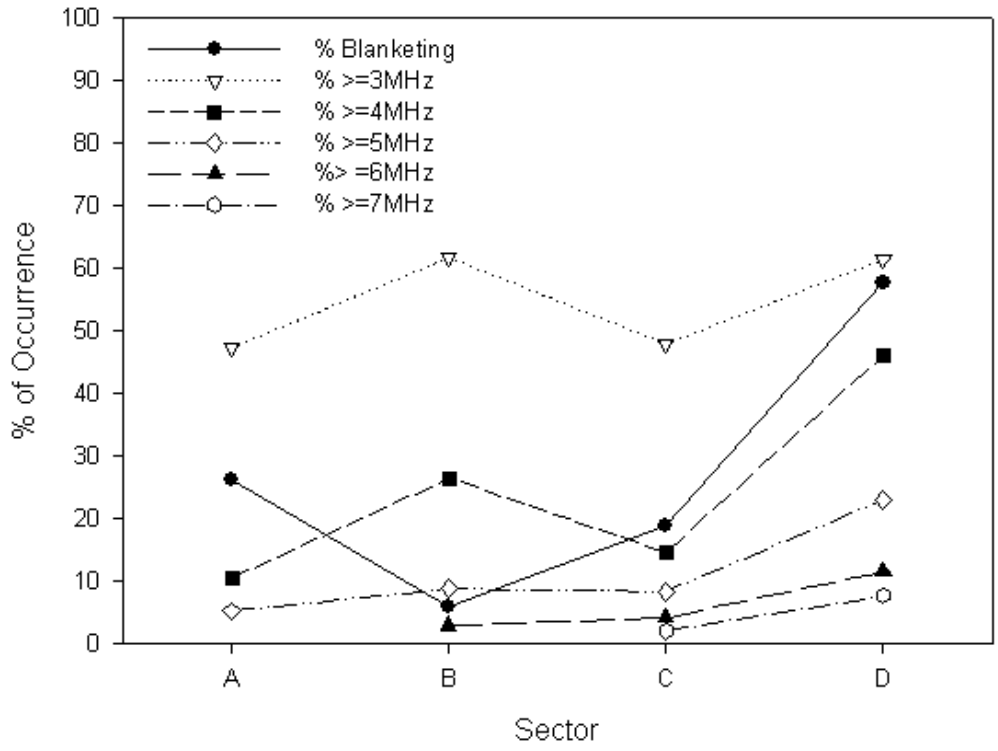

Figure 105. Percentage occurrence of incrementing levels of critical frequency and the percentage occurrence of blanketing that occurs.

There is a similar occurrence of blanketing across all sectors and a familiar pattern of increase and decrease across the four sectors continues. In this hour the rise of the critical frequencies thresholds of 5, 6 & 7 MHz occurs in earlier sectors but maintains similar levels in sector D.

4.7.3 The Third Hour Following SSC (f_oE_2 to f_oE_3)

The polar plot in figure 106 captures the difference between foE measured on the second hour following the SSC (foE_2) and the foE measured on the third hour following the SSC occurring (foE_3). The red dots indicate where full blanketing of the F layers occurred. Table 21 captures the statistics of the polar plot sector by sector.

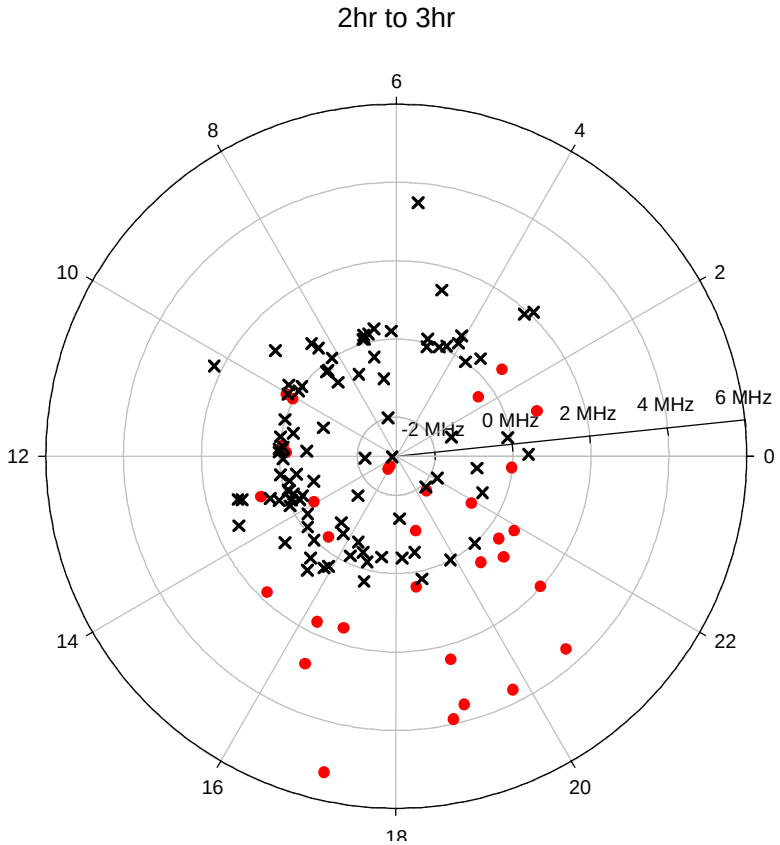

Figure 106. Polar Diagram of the difference between E_s measured on the second hour following the SSC occurrence (foE_2) and on the third hour following the SSC (foE_3). The red dots indicate where full blanketing has occurred.

Sector	No. events	Blanketing	Min. Change	Max. Change	Mean Change	Median Change	Std. Dev.	25% Quart	75% Quart
		%	*MHz*	*MHz*	*MHz*	*MHz*	*MHz*	*MHz*	*MHz*
A	18	22	-1.5	3.5	0.54	0.3	1.11	0	0.73
B	34	12	-2	2.2	-0.04	0	0.67	-0.2	0.2
C	46	24	-2.9	5.3	0.03	-0.1	1.37	-0.4	0.4
D	25	60	-1.9	3.9	0.44	0	1.78	-0.7	0.8

Table 21. Statistics capturing the change in E_s from the second hour after the SSC (foE_2) to the third hour after the SSC occurs (foE_3).

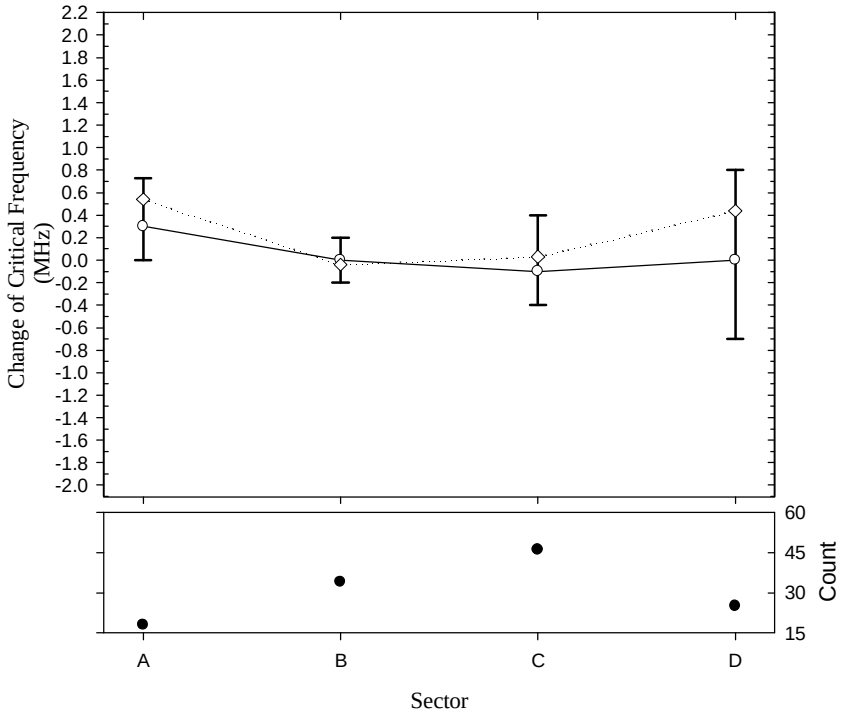

Figure 107. Line, scatter and range bar plot of mean (diamond) and median (circles) values of $\Delta foE_{2\text{-}3}$ per sector, the 25% and 75% percentiles between vertical range bars and the count of events in the lower panel.

Of significance in this hour is:

- § $\Delta f_o E_{2\text{-}3}$ at 2.1 MHz continues to be a milestone indicator that guarantees blanketing will occur, with only one exception;
- § The extensive occurrence of blanketing greatly increases above $\Delta f_o E_{2\text{-}3}$ = 0.5 MHz which is significantly less than in previous hours. This is probably an indication of F-layer ionisation reduction and the lack of an F-layer reflecting plane even if the E-layer is penetrated;
- § A higher number blanketing events starts to occur in sector B in this hour;
- § There is a similar level of variability as seen in the two previous hours.

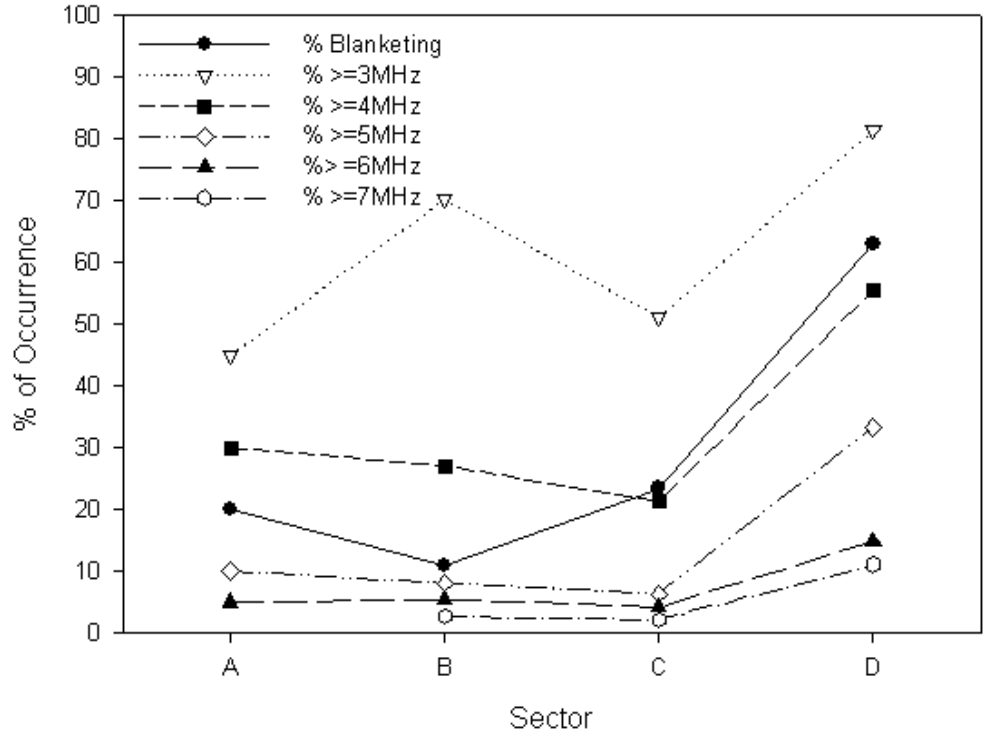

Figure 108. Percentage occurrence of incrementing levels of critical frequency and the percentage occurrence of blanketing that occurs.

Once again the occurrence of blanketing follows the same pattern across sectors although exceeding 60% for example, in sector D. The occurrence of critical

frequencies greater than 5, 6 and 7 MHz now occurs in all sectors. Critical frequencies are generally higher in this third hour following the SSC.

4.7.4 The Fourth Hour Following SSC (f_oE_3 to f_oE_4)

The polar plot in figure 109 captures the difference between foE measured on the third hour following the SSC (foE_3) and the foE measured on the fourth hour following the SSC occurring (foE_4). The red dots indicate where full blanketing of the F layers occurred. Table 22 captures the statistics of the polar plot sector by sector.

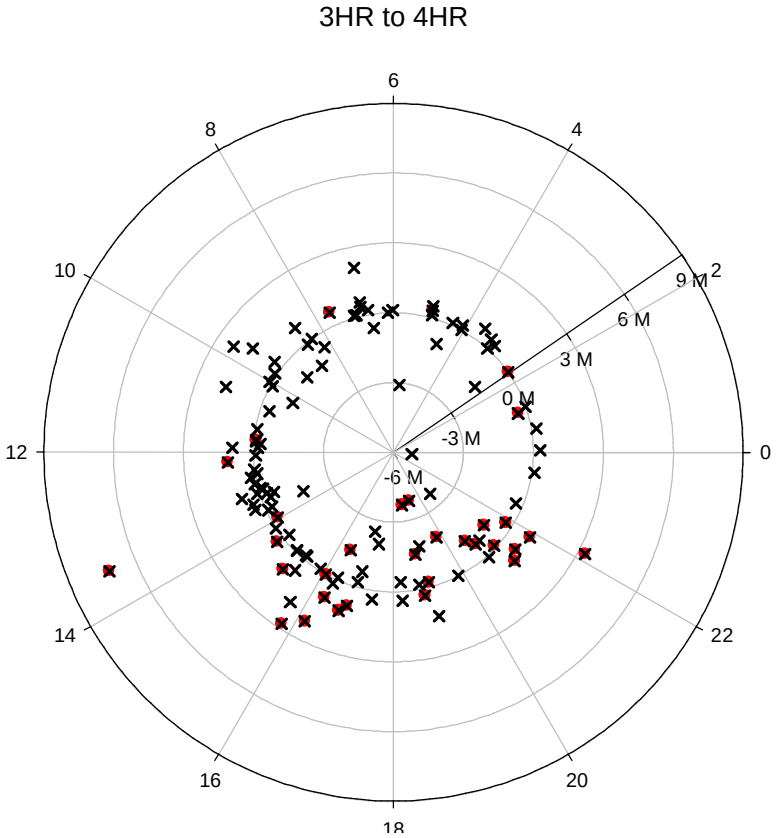

Figure 109. Polar Diagram of the difference between E_s measured on the third hour following the SSC occurrence (foE_3) and on the fourth hour following the SSC (foE_4). The red dots indicate where full blanketing has occurred.

Sector	No. events	Blanketing	Min. Change	Max. Change	Mean Change	Median Change	Std. Dev.	25% Quart	75% Quart
		%	*MHz*	*MHz*	*MHz*	*MHz*	*MHz*	*MHz*	*MHz*
A	18	17	-3.1	0.6	-0.17	0.1	0.9	0	0.3
B	32	6	-1.2	2.2	0.18	0.1	0.82	-.13	0.45
C	45	29	-2.5	7.2	0.23	-0.1	1.42	-0.2	0.4
D	27	56	-5.2	3.3	-0.68	-0.3	1.79	-1.3	0.2

Table 22. Statistics capturing the change in E_s from the third hour after the SSC (foE_3)

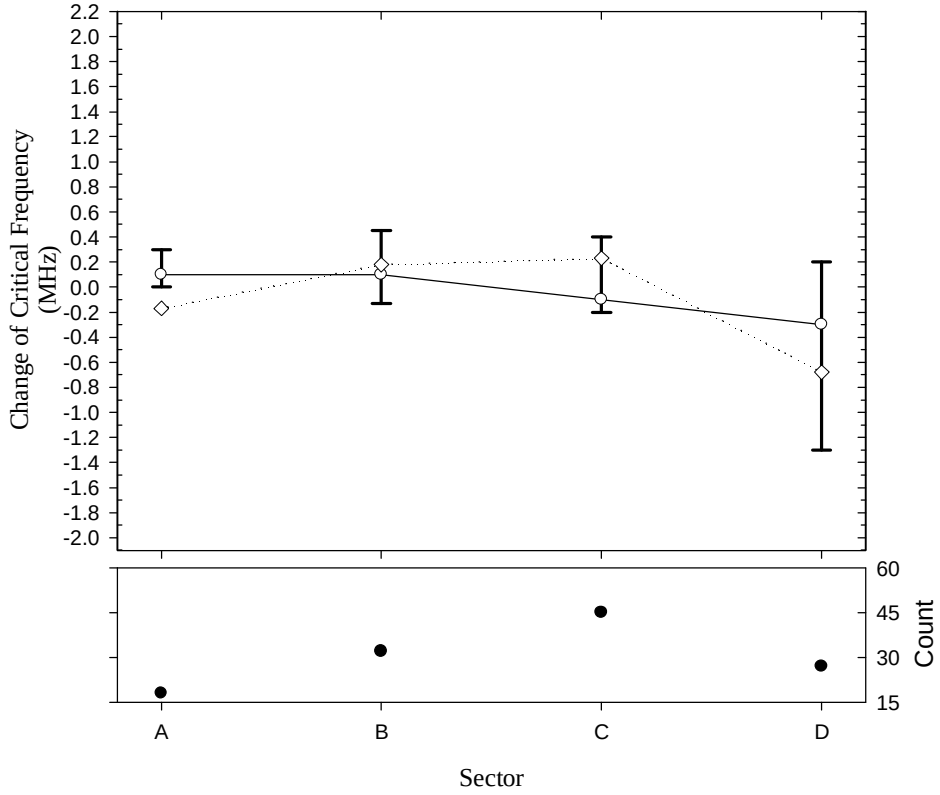

to the fourth hour after the SSC occurs (foE_4).

Figure 110. Line, scatter and range bar plot of mean (diamond) and median (circles) values of $\Delta foE_{3\text{-}4}$ per sector, the 25% and 75% percentiles between vertical range bars and the count of events in the lower panel.

Of significance in this hour is:

- § Δf_oE_{3-4} at 3 MHz is now a new milestone indicator that guarantees blanketing will occur;
- § The extensive occurrence of blanketing at negative values of Δf_oE_{3-4} indicates that F-layer ionisation has dramatically reduced and that there is no F-layer reflecting plane even if the E-layer is penetrated;
- § Blanketing events now occur with Δf_oE_{3-4} as low as -4 MHz;
- § In sector A the location of the calculated average (diamond symbol) reflects the large outlier (minimum change of -3.1 MHz) that skews the distribution.

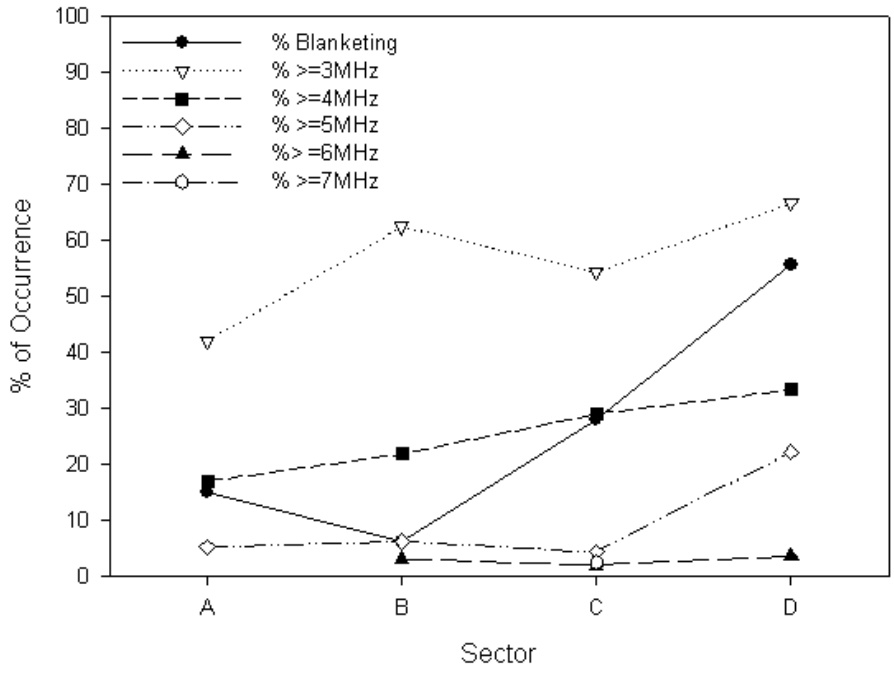

Figure 111. Percentage occurrence of incrementing levels of critical frequency and the percentage occurrence of blanketing that occurs.

A very familiar pattern is seen in figure 111. The percentage occurrence of blanketing starts at a low value in sector A, drops in sector B and then increases through sector C to a maximum in sector D. Again there is a general increase of all critical frequency thresholds in sector D.

4.7.5 The Fifth Hour Following SSC (f_oE_4 to f_oE_5)

The polar plot in figure 112 captures the difference between foE measured on the fourth hour following the SSC (foE_4) and the foE measured on the fifth hour following the SSC occurring (foE_5). The red dots indicate where full blanketing of the F layers occurred. Table 23 captures the statistics of the polar plot sector by sector.

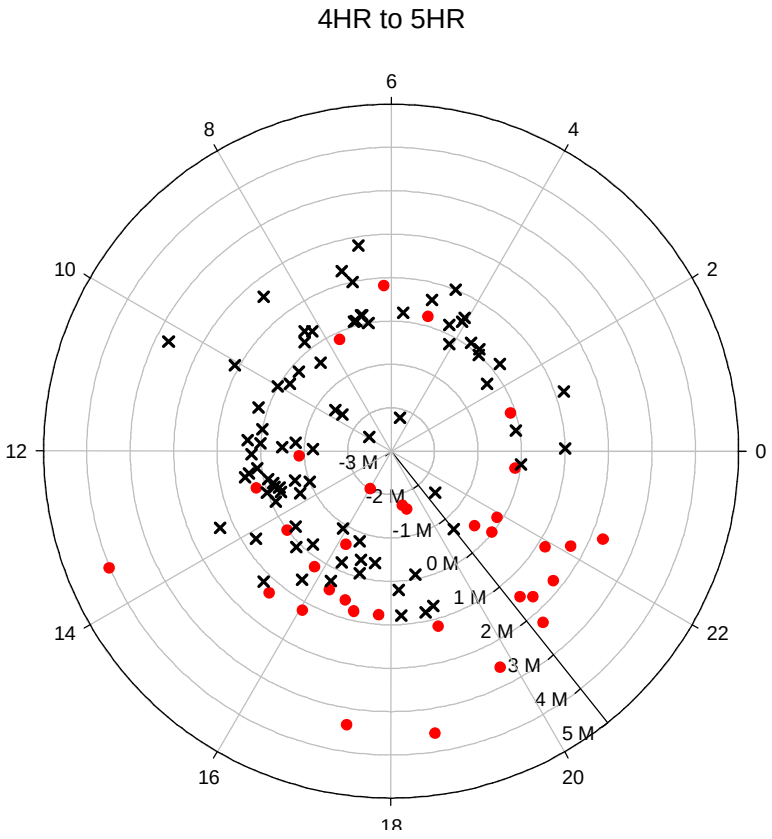

Figure 112. Polar Diagram of the difference between E_s measured on the fourth hour following the SSC occurrence (foE_4) and on the fifth hour following the SSC (foE_5). The red dots indicate where full blanketing has occurred.

Sector	No. events	Blanketing	Min. Change	Max. Change	Mean Change	Median Change	Std. Dev.	25% Quart	75% Quart
		%	*MHz*	*MHz*	*MHz*	*MHz*	*MHz*	*MHz*	*MHz*
A	18	11	-2.2	1.2	0.16	0.2	0.73	-0.08	0.48
B	30	7	-2.4	2.7	0.11	0.1	1.03	-0.2	0.38
C	43	35	-2	4	0.19	0	1.05	-0.3	0.58
D	24	67	-1.7	3.6	0.67	0.75	1.39	-0.1	1.7

Table 23. Statistics capturing the change in E_s from the fourth hour after the SSC (foE_4) to the fifth hour after the SSC occurs (foE_5).

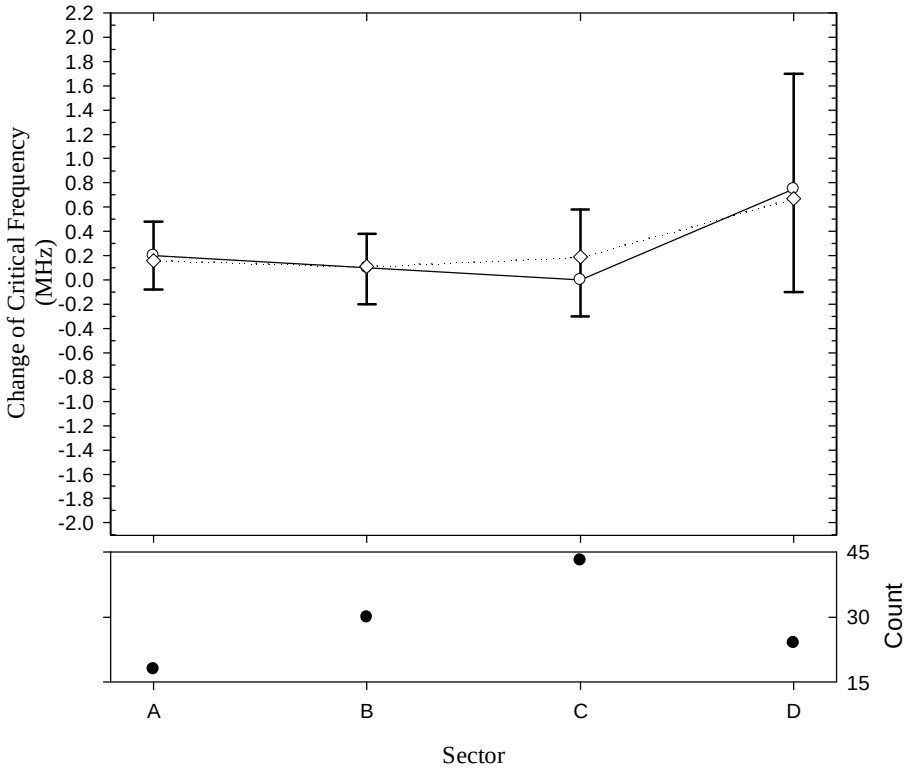

Figure 113. Line, scatter and range bar plot of mean (diamond) and median (circles) values of $\Delta foE_{4\text{-}5}$ per sector, the 25% and 75% percentiles between vertical range bars and the count of events in the lower panel.

Of significance in this hour is:

- Extensive blanketing occurs now occurs above ΔfoE_{3-4} of 1..5 MHz;
- ΔfoE_{3-4} of 2.1 MHz again provides a good threshold with exclusive blanketing in sectors C and D above this level;
- There are two occurrences of blanketing in sector B;
- We see very large values of ΔfoE_{4-5} (approaching 4 MHz);
- There is similar variability in all sectors.

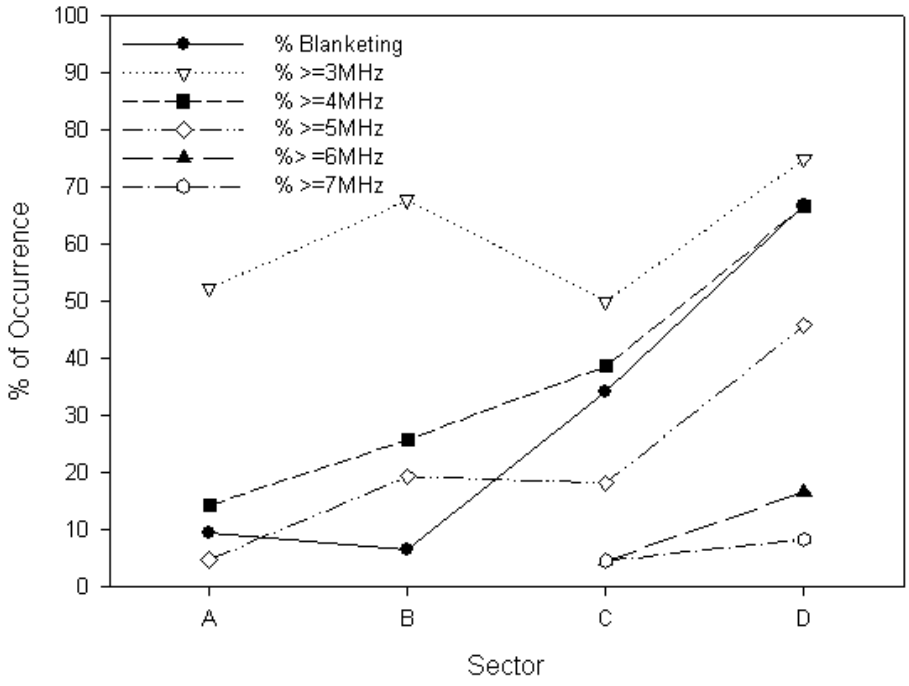

Figure 114. Percentage occurrence of incrementing levels of critical frequency and the percentage occurrence of blanketing that occurs.

Figure 114 shows an almost identical pattern to all previous graphs.

4.7.6 The Sixth Hour Following SSC (f_oE_5 to f_oE_6)

The polar plot in figure 115 captures the difference between foE measured on the fifth hour following the SSC (foE_5) and the foE measured on the sixth hour following the

SSC occurring (foE_6). The red dots indicate where full blanketing of the F layers occurred. Table 24 captures the statistics of the polar plot sector by sector.

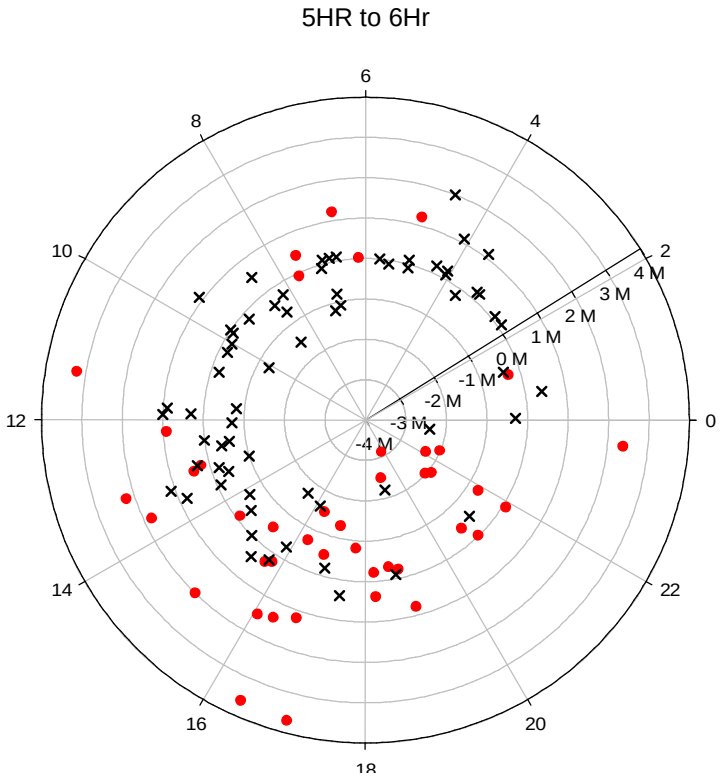

Figure 115. Polar Diagram of the difference between E_s measured on the fifth hour following the SSC occurrence (foE_5) and on the sixth hour following the SSC (foE_6). The red dots indicate where full blanketing has occurred.

Sector	No. events	Blanketing	Min. Change	Max. Change	Mean Change	Median Change	Std. Dev.	25% Quart	75% Quart
		%	*MHz*	*MHz*	*MHz*	*MHz*	*MHz*	*MHz*	*MHz*
A	20	10	-0.4	2	0.28	0.1	0.61	-0.1	0.25
B	29	21	-1.5	3.2	-0.01	-0.1	0.93	-0.4	0.3
C	42	50	-8	3.7	0.02	-0.05	1.75	-0.58	0.7
D	20	85	-3.1	2.4	-0.86	-0.45	1.38	-2.1	-0.08

Table 24. Statistics capturing the change in E_s from the fifth hour after the SSC (foE_5) to the sixth hour after the SSC occurs (foE_6).

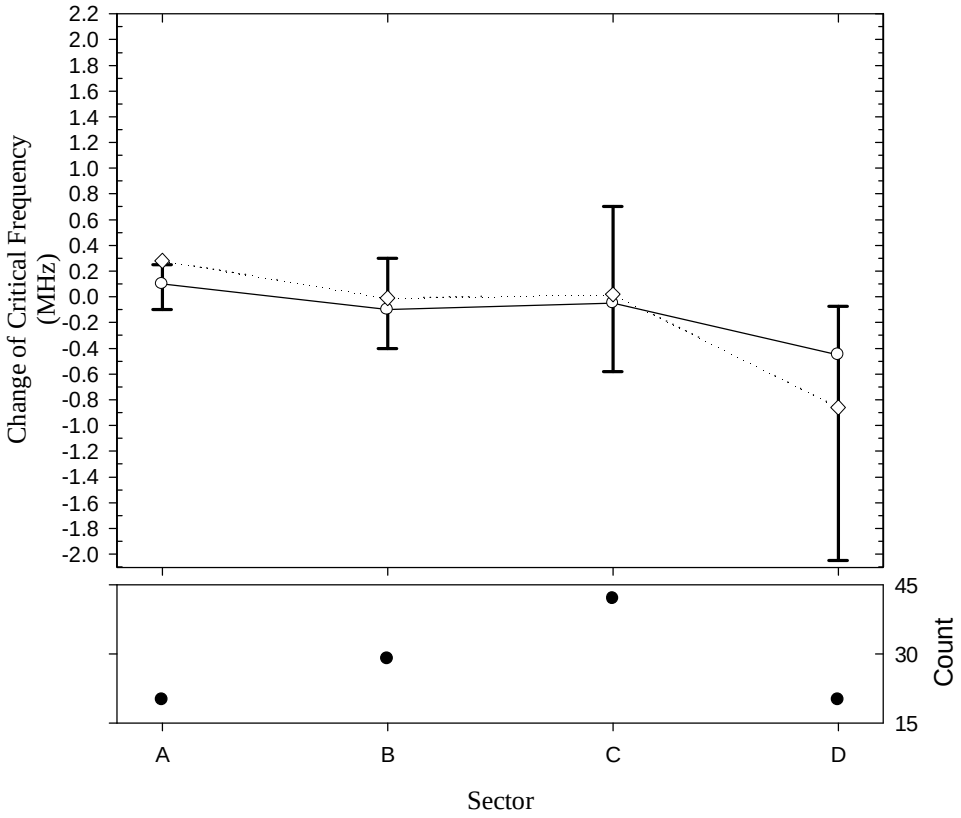

Figure 116. Line, scatter and range bar plot of mean (diamond) and median (circles) values of $\Delta foE_{5\text{-}6}$ per sector, the 25% and 75% percentiles between vertical range bars and the count of events in the lower panel.

Of significance in this hour is:

- Extensive blanketing occurs when $\Delta foE_{5\text{-}6}$ exceeds 0.5 MHz;
- There is still limited blanketing occurring in sector B;
- There are larger minimum and maximum values of change in most sectors;
- There are large negative values of $\Delta foE_{5\text{-}6}$ in sector D although 85% of these still blanket.

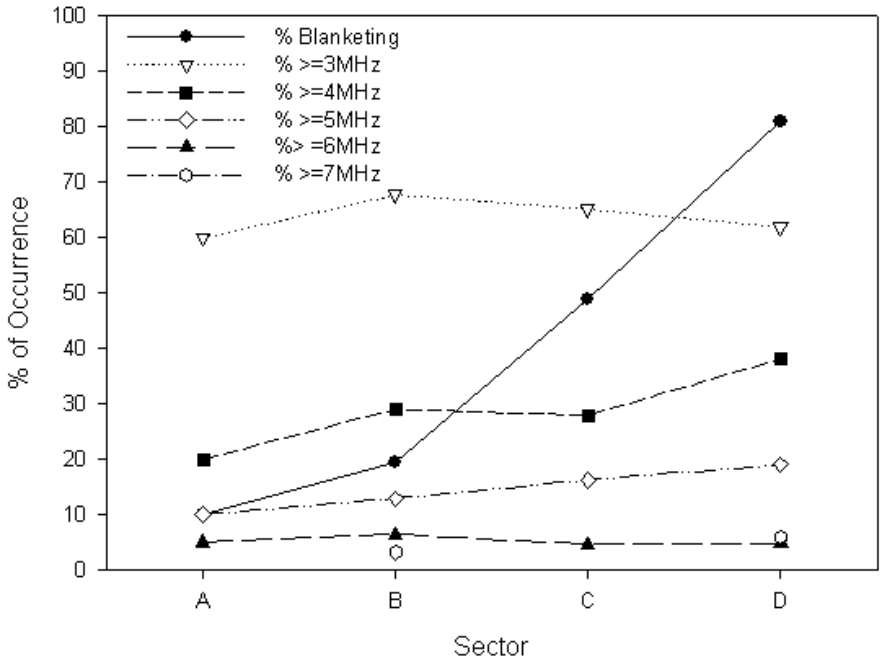

Figure 117. Percentage occurrence of incrementing levels of critical frequency and the percentage occurrence of blanketing that occurs.

In figure 117 the pattern has changed slightly in that there is no decrease during Sector B in this hour. The critical frequency thresholds of 5 and 6 MHz now occur in all sectors.

4.7.7 Conclusions on the Variability of Sporadic-E

A table of all the results in this subsection are collected together following the summary of this chapter (table 25) for readers who prefer table of values as opposed to graphical representations. The histogram in figure 118 captures the number of data points reflecting $\Delta foE_{m\text{-}n}$ against the hour (in MLT) in which the SSC occurred. Overall, each bar shows the number of data points that occur in each hour. The lower division of the bar (unshaded portion) shows the number of data points which did not blanket upper layers and the top division of each bar (shaded portion) shows the

number of data points which did blanket upper layers. The scatter plot with dropped horizontal lines on the top of the histogram reflects the percentage blanketing that is shown by each stacked bar. The histogram shows a clear increase in blanketing events between 16:00 MLT and 3:00 MLT, i.e. early evening, through midnight to the early morning hours.

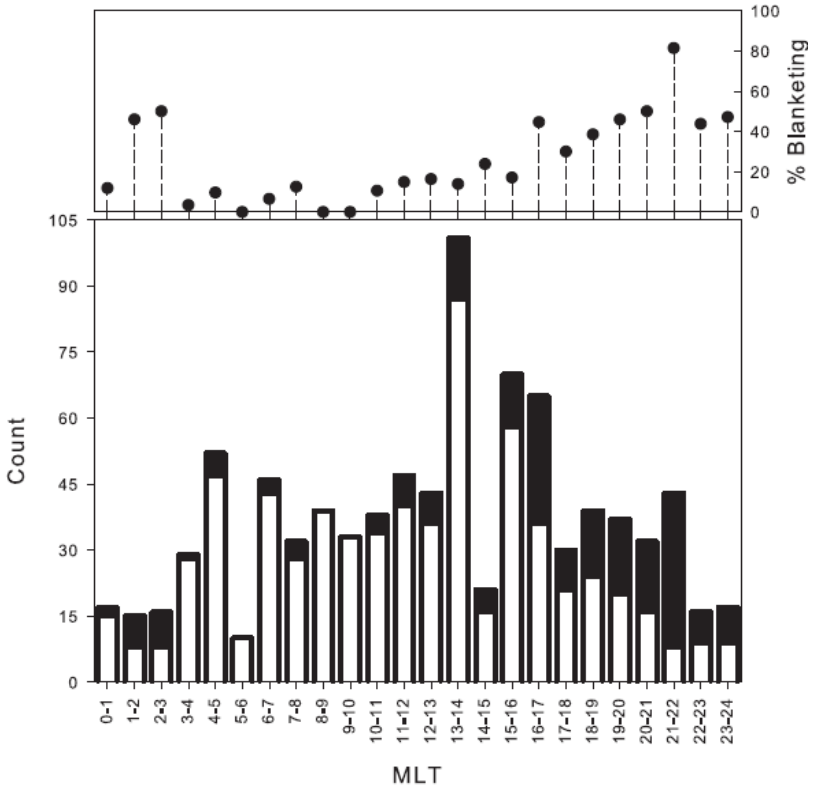

Figure 118. Histogram of the occurrence of blanketing events

4.8 The Threshold of Blanketing

From the literature it appears that best practice in the study of Sporadic-E is undertaken on the basis of f_oE exceeding 5 MHz or 7 MHz. Since the worldwide study undertaken by Smith (1957) the occurrence of sporadic-E has been linked to the value of f_oE exceeding 5 MHz. Smith (1957) deemed $f_oE \geq 5$ MHz as generally applicable for his study of long term statistics of monthly median values, even though he noted that this threshold ($f_oE \geq 5$ MHz) is not suitable when examining data from

Sodankyla as this station was found to be strongly influenced by temperate zone effects. The probability of $f_oE \geq 3$ MHz behaved as at a temperate zone station whereas the probability of $f_oE \geq 5$ MHz behaved as at an auroral station.

This section proposes a threshold value that is more suitable when attempting to define:

- The statistical occurrence of screening seen on vertical ionosonde. This is directly applicable to NVIS and through an appreciation of the scant law and knowledge of the ray path through the ionosphere, applicable to services using reflecting paths in the auroral zone which are disturbed for long periods following storm commencement. See chapter one for an explanation and chapter three for case studies showing the effects.
- The E-layer cut-off value given by: $x \equiv \frac{f_0F_2}{f_0E}$, the dimensionless value of *x*, determines the extent of E-layer cutoff of F_2 modes. As $x \to 0$ the range of take-off angles and the span of ground ranges that is accessible to F layer propagation is reducing[12]. See chapter five for both an explanation and a case study showing the effects.

[12] By definition we cannot determine x=0 or x<0 without a topside ionosonde in some cases a calibrated oblique sounder as the vertical ionosonde cannot penetrate the E-layer in order to measure the value of the F layer.

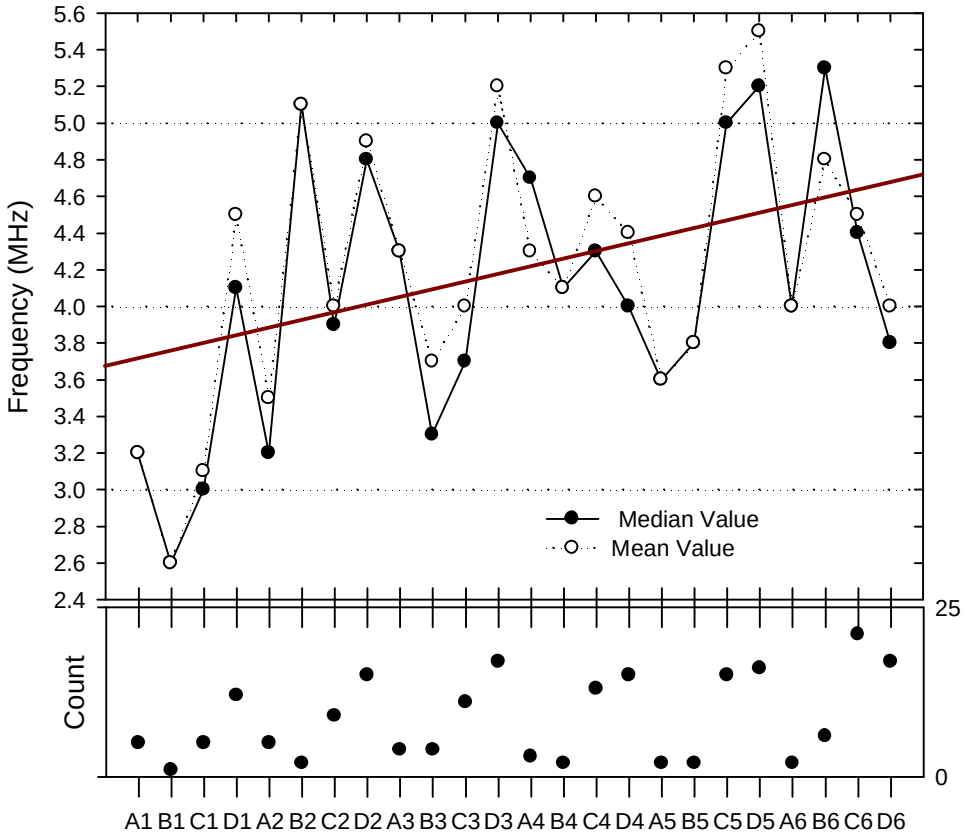

Figure 119. Median and Mean values of critical frequency at which blanketing occurs across sectors and hour following an SSC.

Figure 119 captures the mean and median values of foE, that is the critical frequency (not Δf_oE) at which blanketing occurs in each sector across the six hours following the SSC. The count of the number of blanketing events in each sector is shown in the lower panel. The fitted curve provides an indication of the increasing median as we move away from the start of the disturbance and the ionisation of the E-layer increases as the storm increases.

It is clear from figure 119 that both $f_oE > 5$ MHz or $f_oE > 7$ MHz is not an appropriate value because using $f_oE > 5$ MHz would have resulted in missing the vast majority of

blanketing events that occurred over the six year period of this study. A value greater than 3 MHz and less than 5 MHz would be a better indicator of F-layer screening and E-layer cut-off. It would be, however, simplistic just to set a level of 4 MHz being half way between the two values. We need to take into account the influence that local time has on the value of blanketing f_oE as well to account for the significant variation we see in the data.

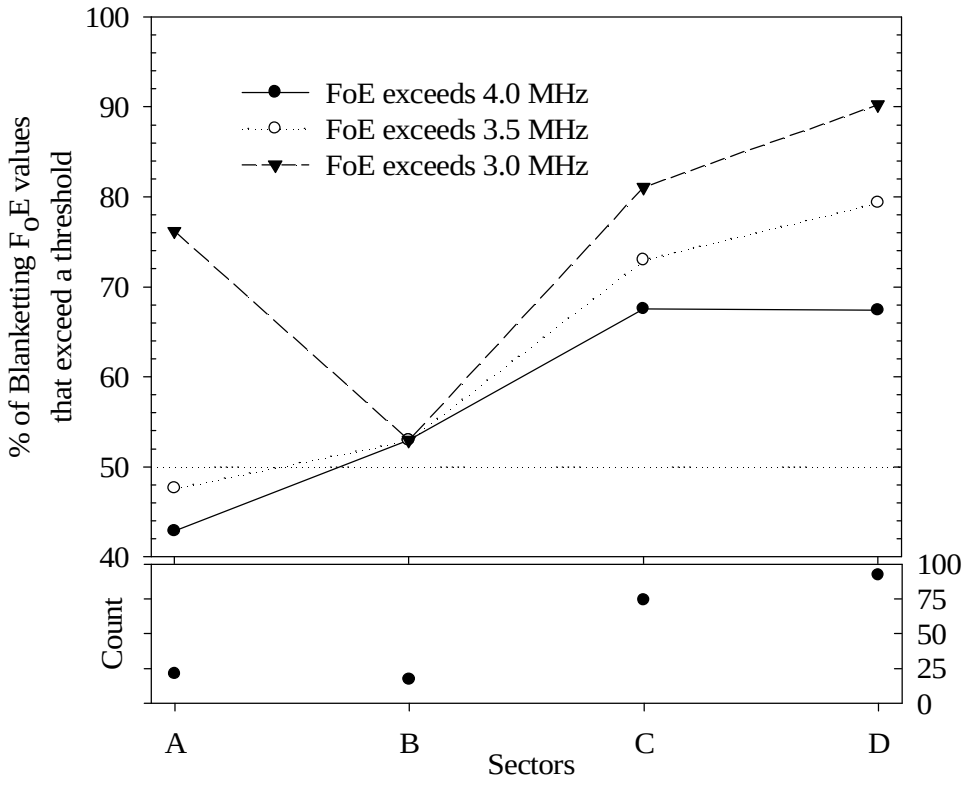

Figure 120. Percentage of blanketing foE values exceeding set thresholds in each sector.

Figure 120 shows how important it is to include local time as well as the absolute value of f_oE (not average or median values) with whatever blanketing threshold level is used. The vertical axis on the top scatter plot is the percentage of blanketing events that exceed the three thresholds in each sector. The lower graph is the count of the number of events in the six year period of this study.

Using 50% as a judge of usefulness, a threshold of 4 MHz (solid dots - ● – in figure 120) is inadequate in sector A and barely adequate in sector B. A threshold of 3.5 MHz (open dots - ○ - in figure 120) has similar inadequacies in sector A and B. A threshold of 3 MHz (solid inverted triangles - ▼ - in figure 120) is far more appropriate as a measure in all but sector B. In sector A, 76% of blanketing foE exceeds 3 MHz; this falls in sector B to 53% and rises to 82% in sector C and 90% in sector D.

The histogram in figure 121 captures the number of data points reflecting ΔfoE_{m-n} against the sector in which the SSC occurred. Overall, each bar shows the number of data points that occur in each sector. The lower division of the bar shows the number of data points which did not blanket upper layers and the top division of each bar shows the number of data points which did blanket the upper layers. The percentage blanketing that is shown by each stacked bar is indicated in the top division of each bar. The scatter plot with vertical lines indicates the number of data points where ΔfoE_{m-n} was equal to or exceeded 3 MHz.

The histogram of figure 121 exposes one of the major problems in attempting to determine a threshold that adequately captures a high percentage of blanketing foE, while at the same time not selecting a low threshold which would have the effect of overestimating the occurrence of a blanketing layer. In sector D, the level appears to be correct. There were approximately 175 data points tied to an SSC that occurred in this sector. Of those, 53.3% were blanketing the upper layers and of those 175 data points approximately 60% equalled or exceeded a f_oE of 3 MHz. In sector C there were approximately 335 data points tied to an SSC that occurred in this sector. Of

those, 23% were blanketing the upper layers and of those 335 data points approximately 55% equalled or exceeded a f_oE of 3 MHz. In sector B there were approximately 240 data points tied to an SSC that occurred in this sector. Of those, 7.7% were blanketing the upper layers and of those 240 data points approximately 65% equalled or exceeded a f_oE of 3 MHz. In sector A there were approximately 140 data points tied to an SSC that occurred in this sector. Of those, 16.5% were blanketing the upper layers and of those 140 data points approximately 50% equalled or exceeded a f_oE of 3 MHz.

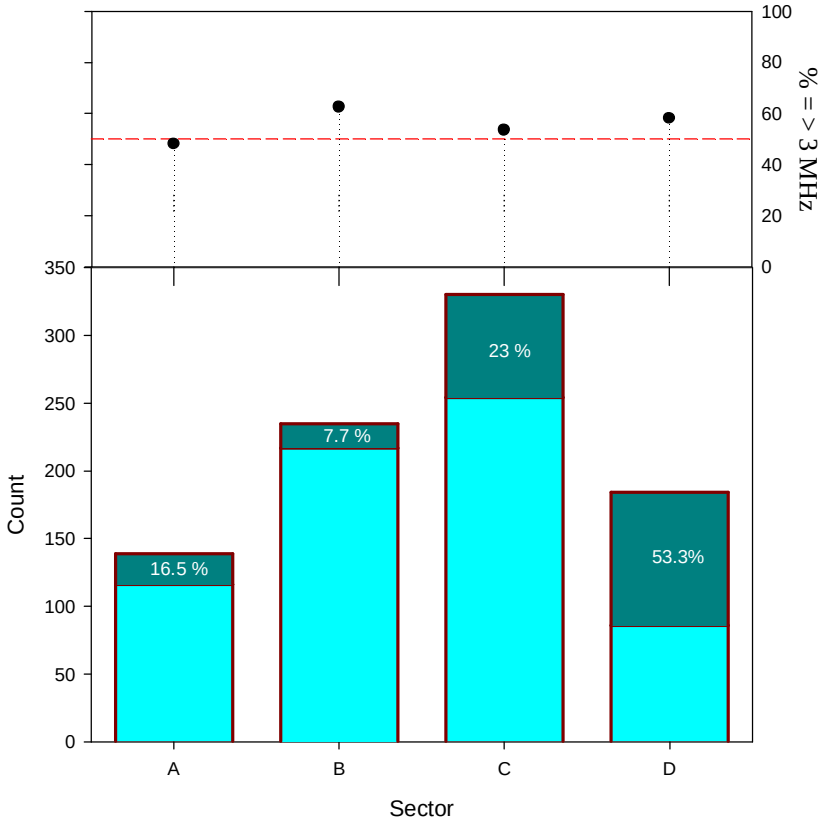

Figure 121. Histogram of occurrence of blanketing and non-blanketing data points.

While the proposed threshold of 3 MHz lacks accuracy in some sectors, it is clearly a better indication of blanketing than values such as $f_oE \geq 5$ MHz or $f_oE \geq 7$ MHz which have been used to indicate the occurrence of sporadic-E without regard to levels of

critical frequency that cause complete blanketing of the ionospheric layers above the E-layer.

4.9 Conclusions

1st Objective – a review of current knowledge on Sporadic-E layers at high latitudes.

A review of the literature is carried out looking at the cause and forms of sporadic-E, leading to a definition of Sporadic-E for the purposes of this study. The current knowledge of the worldwide distribution of sporadic-E and the limitations of the study are discussed.

2nd Objective - to introduce the ionosonde as a measurement tool of Sporadic-E characteristics and the F-plot as a presentation tool of ionosonde results.

The technique of radio sounding and how the records of this sounding, known as ionograms, are interpreted is discussed. An example is given in order to demonstrate the difficulties that occur when examining real ionograms. The development and use of the F-plot are elaborated and an example covering a SSC event is interpreted as an example.

3rd Objective - to characterise the change in the E-layer critical frequency that occurs in the six hours following an SSC event and to check for any diurnal, seasonal or solar activity dependency in the data.

The research undertaken shows that the median value of Δf_oE_s has no clear solar dependency. This supports the assertion that particle precipitation is the dominant source of ionisation following the onset of a storm. There is, however, a correlation between solar activity and the variability of Δf_oE_s. Using all the data points across all six hours there is a clear reduction in the variability of Δf_oE_s as solar activity increases. The reason for this reduction in variability is not clear.

Also noted is that while during the first hour following an SSC there is a greater variability of Δf_oE_s in summer and autumn than in winter and spring, overall the variability of Δf_oE_s does not appear to have any seasonal dependency.

In the first, second and fifth hour the median value is elevated but this is not the case in the third, fourth and fifth hour and even a decrease occurs in the sixth hour. Overall there appears to be a propensity for higher median values of Δf_oE_s in the winter months.

The investigation shows that the percentage of blanketing events has a clear diurnal dependency with blanketing events dominating between 16:00 MLT and 3:00 MLT, i.e. early evening, through midnight to the early morning hours. Again, this is not surprising taking into account that during this period the geomagnetic field lines are open to the magnetopause permitting direct particle injection.

The extensive detail in this chapter characterises the change in the E-layer critical frequency that occurs in the six hours following an SSC event. The day is divided into four sectors and there are clear differences in each sector justifying the individual treatment of each sector. The highest $\Delta f_oE_{0\text{-}1}$ values occur in sector D (18-24MLT). Sector A and Sector C have similar statistics and variance reflecting their intermediate

position between sector D and sector B. This is not surprising as sector D is when the field lines are open to direct particle injection from the magnetopause, directly opposite to sector B (9-12 MLT).

In the first hour following the SSC:

- $\Delta f_o E_{0\text{-}1}$ can be positive and negative, this depends on whether or not storm induced precipitation has commenced in this hour;
- Full blanketing can occur even when $\Delta f_o E_{0\text{-}1}$ is negative. This implies that the F-layer ionisation has dramatically reduced so even though the E-layer is penetrated, no F-layer reflecting plane exists;
- Full blanketing can occur when $\Delta f_o E_{0\text{-}1}$is zero implying a F-layer disappearance or particle precipitation maintaining what would otherwise be a decrease in critical frequency;
- Blanketing is guaranteed in the first hour following SSC when the value of $\Delta f_o E_{0\text{-}1}$exceeds 2.1 MHz;
- Blanketing occurs in all sectors $\Delta f_o E_{0\text{-}1}$except between 6 – 12 MLT (Sector B) where only one out of 33 events over a six year period caused blanketing in the first hour.

In the second hour following the SSC:

- The percentage blanketing in each sector is comparable to those occurring in the previous hour;
- Blanketing occurs extensively when $\Delta f_o E_{1\text{-}2}$ exceeds 1 MHz and exclusively when $\Delta f_o E_{1\text{-}2}$ exceeds 2.1 MHz. This last value is identical to the previous hour;

- Once again limited blanketing occurs in sector B and reaches a maximum (60% of events) in sector D;
- There is a slightly greater variability in Sector A and similar variations in the three other sectors.

In the third hour following the SSC:

- $\Delta f_o E_{2\text{-}3}$ at 2.1 MHz continues to be a milestone indicator that guarantees blanketing will occur, with only one exception;
- The extensive occurrence of blanketing greatly increases above $\Delta f_o E_{2\text{-}3}$ = 0.5 MHz which is significantly less than in previous hours. This is probably an indication of F-layer ionisation reduction and the lack of an F-layer reflecting plane even if the E-layer is penetrated;
- A higher number blanketing events starts to occur in sector B in this hour;
- There is a similar level of variability as seen in the two previous hours.

In the fourth hour following the SSC:

- $\Delta f_o E_{3\text{-}4}$ at 3 MHz is now a new milestone indicator that guarantees blanketing will occur;
- The extensive occurrence of blanketing at negative values of $\Delta f_o E_{3\text{-}4}$ indicates that F-layer ionisation has dramatically reduced and that there is no F-layer reflecting plane even if the E-layer is penetrated;
- Blanketing events now occur with $\Delta f_o E_{3\text{-}4}$ as low as -4 MHz;

- In sector A the location of the calculated average (diamond symbol) reflects the large outlier (minimum change of -3.1 MHz) that skews the distribution.

In the fifth hour following the SSC:

- Extensive blanketing occurs now occurs above ΔfoE_{3-4} of 1.5 MHz;
- ΔfoE_{3-4} of 2.1 MHz again provides a good threshold with exclusive blanketing in sectors C and D above this level;
- There are two occurrences of blanketing in sector B;
- We see very large values of ΔfoE_{4-5} (approaching 4 MHz);
- There is similar variability in all sectors.

In the sixth hour following the SSC:

- Extensive blanketing occurs when ΔfoE_{5-6} exceeds 0.5 MHz;
- There is still limited blanketing occurring in sector B;
- There are larger minimum and maximum values of change in most sectors;
- There are large negative values of ΔfoE_{5-6} in sector D although 85% of these still blanket.

4th Objective - to determine the occurrence of full blanketing E-layer formation at high latitudes as seen on vertical ionosondes in Northern Finland (67^0 Latitude).

From section 4.8, in particular from figure 119, it is clear that both $f_oE > 5$ MHz or $f_oE > 7$ MHz is not an appropriate value because using $f_oE > 5$ MHz would have resulted in missing the vast majority of blanketing events that occurred over the six year period of this study. A value greater than 3MHz and less than 5 MHz would be a better indicator of F-layer screening and E-layer cut-off. It is necessary to take into account

the influence that local time has on the value of blanketing f_oE as well to account for the significant variation we see in the data.

5th Objective - to determine the appropriate value of f_oE that should be used as a threshold of blanketing, which defines a good probability of blanketing occurring following the commencement of ionospheric storms.

It is necessary to include local time as well as the absolute value of f_oE (not average or median values) with whatever blanketing threshold level is used. Using an occurrence value of 50 % as a judge of usefulness, a threshold of 4 MHz is inadequate in sector A and barely adequate in sector B. A threshold of 3.5 MHz has similar inadequacies in sector A and B. A threshold of 3 MHz is far more appropriate as a measure in all but sector B. In sector A, 76% of blanketing f_oE exceeds 3 MHz; this falls in sector B to 53% and rises to 82% in sector C and 90% in sector D.

On the balance of the evidence presented, it appears that the threshold value of f_oE equalling or exceeding 3 MHz is a more appropriate value of f_oE, which defines a good probability of blanketing occurring following the commencement of ionospheric storms.

4.10 Summary of All Sectors

For readers who prefer tables to graphs a collation of all statistics capturing the change in E_s over the full period of six hours is given in table 25.

Sector / hour	No. events	Blanketing	Min. Change	Max. Change	Mean Change	Median Change	Std. Dev.	25% Quart	75% Quart
		%	*MHz*	*MHz*	*MHz*	*MHz*	*MHz*	*MHz*	*MHz*
A_1	19	26	-1.2	1.6	0.37	0.3	0.65	0.05	0.7
A_2	18	27.8	-1.4	2.2	-0.01	0.05	0.92	-0.68	0.28
A_3	18	22	-1.5	3.5	0.54	0.3	1.11	0	0.73
A_4	18	17	-3.1	0.6	-0.17	0.1	0.9	0	0.3
A_5	18	11	-2.2	1.2	0.16	0.2	0.73	-0.08	0.48
A_6	20	10	-0.4	2	0.28	0.1	0.61	-0.1	0.25
B_1	33	3	-0.7	2	0.22	0.1	0.56	0	0.3
B_2	33	6	-1	1.6	0.22	0.2	0.52	0	0.4
B_3	34	12	-2	2.2	-0.04	0	0.67	-0.2	0.2
B_4	32	6	-1.2	2.2	0.18	0.1	0.82	-.13	0.45
B_5	30	7	-2.4	2.7	0.11	0.1	1.03	-0.2	0.38
B_6	29	21	-1.5	3.2	-0.01	-0.1	0.93	-0.4	0.3
C_1	51	10	-1	2.1	0.1	0	0.61	-0.2	0.3
C_2	48	19	-1.9	3.9	0.05	-0.1	1.03	-0.3	0.1
C_3	46	24	-2.9	5.3	0.03	-0.1	1.37	-0.4	0.4
C_4	45	29	-2.5	7.2	0.23	-0.1	1.42	-0.2	0.4
C_5	43	35	-2	4	0.19	0	1.05	-0.3	0.58
C_6	42	50	-8	3.7	0.02	-0.05	1.75	-0.58	0.7
D_1	28	43	-1.3	4.7	0.9	0.3	1.53	-0.03	2.03
D_2	25	60	-2.1	3.6	0.57	0.5	1.43	-0.2	1.4
D_3	25	60	-1.9	3.9	0.44	0	1.78	-0.7	0.8
D_4	27	56	-5.2	3.3	-0.68	-0.3	1.79	-1.3	0.2
D_5	24	67	-1.7	3.6	0.67	0.75	1.39	-0.1	1.7
D_6	20	85	-3.1	2.4	-0.86	-0.45	1.38	-2.1	-0.08

Table 25. Collation of all Statistics capturing the change in E_s over the full period of six hours.

CHAPTER 5

Conclusions

5.0 Introduction

There are three typical features of high-latitude HF radio communications following the onset of a disturbed ionosphere; an increase in ionospheric absorption; a reduction in operational frequencies as electron density in the reflective layers changes; and variations in the expected mode of propagation. This thesis moves to model these changes based around a methodology of determining the change that occurs during disturbed periods relative to median quiet time values. It is accepted that in general the use of current propagation prediction methods is adequate for a "quiet" ionosphere.

The key to this methodology is defining the point of transition between a quiet and a disturbed ionosphere. This transition point used in this thesis is the occurrence of a storm sudden commencement (SSC) as the marker defining the change from a quiet to a disturbed ionosphere.

Chapter two of this thesis cobtains a multi-instrument case study that examines the effect of SSC on the high-latitude ionosphere. This case study clearly shows the complex mode changes that a high-latitude HF link experiences following SSC,

demonstrates the two effects of SCA and Sporadic-E and corroborates the research undertaken in the subsequent chapters.

In Chapter 3, sudden commencement absorption (SCA), the absorption spike that occurs coincidently with the SSC, is statistically analysed in detail and empirically modelled based on the change in interplanetary magnetic field (IMF) strength.

An assessment is made of the variability of the Sporadic-E layer during disturbed periods in chapter 4. As part of this assessment of E-layer variability, it has been possible to empirically model the change from the quiet time critical frequency through the six hours immediately following the onset of a disturbed ionosphere. In addition, the value of E-layer critical frequency that can be used to indicate the onset of a fully-blanketing E-layer has been developed.

5.1 Setting the Scene

Chapter one introduces the main services that make use of the HF bands. This includes defining the requirements of these services which reveals the importance of accurate propagation prediction methods to ensure these services reach the intended audience. The role of prediction and planning tools is defined and the different approaches to prediction (statistical, deterministic, intuitive and inertial) are explained. It is noted that the prediction of perturbed conditions is a complex problem and so far has been difficult to achieve.

To reveal the practical side of the theory, a case study has been done of the broadcasting service and the primary prediction method used by this service is analysed. The prediction method (ITU-R P.533) analysed has been developed to service the needs of the broadcast industry but is also used by fixed service, mobile and military system planners. The flaws in the methodology are pointed out and while it is noted that some high-latitude features (e.g. auroral absorption) have been crudely taken into account, a number of other effects such as sudden ionospheric disturbances (SIDs) and polar cap absorption (PCA) have not been thoroughly assessed.

Chapter one also describes the solar-terrestrial system, as summarised in figure 122. Starting at the Earth's surface, the ionosphere is described in terms of ionospheric regions with the focus on electron density due to ionisation.

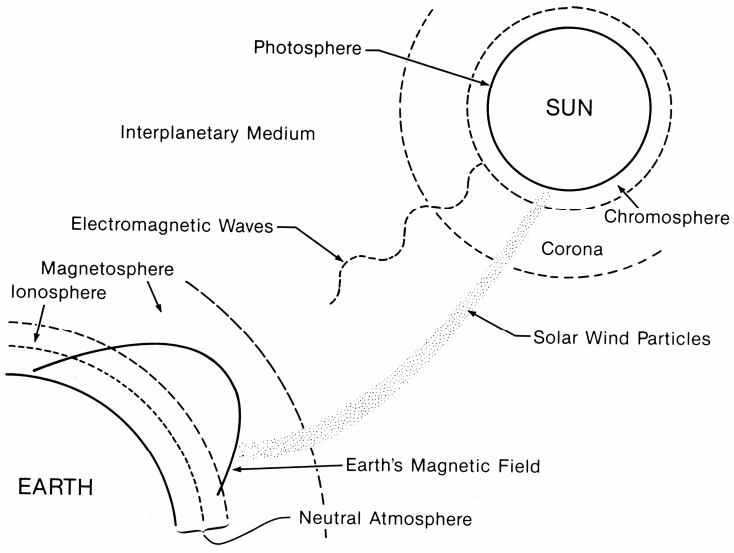

Figure 122. Solar-terrestrial system and solar ionising radiations (Davies, 1990)

Three aspects of ionisation are discussed; production, loss and transport. The limitations and difficulties in predicting the state of the ionosphere are elaborated on.

The high-latitude ionosphere and the consequences of its direct connection to the outer magnetosphere are reviewed.

Considering our move from the Earth towards the Sun, with reference to figure 122, the magnetosphere is described in terms of its interface role between the ionosphere and the solar wind. As this thesis deals with the consequences of particle precipitation on HF communications, introductory material on the magnetosphere location, radius and shape as well as the radiation belts is included. The solar wind is treated as the transport mechanism between solar disturbances and the ionosphere, via the magnetosphere. Events that are particular to the high-latitude ionosphere are briefly discussed.

The main difficulty identified is that magnetospheric processes and solar inputs have an important effect on the morphology of the high-latitude ionosphere, and that the observational databases are still too sparse to enable the development of an empirical model which has adequate parameters to describe the dependence on the various ionospheric drivers.

5.2 Detailed Case Studies

In keeping with the practice of presenting case studies to demonstrate cause and effect, theory in practice and to show the author's grasp of the material, chapter two contains three case studies utilising seven different instruments to show the cause and effect of enhanced E_s-layers immediately following an SSC. These studies demonstrate the profound effects these sporadic layers have on high-latitude HF

circuits by dramatically extending the E-layer maximum usable frequency (MUF) and/or “shielding” any F-layer ray paths.

The first simple case study is of a high-latitude link which shows the correlation between ionospheric absorption and SNR on a high-latitude HF link. But, more importantly, the case study shows the dominance of the E-layer in the high-latitude region during particle precipitation and the effect of the dominant E-layer (which dominates due to enhanced ionisation caused by precipitating particles) on the link. The case study demonstrates many of the problems in predicting the state of the ionosphere, especially at high latitudes (e.g. rapidly varying virtual heights of reflection layers, D-layer absorption and frequent propagation mode changes), and shows the dominance of the E-layer over the F-layer during particle precipitation events.

Data from the ACE satellite is used to show the magnitude of changes that occur in the solar wind due to disturbances in the solar wind, such as when shock waves and dynamic pressure pulses move past the satellite on their way to impinging on the Earth’s magnetosphere. The step changes in total magnetic field strength, particle density and velocity as well as changes in direction of the B_z component are shown. The observation of sudden changes in the solar wind which are the cause of SSC is well understood, as is the prediction of the time delay between observation by the ACE satellite platform and the arrival of the disturbance at the Earth’s surface. However, for the first time the linkage between SSC and the enhanced E-layer ionisation is exposed in both of the more detailed case studies.

Ionosonde records show how the usefulness of the F-layer is reduced as its electron density decreases and its virtual height increases following disturbances initiated by the SSC. The records further show the enhancement of the E_s-layer for extended periods, in both cases for at least two hours and in one case as long as three hours. The enhancement is so great in some cases that the F-layer is completely screened off from the ground. The Tromsø ionosonde, close to the centre of the first case study link path demonstrates the change that occurs in the height of the F-layer around the single reflecting control point. This knowledge allows a more realistic ray tracing geometry to be used when attempting to model and predict propagation during such disturbances.

The ISR records reveal the sudden enhancement of electron density in the E-region coincident with the SSC as well of the scale of the increase in electron density that can be expected. The effect of storms and sub-storms on the significant modulation of electron density at E_s altitudes is clearly demonstrated. The ISR records support the longevity of enhancement of the E_s-layer electron density that is seen in the ionosonde and oblique sounder records.

Key to both detailed case studies are records from the oblique sounder which reveals the practical effects of an enhanced E_s-layer. The majority of all HF communication links are planned assuming the use of the F2 layer as the refracting layer as well as assuming a fixed reflection height (normally 250 km). An HF system designed to reach a particular point or area such as point-to-point links and targeted broadcasting uses complex antennas that concentrate the radiated power in both azimuth and elevation. These two assumptions are perfectly valid when dealing with a quiet

ionosphere. However, the variations in the height of the F-layer, the reduction of the height of the expected reflecting layer from 250 km to 100 km, as well as the phenomena of the E_s-layer screening the F-layer, has severe implications. The change in reflection layer from the F- to the E_s-layer has the most drastic effect as the elevation angle changes from double figures to single figures, and is beyond the capabilities of many types of specialist antenna.

As noted by a reviewer of the published case study (Ritchie and Honary 2009b) "the case study combines space weather data from a number of sources in the temporal neighborhood of SSC (in two special cases) and associates the impacts on transauroral HF propagation. While the impact of auroral E_s on HF propagation has been published before, the present paper offers a more comprehensive look at two specific links with a variety of sensors and techniques, some of which were not available until recent years".

In all the studies undertaken the occurrence of absorption and E_s was noted and to the author's knowledge there has not been any published work that quantifies the expected changes in the lower ionosphere (the D and E-regions) due to particle precipitation. In a paper by Hunsucker (1992) the claim is made that HF-propagation mode structure and losses at high latitudes are impossible to describe, so predictions of paths that include ionospheric reflections and points of D-region penetration in the auroral and polar ionosphere are almost useless. While it is accepted that mode structure and losses are difficult to describe we must attempt, at least empirically, to start the analysis and see were this may lead us. Therefore it is proposed that the way forward at the present time is to look at how to adapt the current propagation

prediction models, which are adequate for “quiet” conditions, with empirical data based on measurements from clearly definable disturbed periods.

A primary part of the problem is establishing when the transition from a “quiet” high latitude ionosphere to a “disturbed” high latitude ionosphere starts. A “quiet” high latitude ionosphere for the purposes of this research is one that behaves like a mid-latitude ionosphere in the absence of solar and geophysical activity. A “disturbed” high latitude ionosphere is one under the influence of particle precipitation. As shown in the case study, even during low solar and geophysical activity, particle precipitation has a significant effect. Some effort is required to predict the variances in E-layer critical frequency in order to better plan high-latitude communications, particularly when ionospheric reflection points occur within the disturbed high-latitude ionosphere.

Although modelling of the high-latitude ionosphere has improved in recent years, most of the modelling attempts are only case studies (e.g. Sojka and Schunk, 1988). The main difficulty is that magnetospheric processes and solar inputs have an important effect on the morphology of the high-latitude ionosphere, and that even with the most extreme simplifying assumptions, the high-latitude ionosphere cannot be treated analytically (Cander et al., 1998) - hence the empirical and statistical analysis approach undertaken in this thesis .

5.3 Defining, Analysing and Modeling SCA

Having adopted the SSC as the transition point, the first requirement is to understand what an SSC is and what causes it. The literature review in Chapter three revealed that a geomagnetic SSC is caused by a solar wind shock or impulse. The shock or impulse excites an MHD disturbance in the magnetosphere. This disturbance propagates toward the Earth to be detected as an SSC signature on the ground.

During the impact of a pressure pulse on the magnetosphere, the outer magnetosphere is compressed. The breaking of the first adiabatic invariant by the compression increases the perpendicular-to-parallel ratio of particle energy and promotes the growth of loss cone instability. This in turn increases the amount of particles that are scattered into the loss cone by wave-particle interactions (Zhou and Tsurutani, 1999). Any violation of the first two invariants causes changes of the pitch angle (pitch angle scattering). This can lead to losses of particles when the pitch angle becomes so small, that the corresponding mirror points move down into the atmosphere where the particles can be scattered and absorbed. As the periods of the first two invariants are short, their violation is mainly caused by particle and particle-wave interactions.

Violation of the adiabatic invariants appear to be responsible for some of the precipitation, but since the adiabatic changes in particle trajectories can only increase the pitch angle, adiabatic effects alone cannot increase the particle flux within the loss cone and thus cannot account for all the absorption seen. With the assumed absence of other scattering mechanisms during the initial perturbation, the increase absorption seen must result from wave-induced precipitation (Gail et al., 1990a). It has been conclusively demonstrated that the Energetic electrons associated with SSC originate

in the trapped radiation belt within the plasmasphere where the closed field lines are limited in latitude and that SCA is caused by the precipitation of high energy electrons and protons into the atmosphere where they generate excess ionization at low altitudes. Typically, the processes causing ionospheric absorption of radio waves take place at altitudes in the range of 60 to 100 km (Stauning, 1996).

This absorption, coincident with the SSC, is known as sudden commencement absorption (SCA). A literature survey revealed that no analysis of SCA has been published. Hence a detailed examination of sudden commencement absorption has been undertaken and published (Ritchie and Honary, 2009a). The results in this chapter have a direct application to real-time and near-time ionospheric propagation prediction in respect of the prediction of the occurrence and expected amplitude of sudden commencement absorption.

By design the dataset used in the investigation spanned more than half a solar cycle and this was used to determine if solar activity, using the relevant sunspot count as a proxy, influences the value of SCA. By evaluating the link between SCA and solar activity and the link between the change in IMF magnitude and solar activity it is concluded that in both cases there is no causal link, other than in the number of SSC events that occur. This last point is not unexpected as higher sunspot levels reflect the increase in the number of active regions on the Sun that are the source of shocks leading to SSC events.

Following the presentation of the basic database statistics, the influence of local time on SCA amplitude was investigated by dividing the dataset into day events (6 – 18

MLT) and night events (18 – 6 MLT). While the number of SSC events is slightly greater during the day, there is no significant difference in the mean or median SCA values between the two sectors. This confirms that the immediate response of the magnetosphere to the shock is a global disturbance directly driven by the solar wind.

In considering all the possible combinations of how the direction of B_z might change during the shock, the similarity between the statistics calculated for each of the four possible combinations leads to the conclusion that the change in the direction of B_z in whatever combination has very little impact on the value of SCA. This supports an assertion that SCA is caused by particles already captured in the magnetosphere. If it was the alternative option that solar wind-carried particles were gaining direct access to high-latitude zones then the change in solar wind – magnetosphere coupling, caused by changes in B_z direction, would be clearly evident, which is not the case.

In an attempt to model the expected SCA values after a shock has occurred, solar wind and IMF parameters were correlated in turn against the absolute, mean and median values of SCA. A strong correlation (R2=0.852) was found between the median value of SCA measured and the step change in IMF magnitude that occurred during the shock. In some ways this is not surprising as ΔB is fundamentally an indirect measure of the changes in solar wind proton velocity (Vp). The fit is particularly good at ΔB values less than 25 nT which accounts for 97% of the SSC events in the database. In addition, due to proton contamination of the ACE SWEPAM instrument during large events, solar wind data is not reported, leaving the use of ΔB as the only reliable predictor of SCA during these times.

In summary the key findings of chapter three are:

i. There is no causal link between the amplitude of SCA and solar activity;

ii. There is no causal link between the delta of IMF magnitude, caused by the passage of the shock wave past the ACE satellite, and solar activity.

These first two points are very relevant to radio engineers in that most propagation prediction programs only use a solar activity index to predict performance – the implication is that some other method is required – which this paper presents, namely an empirical relationship based on the change in IMF.

iii. SCA occurs with similar statistical characteristics during both the day and night.

iv. The direction of B_z before and after the shock has little impact on the expected value of SCA.

The implication of these two points is that both of these variables can be ignored when predicting SCA.

v. The change in the strength of the IMF is the best predictor for small to medium shocks and the only predictor that can be used during large shocks.

5.4 Variability of the E-layer, Blanketing and the Threshold of Blanketing

The second investigation centered on the occurrence and effects of sporadic-E on high-latitude communications following an SSC. Chapter four reviews the current knowledge of sporadic-E layers at high latitudes, looking at the cause and forms of sporadic-E. This leads to a definition of sporadic-E for the purposes of this study. The current knowledge of the worldwide distribution of sporadic-E and the limitations of the study are discussed. The technique of radio sounding and how the records of this sounding, known as ionograms, are interpreted is discussed. An example is given in order to demonstrate the difficulties that occur when examining real ionograms. The development and use of the F-plot (an important reporting tool used extensively in this chapter) is elaborated on and an example covering a SSC event is interpreted as an example.

A substantial amount of F-plot analysis of the data base covering half a solar cycle was undertaken in order to characterise the change in the E-layer critical frequency that occurs in the six hours following an SSC event and to check for any diurnal, seasonal or solar activity dependency in the data. The research results show that the median value of $\Delta f_o E_s$ has no clear solar dependency. This supports the assertion that particle precipitation is the dominant source of ionisation following the onset of a storm. There is however a correlation between solar activity and the variability of $\Delta f_o E_s$. Using all the data points across all six hours there is a clear reduction in the variability of $\Delta f_o E_s$ as solar activity increases. The reason for this reduction in variability is not clear and is one area for further investigation.

It was shown that while during the first hour following an SSC there is a greater variability of $\Delta f_o E_s$ in summer and autumn than in winter and spring, overall the variability of $\Delta f_o E_s$ does not appear to have any seasonal dependency. In the first, second and fifth hour the median value is elevated but this is not the case in the third, fourth and fifth hour and even a decrease occurs in the sixth hour. Overall, there appears to be a propensity for higher median values of $\Delta f_o E_s$ in the winter months.

The research findings show that the percentage of blanketing events has a clear diurnal dependency with blanketing events dominating between 16:00 MLT and 3:00 MLT, i.e. early evening, through midnight to the early morning hours. Again, this is not surprising taking into account that during this period the geomagnetic field lines are open to the magnetopause permitting direct particle injection.

The extensive detail in chapter four characterises the change in the E-layer critical frequency that occurs in the six hours following an SSC event. The day is divided into four sectors and there are clear differences in each sector justifying the individual treatment of each sector. Some key findings are:

- In the first hour following the SSC, $\Delta f_o E_{0\text{-}1}$ can be positive and negative; this depends on whether or not storm induced precipitation has commenced in this hour. In addition, full blanketing can occur even when $\Delta f_o E_{0\text{-}1}$ is negative, implying that the F-layer ionisation has dramatically reduced so even though the E-layer is penetrated, no F-layer reflecting plane exists. Full blanketing can occur when $\Delta f_o E_{0\text{-}1}$is zero implying an F-layer disappearance or particle precipitation maintaining what would otherwise be a decrease in critical

frequency and blanketing is guaranteed in the first hour following SSC when $\Delta f_oE_{0\text{-}1}$exceeds 2.1 MHz.

- In the second hour following the SSC, blanketing occurs extensively when $\Delta f_oE_{1\text{-}2}$ exceeds 1 MHz and exclusively when $\Delta f_oE_{1\text{-}2}$ exceeds 2.1 MHz. This last value is identical to the previous hour. There is a slightly greater variability in Sector A and similar variations in the three other sectors.

- In the third hour following the SSC, $\Delta f_oE_{2\text{-}3}$ at 2.1 MHz continues to be a milestone indicator that guarantees blanketing will occur, with only one exception. The extensive occurrence of blanketing greatly increases above $\Delta f_oE_{2\text{-}3}$ = 0.5 MHz which is significantly less than in previous hours. This is probably an indication of F-layer ionisation reduction and the lack of an F-layer reflecting plane even if the E-layer is penetrated. There is a similar level of variability as seen in the two previous hours.

- In the fourth hour following the SSC, $\Delta f_oE_{3\text{-}4}$ at 3 MHz is now a new milestone indicator that guarantees blanketing will occur. The extensive occurrence of blanketing at negative values of $\Delta f_oE_{3\text{-}4}$ indicates that F-layer ionisation has dramatically reduced and that there is no F-layer reflecting plane even if the E-layer is penetrated. Blanketing events now occur with $\Delta f_oE_{3\text{-}4}$ as low as -4 MHz.

- In the fifth hour following the SSC, extensive blanketing now occurs above $\Delta f_oE_{3\text{-}4}$ of 1..5 MHz. An $\Delta f_oE_{3\text{-}4}$ of 2.1 MHz again provides a good threshold

with exclusive blanketing in sectors C and D above this level. We see very large values of $\Delta f_oE_{4\text{-}5}$ (approaching 4 MHz).

– In the sixth hour following the SSC, extensive blanketing occurs when $\Delta foE_{5\text{-}6}$ exceeds 0.5 MHz. There is still limited blanketing occurring in sector B. There are large negative values of $\Delta f_oE_{5\text{-}6}$ in sector D although 85% of these still blanket.

This detailed analysis allowed the occurrence of full blanketing E-layer formation at high latitudes as seen on vertical ionosondes in Northern Finland (67^0 Latitude) to be determined. It is revealed that both $f_oE > 5$ MHz or $f_oE > 7$ MHz is not an appropriate value because using $f_oE > 5$ MHz would have resulted in missing the vast majority of blanketing events that occurred over the six year period of this study. A value greater than 3 MHz and less than 5 MHz would be a better indicator of F-layer screening and E-layer cut-off. It is necessary to take into account the influence that local time has on the value of blanketing f_oE, as well to account for the significant variation we see in the data.

Directly following on from this, it was then possible to determine the appropriate value of f_oE that should be used as a threshold of blanketing, which defines a good probability of blanketing occurring following the commencement of ionospheric storms. It is necessary to include local time as well as the absolute value of f_oE (not average or median values) with whatever blanketing threshold level is used. On the balance of the evidence presented it appears that the threshold value of f_oE equalling or exceeding 3 MHz is a more appropriate value of f_oE, which defines a good

probability of blanketing occurring following the commencement of ionospheric storms.

To the author's knowledge this is the first time the variability of the E-layer and the screening effect of sporadic-E has been quantified (Ritchie and Honary, 2009c).

5.5 Final Comments

Following an SSC event or during magnetic storms, one rational approach toward using the ionosphere for HF communications in high-latitude regions is to rely solely on E-layer modes and to provide higher power or increased antenna gain in bands appropriate for E_s-layer propagation. Overcoming these problems may prove to be economically challenging for operators of fixed-links and broadcasting services. However, with relevance to tactical links and safety of life transmissions, the oblique sounder reveals, counter-intuitively perhaps, that instead of reducing the frequency of operation to re-establish disrupted links, it would be better to increase the frequency of operation to fully utilise the enhanced E-layer while overcoming some of the effects of absorption. As explained in the case studies, in order to implement this mitigation technique, equipment at both ends of the link will need to be sufficiently frequency agile and have access to antenna with take-off angles appropriate for E_s-layer operation.

Glossary and References

Glossary

Adiabatic Invariant: In a nearly collisionless, ionised gas, electrically-charged particles orbit around magnetic lines of force. Certain physical quantities are approximately constant for slow (adiabatic) changes of the magnetic field in time or in space and these quantities are called adiabatic invariants.

Alfvén Wave (magnetohydrodynamic shear wave): A transverse wave in magnetised plasma characterised by a change of direction of the magnetic field with no change in either the intensity of the field or the plasma density.

Anisotropic Plasma: A plasma whose properties vary with direction relative to the ambient magnetic field direction. This can be due, for example, to the presence of a magnetic or electric field.

Auroral Oval: An elliptical band around each geomagnetic pole ranging from about 75^0 magnetic latitude at local noon to about 67^0 magnetic latitude at midnight under average conditions. It is the locus of those locations of the maximum occurrence of auroras, and widens to both higher and lower latitudes during the expansion phase of a magnetic substorm.

Bow Shock: A collisionless shock wave in front of the magnetosphere arising from the interaction of the supersonic solar wind with the Earth's magnetic field.

Cusp: In the magnetosphere, two regions near local magnetic noon and approximately 15^0 of latitude equatorward of the north and the south magnetic poles. The cusps mark the division between geomagnetic field lines on the sunward side and the field lines in the polar cap that are swept back into the magnetotail by the solar wind. The term cusp implies the conical symmetry around the central axis of the polar magnetic

fields lines. In practice it appears that the terms 'Cusp' and 'Cleft' are often used interchangeably. However, 'cleft' implies greater extension in longitude (local time) and hence a wedge-shaped structure.

Cyclotron Frequency: When a particle of charge *q* moves in a magnetic field B, the particle orbits, or gyrates around the magnetic field lines. The cyclotron frequency is the frequency of this gyration and is given by:

$$w_c = \frac{q|B|}{m\,c}$$

m = Particle mass

c – velocity of light

Cyclotron Resonance: The frequency at which a charged particle experiences a Doppler shifted wave at the particle's cyclotron frequency. Because the particle and wave may be travelling at different speeds and in different directions, there is usually a Doppler shift involved.

Diffusion: The slow, stochastic motion of particles.

Diffusive Shock Acceleration: Charged particle acceleration at a collisionless shock due to stochastic scattering processes caused by waves and plasma turbulence.

Dipole Magnetic Field: A magnetic field whose intensity decreases as the cube of the distance from the source. A bar magnet's field and the magnetic field originating from the Earth's core are both approximately dipole magnetic fields.

Drift (of ions/electrons): As particles gyrate around magnetic field lines, their orbits may 'drift' perpendicular to the local direction of the magnetic field. This occurs if there is a force also perpendicular to the field – e.g. an electric field, curvature in the magnetic field direction or gravity.

Energetic Particle: Energetic particles are defined relative to the background thermal plasma so that any particle having a larger energy than the thermal energy is an energetic particle.

Field Aligned Current: A current flowing along (or opposite to) the magnetic field direction.

Hardening of precipitation: This means higher energy particles are precipitating (usually leading to higher electron density at lower altitudes).

Isotropic Plasma: A plasma which is not anisotropic – whose properties are the same in all directions.

Loss Cone Stability: An instability generated by a plasma anisotropy where the temperature perpendicular to the magnetic field is greater than the temperature parallel to the field. This instability gets its name because this condition exists in the Earth's magnetosphere and the 'loss-cone' particles are those that are lost into the upper atmosphere.

Magnetohydrodynamic (MHD): The MHD plasma theory deals with a compressible, conducting fluid immersed in a magnetic field. The wave modes derived using this theory are called magnetohydrodynamic or MHD waves. In the general case, with the wave propagation in an arbitrary direction with respect to external magnetic field ***B***, three MHD wave modes are found:

i. Pure (or oblique) Alfvén wave;

ii. Slow MHD wave;

iii. Fast MHD wave .

Magnetopause: The boundary surface between the solar wind and the magnetosphere, where the pressure of the magnetic field of the Earth effectively equals the ram pressure of the solar wind.

Magnetosheath: The region between the bow shock and the magnetopause, characterised by very turbulent plasma. This plasma has been heated (shocked) and slowed as it passed through the bow shock. For the Earth, along the Earth-Sun axis, the magnetosheath is about 3 R_e thick.

Magnetosonic Speed: The speed of sound waves in a magnetised plasma. It is the equivalent of the sound speed in a neutral gas or non-magnetised plasma. It appears to be sometime referred to as acoustic speed.

Magnetosphere: The magnetic cavity surrounding a magnetised planet, carved out of the passing solar wind by virtue of the planetary magnetic field, which prevents, or at least impedes, the direct entry of the solar wind plasma directly into the cavity.

Magnetotail: The extension of the magnetosphere in the antisunward direction as a result of interaction with the solar wind. In the inner magnetotail, the field lines maintain a roughly dipolar configuration. But at greater distances in the antisunward direction, the field lines are stretched into northern and southern lobes, separated by a plasmasheet.

Pitch Angle: In a plasma, the angle between the instantaneous velocity vector of a charged particle and the direction of the ambient magnetic field.

Plasma: A gas that is sufficiently ionised so as to affect its dynamical behaviour. A plasma is a good electrical conductor and is strongly affected by magnetic fields.

Plasma Instability: When a plasma (or ion or electron) is sufficiently anisotropic, plasma waves grow, which in turn alter the distribution via wave-particle interactions. The plasma is unstable.

Plasma Wave: A wave generated by plasma instabilities or other unstable modes of oscillation allowable in a plasma.

Plasma Sheet: The region of closed field lines in the equatorial magnetotail. The Plasma sheet is typically divided into plasma sheet proper, or central plasma sheet, and plasma sheet boundary layer (PSBL), the latter being at higher latitudes adjacent to the tail lobes. It is also divided into two parts by the cross-tail current sheet in the equatorial plane.

Polar Cusp: A region in which the magnetosheath plasma has direct access to the ionosphere. It exists whether the interplanetary magnetic field is northward or southward. In a non-reconnecting magnetosphere the location of the cusp depends on the shape of the magnetopause but when the magnetosphere reconnects with either southward or northward interplanetary magnetic field the location of the cusp is altered.

Radiation Belt (inner): The trapping regions of high-energy charged particles surrounding the Earth are called radiation or van Allen belts. The inner one, located between about X = 1.1 - 3.3 R_e (Earth radii, geocentric) in the equatorial plane, contains primarily of protons with energies exceeding 10 MeV. Flux maximum is at about X = 2 R_e.

Radiation Belt (Outer): The trapping regions of high-energy charged particles surrounding the Earth are called radiation or van Allen belts. The outer belt contains mainly electrons with energies up to 10 MeV.

R_e: Symbol used to represent Earth Radius (or radii). $1R_e$ = 6371 km.

Shock Wave (Collisionless): A shock wave is characterised by a discontinuous change in pressure, density, temperature and particle streaming velocity, propagating through a compressible fluid or plasma. Collisionless shock waves occur in the solar wind when fast solar wind overtakes slow solar wind with the difference in speeds being greater that the magnetosonic speed.

Solar Wind: The concept of continuous solar wind developed in 1950's as a result of observed comet tails as they passed close to the Sun, and explained the observed tail deflection by a continuous flux of protons from the Sun. It was then shown (Parker, 1959) that the solar corona must expand, and called the outward streaming coronal gas 'solar wind'. The outermost region of the Sun, corona, is indeed very hot, so hot that the hydrogen and helium can escape gravitational attraction and form a steadily streaming outflow of material called the solar wind. The expanding solar wind drags also the solar magnetic field outward, forming what is called the interplanetary magnetic field (IMF). The region of space in which this solar magnetic field is dominant is called the heliosphere.

Solar Wind Shock: A shock wave propagating in the solar wind.

Van Allen radiation belts: Are composed of energetic ions and electrons, gradient-curvature drifting in orbits encircling the Earth. The energetic ions comprising the proton radiation belt are confined mainly to the inner regions of the magnetosphere, inside distances of perhaps 2-3 Earth Radii (R_e) from the centre of the Earth, and result primarily from the decay of neutrons freed by cosmic rays impinging on the upper atmosphere (Walt, 1966). The electron radiation belts, on the other hand, divide themselves into two distinct regions: an inner zone belt, extending from a few hundred kilometres above the surface of the Earth to distances of 2-2.5 Re, and an outer zone population between 5 and 7 R_e.

Wave-particle interaction: Particle velocity changes (scattering) due to interaction with wave electric or magnetic fields. Since in a magnetised plasma, the particles gyrate rapidly about the magnetic field, this interaction is accomplished though a cyclotron resonant interaction (a.k.a Landau resonance).

References

A

Abel, B., R.M. Thorne, and A.L. Vampola, Solar cyclic behaviour of trapped energetic particles in earth's inner radiation belt, Journal of Geophysical Research, 99, 19427, 1994

AGARD, The effect of disturbances of solar origin on communications, Papers presented at the symposium of the AGARD ionospheric research committee, Editor, G.J. Gassmann, AGARDograph 59, NATO Advisory Group for Aerospace Research and Development, 1963.

AGARD, Arctic Communications, Proceedings of the 8th meeting of the AGARD ionospheric research committee, Editor, B. Landmark, AGARDograph 78, NATO Advisory Group for Aerospace Research and Development, 1964.

AGARD, Media effects on electronic systems in the high latitude region, AGARD lecture series number 162, NATO Advisory Group for Aerospace Research and Development, ISBN92 835 0478 X, 1988.

AGARD, High Frequency Radio Communications, Edited by Eriksen and Landmark, AGARDograph 104, NATO, Lib. Cong. 67-22235, 1967

Akasofu, S.-I and S. Chapman, The Development of the Main Phase of Magnetic Storms, Journal of Geophysical Research, 68, 125, 1963.

Akasofu, S.-I., A source of the energy for geomagnetic storms and auroras, *Planetary Space Science*, 12, 801, 1964.

Akasofu, S.-I., The development of geomagnetic storms after a negative sudden impulse, Planetary Space Science, 12, 573-578, 1964.

Akasofu, S-I., Polar and Magnetospheric Substorms, Astrophysics and space science libarary, D.Reidel Publishing Company, Volume 11, 1968.

Akasofu, S.-I., Energy coupling between the solar wind and the magnetosphere, Space Science Rev., 28, 121-190, 1981.

Albert, J. M., G. P. Ginet, and M. S. Gussenhoven, CR-RES Observations of radiation belt protons, 1. Data overview and steady state radial diffusion, Journal of Geophysical Research, 103, A5, 9261 - 9274, 1998.

Albert, J.M., Nonlinear interaction of outer zone electrons with VLF waves, Geophysical Research Letters, 29, 8, 1275, 2002.

Ames, J.W., Egan, R.D. and McGintie, G.F., 'Short-term prediction of HF communication circuit performance'. *Ionospheric Forecasting*. Ed. V. Agy, AGARD Conf. Proc. No.49, Paper No.22, 1970.

Anderson, B.J. and Hamilton, D.C., Electromagnetic ion–cyclotron waves stimulated by modest magnetospheric compressions. Journal of Geophysical Research 98, p. 11369, 1993.

Anderson, K.A, Soft Radiation Events at High Altitude during the Magnetic Storm of August 29-30, 1957, Physical Review, 111, 5, 1397-1405, 1958.

Anderson, K.A., Wave-energetic particle associations in the magnetosphere, Earth's particles and fields, edited by B.M. McCormack, p 429-439, Reinhold, New York, 1968.

Anderson, D. N., M. Mendillo, and B. Herniter, (1987) 'A Semi-Empirical Low-Latitude Ionospheric Model', Radio Sci. 22, 292, 1987.

Anderson, D.N., J.M. Forbes, and M. Codrescu, "A Fully Analytical, Low-and Middle-Latitude Ionospheric Model", Journal Geophysics Res. 94:1590, 1989.

Anderson, D.N., 'Global ionospheric modelling', Modern Radio Science 1993, edited by H Matsumoto, Oxford University Press, 159, 1993.

Appleton, E.V., A note on the sluggishness of the atmosphere, Journal of Atmospheric and Terrestrial Physics, 3, 282-284, 1953.

Appleton, E.V., and R. Naismith, Weekly measurements of upper-atmospheric ionization, Proceedings of the Physical Society, 45, 389-398, 1933.

Araki, T., Global structure of geomagnetic sudden commencements, Planet. Space Sci., 25, 373-384, 1977.

Araki, T., and J. H. Allen, Latitudinal reversal of polarization of the geomagnetic sudden commencement, Journal of Geophysical Research, 87, 5207-5216, 1982.

Araki, T., A physical model of the geomagnetic sudden commencement, in Solar wind sources of Magnetospheric Ultra-Low-Frequency Waves, Geophysical Monograph Series, Vol 81, edited by M.J Engerbretson, K. Takahashi, and M. Scholer, 183-200, AGU, Washington D.C., 1994.

Araki, T., S. Fujitani, M. Emoto, K. Yumoto, K. Shiokawa, T. Ichinose, H. Luehr, D. Orr, D. K. Milling, H. Singer, G. Rostoker, S. Tsunomura, Y. Yamada, and C. F. Liu, The anomalous sudden commencement on March 24, 1991, Journal of Geophysical Research, Vol 102, A7, 14 075 – 14086, July, 1997.

Arnoldy, R. L., T.E. Moore, and S.-I. Akasofu, Plasma injection events at synchronous orbit related to positive Dst, Journal of Geophysical Research, 87, 77-84, 1982.

Arnoldy, R.L., Signature in the interplanetary medium for substorms, Journal of Geophysical Research, 76, 5189-5201, 1971.

B

Baggaley, W.J., Ionosphere sporadic-E parameters: long term trends, Science, 225, 4664, 830, 1984.

Bailey, D.K., Some quantitative aspects of electron precipitation in and near the auroral zone, Reviews of Geophysics, 6, 289-346, 1968.

Baker, D. N., J. H. Allen, S. G. Kanekal, G. D. Reeves, Disturbed space environment may have been related to pager satellite failure, Eos Trans. AGU, 79(40), 477-477, 10.1029/98EO00359, 1998b.

Baker, D.N., X. Li, N. Turner, J. H. Allen, L. F. Bargatze, J. B. Blake, R. B. Sheldon, H. E. Spence, R. D. Belian, G. D. Reeves, S. G. Kanekal, B. Klecker, R. P. Lepping, K. Ogilvie, R. A. Mewaldt, T. Onsager, H. J. Singer, G. Rostoker, Recurrent geomagnetic storms and relativistic electron enhancements in the outer magnetosphere: ISTP coordinated measurements, Journal of Geophysical Research, 102, A7, 14141 – 14148, 1997.

Baker, D. N., P.R. Higbie, E.W. Hones, R.D. Belian, High-resolution energetic particle measurements at 6.6RE 3. Low-energy electron anisotropies and short-term substorm predictions, Journal of Geophysical Research, 83, A10, 4863-4868, 1978.

Baker, D. N., E.W. Hones, P.R. Higbie, R.D Belian, P. Stauning, Near-equatorial, high-resolution measurements of electron precipitation at L approximately equal to 6.6, Journal of Geophysical Research, 86, 2295-2313, 1981.

Baker, D.N., X. Li, N. Turner, J. H. Allen, L. F. Bargatze, J. B. Blake, R. B. Sheldon, H. E. Spence, R. D. Belian, G. D. Reeves, S. G. Kanekal, B. Klecker, R. P. Lepping, K. Ogilvie, R. A. Mewaldt, T. Onsager, H. J. Singer, G. Rostoker, Recurrent geomagnetic storms and relativistic electron enhancements in the outer magnetosphere: ISTP coordinated measurements, Journal of Geophysical Research, 102, A7, 14141 – 14148, 1997.

Baker, K.D., The Birkeland Symposium on Aurora and Magnetic Storms, Edited by J. Holtet and A. Egeland, pg. 305, 1968.

Banks. P.M., Dynamical behaviour of the polar topside ionosphere, In Magnetosphere-ionosphere interactions, edited by K. Folkestad, Scandinavian University Books, ISBN: 82 00 02263 3, 1972.

Banks, P.M., and C. Kockarts, Aeronomy Part A, 253 – 256, Academic Press, New York, 1973.

Barcus, J.R., Electron precipitation following a geomagnetic storm sudden commencement, Annales Geophysicae, 24, 533-539, 1968.

Barghausen, A.F., J.W. Finney, L.L. Proctor, and L.D. Shultz, (1969), Predicting Long-Term Operational Parameters of High Frequency Skywave (NTIS Doc. No. N70-24144), Boulder, Colorado.

Barnes, R.I., R. S. Gardiner-Garden and T. J. Harris, Real time ionospheric models for the Australian Defense Force, Proceedings of a Workshop on the Applications of Radio Science, La Trobe University, 27-29 April, 2000.

Baron, M.J., Electron densities within aurora and other auroral E-region characteristics, Radio Science, 9, 2, 341-348, 1974.

Bates, H.F., and R.D. Hunsucker, Quiet and disturbed electron density profiles in the auroral zone ionosphere, Radio Science, 9, 4, 455-467, April 1974.

Batista, I.S., E.R. Paula, M.A. Abdu, and N.B. Trivedi, Ionospheric effects of the March 13, 1989, magnetic storm at low and equatorial latitudes, Journal of Geophysical Research, 96, 13 943 – 13952, 1991.

Baumjohann, W., O.H. Bauer, G. Haerendal, and H. Junginger, Magntospheric plasma drifts during a sudden impulse, Journal of Geophysical Research, 88, 9287, 1983.

Baumjohann, W., and Y. Kamide, Hemispherical joule heating and the AE indices, Journal of Geophysical Research, 89, 383, 1984.

Bent, R. B., S. K. Llewellyn, and P. E. Schmid, (1972) A Highly Successful Empirical Model for the Worldwide Ionospheric Electron Density Profile, DBA Systems, Melbourne, Florida,.

Bilitza, D., (1992), 'Solar-terrestrial models and application software', Planet Space Science, 40, 541.

Blagoveshchensky, D.V., and T.D. Borisova, Substorm effects of ionosphere and HF propagation, Radio Science, 35, 5, 1165-1171, 2000.

Blagoveshchensky, D.V., V.M. Vystavnoi and M.A. Sergeeva, HF radio propagation through the auroral oval during substorms, Journal of Atmospheric and Solar-terrestrial Physics, 67, 1618-1625, 2005.

Blagoveshchensky, D.V., A.S. Kalishin and M.A. Sergeeva, Space weather effects on radio propagation: Study of the CEDAR, GEM and ISTP storm events, Annales Geophysicae, 26, 1479-1490, 2008

Blake, J.B., A. Kolasinki, R.W. Fillius, and E.G. Mullen, Injection of electrons and protons with energies of tens of MeV into L<3 on March 24, 1991, Geophysical Research Letters, 19, 821, 1992.

Boudouridis, A., E. Zesta, L. R. Lyons, P. C. Anderson, D. Lummerzheim, Magnetospheric reconnection driven by solar wind pressure fronts, Annales Geophysicae, 22, 1367-1378, 2004.

Bowles, K. L., R. Cohen, G.R. Ochs, B. Balsley, Radio echoes from field-aligned ionization above the magnetic equator and their resemblance to auroral echoes, Journal of Geophysical Research, 65, 1853-1855, 1960.

Bradley, P.A., and Dudeney, J.R. (1973) 'A simple model of the vertical distribution of the electron concentration in the ionosphere', Journal Atmospheric and Terrestrial Physics, 35, 2131.

Bradley, P.A., "HF Applications and Prediction", Chapter 17 of "Propagation of Radiowaves, IEE, 1996.

Breit, G., and M.A. Tuve, A test for the existence of the conducting layer, Physical Review, 28, 554-575, 1926.

Brekke, A., The effective recombination coefficient measured in the auroral E-region during a sudden commencement electron precipitation event, Journal of Atmospheric and Terrestrial Physics, 37, 825 – 833, 1975.

Bröms, M., and B. Lundborg, Results from Swedish oblique sounding campaigns, Annali di Geofisica, Vol XXXVII, N.2, 1994.

Brown, R. R. and Driatsky, V. M., Further Studies of Ionospheric and Geomagnetic Effects of Sudden Impulses, Planet. Space Sci., 21, 1931–1935, 1973.

Brown, R. R., T.R. Hartz, B. Landmark, H. Leinbach, H., and J. Ortner, Large-Scale Electron Bombardment of the Atmosphere at the Sudden Commencement of a Geomagnetic Storm, Journal of Geophysical Research, 66, 1035–1041, 1961.

Brown R.R, Sudden commencement and sudden impulse absorption events at high latitudes, Journal Geophysics Research, 78, 5698, 1973.

Brown, R.R., Auroral-zone electron precipitation accompanying a sudden impulse in the geomagnetic field, Journal Geophysical Research, 72, 2448-2451, 1967.

Brown, R.R., X-rays accompanying the magnetic storm of June 27, 160, Arkiv Geofysik, 3, 435-439, 1961.

Brown, R.R., H. Leinbach, S.-. Akasofu, Quadruple conjugate pair observations of the sudden commencement absorption event on June 17, 1965, Journal of Geophysical Research, 77, 28, 5602 – 5607, 1972.

Browne, S, J.K.Hargreaves and B. Honary, An imaging riometer for ionospheric studies, Electronics and Communications Engineering Journal, 1995.

Bryant, D.A., K. Aarsnes, G.M. Courtier, H.R. Lindalen, K. Maseide, G. Skovli, Electron density and electron flux in a glow aurora (Lower E region recombination coefficients from electron density and flux measurements in glow aurora by Nike-Apache rocket), Journal of Atmospheric and Terrestrial Physics, 32, 1695-1704, 1970.

Buchau, J., G.J. Gasman, C.P. Pike, R.A. Wagner and J.A. Whalen, Precipitation patterns in the Arctic ionosphere determined from airborne observations, Annales de Geophysique, 28, 443-453, 1972.

Budden, K.G., The propagation of radio waves, the theory of radio waves of low power in the ionosphere and magnetosphere, Cambridge University Press, New York, 669, 1985.

Burch, J.L., Preconditions for the triggering of polar magnetic sub storms by storm sudden commencements. Journal of Geophysical Research, 77, 5629, 1972.

Burlaga, L.F., and K.W. Ogilvie, Causes of Sudden Commencements and Sudden Impulses Journal Geophysical Research, 74, 2815, 1969.

Burton, R.K., R.L. McPherron and C.T. Russell, An empirical relationship between interplanetary conditions and Dst., Journal of Geophysical Research, 80, 4204, 1975.

Buonsanto, M.J., Ionospheric storms – a review, Space Science Reviews, 88, 563-601, 1999.

C

Cabral, J.J., ICAO High frequency management guidance material for the North Atlantic region, Nat Doc 003, North Atlantic systems planning groups, ICAO aeronautical communications group, 30 Sept 2003.

Cahill, L.J., and P.G. Amazeen, The boundary of the geomagnetic field, Journal of Geophysical Research, 68, 1835, 1963.

Cander, Lj.R., R. Leitinger and M.F. Levy, Ionospheric models including the auroral environment, in proceedings of ESA Workshop on Space Weather, ESTEC, Noordwijk, The Netherlands, 11-13 November 1998.

Cannon, P., Propagation in the ionosphere, in AGARD lecture series 196, Propagation modelling and decision aids for communications, radar and navigation systems, AGRAD, ISBN 92-836-1004-0, 1994.

Cannon, P.S., Morphology of the high latitude ionosphere and its implications for HF Communications systems, Procedures of the Institute of Electrical Engineers, 136(1), 1-10, 1989.

Cannon, P.S., J.A. Weitzen, J. Ostergaard, J.E. Rasmussen, Relative impact of meteor scatter and other long-distance high-latitude propagation modes on VHF communication systems, Radio Science, 31(5), 1129-1140, September-October 1996.

Carpenter, D.L, Whistler evidence of a “knee” in the magnetospheric ionisation density profile, Journal of Geophysical Research, 68, 1675, 1963.

Carpenter, D.L, and C.G. Park, On what ionospheric workers should know about the plasmapause-plasmasphere, Reviews of Geophysics and Space Physics, 11, 133, 1973.

Carpenter, D. L., Recent research on the magnetospheric plasmapause, Radio Science, 3, 719-725, 1968.

CCIR, Report 252-2, CCIR interim method for estimating sky-wave field strength and transmission loss at frequencies between the approximate limits of 2 and 30 MHz, in Recommendations and reports of the CCIR, Vol 2, Part 2, Propagation in ionised media, ITU, Geneva, 1970.

CCIR, Supplement to Report 252-2, Second CCIR computer based interim method for estimating sky-wave field strength and transmission loss at frequencies between 2 and 30 MHz, Geneva, 1982.

CCIR, Report 894, Simple HF prediction method for MUF and field strength, Report 894-1, pp. 239-245, in Recommendations and reports of the CCIR, Vol VI, Propagation in ionised media, ITU, Geneva, 1986.

Chapman, S., The absorption and dissociative or ionising effect of monochromatic radiation in an atmosphere on a rotating earth, Proceedings of the Physical Society, 43, 26-45, 1931.

Chapman, S., and V.C.A. Ferraro, A new theory of magnetic storms, Terrestrial Magnetism and Atmospheric Electricity., 36, (3) 171 – 186, 1931.

Chapman, S., and V.C.A. Ferraro, The theory of the first phase of a geomagnetic storm, Terrestrial Magnetism and Atmospheric Elec., 45, 245-268, 1940.

Chen, L., and A. Hasegawa, A theory of long period magnetic pulsations 1. steady state excitation of filed line resonance, Journal of Geophysical Research, 79, 1024, 1974.

Ching B. K. and Chiu Y. T., (1973) 'A Phenomenological Model of Global Ionospheric Electron Density in the E-, F1-, and F2-Regions', J. Atmos. Terr. Phys. 35, 1615.

Chiu, Y. T. (1975) 'An Improved Phenomenological Model of Ionospheric Density', J. Atmos. Terr. Phys. 37, 1563.

Cornilleau-Wekrlin, N., J. Solomon, A Korth, and G. Kremser, Experimental evidence of the relationship between energetic electrons and ELF waves observed onboard GEOS: A support to quasi-linear theory, Journal of Geophysical Research, 90, 4141, 1985.

Collier, M.R., J. A. Slavin, R. P. Lepping, K. Ogilvie, A. Szabo, H. Laakso, and S. Taguchi, Multispacecraft observations of sudden impulses in the magnetotail caused by solar wind pressure discontinuities: Wind and IMP 8, Journal of Geophysical Research, 103, A8, 17293–17306, 1998.

Collis, P.N., and I. Haggstrom, High latitude ionospheric response to a geomagnetic sudden commencement, Journal of Atmospheric and Terrestrial Physics, 53, 3/4, 241-248, 1991.

Cornwall, J.M., Diffusion processes influenced by conjugate-point wave phenomena, Radio Science, 3, 740, 1968.

Coroniti, F.C., and C.F. Kennel, Changes in magnetospheric configuration during the substorm growth phase, Journal of Geophysical Research, 77, 3361-3370, 1972.

Coroniti, F. V. and Kennel, C. F., Electron precipitation pulsations, Journal of Geophysical Research, 75, 1279–1289, 1970.

D

Damtie, B., T. Nygrén, M.S. Lehtinen, and A. Huuskonen, High resolution observations of sporadic-E layers within the polar cap ionosphere using a new incoherent scatter radar experiment, Annales Geophysicae, 20, 1429-1438, 2002.

Davé, N., The use of mode structure diagrams in the prediction of high-latitude HF propagation, Radio Science, 25, 4, 309 – 323, 1990.

Davies, K., Ionospheric radio propagation, NBS Monogram 80, Chapter 4, pp. 165-192, April, 1965.

Davies, K., Ionospheric Radio propagation, Dover Publications, 1966.

Davies, K., Ionospheric Radio, Peter Peregrinus Press, IEE Electromagnetic Waves Series 31, London, ISBN 086341186X ,1990.

Desorgher, L., P. Buhler. A. Zehnder, E. Daly and L. Adams, Outer radiation belt variations during 1995, Advances in Space. Research, 22, 83, 1998.

Di Giovanni, G., Radicella, S.M., and Zhang, M-L (1992) 'Further development of the DGR ionospheric model and comparison with the IRI current model', COST238TD(92)021, May 1992.

Donnelly, R.F. Ed. Solar-Terrestrial Predictions Proceedings:
Vol. I (1979) Prediction Group Reports,
Vol. II (1979) Working Group Reports and Reviews,
Vol. III (1980) Solar Activity Predictions,
Vol. IV (1980) Predictions of Terrestrial Effects of Solar Activity. US Dept. of Commerce, US Govt. Printing Office, Washington, DC..

Dressler, A. J., The propagation velocity of world-wide sudden commencements of magnetic storms, Journal of Geophysical Research, 63, 405-408, 1958.

Dressler, A.J and E.N. Parker, Hydromagnetic theory of geomagnetic storms, Journal of Geophysical Research, 64, 2239-2252, 1959.

Dungey, J.W., Interplanetary magnetic field and the auroral zones, Physics Reviews Letters, 6, 47-48, 1961.

Dudeney, J.R.,'An improved model of the variation of electron concentration with height in the ionosphere', Journal Atmospheric and Terrestrial Physics, 40, 195, 1978.

Dudeney, J.R., and R.I. Kressman, Empirical models of the electron concentration of the ionosphere and their value for radio communications purposes, Radio Science, 21(3), 319, 1986.

E

Eather, R. H., Secondary processes in proton auroras, Journal of Geophysical Research, 72, 1481, 1967.

Eather, R.H., and S.B.Mende, High latitude particle precipitating and source regions in the magnetosphere, Proceedings of the advanced study institute at Delseter, Norway, 14-23 April (ISBN 82 00 02263 3), 1971.

Eather, R.H., and S.B. Mende, High Latitude particle precipitation and source regions in the magnetosphere, In Magnetosphere-ionosphere interactions, edited by K. Folkestad, Scandinavian University Books, ISBN: 82 00 02263 3, 1972.

Edwards, K.J., L. Kersley and L.F. Shrubsole, Sporadic E propagation at frequencies around 70 MHz, Radio Elect. Eng., 54, 231-237, 1984.

Eriksen, K. W., B, Landmark, L. Finn, B. Machlum, E.V. Thrane, Agardograph 104 - High Frequency Radio Communications with Emphasis on Polar Problems, Technivision, Maidenhead, 1967.

Etcheto, J., R. Gendrin, J. Solomon, and A. Roux, A self-consistent theory of magnetospheric ELF hiss, Journal of Geophysical Research, 78, 34, 8150-8166, 1973.

F

Fairfield, D.H., Average and unusual locations of the earth's magnetopause and bow shock, Journal of geophysical research, 76, 6700-6719, 1971.

Fairfield, D. H., J. Jones, Variability of the tail lobe field strength, Journal of Geophysical Research, 101, A4, 7785-7792, 1996.

Farrugia, C.J., M.P. Freeman, S.W.H. Cowley, D.J. Southwood, M. Lockwood and A. Etemadi, Pressure-driven magnetopause motions and attendant response on the ground, Planetary Space Science, 37, 5, 589 -607, 1989.

Ferraro, V.C.A., On the theory of the first phase of a magnetic storm: a new illustrative calculation based on an idealised model field distribution, Journal of Geophysical Research, 57, 15-49, 1952.

Ferraro, V.C.A., Theory of sudden commencements and of the first phase of a magnetic storm, Review of Modern Physics, 32, 934-940, 1960a.

Ferraro, V.C.A., An approximate method of estimating the size and shape of the stationary hollow carved out in a neutral ionised stream of corpuscles impinging on the geomagnetic field, Journal of Geophysical Research, 65, 3951-3953, 1960b.

Ferraro, V. C. A., W. C. Parkinson, and H. W. Unthank, Sudden commencement and sudden impulses in geomagnetism: Their hourly frequency at Cheltenham (MD.), Tucson, San Juan, Honolulu, Huancayo and Watheroo, Journal of Geophysical Research, 56, 177-195, 1951.

Fricker, R., 1987, "A Microcomputer Program for HF Field Strength Prediction", IEE Conf.Pub.#274, Fifth International Conference on Antennas and Propagation, ICAP'87, pp.293-296, IEE, UK.

Friedrich, M., Data coverage for D-region modelling, in the proceedings of XXVIIth General Assembly of the International Union of Radio Science, Maastricht, the Netherlands, 17-24 August 2002.

Frihagen, J., Electron density profiles in the ionosphere and exosphere, Proceedings of NATO advanced Study, Finse, Norway, 1965.

G

Gail, W.B., U. S. Inan, R. A. Helliwell, D. L. Carpenter , Gyroresonant wave-particle interactions in a dynamic magnetosphere, Journal of Geophysical Research, 95, A9, 15103 – 15112, 1990a.

Gail, W.B., U.S. Inan, R.A. Helliwell, D.L. Carpenter, S. Krisnaswamy, T.J. Rosenberg and L.J. Lanzerotti, Characteristics of wave-particle interaction during sudden commencements. 1. Ground-based observations, Journal of geophysical research, 95, 119-137, 1990b.

Gail, W.B., and U.S. Inan, Characteristics of wave-particle interactions during sudden commencements. 2. Spacecraft observations, Journal of Geophysical Research, 95, A1, 139-147, 1990c.

Gannon, J.L., X. Li and M. Temerin, Parametric study of shock-induced transport and energisation of relativistic electrons in the magnetosphere, Journal of Geophysical Research, 110, 2005.

Gardiner-Garden, R., A. Heitmann, B. Northey and M. Turley, Modeling uncertainty in a real-time model (nowcast) of the ionosphere, 12th International Ionospheric Effects Symposium, IES2008, 13-15 May, 2008.

Gikas Stefanos S., A Comparison of High-Latitude Ionospheric Propagation Predictions from Advanced Prophet 4.0 with Measured Data, Masters Thesis, Naval Postgraduate School, Monterey. California, 1990.

Gonzalez, W.D., J.A. Joselyn, et al., What is a geomagnetic storm?, Journal of Geophysical Research, 99, 5771-5792, 1999.

Goodman J.M., 'HF Communications': Science and Technology, Van Nostrand Reinhold, New York, 1991/92.

Goodman, J.M., (1991), "A Review of Methods for Coping with Ionospheric Variability in Connection with FIF Systems", Fifth International Conference on HF Radio Systems and Techniques; Conf.Pub.No339, IEE, London, UK.

Goodman, J.M., and J.W. Ballard, Dynamic management of HF communication and broadcasting systems, IEE Colloquium on Frequency Selection and Management Techniques for HF Communications pp 18/1 – 18/05, 1999.

Goodman, J.M. and J.W. Ballard, An examination of elevated frequency propagation over a transpolar path, Radio Science, Vol 39, RS1S29, doi 10.1029/2002RS002850, 2004.

Goodman, J.M., J.W. Ballard and E. Sharp, A long term investigation of the HF communication channel over middle- and high-latitude paths, Radio Science, Vol 32, No. 4, 1705-1715, 1997.

Gosling, J. R. Asbridge, S. J. Bame, Jr., A. J. Hundhausen, and I. B. Strong, Discontinuities in the Solar Wind Associated with Sudden Geomagnetic Impulses and Storm Commencements, J. Geophysical Research., 72, 3357, 1967.

Gosling, J.T., S.J. Bame, D.j. McComas and J.L. Phillips, Coronal mass ejections and large geomagnetic storms, Geophysical research letters, 17, 901-904, 1990.

Gussenhoven, M.S., E.G. Mullen and E. Holeman, Radiation belt dynamics during solar minimum, IEEE Transactions on Nuclear Science, 36, 2008, 1989.

Gussenhoven, M.S., E.G. Mullen and M.D. Violet, Solar particle events as seen on CRRES, Advances in Space Research, 14, 10, 619-629, 1994.

Gustafsson, G., Ionization in the D-region during auroral break-up events, Planetary and Space Science, 12, 3, 195-208, 1964.

H

HAARP, Website text, "Occasional spikes in the received signal that go above the quiet day curve are caused by interference from broadcast signals in the 30 MHz band", http://137.229.36.30/cgi-bin/riometer/riom2_sel.cgi, downloaded 10 July 2008.

Haerendel, G., Acceleration from field-aligned potential drops, Astrophysical Journal Supplement Series, 90, 2, 765-774, 1994.

Hargreaves, J.K., The Solar-terrestrial Environment, Cambridge Atmospheric and Space Science Series No. 5, Cambridge University Press, 1995.

Hargreaves, J.K., Auroral motions observed with riometers: latitudinal movements and a median global pattern, Journal of Atmospheric and Terrestrial Physics, 30, 1461-1470, 1968.

Hargreaves, J.K., The Solar–Terrestrial Environment, Cambridge University Press, Cambridge, UK, 1992.

Hargreaves, J.K., 1969. Auroral absorption of HF radio waves in the ionosphere: A review of results from the first decade of riometry, Proceedings of the IEEE 57, 1348–1373.

Hartz, T.R., Multi-station riometers observations, in Radio Astronomical and Satellite Studies of the Atmosphere, ed. J. Aarons, North-Holland, Amsterdam, 1963.

Hartz, T.R., and N.M. Brice, The general pattern of auroral particle precipitation, Planetary Space Science, 15, 301-329, 1967.

Hatfield, V.E., (1980), "HF Communications Predictions, 1978 (An Economical Up-to-Date Computer Code, AMBCOM)", Solar-Terrestrial Predictions Proceedings vol.4, pp. D2 1-15, R.F. Donnelly (editor), U.S. Gov. Print Office, Washington DC.

Hayashi, K., S. Kokubun and T. Oguti, Polar chorus emission and worldwide geomagnetic variation, Report on Ionospheric and Space Research in Japan, 22, 149, 1968.

Hedin, A.E. and A.O. Nier, A Determination of the Neutral Composition, Number Density, and Temperature of the Upper Atmosphere from 120 to 200 Kilometres with Rocket-Borne Mass Spectrometers, Journal of Geophysical Research, 71, 4121, 1966.

Helliwell, R.A., Whistlers and related ionospheric phenomena, Stanford University press, Stanford, California, 1965.

Herman, J.R. and R.B Penndorf, Reception of mid-latitude transmissions in northern Canada, in Arctic Communications, Edited by B. Landmark, AGARDograph 78, pp 97-119, 1963.

Hess, W.N., The radiation belt and Magnetosphere, pg 293 – 300, Blaisdell publishing company, 1968.

Hill, T.W. and M.E. Rassback, Interplanetary magnetic field direction and the configuration of the day side magnetosphere, Journal of Geophysical Research, 80, 1-6, 1975.

Hinteregger, H. E., L. A. Hall and G. Schmidtke, Solar XUV radiation and neutral particle distribution in July 1963 thermosphere. Space Research V, Amsterdam, North-Holland Publ. Co., 1175-1190, 1965.

Hirshberg, J., Note on ring currents in the absence of sudden commencement storms, *Journal Geophysical Research*, 68, 6201, 1963.

Hirshberg, J., A. Alksne, D. S. Colburn, S. J. Bame, and A. J. Hundhausen, Observation of a Solar Flare Induced Interplanetary Shock and Helium-Enriched Driver Gas, J. Geophysical Research., 75, 1, 1970.

Hoffman, D.J., and J.R. Winckler, Simultaneous balloon observations at Fort Churchill and Minneapolis during the solar cosmic ray events of July 1961, Journal of Geophysical Research, 68, 2067-2098, 1963.

Huang C., Foster J.C., Goncharenko L.P., Erickson P.J., Rideout W, Large increase of the midlatitude ionospheric electron density in response to a magnetic storm, Presentation at the CEDAR workshop, Sante Fe, New Mexico, June 27 – July 2, 2004.

Hudson, M.K., A.D. Kafelnikov, X. Li, I. Roth, J.R. Wygant, J.R., M. Temerin, J.B. Blake, and M.S. Gussenhoven, Simulation of proton radiation belt formations during the March 24, 1991 SSC, Geophysical Research Letters, 22(3), 291-294, February 1995.

Hudson, M.K., S.R. Elkington, J.G. Lyon, V.A. Marchenko, I.Roth, M. Tererin, J.B. Blake, M.S. Gussenhoven and J.R. Wygant, Simulations of radiation belt formation during storm sudden commencements, Journal of Geophysical research, Vol 102, A7, 14 087 – 14102, July, 1997.

Hudson, M. K.; V.A. Marchenko, I. Roth, M. Temerin, J.B. Blake, and M.S. Gussenhoven, Radiation belt formation during storm sudden commencements and loss during main phase, Advances in Space Research, Vol 21, Issue 4, p. 597-607, 1998.

Hughes, W.J., The magnetopause, magnetotail and magnetic reconnection, in Introduction to Space Physics, edited by M.G. Kivelson and C.T. Russel, pg. 227-287, Cambridge University Press, New York, 1995.

Hunsucker, R.D., Auroral and polar-cap ionospheric effects on radio propagation, IEEE Transactions on Antennas and Propagation, 40, 818-828, 1992.

Hunsucker, R.D., Anomalous propagation behaviour of radio signals at high-latitudes, in Proceedings of AGARD Conference, CP-332, 11-1 to 11-15, 1983.

Hunsucker, R.D., Chatanika radar investigation of high latitude E-region ionisation structure and dynamics, Radio Science, 10, 3, 277-288, 1975.

Hunsucker, R.D., Final report on PENEX data analysis project for the naval postgraduate school, Naval Postgraduate School, Monterey, California, 1999.

Hunsucker, R.D., and H.F. Bates, Survey of polar and auroral region effects on HF propagation, Radio Science, 4, 347-365, 1969.

Hunsucker, R.D., and J.K. Hargreaves, The high-latitude ionosphere and its effects on radio propagation, Cambridge University Press, ISBN 0 521 33083 1, 2003.

Hunsucker R.D and J.K. Hargreaves, The high-latitude ionosphere and its effects on radio propagation, Cambridge, Cambridge atmospheric and space science series, Cambridge University Press, 2003.

Hunsucker, R.D., R.B. Rose, R.W. Adler and G.K. Lott, First results from the Alaska auroral-E propagation experiment, in Solar-Terrestrial Predictions – IV, Volume 3, 1992

Hunsucker, R.D., R.B. Rose, R.W. Adler, G.K. Lott, Auroral-E mode oblique HF propagation and its dependence on auroral oval position, IEEE Transactions on Antennas and Propagation, 44, 3, 383 – 388, 1996.

Hunten, D.M., and M.B. McElroy, Metastable O_2 as a major source of ions in the D-region, Journal of Geophysical Research, 73, pg 2421, 1968.

I

IAGA Bulletin No. 32t, Geomagnetic Data 1989, Berthelier. A. and Menvielle. M (editors), ISGI Publications Office, Saint Maur des Fosses Cedex, France.

Imhof, W. L., J.B. Reagan, H.D. Voss, E.E. Gaines, D.W. Datlowe, J. Mobilia, R.A. Helliwell, U.S. Inan, J. Katsufrakis, and R.G Joiner, Direct observation of radiation belt electrons precipitated by the controlled injection of VLF signals from a ground-based transmitter, Geophysical Research Letters, 10, 361-364, 1983.

ISGI (2008), Service International des Indices Geomagnetiques, Bureau des publications du SIIG, at http://isgi.cetp.ipsl.fr/lesdonne.htm, 23 March 2008.

ITU, Handbook on the ionosphere and its effects of Radiowave propagation, Radiocommunications Bureau, The International Telecommunications Union, 1998.

ITU, Prediction of Sporadic E, Report 344-1, Study programme 4A-1/6, ITU, 1970.

ITU, HF Propagation prediction methods, P.533, ITU, Geneva, 1995.

ITU, ITU-R Recommendation F.339-6, Bandwidths, Signal-to-noise ratios and fading allowances in complete fixed systems, 2006.

ITU, About the ITU, http://www.itu.int/net/about/index.aspx, 2007.

ITU Recommendation ITU-R P.1239, ITU-R Reference Ionospheric Characteristics, 1997, The International Telecommunications Union, Geneva.

ITU Recommendation ITU-R P.1240, ITU-R methods of basic MUF, operational MUF and ray-path prediction, 1997, The International Telecommunications Union, Geneva.

ITU Recommendation ITU-R F.348, Arrangement of channels in multi-channel SSB and ISB transmitters for long-range circuits operating at frequencies below 30 MHz, June 1990.

ITU Recommendation ITU-R TF. 768, Standard frequencies and time signals, May 2003.

IUGG Publications, "A Hundred Year Series of Geomagnetic Data 1868-1967". IAGA Bulletin #33, 39 ter rue Gay-Lussac, 75005 Paris France.

Ivanov, V.A., V.I. Kurkin, V.E. Nosov, V.P. Uryadov and V.U. Shumaev, Chirp ionosonde and its application in the ionospheric research, Radiophysics and Quantum Electronics, 46, 11, 821 – 851, 2003.

Ivanov-Kholodny, G.S., and A.V. Mikhailov, The prediction of ionospheric conditions, Geophysics and Astrophyics Monographs, D. Reidel Publishing Company, ISBN 90 -277-2143-2, 1986.

J

Johnson, C.Y., Ion and neutral composition of the ionosphere, Annals IQSY, 5, 197, 1969

Joselyn, J.A., and B.T. Tsurutani, A note on terminology: Geomagnetic sudden impulses (Sis) and storm sudden commencements (SSCs), Eos Transactions, AGU, 71, 1808, 1990.

Jones, K.L., and H. Rishbeth, The origin of storm increases of mid-latitude F-layer electron concentration, Journal of Atmospheric and Solar Terrestrial Physics, 33(3), 391, 1971.

Jull, G.W., D.J. Doyle, J.P. Murray, Frequency sounding techniques for HF communications over auroral paths, Proceedings of the IRE, 50(7), 1676-1682, 1962.

Jull, G.W., HF propagation in the artic, Chapter 15 in Arctic Communications, Edited by B. Landmark, pp 157-176, Pergamon, New York, 1964.

Jursa, A.S., Handbook of geophysics and the space environment, 4th edition, Final Report Air Force Geophysics Lab., Hanscom AFB, MA., 1985.

K

Kamiyama, H.J., The electron density distribution in the lower ionosphere produced through impact ionisation by precipitating electrons and through photo ionisation by

the associated Bremsstrahlung X-Rays, Journal of Geomagnetism and Geoelectricity, 19, 27, 1967.

Kan, J.R, and S.-I. Akasofu, A model of the open magnetosphere, Coroniti, F.C., and C.F. Kennel, Journal of Geophysical Research, 79, 1379-1384, 1974.

Kaufmann, R. L., and D.N. Walker, Hydromagnetic waves excited during an SSC, Journal of Geophysical Research, 79, 5187-5195, 1974.

Kauffman, R.L., and A. Konradi, Explorer 12 magnetopause observations: Large scale no uniform motion, Journal of Geophysical Research, 74, 3609, 1969.

Kavanagh, A. J., F. Honary, I. W. McCrea, E. Donovan, E. E.Woodfield, J. Manninen, and P. C. Anderson, Substorm related changes in precipitation in the dayside auroral zone – a multi instrument case study, Annales Geophysicae, 20, 1321–1334, 2002.

Kawano, H., T. Yamamoto, S. Kokubun, R. P. Lepping, Rotational polarities of sudden impulses in the magnetotail lobe, Journal of Geophysical Research, 97, A11, 17177–17182, 1992.

Kawasaki, K., S.-. Akasofu, F. Yasuhara, C.-.Meng, Storm sudden commencements and polar magnetic substorms, Journal of Geophysical Research, 76, 28, 6781-6789, 1971.

Kennel, C.F., and H.E. Petschek, Limit on stably trapped particle fluxes, Journal of Geophysical Research, 71, 1 - 28, 1966.

Kennel, C.F., Consequences of a magnetospheric plasma, Reviews of Geophysics and Space Physics, 7, 379-419, 1969.

Kikuchi. T.: Evidence of transmission of polar electric fields to the low-latitude at times of geomagnetic sudden commencements, Journal of Geophysical Research, 91, 3101-3105, 1986.

Kikuchi, T. and T. Araki, Horizontal transmission of the polar electric field to the equator, Journal of Atmospheric and Terrestrial Physics, 41, 927, 1979b.

Kikuchi, T and H. Yamagishi, Latitudinal features of cosmic noise absorption at the time of SSC-triggered substorm a observed with scanning beam riometer, Proceedings of the NIPR symposium on upper atmospheric physics, 2, 9-14, 1989.

Kikuchi, T., T. Araki, H. Maeda, and K. Maekawa, Transmission of polar electric fields to the equator, Nature, 273, 650, 1978.

Kikuchi, T., and T. Araki, Transient response of uniform ionosphere and preliminary reverse impulse of geomagnetic storm sudden commencement, Journal of Atmospheric and Terrestrial Physics, 41, 917 – 925, 1979a.

Kim, H.-J and A.A. Chan, Fully adiabatic changes in storm-time relativistic electron fluxes, Journal of Geophysical Research, 102, A10, 22107 - 22116, 1997.

King, G.A.M., The night E layer, in Ionospheric Sporadic E, edited by E.K. Smith and S. Matsushita, p. 219, Pergamon Press, New York, 1962.

Kirby, S.S., and E.B. Judson, Recent Studies of the Ionosphere, Proceedings of the Institute of Radio Engineers, 23, 7, 733-751, 1935.

Kirkwood, S., and H. Nilsson, High-latitude sporadic –E and other thin layers – the role of magnetospheric electric fields, Space Science Reviews, 91, 579 – 613, 2000.

Knecht, R.W., and R.E. McDuffie, On the width of the equatorial E_s belt, Ionospheric Sporadic E, edited by E.K. Smith and S. Matsushita, Pergamon Press, Oxford, pp. 215 – 219, 1962.

Knecht, R.W., Statistical results and their shortcomings concerning the ionosphere within the auroral zone, pg 109 – 119, in Polar Atmosphere Symposium, part II, ionospheric section, AGARD, 1957.

Knecht, R. W., Relationships Between Aurora and Sporadic-E Echoes at Barrow, Alaska., Journal of Geophysical Research, 61, pp 59, 1956.

Knott, K., D. Fairfield, A. Korth, and D.T. Young, Observations near the magnetopause at the onset of the July 29, 1977, sudden storm commencement, Journal of Geophysical Research, 87, 5888, 1982.

Kohnlein, W., 1978, "Electron Density Models of the Ionosphere", Reviews of Geophysics and Space Physics 16(3): 341-354.

Kokubun, S., and T.Oguti, Hydromagnetic emissions associated with storm sudden commencements, Reports on Ionospheric and Space Research in Japan, 22, 45-59, 1968.

Kokubun, S., Characteristics of storm sudden commencement at geosynchronous orbit, Journal of Geophysical Research, 88, 10, 10025-10033, 1993.

Kokubun, S., R. L. McPherron, and C. T. Russell, Triggering of substorms by solar wind discontinuities, Journal of Geophysical Research, 82, 74, 1977.

Korth, A., G. Kremser, N. Cornilleau-Wekrlin, and J. Solomon, Observations of energetic electrons and VLF waves at geostationary orbit during storm sudden commencements (SCC), Proceedings of the Chapman Conference on Solar Wind – Magnetosphere Interactions, 1986.

Koskinen, H.E.J., Observations of magnetospheric waves and their relation to precipitation, Space Science Reviews, 80, 133-152, 1997.

Kuwashima, M., and H. Fukunishi, Local time asymmetries of the SSC-associated hydromagnetic variations at the geosynchronous altitude, Planetary Space Science, 33, 711, 1985.

L

LAGA Bulletin 33: "A Hundred Years` Series of Geomagnetic Data, 1868-1967. Indices aa and storm sudden commencements".

Lakhina, G.S., Tsurutani, B.T., Kojima, H., Matsumoto, H., A generation mechanism for the polar cap boundary layer broadband plasma waves, Journal of Geophysical Research, 104, A1, 279–292, 1999.

Landmark, B., Summary of Discussion, Chapter 14 of Arctic Communications, AGARDograph 78, pp 151-153, 1963.

Lane, G., Signal-to-Noise Predictions Using VOACAP, Including VOAAREA – A users guide, Rockwell Collins, 523-0780552-10111R, 2001.

Larsen, T.R., Disturbances in the high latitude lower ionosphere, NDRE Report no. 62, Norwegian Defence research Establishment, March 1973.

Larsen, T.R., Effects of D-region ionisation on radio wave propagation, in Donnelly, R.F.(Ed.): Solar-terrestrial predictions proceedings II, US GPO, Washington DC, pg 617, 1979.

Lauben, D.S., Inan, U.S., Bell, T.F., Kirchner, D.L., Hospodarsky, G.B. and Pickett, J.S., VLF chorus emissions observed by POLAR during the January 10, 1997 magnetic cloud. Geophysical Research Letters 25, p. 2995, 1998.

Layzer, D., The turbulence criterion in stably stratified shear flow and the origin of Sporadic E, in Ionospheric Sporadic E edited by E.K. Smith and S. Matsushita, Macmillan, New York, 1962.

Lee, D.-Y., L.R. Lyons, and K. Yumoto, Sawtooth oscillations directly driven by solar wind dynamic pressure enhancements, Journal of Geophysical Research, 109, A04202, 2004a.

Lee, D.-Y., J.A. Hwang, E.S. Lee, K.W. Min, W.Y. Han and U.W. Nam, How are storm time injections different from nonstorm time injections?, Journal of Atmospheric and Solar-Terrestrial Physics, 66, 18, 1715-1725, 2004b.

Leftin, M., Numerical representation of monthly median critical frequencies of the regular E region (f_oE), OT Report 76-88, US Govt. Printing Office, Washington, DC 20402, 1976 – as quoted in Davies, 1990.

Leid, F., High frequency radio communications with emphasis on polar problems, AGARDograph 104, Technivision, Maidenhead, UK, 1967.

Leighton, H.I., A.H. Shapley, and E.K. Smith, The occurrence of sporadic E during the I.G.Y., in Ionospheric Sporadic E, edited by E.K. Smith and S. Matsushita, p. 166, Pergamon Press, New York, 1962.

Leinbach, H, R.J. Schmidt, and R.R Brown, Conjugate observations of an electron precipitation event associated with the sudden commencement of a magnetic storm, Journal of Geophysical Research, 75, 7099, 1970.

Li, X., I. Roth, M. Temerin, D. Larson, R.P. Lin, G.D. Reeves, M. Looper, S.G. Kanekal and R.A. Mewaldt, Are energetic electrons in the solar wind the source of the outer radiation belt?, Geophysical Research Letters, 24, 923, 1997.

Li, X., and M. Temerin, The electron radiation belt, Space Science Reviews, 95, 569, 2001.

Li, X., I. Roth, M. Temerin, J.R. Wygant, M.K. Hudson, and J.B. Blake, Simulation of the prompt energisation and transport of radiation belt particles during the March 24, 1991 SSC, Geophysical Research Letters, 20, 2423, 1993.

Little, C.G., and H. Leinbach, 1959. The riometer – a device for the continuous measurements of ionospheric absorption, Proceedings of the Institute of Radio Engineers 37, 315-320.

Liou, K., P. T. Newell, C.-I. Meng, C.-C. Wu, R. P. Lepping, On the relationship between shock-induced polar magnetic bays and solar wind parameters, Journal of Geophysical Research, 109, A06306, 2004.

Lopez, R.E., C. Goodrich, M. Wiltberger and J. Lyon, Solar wind-magnetosphere energy coupling under extreme interplanetary conditions: MHD simulations, Journal of Atmospheric and Solar-Terrestrial Physics, Volume 62, Issue 10, p. 865-874, 2000.

Lombry, T., A Review of HF propagation analysis & prediction programs, http://www.astrosurf.com/luxorion/qsl-review-propagation-software.htm, accessed 8 December 2008.

Looper, M.D., J. Blake, R. Mewaldt, J. Cummings, and D. Baker, Observations of the remants of the ultrarelativistic electrons injected by the strong SSC of 24 March 1991, Geophysical research letters, 21, 2079, 1994.

Luhmann, J. G., T-L. Zhang, S. M. Petrinec and C. T. Russell, Solar cycle 21 effects on the interplanetary magnetic field and related parameters at 0.7 and 1.0 AU, Journal of Geophysical Research, 98, 5559-5572, 1993.

Lundborg, B., M. Bröms and H. Derblom, Oblique sounding of an auroral ionospheric HF channel, Journal of Atmospheric and Terrestrial Physics, Vol 57, No 1, 51 – 63, 1995.

Lucas, D. and G.W. Haydon, 1966, "Predicting Statistical Performance Indices for High Frequency Telecommunications Systems", Report IER 1-ITSA 1, U.S. Department of Commerce, Boulder, Colorado.

Lyons, L. R., R.M. Thorne, and C.F. Kennel, Pitch-angle diffusion of radiation belt electrons within the plasmasphere, Journal of Geophysical Research, 77, 3455 – 3474, 1972.

Lyons, L.R., and A.D. Richmond, Low latitude E region ionisation by energetic ring current particles, Journal of Geophysical Research, 83, 2201 – 2204, 1978.

Lyons, L.R., and R.M. Thorne, Equilibrium structure of radiation belt electrons, Journal of Geophysical Research, 78, 2142, 1973.

Lyons, L.R., and D.J. Williams, Quantitative aspects of magnetic physics, D. Reidel, Boston, 1984.

Lysak, R.L., Song, Y., Grieger, J.C., Coupling of the magnetopause to the ionosphere by means of Alfvén waves and field-aligned currents. In: Song, P., Sonnerup, BUÖ., Thomsen, M.F. (Ed.), The Physics of the Magnetopause. American Geophysical Union, Washington, DC, 1995.

M

Machin, K.E., M. Ryle, D.D. Vonberg, The design of an equipment for measuring small radio-frequency noise powers, Proc. IEE, 99, pt3, 127, 1952.

Maeda, H., K. Sakurai, T. Ondoh, and M. Yamamoto, Solar terrestrial relationships during the IGY and IGC, Ann. Geophys, 18, 305, 1962.

Maeda, K., Diffusion of low energy auroral electrons in the atmosphere, Journal of Atmospheric and Terrestrial Physics, 27, 259, 1965.

Maezawa, K., Statistical study of the dependence of geomagnetic activity on solar wind parameters, in Quantitative Models of the Magnetosphere, AGU Monograph Series, 1979.

Maggs, J.E., Coherent generation of VLF hiss, Journal of Geophysical Research, 81, 1707, 1976.

Majeed, T., Comparison of percentage occurrence of E_s in Karachi and Islamabad under magnetic conditions, Indian Journal of Radio and Space Physics, 11, 3, 120, 1982.

Maksyutin, S.V., A.N. Fahrutdinova and O.N. Sherstyukov, E_s layer and dynamics of neutral atmosphere during the periods of geomagnetic disturbances, Jounral of Atmospheric and Solar-Terrestrial Physics, 63, 545-549, 2001.

Maltsev, Yu.P., and W.B. Lyatsky, Field-aligned currents and erosion of the dayside magnetopause, Planetary Space Science, 23, 1257-1260, 1975.

Marcos . T. D., A Comparison of High Latitude Ionospheric Propagation Predictions from IONCAP-PC 2.5 with Measured Data, Masters Thesis, Naval Postgraduate School, Monterey. California, 1990.

Martyn, D.F., The theory of magnetic stroms and auroras, Nature, 167, 92-94, 1951.

Mathews, J.D., Sporadic E: current views and recent progress, Journal of atmospheric and solar-terrestrial physics, 60, 4, 413-435, 1998.

Matsushita, S., On geomagnetic sudden commencements, sudden impulses and storm durations, Journal of Geophysical Research, 67, 10, 3753 - 3777, 1962.

Matsushita, S., Increase of ionisation associated with geomagnetic sudden commencements, Journal of Geophysical Research, 81, 2289, 1961.

Matsushita, S., On the sporadic E, Report on Ionospheric and Space Research in Japan, 7, 72-73, 1953.

Matsushita, S., Studies on sudden commencements of geomagnetic storms using IGY data from United States stations, J. Geophys. Res., 65, 1423, 1960.

Mayaud, P.N., Analysis of storm sudden commencements for the years 1868-1967, Journal of Geophysical Research, 80, 111, 1975.

McNamara, L.F., The ionosphere: Communications, Surveillance and Direction Finding, Krieger Publishing Company, Florida, 0-89464-040-2, 1991.

McIlwain, C.E., Coordinates for mapping the distribution of magnetically trapped particles, Journal of Geophysical Research, 66, 3681, 1961.

Mead, G.D., and D.B. Beard, Shape of the geomagnetic solar wind boundary, Journal of Geophysical Research, 69, 1169, 1964.

Milsom, J.D., 1987, "Outstanding Problems in Short-Term Ionospheric Forecasting", Fifth International Conference on Antennas and Propagation: A Hundred Years of Antennas and Propagation; Part 2: Propagation, ICAP 87, IEE Conf. Pub. No. 274, pp. 316-319, 1EE, London, UK.

Mitra, S.K., The upper atmosphere, 2nd Edition, Vol 5 of the Monograph Series, The Asiatic Society, Culcutta, 1952.

Morozumi, H.M., Enhancement of VLF chorus and ULF at the time of SC, Report on ionospheric and space research in Japan, 19, 371, 1965.

Morton, Y.T., and J.D. Mathews, Effects of the 13-14 March 1989 geomagnetic storm on the E-region tidal ion layer structure at Arecibo during AIDA, Journal of Atmospheric and Terrestrial Physics, 55, 467-485, 1993.

Muldrew, D.B., F-layer ionisation troughs deduced from Alouette data, Journal of Geophysical Research 70, 2635, 1965.

Muggleton, L.M., A method of predicting f_oE at any time and place, Telecommunication Journal, 42, VIII, 1975.

N

Nagano, H. and Araki, T., Seasonal variation of amplitude of geomagnetic sudden commencements near midnight at geostationary orbit, Planetary and Space Science, 34, 2, 205-217, 1986.

Nakai, H., Y. Kamide, C. T. Russell, Influences of solar wind parameters and geomagnetic activity on the tail lobe magnetic field: A statistical study, Journal of Geophysical Research, 96, A4, 5511–5523, 1991.

Naridner, N., I. Steen Mikkelsen and T. Stockflet Jørgensen, On the formation of high latitude E_s-layers, Journal of Atmospheric and Terrestrial Physics, 42 841 – 852, 1980.

Ness, N.F., The geomagnetic tail, Review of Geophysics, 7, 97 – 125, 1969.

Newton, R.S., D.J. Southwood, and W.J. Hughes, Damping of geomagnetic pulsations by the ionosphere, Planetary Space Science, 26, 201, 1978.

Nishida, A., Transmission of SSC through the interplanetary space: shock wave and non-shock mode, Report of Ionospheric and Space Research in Japan, 18, 295, 1964.

Nishida, A., and L.J. Cahill, Sudden impulses in the magnetosphere observed by Explorer 12, Journal of Geophysical Research, 69, 2243, 1964.

Nishida, A., Interpretation of SSC rise time, Report of Ionospheric and Space Research in Japan, 20, 42, 1966.

Nishida, A., Geomagnetic diagnosis of the magnetosphere, p23, Spriger-Verlang, New York, 1978.

Nishida, A., Ionospheric screening effects and sudden commencements, Journal of Geophysical Research, 69, 1761, 1964.

Nishida A, Jacobs J.A, Equatorial enhancement of world-wide changes, Journal Geophysical Research, 67, 4937, 1962.

NOAA, Space Weather Highlights for 26 July – 01 Aug 1999, SWO PRF 1248, issued 03 August 1999, 1999a.

NOAA, Space Weather Highlights for 13-19 September 1999, SWO PRF 1255, issued 21 September, 1999b.

NOAA 2005 –The U.S. Department of Commerce, National Oceanic and Atmospheric Administration, National Weather Service, Space Environment Center, Webpage on Space Weather Data and Products, www.sec.noaa.gov/Data/.

Northrop, T.G., The adiabatic motion of charged particles, Interscience Publishers, 1963.

Norman, R.J., I.G. Platt, P.S. Cannon, A HF ionospheric propagation model using analytic ray tracing, IEE Colloquium on HF Antennas and Propagation, pp. 8/1 – 8/6, 14 Nov 1995.

NTIA, High frequency radio automatic link establishment (ALE) application handbook, National Communications System Office of Technology and Standards, NTIA Boulder, September 1998.

Nygréen, T., L. Jalonen, J. Oksman, and T.Turunen, The role of electric field and neutral wind direction in the formation of sporadic E layers, Journal of Atmospheric and Terrestrial Physics, 46, 373-381, 1984.

O

Obayashi, T. and N. Matuura, Theoretical model of F-region storms, in Solar-terrestrial Physics, part IV, edited by E.R.Dyer, pp 199-211, D.Reidel, Norwell, Mass, 1970.

Ochs, A., "The Forecasting System of the Fernmeldetechnischen Zentralamt (FTZ)", in Ionospheric Forecasting, NATO-AGARD-CP-49, edited by V. Agy, paper no.43, 1970.

Odishaw, H (Editor), Research on Geophysics, Vol 1, The M.I.T. Press, pg 301, 1964.

Ogilvie, K.W., L.F. Burlage and T.D. Wilkerson, Plasma observations on Explorer 34, Journal of Geophysical Research, 73, 6809, 1968.

Olson, W.P., The shape of the tilted magnetopause, Journal of Geophysical Research, 74, 5642, 1969.

Olsen, J.V. and Lee, L.C., PC1 wave generation by sudden impulses. Planetary and Space Science 31, p. 295, 1983.

Omholt, A., The optical aurora (Physics and chemistry in space), pg 26, 180-182, Springer-Verlag, ISBN: 0387054863, New York, 1971.

Ondoh, T., Longitudinal distribution of ssc rise times, Journal of Geomagnetism and Geoelectricity, 14, 198, 1963.

Ortner J, Hultqvist B, Brown R.R, Hartz T.R, Holt O, Landmark B, Hook L and Leinbach H, Cosmic noise absorption accompanying geomagnetic storm sudden commencements, Journal Geophysics Research, 67, 4169, 1962.

Ostergaard, J., Short range communication systems, design and operation at very high latitudes, IEE International Conference on HF radio systems and techniques, IEE Conference Publication no. 284, London, 11-14 April 1998.

Owren, L., J. Ortner, K. Folkestad and R. Hunsucker, Arctic Propagation studies at ionospheric modes of propagation, Final report on contract no. AF 19(604) – 5574, The Geophysical Institute, University of Alaska, 1963.

P

Parker, E.N., Interplanetary dynamical process, Interscience, New York, 1963.

Parkinson, M.L., P.L. Dyson, D.P. Monselesan, and R.J. Morris, On the role of electric field direction in the formation of sporadic E-layers in the southern polar cap ionosphere, Journal of Atmospheric and solar-terrestrial physics, 60, 471-491, 1998.

Patel, V.L., and P.J. Coleman, Sudden impulses in the magnetosphere observed at synchronous orbit, Journal of Geophysical Research, 75, 7255 – 7260, 1970.

Paul, A.K., F-region tilts and ionogram analysis, Radio Science, 20, 4, 959 – 971, 1985.

Paulikas, G.A., and J.B. Blake, Effects of the solar wind on magnetospheric dynamics: Energetic electrons at he synchronous orbit, in Quantitative modelling of Magnetospheric Processes, Vol 21, edited by W.P. Olsen, pg 180, AGU, Washington D..C., 1979.

Paulikas, G.A., and J.B. Blake, Effects of Sudden Commencements on solar protons at the synchronous orbit, Journal of Geophysical Research, 75, 4, 734-742, 1970.

Paulikas G.A., G.A., Effects of solar particle events on the energetic particle population in the earth's magnetosphere, Solar Activity Observations and Predictions, Edited by Patrick S. McIntosh and Murray Dryer, Progress in Astronautics and Aeronautics, An American institute of Aeronautics and Astronautics series, Vol 30, Pp 265 – 283, The MIT press, Cambridge Massachusetts and London England, ISBN 0262130866, 1972.

Perona, G.E., Theory on the precipitation of magnetospheric electrons at the time of sudden commencements, Journal of Geophysical Research, 77, 101-111, 1972.

Perreault, P., and S.-I. Akasofu, A study of geomagnetic storms, Geophysical Journal of the Royal Astronomical Society, 54, 3, 547-573, 1978.

Pfotzer, G., Balloon measurements of solar protons and auroral X-rays, in Proceedings of a symposium on High latitude particles and the ionosphere, Alpbach 1964, edited by B. Mæhlum, 167 – 220, Academic Press, 1965.

Piddington, J.H., The transmission of geomagnetic disturbances through the atmosphere and interplanetary space, Geophysical Journal of the Royal Astronomical Society, 2, 173-189, 1959.

Piddington, J. H., Theories of the geomagnetic storm main phase, Planetary Space Science, 11, 1277, 1963.

Piddington, J.H., A theory of auroras and the ring current, Journal of Atmospheric and Terrestrial Physics, 29, 87, 1967.

Piggott, W.R., and R. Rawer, URSI Handbook of ionogram interpretation and reduction, 2nd Edition, Report UAG-23, World Data Centre A for solar terrestrial physics, NOAA, Boulder, Colorado, 1972.

Piggott, W.R., High-Latitude Supplement To The URSI Handbook On Ionogram Interpretation And Reduction, edited by W.R. Piggott, Report UAG-50, 1975.

Pytte, T., and H.I. Jr West, Ground-satellite correlations during presubstorm magnetic field configuration changes and plasma sheet thinning in the near-earth magnetotail, Journal of Geophysical Research, 83, A8, 1978.

Q

R

Radicella, S.M., R. Leitinger, G. Hochegger, B. Nava and P. Coïsson, Ionospheric model developments for satellite navigation and communication applications, Proceedings of the URSI General Assembly, 2002.

Ranta, A and Ranta, H., Storm sudden commencements observed in ionospheric absorption, Planetary Space Science, 38, 3, 365-372, 1990.

Rasinkangas. R, Mursula. K, Ulich. T. and Kangas. J, Oulu Space Physics Textbook, University of Oulu, http://www.oulu.fi/~spaceweb/textbook/, May 2005.

Rastogi, R.G., Pathan, B.M, Rao, D.R.K., Sastry, T.S., Sastri J.H., On latitudinal profile of Storm Sudden Commencement in H, Y and Z at Indian Geomagnetic Observatory chain, Earth Planets Space, No. 53, pp. 121 – 127, 2001.

Rastogi, R.G., D.R.K. Rao, S. Alex, B.M. Pathan, T.S. Sastry, An intense SFE and SSC event in geomagnetic H, Y and Z fields at the Indian chain of observatories, Ann. Geophysicae 15, 1301-1308, 1997.

Rastogi, R.G., Trivedi, N.B and Kaushika, N.D, Some relations between the sudden commencement in H and the equatorial electojet, Journal of Atmospheric and Terrestrial Physics, No.26, pp. 771-776, 1964.

Rastogi, R.G., Longitudinal variation of sudden commencement of geomagnetic storm at equatorial stations, Journal of Geophysics Research, No.98, pp. 15411 - 15416, 1993.

Ratcliffe, J.A., and E.L.C. White, An automatic recording method for wireless investigations of the ionosphere, Proceedings of the Physical Society, 45, 399-413, 1933.

Ratcliffe, J.A., A survey of solar eclipses and the ionosphere, in Solar eclipses and the ionosphere, pgs. 1 – 13, Edited by W.J.C. Beynon and G.M. Brown, Pergamon Press, Oxford, 1956.

Rawer, K., (1975), "The Historical Development of Forecasting Methods for Ionospheric Propagation of HF Waves", Radio Science 10(7): 669-679.

Rawer, K., Definitions of frequency parameters of E_s-layers and their accuracy, in Ionospheric Sporadic E edited by E.K. Smith and S. Matsushita, Macmillan, New York, 1962.

Rees, M.H., Auroral ionisation and excitation by incident energetic electrons, Planetary Space Science, 11, 1209-1218, 1963.

Rees, M.H., Note on the penetration of energetic electrons into the earth's atmosphere. Planetary Space Science, 12, 722, 1964.

Reid, C.R, Ionospheric effects of solar activity, pg 294 of Solar Activity Observations and Predictions, Edited by P.S. Mcintoch and M. Dryer, MIT Press, ISBN: 0-262-13086-6, 1972.

Reid, G.C., Ionospheric effects of particles, in Proceedings of a symposium on High latitude particles and the ionosphere, Alpbach 1964, edited by B. Mæhlum, 221 - 231, Academic Press, 1965.

Reilly, M.H., Rhoads, F.J. and Goodman, J.M. (1991), 'Update climatological model predictions of ionospheric and HF propagation parameters', Radio Science, 26,1017.

Reinisch, B. W., Modern Ionosondes, in Modern Ionospheric Science, edited by H. Kohl, R, Rüster and K. Schlegel, European Geophysical Society, ISBN 3-9804862-1-4, 1996.

Reinisch, B. W., I. A. Galkin, G. Khmyrov, A. Kozlov, and D. F. Kitrosser, Automated collection and dissemination of ionospheric data from the digisonde network, Advances in Radio Science, 2, 241-247, 2004.

Rishbeth, H., F-region storms and thermospheric circulation, in Electromagnetic coupling polar cleft and caps, proceedings of the NATO advanced research workshop, Lillehammer, September 20-24, Dordrecht, 393-406, 1989.

Ritchie, S.E., and F. Honary. Case Studies of Enhanced E-Layer Formation at High-Latitudes Following Sudden Commencement Absorption Events. In Proceedings of the 10th International Conference on Ionospheric Radio Systems and Techniques (IRST 2006). IC517. London, UK. 18th-21st July 2006.

Ritchie, S.E. and F. Honary, Observed characteristics of sudden commencement absorption, Journal of Atmospheric and Solar-Terrestrial Physics, doi:10.1016/j.jastp. 2008.11.011, 71 (5), 2009a.

Ritchie, S.E. and F. Honary, Observations on the variability and screening effect of sporadic-E, Journal of Atmospheric and Solar-Terrestrial Physics, doi: 10.1016/j.jastp.2009.05.008, Article in press, 2009b.

Roederer, J.G, Dynamics of geomagnetically trapped radiation, Springer-Verlag, 1970.

Rose R. B., Martin J. N., and Levine P. H., MINIMUF-3: A Simplified HF MUF Prediction Algorithm, Naval Ocean Systems Center, Report 186, San Diego, California, 1978.

Rose R.B., MINIMUF: A Simplified MUF Prediction Program for Microcomputers, QST 66(12), 36-28, 1982.

Rose, R.B., "MINIMUF Revisited", p. 46 (Technical Correspondence), QST, March, 1984.

Rosenberg, T.J., R.A. Helliwell, J.P. Katsufrakis, Electron precipitation associated with discrete very-low-frequency emissions, Journal of Geophysical Research, 76, 34, 8445-8452, 1971.

Rostoker, G., Jackel, B. and Arnoldy, R.L., The relationship of periodic structures in auroral luminosity in the afternoon sector of ULF pulsations. Geophysical Research Letters, 19, 613, 1992.

Rostocker, G., and C.-G. Fälthammar, Relationship between changes in the IMF and variations in the magnetic field at the Earth's surface, Journal of Geophysical Research, 72, 23, 5853-5863, 1967.

Rush C. M., Ionospheric Radio Propagation Models and Predictions-A Mini-Review, IEEE Trans. Antennas Propag. AP-34, 1163, 1986.

Rush, C.M., Miller, D. and Gibbs, J. (1974) The relative daily variability of *fo*F2 and hmF2 and their implications for HF radio propagation. ***Radio Sci.***, Vol. 9, 749-756.

Russell, C.T., The Magnetosphere, In The Solar Wind and the Earth, edited by S. -I. Akasofu and Y. Kamide, pp 73-100. Copyright by Terra Scientific Publishing Company (TERRAPUB), Tokyo, 1987.

Russell, C.T., M. Ginskey, S. Petrinec, and G. Le, The effect of solar wind dynamic pressure changes on low and midlatitude magnetic records, Geophysical Research Letters, 19, 1227-1230, 1992.

Russell, C.T., M. Ginskey, S. M. Petrinec, Sudden impulses at low-latitude stations: Steady state response for northward interplanetary magnetic field, Journal of geophysical Research, 99, A1, 253-262, 1994a.

Russell, C.T., M. Ginskey, S. M. Petrinec, Sudden impulses at low-latitude stations: Steady state response for southward interplanetary magnetic field, Journal of geophysical Research, 99, A7, 13403 – 13408, 1994b.

Russell, C.T. Working group report entitled: Magnetospheric Predictions, solar wind and magnetosphere interactions, in Solar-terrestrial predictions proceedings, Vol 2, Editor Richard Donnelly, 1979.

Russell, C. T., J.G. Luhmann, G. Lu, Nonlinear response of the polar ionosphere to large values of the interplanetary electric field, Journal of Geophysical Research, 106, A9, 18 495, 2001.

S

Saito, T., F. Takahashi, A. Morioka, and M. Kuwashima, Fluctuation of electron precipitation to the dayside auroral zone modulated by compression and expansion of the magnetosphere, Planet. Space Science, 22, 939 – 953, 1974.

Schieldge, J. P., G.L. Siscoe, A correlation of the occurrence of simultaneous sudden magnetospheric compressions and geomagnetic bay onsets with selected geophysical indices, Journal of Atmospheric and Terrestrial Physics, 32, 1819, 1970.

Schulz, M., and L. Lanzerotti, Particle diffusion in the radiation belts, Springer, New York, 1974.

Schunk, R.W. (1988) 'A mathematical model of the middle and high latitude ionosphere', Pure and Applied Geophysics, 127, 255.

Schunk, R.W. and J.J. Sojka, Ionospheric-thermosphere space weather issues, Journal of Atmospheric and Solar Terrestrial Physics, 58(14), 1527, 1997.

Schutz, S., G.J. Adams, and F.S. Mozer, electric and magnetic fields measured during a sudden impulse, Journal of Geophysical Research, 79, 2002, 1974.

SEC 07, Explanation of Real-Time Solar Wind data dials, NOAA National Weather Service Space Environment Center, http://www.sec.noaa.gov/SWN /sw_dials.html, 2007.

Shallon, S.C., "MINIMUF for Polar Paths", p. 48 (Technical Correspondence), QST, October, 1983.

Shinbori, A., T. Ono, M. Lizima, A. Kumamoto and H. Oya, Sudden commencements related plasma waves observed by the Akebono satellite in the polar region and inside the plasmasphere region, Journal of Geophysical Research, 108, A12,1457, 2003.

Sibeck, D.G., R.E. Lopez and E.C. Roelof, Solar wind control of the magnetopause shape, location and motion, Journal of geophysical research, 96, A4, 5489-5495, 1991a.

Sibeck, D. G. and Croley Jr, D. J.: Solar wind dynamic pressure variations and possible ground signature of flux transfer events, Journal of Geophysical Research, 96, 1669-1683, 1991b.

Sibeck, D.G., W. Baumjohann, R.C. Elphic, D.H. Farichild, J.F. Fennel, W.B. Gail, L.J. Lanzerotti, R.E. Lopez, H. Luhr, A.T.Y Lui, C. G. Maclennan, R.W. McEntire, T.A. Potemra, T.J Rosenberg and K. Takahashi, The magnetospheric response to 8-minute period strong-amplitude upstream pressure variations, Journal of Geophysical Research, 94, 2505-2519, 1989.

Sikdar, P., Ionospheric E-region parameter extraction using a fuzzy-equivalence clustering technique, Master of Science Thesis, Utah State university, 2004.

Smith, E.K., World-wide occurrence of Sporadic E, Circular 582, National Institute of Standards and Technology, Gaithersburg, Md., 1957.

Smith, E.K., The occurrence of sporadic E, in Ionospheric Sporadic E, edited by E.K. Smith and S. Matsushita, p. 219, Pergamon Press, New York, 1962.

Smith, E.K., Temperate-latitude sporadic E, in Physics of geomagnetic phenomena, edited by S. Matsushita and W.H. Campbell, Volume 1, pg 615, Academic Press, 1967.

Smith E.K. Jr., The morphology of Sporadic E, in Monograph on ionospheric Radio, edited by W.J.G. Beynon, Pg 55- 58, Elsevier, 1962.

Sojka, J.J. and Schunk, R.W.,'A model study of how electric field structures affect the polar cap F region, *J. Geophys. Res*, 93, 884, 1988.

Sojka, J.J. (1989), "Global scale, physical models of the F region ionosphere', Reviews of Geophysics and Space Physics; (USA); 27, 371.

Sojka, J.J., and R.W. Schunk, A model study of how electric field structures affect the polar cap *F* region, Journal of Geophysical Research , 93, A2, 884 – 896, 1988.

Sojka, J.J. and Schunk R.W., 1985, "A Theoretical Study of the Global F Region for June solstice, Solar Maximum, and Low Magnetic Activity," Journal of Geophysical Research. 90 (A6): 5285-5298.

Sojka, J.J., Schunk, R.W., 1983. A theoretical study of the high latitude F-region's response to magnetospheric storm inputs. Journal of Geophysical Research 88, 2112-2122, 1983.

Spreiter, J.R., and B.J. Hyett, The effect of a uniform external pressure on the boundary of the geomagnetic field in a steady solar wind, Journal of Geophysical Research, 68, 1631-1642, 1963.

St. Maurice, J.-P., Torr, D.G., 1978. Non-thermal rate coefficients in the ionosphere-the reactions of 0^+ with N_2, O_2, and NO. Journal of Geophysical Research 53, 969, 1978.

Stauning, P., Investigations of ionospheric radio wave absorption processes using imaging riometer techniques, Journal of Atmospheric and Terrestrial Physics, 58, 6, 753-764, 1996.

Stocker, Alan., Telephone conversation, June 2005 (A).

Stocker, A., Private email correspondence, November 2007.

Stone, E. C., Frandsen, A. M., Mewaldt, R. A., Christian, E. R., Margolies, D., Ormes, J. F., Snow, F., The Advanced Composition Explorer, Space Science Reviews 86 (1/4), 1-22., 1998.

Suess, S.T., and B.T. Tsurutani, From the Sun, Auroras, Magnetic Storms, Solar flares, Cosmic Rays, American Geophysical Union, Washington, DC, ISBN: 0-87590-292-8, 1998.

Sugiura, M., Some evidence of hydromagnetic waves in the earth's magnetic field, Phys. Rev. Letters, 6, 255-257, 1961a.

Sugiura, M., Evidence of low frequency hydromagnetic waves in the exosphere, Journal of Geophysical Research, 66, 4087-4095, 1961b.

Sugiura, M., M. Taxima and T. Nagata, Anomalous ionisation in the upper atmosphere and the auroral zone during magnetic storms, Report of Ionospheric Research in Japan, 6, 147, 1952.

Sugiura, M., and S. Chapman, The average morphology of geomagnetic storms with sudden commencement, Abh. Akad. Wiss. Göttingen Math. Phys. Kl., 4, 1, 1960.

Sugiura, M., The solar diurnal variation in the amplitude of sudden commencements of magnetic storms at the geomagnetic equator, Journal Geophysical Research., 58, 558-559, 1953.

T

Takeuchi, T., T. Araki, A. Viljanen, and J. Watermann, Geomagnetic negative sudden impulses: Interplanetary causes and polarization distribution, Journal of Geophysical Research, Vol. 107, 0, 1029, 2002a.

Takeuchi, T., C. T. Russell, T. Araki, Effect of the orientation of interplanetary shock on the geomagnetic sudden commencement, Journal of Geophysical Research , 107, A12, 1423, 2002b.

Tamao, T., Hydromagnetic coupling oscillations and drift wave instabilities in nonuniform, collisionless plasma, Physics of Fluids, 12, 1458 - 1470, 1969.

Tamao, T., A hydromagnetic interpretation of geomagnetic SSC*, Report of Ionospheric and Space Research in Japan, 18, 16, 1964b.

Tamao, T., Unsteady interactions of solar wind disturbances with the magnetosphere, Journal of Geophysical Research 80 (31), 4230-4236, 1975.

Tamao, T., The structure of three-dimensional hydromagnetic waves in a uniform cold plasma, Journal Geomagnetic Geoelectr, 16, 89, 1964a.

Tascione, T.F., Kroehl, H.W., Creiger, R., Freeman Jnr, J.W., Wolf, R.A., Spiro, R.W., Hilmer, R.V., Shade, J.W. and Hausman, B.A. (1988) 'New ionospheric and magnetospheric specification models', Radio Science, 23, 211.

Tascione, T.F., K.W. Kroehl, and B.A. Hausman, A technical description of the ionospheric conductivity and electron density profile model (ICED, version 196-II), Syst. Doc Vol. VII, Air Weather Serv., U.S. Air Force, Scott Air Force Base, Ill., 1987.

Temerin, M., I. Roth, M.K. Hudson, and J.R. Wygant, New paradigm for the transport and energisation of radiation belt particles, Eos Transactions of the AGU, 75, 44, 1994.

Thorne, R.M., E.J. Smith, R.K. Burton and R.E. Holzer, Plasmaspheric hiss, Journal of Geophysical Research, 78, 1581, 1973.

Tinsley, B.A., Energetic neutral atom precipitation during magnetic storms: optical emission, ionisation, and energy deposition at low and middle latitudes, Journal of Geophysical Research, 84, 1855-1864, 1979.

Tkalcevic, S., U.S. Inan, and R.A. Helliwell, Nonlinear pitch-angle scattering and trapping of energetic particles during Landau resonance interactions with whistler mode waves, Journal of Geophysical Research, 89, 10813, 1984

Trautmann, E., NATO HQ C3 Staff, Document Civ/Mil(04)02, The military Use of Spectrum, presented to the CEPT/ECC Civil/Military Meeting, Best 23 – 25 March 2004.

Tsagouri, I., Zolesi, B., Belehaki, A., and Cander, L.R. Evaluation of the performance of the real-time updated simplified ionospheric regional model for the European area. Journal of Atmospheric and Solar-Terrestrial Physics 67(12), 1137-1146, 2005.

Tsunomura, S., and M. Kuwashima, On the nature of flux variations of trapped particle associated with SC and SI at synchronous orbit, Memoirs of the National Institute of Polar Research. Special issue, 31, 27-36, 1984.

Tsunomura S, Characteristics of geomagnetic sudden commencements observed in middle and low latitudes, Earth Planets Space, Vol 50, pp 755 – 772, 1998.

Tsurutani, B.T., X. -Y. Zhoua, J. K. Arballoa, W. D. Gonzalezb, G. S. Lakhinac, V. Vasyliunasd, J. S. Pickette, T. Arakif, H. Yangg, G. Rostokerh, T. J. Hughesh, R. P. Leppingi and D. Berdichevskyi, Auroral zone dayside precipitation during magnetic storm initial phases, Journal of Atmospheric and Solar-Terrestrial Physics, Vol 63, Issue 5, Pages 513-522, 2001.

Tsurutani, B. T.; W.D. Gonzalez, A.L.C. Gonzalez, F. Tang, and J.K. Okada, Interplanetary origin of geomagnetic activity in the declining phase of the solar cycle, Journal of Geophysical Research 100 (A11), 21717-21734, 1995.

Tsurutani,B.T., and G.S Lakhina, Some basic concepts of wave-particle interactions in collisionless plasmas, Reviews of Geophysics, 35, 4, 491- 501, 1997.

U

Ullalan, S.L., K. Wilhelm, J. Kangas & W. Riedler, Electron precipitation associated with a sudden commencement of a geomagnetic storm, Journal of Atmospheric and Terrestrial Physics, 32, 1545-1553, 1970.

Ulwick, J.C., Aurora and Airglow (Proceedings of the NATO advanced study institute, august 15-26, 1966), edited by B.M. McCormac, Reinhold, New York, 1967.

University of Leicester, Svalbard Oblique Sounder Page, Retrieved 20 October, 2007, http://www.ion.le.ac.uk/iris/index.html, 2007.

Unti, T., and G. Atkinson, Two-dimensional Chapman-Ferraro problem with neutral sheet, 1, The boundary, Journal of Geophysical Research, 73, 7319-7327, 1968.

V

Vampola, A.K., and A. Korth, Electron Drift Echoes in the inner magnetosphere, Geophysical research letters, 19, 625, 1993.

VOACAP Frequency Asked Questions, Revised 22-FEB-96, http://www.vectorbd.com/bfd/antenna/voacap-faq.

Vondrak, R.M., R.M. Robinson, Measurements of E region ionisation and conductivity produced by solar illumination at high latitudes, Journal of Geophysical Research, 89, 3951, 1985.

Vorob'yev, V.G., SC-associated effects in auroras, Geomagn. Aeron, 14, 72, 1974.

Voss, H,D., W. L. Imhof, M. Walt, J. Mobilia, E. E. Gaines, J. B. Reagan, U. S. Inan, R. A. Helliwell, D. L. Carpenter, J. P. Katsufrakis, and H. C. Chang, Lightning-induced electron precipitation, Nature 312, 740 – 742, 1985.

W

Wagner, R.A., A. L. Snyder and S. -I. Akasofu, The structure of the polar ionosphere during exceptionally quiet periods, Planetary and Space Science, 21, 11, 1911-1916, 1973.

Walker, J.K., Auroral ionosphere models, Journal of Atmospheric and Terrestrial Physics, 34, 1681-1689, 1972.

Walt, M, Source and loss processes for radiation belt particles, in Radiation Belts: Models and Standards, Vol 97, edited by J.F. Lemaire, D. Heynderickz and D.N. Baker, AGU, Washington, D.C., 1966.

Wan W., M.L. Parkinson, P.L. Dyson, A.M. Breed, R.J.A. Morris, A statistical study of the interplanetary magnetic field control of sporadic E-layer occurrence in the southern polar cap ionosphere, Journal of Atmospheric and Solar-Terrestrial Physics, 61, 18, 1357-1366, 1999.

Wang, C., H. Huang, Y.Q. Hu and X.C. Guo, 3D global simulation of the interaction of interplanetary shocks with the magnetosphere, in The Physics of Collisionless Shocks, edited by G. Li, et al., 320 – 324, Am. Int. of Phys., Washington, D.C, 2005.

Wang C., C.X. Li, Z.H. Huang, and J.D. Richardson, Effect of interplanetary shock strengths and orientations on storm sudden commencement rise times, Geophysical Research letters, 33, 2006.

Wang, C.B., J.K. Chao and C.–H. Lin, Influence of the solar wind dynamic pressure on the decay and injection of the ring current, Journal of Geophysical Research, 108, A9, 1341, 2003.

Wang J., Prediction of medium-frequency sky-wave field strength in North America, IEEE Transactions on Broadcasting, Vol. BC-23, 43-49, 1977.

Wang J., A sky-wave propagation study in preparation for the 1605 – 1705 kHz broadcasting conference, IEEE Transactions on Broadcasting, Vol. BC-31, 10-17, 1985.

Whalen, J.A., J. Buchau and R.A. Wagner, airborne ionospheric and optical measurements of noontime aurora, Journal of Atmospheric and Terrestrial Physics, 33, 661, 1971.

Whitehead, J.D., The formation of sporadic-E layer in temperate zones, Journal of Atmospheric and Terrestrial Physics, 20, 49-58, 1961.

Whitehead, J.D, Production and prediction of sporadic E, Review of Geophysical Space Physics, 8, 1, 65-144, 1970.

Whitehead, J.D., Recent work on mid-latitude and equatorial sporadic E, Journal of Atmospheric and Solar-Terrestrial Physics, 51, 5, 401, 1989.

Wilcox, J.M., The interplanetary magnetic field, Solar origin and terrestrial effects, Space Science Reviews, 8, 258-328, 1968.

Wilken, B., C.K. Goertz, D.N. Baker, P.R. Higbie and T.A. Fritz, The SSC on July 29, 1977 and its propagation within the magnetosphere, Journal of Geophysical Research, 87, A8, 5901-5910, 1982.

Wilken, B., D.N. Baker, P.R. Higbie, T.A. Fritz, W.P. Olsen and K.A. Pfitzer, Magnetospheric configuration and energetic particle effects associated with SSC: a case study of the CDAW 6 event on March 22, 1979, Journal of Geophysical Research, 91, A2, 1459-1473, 1986.

Wilkinson, P., Computer aided processing of ionograms and ionosonde records, Proceedings of Session G5 at the XXV General Assembly of the International Union of Radio Science (URSI), Lille, France, UAG-105, 1998.

Williams, J., A 27 day periodicity in outer zone trapped electron intensities, Journal of Geophysical Research, 71, 1815, 1966.

Wilson David J., A Comparison of High-Latitude Ionosphere Propagation Predictions from AMBCOM with Measured Data, Masters Thesis, Naval Postgraduate School, Monterey, California, 1991.

Wilson, A., and P.H. Stoker, Imaging riometer observations on energetic electron precipitation at SANAE IV, Antarctica, Journal of Geophysical Research 107 (A10), 1268, 2002.

Wilson, C.R. and Sugiura, M., Hydromagnetic interpretation of sudden commencements of magnetic storms, Journal Geophysical Research, 66, 4097, 1961.

Wratt, D.S., Ionisation enhancement in the middle latitude D-region due to precipitating high energy electrons, Journal of Atmospheric and Terrestrial Physics, 38, 511 – 516, 1976.

Wright, J.W., R.W. Knecht and K.Davies, Annals of the IGY, III, part 1, Pergamon Press, 1957.

Wygant, J.R., F. Mozer, M. Temerin, J.B. Blake, N. Maynard, H. Singer, and M. Smiddy, Large amplitude electric and magnetic field signatures in the inner magnetosphere during injection of 15 MeV electron drift echoes, Geophysical Research Letters, 21, 1739, 1994.

X

Y

Yahnin, E., E. Titova, A. Lubchich, T. Bosinger, J. Manninen, T.Turunen, T. Hansen, O. Troshichev and A. Kotikov, Dayside high latitude magnetic impulse events: their characteristics and relationship to sudden impulses, Journal of Atmospheric and Terrestrial Physics, 57, 13, 1569- 1582, 1995.

Z

Zesta, E., H.J. Singer, D. Lummerzheim, C.T. Russell, L.R Lyons, M.J. Brittnacher, The Effect of the January 10, 1997, Pressure Pulse on the Magnetosphere-Ionosphere Current System, in Magnetospheric Current Systems, Geophysical Monograph 118, edited by S. Ohtani, R. Fujii, M. Hesse and R. L. Lysak. ISBN 0-87590-976-0; Published by the American Geophysical Union, Washington, DC, p.217, 2000.

Zhou, X.-Y, and B.T. Tsurutani, Rapid intensification and propagation of the dayside aurora: Large scale interplanetary pressure pulses (fast shocks), Geophysical Research Letters, 26, 1097-1110, 1999.

Zhou. X. -Y, and B.T. Tsurutani, Interplanetary shock triggering of nightside geomagnetic activity: Substorms, pseudobreakups, and quiescent events, Journal of Geophysical Research, 106, A9, 18957–18968, 2001.

Zolesi, B., Belehaki, A., Tsagouri, I., and Cander, L.R., Real-time updating of the Simplified Ionospheric Regional Model for operational applications, Radio Science Vol 39, No. 2, doi: 10.1029/2003RS002936, 2004.

Appendix

Survey of Propagation Prediction and Planning Tools

A1.0 Introduction

The function of propagation prediction, when used as an engineering planning tool, is to ensure, as best as possible, that an adequate service can be provided to spectrum users. The term 'adequate service' has two components that must be satisfied. The first component is that a usable field strength is delivered to the reception point. The second component is that the usable field strength is available for the required length of time. Usable field strength is defined as the field strength adequate for communications to occur. For sensitive military receivers coupled to extensive antenna arrays, the field strength required in the reception area is far lower than the field strength required for a cheap, portable HF broadcast receiver using a whip antenna or a small aircraft equipped with a sensitive receiver but using a small fuselage mounted antenna.

In the last three decades there has been a move from the use of mainframe computers to personal computers for propagation prediction planning tools and numerous HF-propagation programs have been developed for use on personal computers. It should be emphasized that most of these programs input median-value data and produce median value of MUF, LUF, signal strength, etc. as output and are basically intended for HF-circuit planning, not real time prediction. Most of the programs take

transmitter and receiver locations, time, month, year, and usually the number of sunspots as input, and provide as output MUF, LUF, mode structure, antenna headings, great-circle distance and root-mean-square median-field-strength values for mid-latitude HF paths.

In order to reach a general characterisation of the problems involved in the prediction of the ionosphere, we must consider the factors determining the state of the ionosphere to understand why it is impossible to produce a fully deterministic calculation. To do this we need to consider three critical issues.

- The state of the ionosphere is determined by a large number of different parameters. The characteristics of the ionised fraction of the upper atmosphere such as electron concentration, ion composition, electron and ion temperatures, particle fluxes and drifts, constitute the basic physical parameters of the ionosphere.

- The parameters of the ionosphere undergo considerable changes with altitude. The concentrations of ions, ni, and electrons ne, at certain altitudes have characteristic maximum peaks, forming the ionospheric layers, E, F1 and F2. As a result, the stratified structure of the ionosphere may be characterized by a set of parameters: the concentration nem at layer maximum, layer altitude and widths, the depths and widths of the troughs between layers etc. In addition to variation with the altitude, ionospheric parameters also vary with the geographical coordinates (latitude φ, longitude λ), and with the geomagnetic coordinates, thus any description of the variation of the ionosphere with time includes several parameters.

- Certain variations in the ionosphere were found to be caused by the variation of active factors such as solar radiation and geomagnetic activity. Therefore, the ionosphere is not merely a geophysical, but also a helio-geophysical entity. Owing to the abundance of the parameters required to describe it, and since each parameter varies differently with the coordinates, time, and activity factors, the behaviour of the ionosphere is extremely complex. As a result, both the study of the ionosphere and its description are also very complex tasks.

In modern prediction methods, quantitative predictions of the state of the ionosphere are made either by extrapolation or by the use of models. In the extrapolation method the future evolution of any given parameter is estimated from a number of observations made during a previous period of time. The magnitude of the parameter at some future point in time is estimated on the assumption that the trend of the evolution will remain unchanged in the future (quasi-inertial prediction). If models are used in prediction, it is possible to compute an entire set of parameters for the object (e.g f_oF_2) of the model. If the state of the object is solely determined by certain conditions or forces, the task of prediction will consist of two stages: 1) prediction of the evolution of these conditions or forces; and 2) description of the state of the object under these predicted conditions.

In the prediction of the ionosphere, the fact that the condition of the ionosphere is chiefly determined by the solar activity level and by the level of geomagnetic perturbations, which may be considered as a result of the solar activity, is usually taken into consideration. Accordingly, ignoring the problem of predicting solar activity for the moment, the task of ionospheric prediction consists of relating the state

of the ionosphere to the parameters of the solar activity, and of furnishing a more or less detailed description of ionospheric parameters. Ionospheric variations are also predicted independently of the solar activity, merely from a series of observations carried out during previous period of time. This method is employed in both short-term and long-term predictions.

Short-term predictions involve timescales from minutes to days and the term forecast is sometimes used to describe those prediction schemes that are based on established cause-and-effect relationships, rather than simple tendencies based upon rudimentary indices. Taken to the limit, a short term forecast becomes a real-time ionospheric assessment or a nowcast. This is achieved in real time channel evaluation (RTCE) using a network of oblique sounders.

Short-term prediction methods typically involve the measurement of either an ionospheric or geophysical parameter that is applied to an empirical model or algorithm. The long-term prediction methods provide the system architect and the frequency planner with useful guidance, but that ionospheric variability with timescales of tens of minutes presents a considerable challenge. Certainly the ubiquitous median models have no intrinsic short-term forecasting capabilities. One should expect very little correlation between the unfiltered real world and the predictions extracted from a median model. Even though long-term models have no capability to assess short-term variability in other than a statistical way, the Achilles heel of short-term forecasting is that there is a danger that analysts may use long-term models improperly. Milsom (1987) has listed the outstanding problems associated with short-term forecasting, and Goodman (1991) has examined ways of coping with short-term variability.

Long-term predictions of ionospheric behaviour are typically based on climatological models developed from historical records for specific solar and/or magnetic activity records, season, time of day and geographical area. Very often the ionospheric prediction itself is based upon a prediction of the solar activity level; in other words, the long-term prediction process relies upon loosely established tendencies and how they relate to relatively simple driving parameters. The result is an estimate of median behaviour. This gives rise to two sources of error occuring in long-term predictions, one arising from an imprecise estimate of the driving parameter, such as the sunspot number, and the second arising from ionospheric variability which is not adequately dealt with in the model.

The author finds it surprising that the process yields any useful results, yet it often does and is used extensively in HF broadcast planning and other spectrum management activities where significant lead times between planning and operation are involved. This review focuses on long-term methods and reviews a number of long term prediction programmes (Lombry, 2008).

A1.1 Historical Development (NTIA 1998)

Current methodologies for HF performance prediction evolved gradually, beginning with uncoordinated studies by workers from many countries and organizations. Serious work to establish prediction methods began in earnest during World War II because of the military communication requirements. The earliest methods by the Allies, Germany, and Japan were of the graphical type to speed analysis, because computer methods were not available. The long-distance methods used by Germany and those used by the Allies form an interesting contrast

In Germany, long-distance propagation was analysed by examination of each mode and path independently. Short paths assumed 1E, 2E, 1F and 2F mode possibilities while for long paths multiple F layer modes alone were considered. At each reflection point the MUF was deduced by extraction of a value of f_oF_2 for that point (from crude maps) and the appropriate MUF factor was applied. The overall MUF was logically determined as the lowest of the set of subhop MUFs for each path to be reckoned. Because of noise extension, scatter effects, and the possibility of ducted or chordal mode propagation, this approach, while intuitively pleasing, was pessimistic. The American long-path approach, influenced by a more global perspective, used a modified reflection point method that accounted for only two minor points along the great circle path linking communication terminals. These two control points were 2 000 km from the communication terminals and produced a rather optimistic result.

In the period during World War II and after, sounding networks were established to provide a basis for the construction of better maps from which f_oF_2 and MUF variation with latitude (and longitude) could be assessed. The French and the United States continued the development of more analytical methods to replace simpler procedures. Significant improvements in mapping resulted from the incorporation of a modified dip latitude concept to account for geomagnetic control of the ionospheric parameters.

A1.2 The Use of Ionospheric Models for Prediction

Because the sources of ionospheric disturbance cannot be adequately monitored at their points of origin and as they propagate, prediction algorithms are inefficient. An additional complication arises as a result of distortion and attenuation experienced by the propagating disturbance. Moreover, the science that allows us to translate the

physical processes in control at the disturbance source to other geographical regimes and times is incomplete. Table 26 shows the hierarchy of ionospheric disturbances and provides an estimate of time duration and occurrence frequency for each class of disturbance.

EFFECT	TIME PERIOD Seconds in ( )	FREQUENCY (Hertz)
Solar Cycle	11 years (3.5 x 108)	2.9 x 10-9
Seasonal	3 months (7.9 x 106)	1.3 x 10-7
Diurnal Cycle	24 hours (8.6 x 104)	1.2 x 10-5
Large-Scale TID	1 hour (3.6 x 103)	2.8 x 10-4
Short-Wave Fade	0.5 Hour (1.8 x 103)	5.6 x 10-4
Small-Scale TID	10 minutes (6 x 102)	1.7 x 10-2
Faraday Fading	0.1 – 10 second	10 - 0.1
Interference Fading	0.01 – 1 second	100 - 1

Table 26. Temporal variations of HF effects (After Goodman, 1992)

As indicated above the nature of ionospheric variability is quite complex, since it arises from temporal and geographic variabilities in upper atmospheric chemistry, ionisation production and loss mechanisms, particle diffusion and electro dynamical phenomena. Generally, the trends are fairly well modelled, and much of the variability is understood from a physical point of view. Unfortunately, an understanding of cause and effect does not always translate into being able to make predictions in the time period desired.

Several models of varying degrees of complexity have been developed for the purpose of making ionospheric or propagation predictions, or for use in theoretical studies. Work by Anderson et al. (1987) has covered the calculation of ionospheric profiles on

a global scale in response to physical driving parameters, such as the underlying neutral composition, temperature, and wind; the magnetospheric and equatorial electric field distributions; the auroral precipitation pattern; and the solar EUV spectrum. A subset of these parameters has been used in profile calculations for the development of the semi-empirical low-latitude ionospheric model (SLIM) (Anderson et al., 1987) (Sojka and Schunk, 1985). This kind of approach is computationally very intensive, but the use of coefficient maps from these calculations, which depend on the appropriate parameter values, has been feasible.

One of the most important parameters in the prediction of HF propagation is the maximum electron density of the ionosphere, since this determines the communication coverage at a specified frequency. The ordinary ray critical frequency, f_oF_2 may be directly related to maximum F_2 layer electron density and f_oF_2 together with the effective ray launch angle, determines the MUF for a specified transmission distance. Thus, the ability to predict the f_oF_2 by knowing the maximum electron density of the ionosphere by some method is the first step in predicting HF propagation.

This is usually accomplished by generating a model of the vertical distribution of electron concentration in the E- and F-regions. This needs to take account of the known large geographic and temporal variations in the ionosphere. The most extensive ionospheric database is that derived from the world network of ionosondes. Predictions of vertical distribution are produced with the parameters of the models given by empirical equations in terms of the ionospheric characteristics which are scaled on a routine basis at all ionosonde stations.

Ionospheric models may be empirical (statistical), semi-empirical or theoretical. Empirical models are based on the generalization of a number of observations of individual ionospheric parameters, which may be presented in graphs, tables or formulas. Statistical models involve charts of planetary distribution of ionospheric parameters as a function of the coordinates, the local time and the level of solar activity.

Theoretical models attempt to solve a set of first principles equations for the ionospheric plasma, starting from the continuity, energy, and momentum equations for electrons and ions (Schunk, 1988; Anderson, 1993). Theoretical ionospheric models have proved their capabilities in reproducing selected sets of non-auroral observations. All these models are essentially confined to modern day supercomputers because of their complexity. The main disadvantage of using theoretical models for prediction and forecasting is the large amount of computer time needed. In addition, an extensive preparation of inputs is needed to obtain meaningful results (Sojka, 1989).

Parametric models simplify the theoretical models by expressing them in terms of solar-terrestrial parameters and geographical locations, giving a realistic representation of the ionospheric spatial and temporal structure using a limited number of numerical coefficients. An example is SLIM – a Semi-Empirical Low-latitude Model, based on theoretically-obtained grid values for electron density profiles normalized to the F_2-peak and then represented by modified Chapman function (Anderson et al., 1987). Electron density profiles (180 km to 1 800 km) are determined for different latitudes (every 4 degrees between 24 N and 24 S dip latitude) and local times (every hour) by solving the continuity equation for O+ ions.

The profiles are normalized to the F_2-peak density and are then represented by Modified Chapman function using six coefficients per individual profiles.

Parametric models allow realistic ionospheric models to be adjusted in real time and to provide an accurate specification of the instantaneous ionosphere, and then to be incorporated in three-dimensional ray tracing programs for HF propagation purposes (Reilly et al., 1991). However, it is clear that parametric models based on theoretical considerations are suitable only for well-specified geophysical problems.

An example of a recently developed empirical model is the COSTPROF electron density height profile model. This model was developed by the COST 251 Action "Improved Quality of Service in Ionospheric Telecommunication Systems Planning and Operations" (Radicella, 2002). COSTPROF provides a fully developed topside formulation of the ionosphere but while empirical, it is suitable for real-time applications. The model is a "profiler" in the sense that they can use ionosonde parameters from various sources as "anchor point" values for the profile (the full set consists of the critical frequencies foE, foF1, foF2 and the propagation parameter M3000(F2). The model is global but used with regional maps of ionosonde parameters becomes a regional model allowing the input of the properties of the F layer peak (height and electron density) instead of input of a full set of "anchor point" values. Since a multitude of different ionospheric models is readily available it is important to note that:

- all-purpose models do not exist;
- all ionospheric models need input data;
- the decision which model to use depends on the aim and the needs of the model users, on available resources and on available input data.

A1.3 IONOCAP/VOACAP Based Propagation Planning Tools

The evolution to VOACAP via IONCAP started with the Program ITSA-1 (Lucas and Haydon, 1966). This model was developed by the U.S Commerce Department. At the time of publication it represented one of the first computer methods for exploiting augmentations in the underlying ionospheric and geophysical databases. ITSA-1 did not include separate D or F1 layers, and sporadic-E was not accounted for. In this program the concepts of circuit reliability and service probability were introduced. MUF variability data were included. ITSA-1 was followed by ITS-78, also known as HFMUFES (Barghausen et al., 1969). ITS-78 actually represents a series of codes developed at ITS in Boulder beginning with ITS-78, and culminating with HFMUFES4. These programs did not include an F1 layer but do include sporadic-E. Most of the features of ITSA-1 were included, but with revised F-layer ionospheric data.

IONCAP: The Ionospheric Communications Analysis and Prediction Program (IONCAP) provides the means to calculate HF propagation parameters at any location. Field strength, mode reliability, the maximum usable frequency (MUF) and the lowest useful frequency (LUF) are some of the parameters calculated by IONCAP. They enable the user to specify antenna gains as a function of take-off angle and to specify required system performance in terms of the signal-to-noise ratio evaluated at the receiving point of the circuit. Required inputs include the transmitter and receiver location, transmitter power, universal time, month, and sunspot number (Rush, 1986).

IONCAP was one of a string of mainframe programs developed by ITS and its predecessor organizations and contained the following improvements over previous ITS models:

- a more complete ionospheric description;
- modification in loss equations;
- empirical adjustment to Martyn's Theorem;
- revised loss statistics to account for E_s and above-the-MUF-losses;
- new methodology for long-distance modelling;
- revision to antenna gain models.

IONCAP uses a F-layer algorithm, has methods for calculating MUFs, and it deals with the range of values of critical frequencies resulting from the statistical variations in the sounding ITU (CCIR) data. The IONCAP program has many other methods beside FOT-MUF-HPF and some give long-term availability figures, the fraction of a month the path would be open, as well as the S/N ratio and reliability. In contrast to Fricker's method which is based only on F-region considerations, IONCAP deals with fluctuations of signal strength, a D-region factor, as well as man-made noise.

The performance of IONCAP has been examined in one in a series of studies, conducted at the Naval Postgraduate School, to establish the relative merits of several computer-based propagation prediction models using a standard set of measured data (Marcos, 1991). IONCAP-PC 2.5 was tested for accuracy over a transpolar communications link, using “noncentric” measured reference data obtained from the University of Leicester. The field strength values predicted by IONCAP-PC 2.5 are extended to take into consideration the specific antenna designs and predicted noise levels are also calculated for the environments involved. The resulting signal-to-noise ratio is compared with the observed signal-to-noise ratio and a statistical analysis is performed on the resulting errors. It is concluded that IONCAP-PC 2.5 predicts the

signal-to-noise ratio with an error of less than 10 dB for 50% of the data. IONCAP is no longer supported as it was used as the basis for VOACAP and ICEPAC.

CAPMAN: This is a propagation prediction and system analysis program that utilised the IONCAP model. The input requirements are data of a near-complete circuit and the output results in several high-resolution graphs. However, excluding its improved graphical interface, which leads to its extended use, it has inherited some of the same inaccuracies as the IONCAP model. It has been replaced by WinCAP WIZARD 3.

GWPROP: Developed in 1994 by Gordon West, this DOS propagation prediction program forecasts between 1.6 and 30 MHz. It is based on a report and program developed by ITS (1978) which was the original basis of IONCAP. From input data of a complete circuit, including solar and geomagnetic conditions and data (e.g. locations) extracted from external data files, GWPROP provides a large choice of outputs from the MUF to detailed tables of the system performance along the concerned paths. It also calculates the absorption factor, excess system loss and the electron gyro-frequency in addition to the usual critical frequencies.

VOACAP: The Voice of America (VOA) invested over $2M in converting IONCAP to an area prediction model (1985 to 1996). In this process, they found and corrected approximately 60 errors in the original code. The VOA used the unpublished IONCAP theory manual as the guide in correcting logic and programming errors. They documented and tested all changes to the code. Considerable effort was given to improving the input and output functions for ease of use on a PC. In essence VOACAP is an enhanced IONCAP model in which the

IONCAP methodology was modified by USIA/VOA to be used for broadcast relay station design and antenna specification.

Most of the large-scale ionospheric data made available in the IONCAP model was collected during the International Geophysical Year (IGY) between 1958 and 1963. Data was then reduced to look up tables, using average calues, which were valid for 2 or 3 month periods at each even hour. These maps were dedicated to the estimation of critical frequencies foE, foF1, foF2, M-3000 (for the MUF) and excess system loss tables. In addition, radio noise was mapped in 3 month groups and 4 hours time interval blocks.

This way to create a model using averaged values was subject to many comments until it was decided by George Lane from the Voice of America broadcasting company, and the Signal Corps Radio Propagation Agency engineers to force the program to give a smooth transition across the days of the month. In parallel John Wang at the FCC developed a medium wave prediction model suited for long distance paths into darkness that was adopted by the ITU-R (Wang 1977, 1985). However, IONCAP and Wang's model used different semi-empirical data set and functions, and from a purely statistical point of view, both models were not compatible and both theories were unfortunately never merged together.

Apart some approximations that have been used, VOACAP does not differ much from the IONCAP interface developed by John Lloyd in 1978. Like IONCAP, there are various models to estimate the absorption, noise level and reliability of a service (mode) at some frequencies. VOACAP deals not only with statistics of F-layer

ionisation (e.g. through the MUF and the like), but also down lower where absorption and noise have their origin. So, like IONCAP, VOACAP has F-region methods which give not only the availability of a path, the fraction of days in a month it is open on a given frequency, but also D-region methods which give the reliability of a mode, and the fraction of time the signal/noise ratio exceeds the minimum required for the mode (VOACAP FAQ 1996).

Like IONCAP which models involve both paths longer than 10 000 km and a "single hop" method for distance less than 3 000 km, VOACAP uses the same functions to consider all possible ray paths for the specified circuit. However, in the specific case of DX where extension of paths require three or more hops (over 5 to 6 000 km away depending on solar conditions), the system concludes that a path is available, which is far from being the case if we take into account the various reflection modes and degree of ionisation of each layer. Therefore VOACAP uses a correction for these multi-hop paths longer than 10 000 km – called Method 21.

If a propagation path does exist in a circuit, it has been shown empirically that usually these circuits are dominated by what we call "control areas" which are the regions within 2 000 km around each end of the circuit (transmitter, receiver). At the transmitter location the control area allows the sky wave to do its first hop up to about 2 000 km away, while the control area at the receiver location allows the remaining signal to be returned after the last hop. In between, the path is simply characterized by a simple loss per distance statistical function, the noise and signal statistics being the same for all paths. If this approximation gives good results, we must recognize that the

VOACAP model is more complete and thus more accurate for shorter paths, say below 5 000 km or 3 hops.

VOACAP relies on the smoothed sunspot number (SSN) and does not include input for planetary indices (A- and K-indices). This lack gives rise to inaccuracies in disturbed conditions, mainly at high latitudes as well as for top band predictions where geomagnetic and gyro-frequencies effects are not taken into account. The SNR Distribution tables and Excess Gain tables that are internal to the model were conceived and calibrated from many user reports against a wide range of solar and geomagnetic conditions and at the higher statistical levels (higher required reliabilities SNRxx). It is for these reasons that any attempt to enter daily sunspot numbers, for example, instead of the SSN can cause inaccuracies in VOACAP predictions.

While considered to be extremely powerful, VOACAP does have some limitations. First, it works only with median values like SSN and provides no real-time updates. It doesn't use A or K index, and thus predictions do not take into account some important effects like short-term disturbances or the aurora oval on short-wave bending at high latitudes. It uses approximations for the F_2-layer and calculating the MUF. Its predictions must be interpreted with care for short-term use and are also almost useless for frequencies below 2 MHz as it ignores the sunrise/sunset effect and the gyro-frequency of ionospheric electron and magneto-ionic effect. Currently, there is no way to adequately model global irregular variations in the ionosphere on a timescale smaller than a month because random values cannot be predicted. They can, however, be described statistically or take into account using near-real-time data. In common with most of the programs described in this chapter, the VOACAP engine

produces monthly medians, deciles, standard deviations, probabilities of service, etc. These monthly statistics are predictable and fairly accurate but the daily predictions for a particular date and hour are just speculations, using interpolations that are not supported by VOACAP.

VOACAP is still a "trial version" using not less than 30 calculation methods, some of them having never been cross-checked with on-the-air results, and are thus not validated by users and show some errors in some specific conditions of use. In spite of these limitations, the VOACAP engine is accepted as an accurate and flexible compromise ionospheric model, freely available for general purpose use.

WinCap Wizard 3: This is the Windows version released in 2003 of the well known CAPMAN program. WinCAP Wizard 3 uses the VOACAP engine and provides HF propagation forecasts taking into account a complete circuit, and even multiple circuits if necessary. WinCAP Wizard 3 displays up to 7 charts displaying MUF, Best Frequency, transmitter antenna takeoff angle, SNR, Reliability (SNRxx), and signal strength at receiver location. It is capable of generating propagation charts or text reports for up to 18 circuits anywhere in the world simultaneously. It has a very useful batch manager. This program is in essence a useful GUI interface for VOACAP and the same 30 inputs are required to get the most accurate forecast for a single point-to-point circuit out of the program.

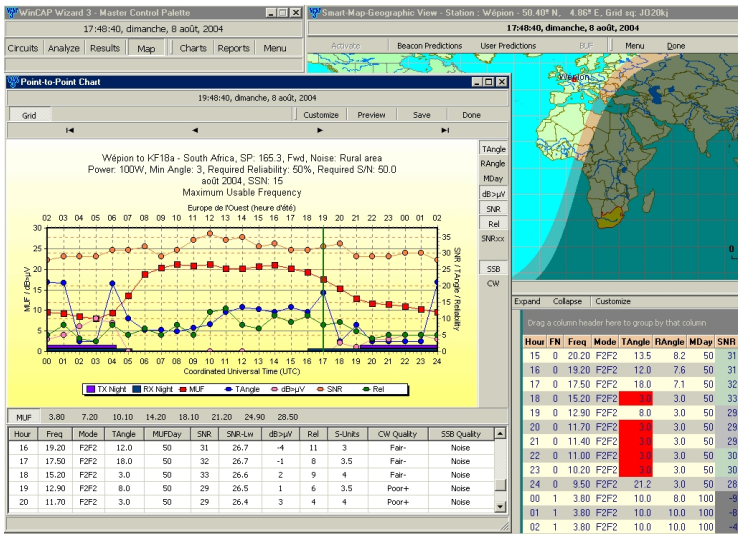

Figure 123. Example of WinCap output.

DXATLAS and HamCap: Both developed by Alex Shovkoplyas, these programs use the VOACAP engine to predict propagation conditions on a global scale. These programs download real-time space weather conditions and use direct, real time ionosonde measurements of the F layer critical frequency to produce real-time ionospheric maps. This removes the uncertainty of K_p influences on f_oF_2 as the realtime f_oF_2 value is used. The program estimates the f_0F_2 distribution, the F_2-layer height in km, the MUF, auroral oval (with the power flux P in $W/m^2/sec$), geomagnetic storms, D-layer peak density, geomagnetic latitude (normal and corrected), and magnetic dip (normal, modified and latitude). CapMan results are displayed either in a chart showing the S/N variation as a function of time over the specified path or on a global ionospheric world map, with the gray line and the MUF in option.

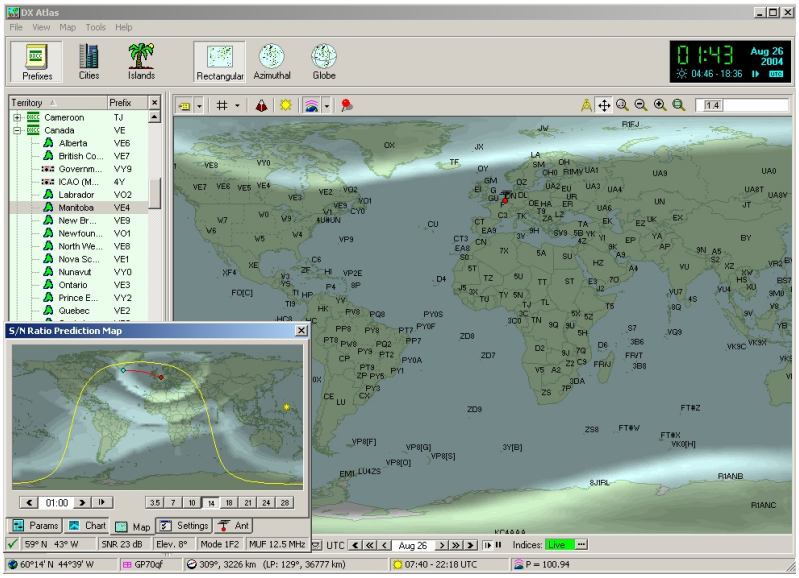

Figure 124. Example of the output of HamCap interfaced with DXAtlas.

These two programs are in essence a useful GUI interface for VOACAP, however, as it does not permit access to all output parameters of VOACAP, it does not predict propagation conditions for a complete circuit.

ACE-HF Pro: ACE stands for "Animated Communications Effectiveness", a coverage display technique originally developed for U.S. Navy submarine communications. Moved into the Windows environment by Richard Buckner, this program uses GeoClock maps, a format that has been chosen in order to match the displays with ACE-VLF (A Very Low Frequency Planning Tools) used by military clients. ACE-HF Pro uses the VOACAP engine without modification of algorithms (thus with the same accuracy and limitations). Representing about 50 MB on disk, 500 files and 50 directories, it is thus not available as a demo. Its main originality over all other VOACAP-based programs is to display animated circuit graphs of SNR, reliability, required power gain, takeoff angle and signal strength. To achieve this, ACE-HF Pro employs cubic spline interpolation to produce chart values at five-minute intervals in order to better describe what happens in the real world. These intermediate values show less precision that hourly predictions. Several charts can

also be displayed, to name the MUF (with HPF and FOT), Best Frequency, and an SNR or reliability summary chart. I understand that there are a great number of professional users of this product. This program is in essence a useful GUI interface for VOACAP.

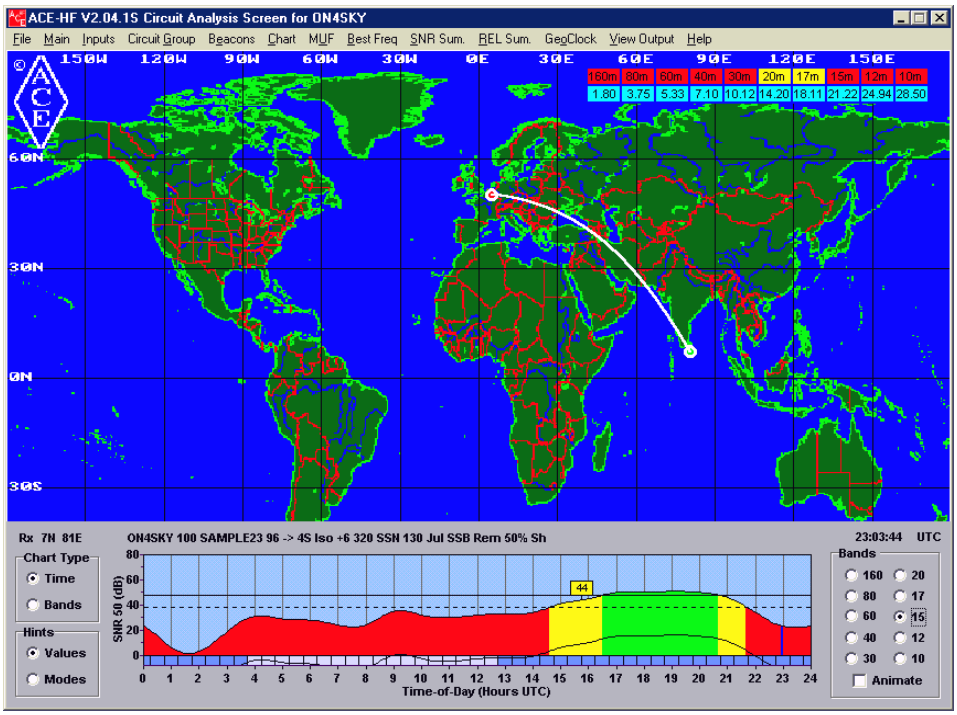

Figure 125. Example of ACE-HF output.

ICEPAC: The NSA funded the National Telecommunications and Information Administration, Institute for Telecommunication Sciences (NTIA/ITS) to develop a PC version of IONCAP that would be useful for circuits at high latitudes. This program became ICEPAC and it has the same functionalities, accuracies and limitations as VOACAP and shares the same data. In addition to its similarities to VOACAP, ICEPAC includes the ICED (ionospheric conductivity and electron density) profile model. This is a statistical model that recognizes the different physical processes that exist in the large-scale features of the northern hemisphere ionosphere. It contains, for example, distinct algorithms for the subauroral trough, the equator-

ward portion of the auroral zone, the poleward region of the auroral zone, and the polar cap (Tascione, 1987).

Unfortunately, this effort was shrouded in mystery as to exactly what changes were made to the IONCAP code. ICEPAC exists in the public sector only in compiled format so that the source code cannot be examined. While ITS has kept the input and output formats of ICEPAC and VOACAP as similar as possible, the two codes are quite dissimilar in terms of their subroutines. It is unclear if ICEPAC contains any or all of the errors VOA found in IONCAP.

ICEPAC was not as extensively validated as VOACAP and it does not take into account a smoothing function between the hop and forward-scatter regions, a feature used in VOACAP. Therefore, in some circumstances, ICEPAC shows discontinuity of nearly 10 dB at mid-path, causing artificial SNR losses exceeding 20 dB. On another side, ICEPAC provides some additional iso-contours maps not available in VOACAP like the SRNxx (Method 20). Results are claimed to be more accurate in high latitudes and the graphs also more complete.

A1.4 Tools Based on ITU Methods.

The ITU has established the following methods which are used extensively and often exclusively for both planning and co-ordination work:

Recommendation ITU-R P.533 (2007): entitled 'Method for the prediction of the performance of HF circuits'. This Recommendation provides methods for the prediction of available frequencies, of signal levels and of the predicted reliability for both analogue and digital modulated systems at HF, taking account not only of the signal to noise ratio but also of the expected time and frequency spreads of the

channel. The Annex of the Recommendation contains the method to be used for the prediction of sky-wave propagation at frequencies between 2 and 30 MHz. This method is described in some detail in the case study of chapter 2.

Recommendation ITU-R P.1239 (1997) entitled ITU-R Reference Ionospheric Characteristics was established for the prediction of long-term ionospheric characteristics to meet the need of prediction methods for radio-circuit design, service planning and frequency band selection. In this Recommendation expressions are provided for the evaluation of the monthly median of f_0F_2, $M(3000)F_2$, f_0E, f_0F_1, $h'F$ and $h'F_2$ and of the monthly median, upper decile and lower decile of f_0E_s and f_bE_s. Also included are representations of the percentage of occurrence of spread-F.

Recommendation ITU-R P.1240 (1997) entitled ITU-R Methods of basic MUF, Operational MUF and Ray Path Prediction is based on the maps of ionospheric characteristics as given in Recommendation P.1239. This Recommendation gives formulations for the prediction of basic and operational MUF and formulations for the prediction of ray paths.

Recommendation ITU-R P.534 (1999) entitled ITU-R Method for Sporadic-E field strength sets out a statistical method for calculating the field strength of signals propagated by means of ionospheric sporadic-E_s at VHF and, possibly, at higher portions of the HF bands, for distances up to 4 000 km. The calculation is based upon the fact that the field strength is very closely correlated with f_oE_s, that is to say, the critical frequency of sporadic-E layer at vertical incidence at the path mid-point. The data provided by the Recommendation are restricted to geomagnetic latitudes between

±60° and a warning is given that caution should be exercised if this method is used in the high latitude regions.

FTZ: This model was developed by the Deutsche Bundespost (Ochs, 1970). It includes an empirical representation of field strength. This method is based upon observations of signal level associated with a large number of circuit-hours and paths, with the majority of the paths terminating in Germany. Since data was obtained without accounting for the individual modes that may have contributed to the result, the model is not fully satisfactory for arbitrary antennas (and patterns). Nevertheless for long-distance communication where elevation angles are minimized, the model is quite useful and still used to this day. Because the modelling computations require a limited amount of machine time, the FTZ model proved to be a valuable method for preliminary screening of a large number of paths. The data collected in this work was used in the three ITU Recommendations mentioned above.

MINIFTZ4: Created by the German FTZ Darmstadt amateur radio club in 1987, the program used tables from the ITU atlas of ionospheric characteristics to generate a field strength prediction for a specified circuit. In 1989 it was improved to predict the MUF. Like its predecessor, MINIMUF, it uses a grid point method to obtain critical frequencies from the ITU noise database and uses interpolation to obtain the spatial and temporal data for making predictions. It is claimed to give a better representation of the ITU-Atlas data for 3 000 km MUFs than does MINIMUF which is plausible as it takes into account the SSN, the time, the antenna gain and power.

HAMFTZ: Created in 1994 by Cedric Baechleris, this program is based on MINIFTZ 4.3. and uses thus the same inputs (SSN, the time reliability, the antenna

gain and power) to calculate the MUF, FOT, LUF and signal strength between two points. It creates two tables, the signal strength in S-unit and modes and takeoff angles.

PP: Standing for Propagation Prediction, this program was written in 1991 by Bernhard Büttner and updated in 2000. Based on MINIFTZ, this program predicts propagation conditions between 2 and 50 MHz. From the fundamental data of a circuit, date, home and target location, power, antenna gain, takeoff angle, path (long/short), and reliability (10%, 50%, 90%), PP provides several screens function of the time and frequency (MUF, LUF, FOT, signal and field strength expressed in various units including S-unit). Moving the cursor on curves the field strength can be displayed.

ASAP: This stands for Advanced Stand Alone Prediction System Developed and was developed by IPS Radio and Space Services, which is part of the Australian Department of Industry, Tourism and Resources. It is based on the ITU P.533 and ITU/CCIR Report 322 (now encompassed in ITU-R P.372) but with modifications. ASAPS HF predictions can be generated based on one of three indices:

- IPS ionospheric T-index;
- 10.7 cm flux;
- sunspot number.

The T Index is an indicator of the effect of solar activity on F region frequencies and was developed by IPS investigators and draws on a previously developed GRAFEX prediction method. The T index is an indicator of the critical frequency (f_oF_2), and the higher the value of the T indexes, the higher the value of the maximum usable frequency. The T Index has the same general scale of the sunspot number. A database

of monthly ionospheric T-indices is supplied with the software and can be updated each month, based on information given in the IPS monthly Solar and Geophysical Summary, and may be updated automatically via the web. The T index can be best regarded as an "equivalent sunspot number" - the sunspot number which would best match the observations made by ionosondes. IPS has a large network of ionosondes and believes that they can derive the most appropriate T index.

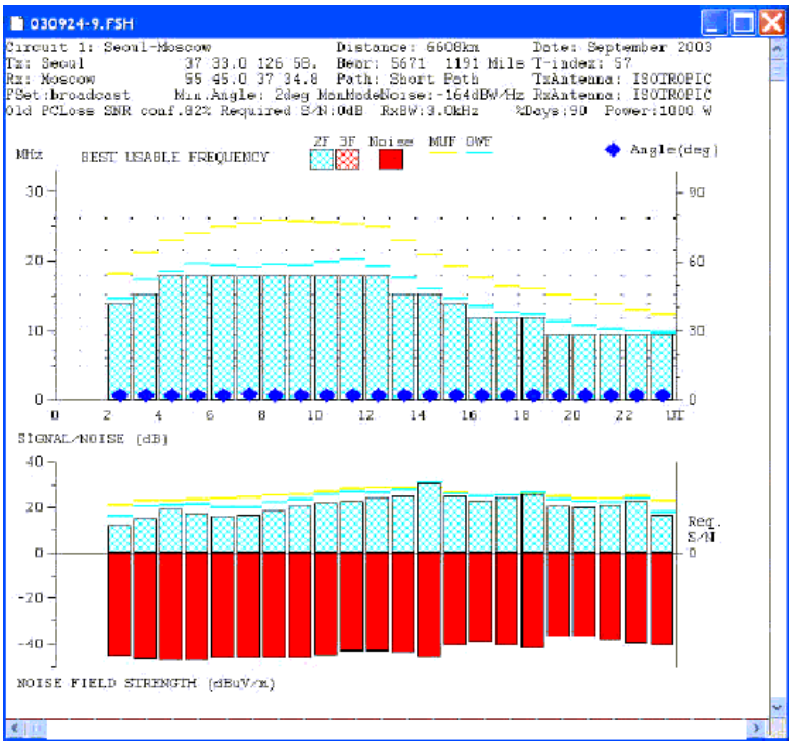

Figure 126. Example of ASAPS output.

PropWiz: This is short for Propagation Wizard and is produced by Rohde & Schwarz. It calculates the field-strength at the receiver location by means of a "MUF" program, determination of the man-made noise, atmospheric noise and galactic noise at the receiver location by means of ITU/CCIR recommendations, calculation of the signal-to-noise-ratio considering the bandwidth, the receiver noise and the Rx antenna gain and comparison of the calculated signal-to-noise-ratio with the required signal-to-noise-ratio for the used modulation.

It takes into account the date (year and month), SSN only, transmitter power, transmit and receive antenna gain, takeoff angle, noise figure at receive, ground properties, and SNR. While available information is lacking, it appears that this programme is an extensive implementation of all the ITU methods and recommendations.

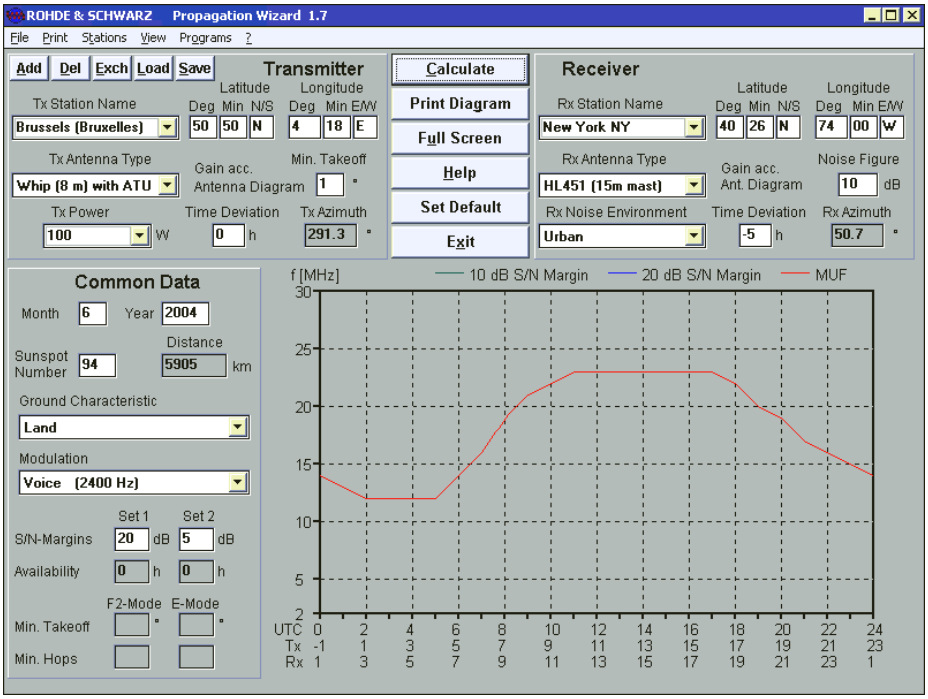

Figure 127. Example of output from Prop Wiz

A1.5 Other Planning Tools

None of the programs listed below use the VOACAP engine, any form of the IRI model or any of the ITU methods. Most of these applications display only a limited number of parameters, the MUF and LUF for either a specified circuit or at a global scale. Some programs provide in addition a point-to-point prediction with a relative indication of field or signal strength or SNR at the target location.

The most recent programs, designed especially for Windows 32-bit platforms, are however more complete, providing for example either critical frequencies or downloading from the Internet space weather bulletins, alerts or images dealing with the current solar and geomagnetic activity.

MINIMUF: In December, 1982, MINIMUF-3.5 (Rose, Martin and Levine, 1978)(Rose, Martin, 1978), developed by the U.S. Naval Ocean Systems Center, appeared in an amateur radio magazine (Rose, 1982). Although it used an incorrect algorithm for control points that are in midnight sun conditions (Shalon, 1983) (Rose, 1984) and for some control points that are in polar night conditions, MINIMUF, for the first time, made practical the prediction of F-layer MUF on microcomputers.

This is a simplified prediction program for the maximal usable frequency (MUF) along an HF propagation path. The model is based on a large number of oblique ionograms from a wide variety of sounding paths. Given the date, transmitter and receiver locations, and the solar flux index or sunspot number, hourly MUF values can be obtained. This is the very widely released and copied ionospheric model for the first IBM PC computers and is a short Basic program with only 242 lines of code (Rose, 1982).

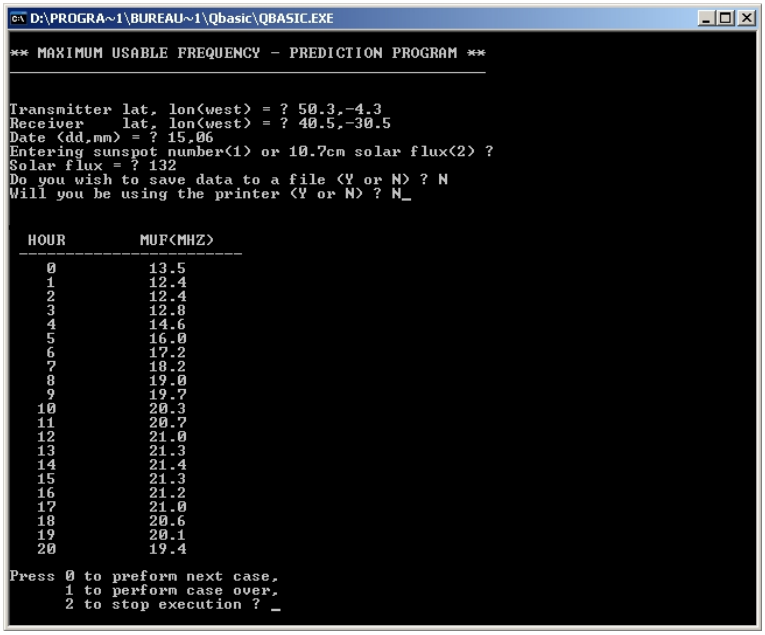

Figure 128. Example of MINIMUF text output.

DXProp/HFProp: Written by Christian Ramade, DXProp and PropHF are both based on the algorithm used by MINIMUF 3.5 and predict the MUF from the Solar Flux Index (SFI), date and time, the transmitter and target locations. The MUF is determined by hop-testing between transmitter and the target location until the radiation angle and the calculation stops in the vicinity of the receiver.

Ionospheric absorption, signal attenuation and the delay of propagation is calculated taking into account the emitted power, frequency of transmission, and antenna gain of the transmitter station. Interestingly the minimum signal level is fixed to a sensitivity of -123 dBm (or 0.15 mV into 50 ohms), common to all professional and semi-professional receivers. The difference between the two programs is the presentation of the predictions.

IONPRED – The Fricker Method: Raymond Fricker from the BBC Worldservice created this propagation program in the 1980's that included a new scheme of hop-testing. Essentially, the program looked at each hop in detail at the points where the E-layer is crossed and at the highest point where the critical frequency of the F-region is important. The hop-testing involves determining whether the mode is reliable by seeing if operating frequency is above or below the E-cutoff frequency by 5% and less than the critical frequency for F-region propagation by 5% (Fricker, 1987).

With an initial choice of radiation angle, the path structure can be sorted according to E- and F-hops, depending on the outcome of the tests along the way. Fricker also adjusted the height of the F-region according to local time so hop lengths are not constant along a path. As a result, the path could over- or under-shoot the target area. If the error is more than 25 km, another radiation angle is chosen and the process starts again. IONPRED also calculates the ionospheric absorption expressed in dB, and adds that to the signal loss due to spatial spreading or attenuation and ground reflections.

HFProp: Developed in 2000 by Julian Moss, the GUI is user-friendly and is a very simple and light propagation program (~700 KB) which takes into account the solar flux or the smoothed sunspot number and planetary indices. HFProp uses Fricker's F2-layer prediction model. The latest version released also includes provision for connection to the Internet for automatic updates of the current solar flux and K index.

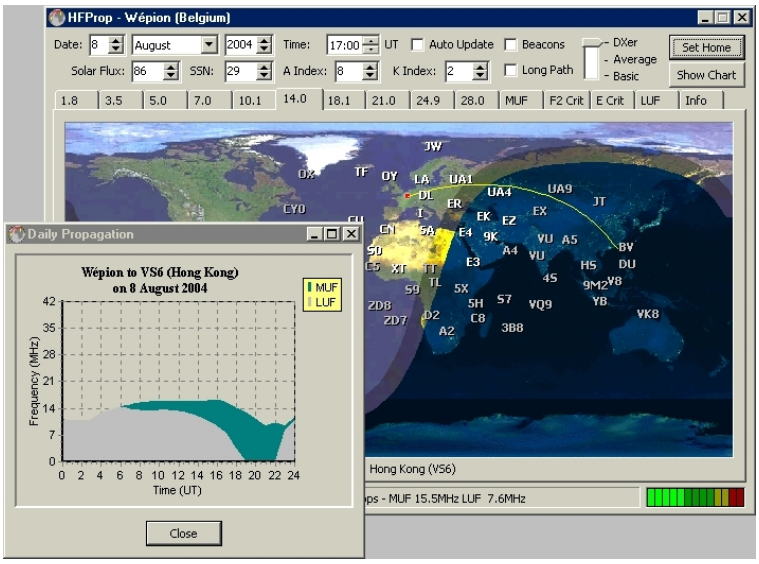

Figure 129. Example of the output of HFProp.

AMBCOM: This program was developed by SRI International in connection with work supported by the Defense Nuclear Agency, and is a companion program to NUCOM, another propagation program specific to the nuclear environment (Hatfield,1980). One difference between the NTIA/ITS series of programs and AMBCOM is that the latter uses a 2-D raytrace program, while the former programs use virtual methods. In addition, AMBCOM contains within its ionospheric submodel structure a considerable amount of high latitude information including auroral absorption models. This should provide for an improved prediction capability for paths through the high-latitude region or within its neighbourhood. A major distinction between AMBCOM and virtual methods used by the ITU is that the ionosphere defines the path of the ensemble of rays in AMBCOM, whereas a predetermined path is used to define the effective part of the ionosphere (i.e., the "control point") in the virtual or "mirror" methods.

AMBCOM documentation is not freely available and appears to be mainframe based. The performance of AMBCOM has been examined in one in a series of studies,

conducted at the Naval Postgraduate School, to establish the relative merits of several computer-based propagation prediction models using a standard set of measured data (Wilson, 1991). AMBCOM was used to model the propagation path between a transmitter located in the polar cap region and several mid-latitude receiver sites. Model predictions were matched to measured data obtained during two high-latitude communication experiments (campaigns). The absolute difference between model signal-to-noise ratio (SNR) and measured SNR was considered as error. AMBCOM exhibited small absolute values of average error, i.e., 7-11 dB, and high percentages of matched records. The average error was typically distributed between -20 and +20 dB.

HF-PROP: Written by Mike Harris in 2002. From the home and target location, the solar flux (SFI) and K-index it only predicts the MUF and LUF for the specified path, but nothing else. It is aimed at yacht enthusiasts whose needs are for a first guess of which frequencies it might be possible to receive weather fax transmissions on.

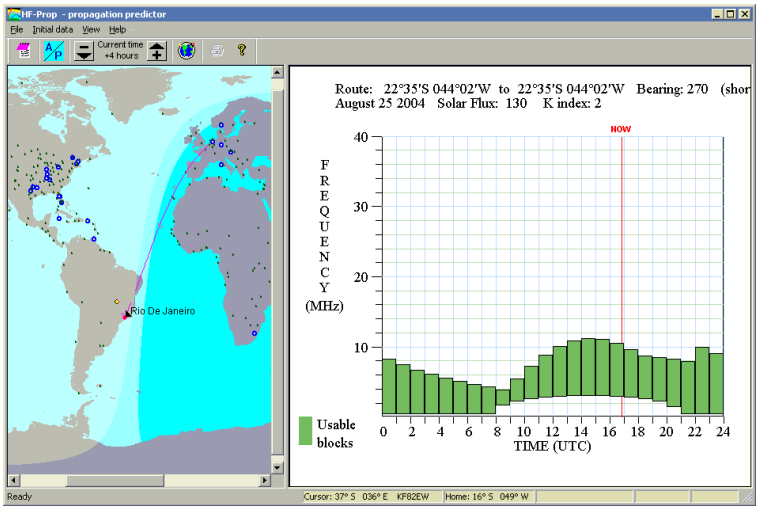

Figure 130. Example of HF-Prop output.

PROPHET: Very little information is freely available on this program. There are restrictions on use of Prophet, according to the U.S. Navy: *The Advanced Prophet system contains information and capability subject to the International Traffic in Arms Regulation (ITAR) or the Export Administration Regulation (EAR) of 1979, which may not be exported, released, or disclosed to any foreign nationals inside or outside the United States without express permission from Chief of Naval Operations under any circumstances.* A request to the Navy Modelling and Simulation Management Office (NAVMSMO), the current system managers for a copy of Prophet, was politely refused.

The performance of PROPHET has been examined in one in a series of studies, conducted at the Naval Postgraduate School, to establish the relative merits of several computer-based propagation prediction models using a standard set of measured data (Gikas, 1991). A 'Noncentric' database of collected high-latitude signal and noise measurements was obtained during 1988 and 1989 by the University of Leicester, U.K. The Advanced Prophet 4.0 HF Ionospheric Propagation Prediction Code was exercised and compared to a portion of the 'Noncentric' database for a transmitter at Clyde River, Canada and a receiver at Leicester, U.K. The Prophet predictions were better during winter months than during summer months. Overall, 70% of the signal strength data from Prophet 4.0 were between -20 dB and +20 dB error, compared to the measured data.

W6ELProp: Written by Sheldon C. Shallon in 2001 this point-to-point model, which takes into account a basic communication circuit, is able to predict the status of the ionosphere on frequencies between 3 and 30 MHz. Inputs include transmitter and

target locations, the SFI (SSN as an alternative), K-index, noise at target location, noise bandwidth and minimum takeoff angle. W6ELProp takes into account the D-, E-, and F-layers of the ionosphere to calculate receiver signal strengths. MUF calculations use Raymond Fricker's F-layer method developed in 1985 combined with the E-layer method developed by the ITU (then the CCIR) in 1983.

SNAPMax: To support his book, "The Friendly Ionosphere", the author, Crawford MacKeand, wrote this short program, updated in 2001, to assist in the practical exercises. While less than 300 KB with all data, it is one of the few programs that predict propagation conditions in the band 1.5 to 45 MHz. SNAPMax takes into account an approximate MF algorithm and gyro-frequency for medium wave propagation. In addition, terrestrial reflection points are checked to take correct account of reflection from lands and oceans for ground-wave coverage calculations, and E-layer paths are also assessed. The Ap or Kp index is used to determine polar path auroral losses, as well as MUF depression during storm events. MUF is determined using Fricker's algorithms, losses being determined by George and Bradley's method using an internal world-wide vertical absorption map.

MINIPRO: Developed in 1985 by Sheldon C. Shallon, it combined the prediction of signal levels, F-layer MUF with corrections over MINIMUF 3.5 for the midnight Sun and polar night conditions. At the same time, improved ionospheric propagation models were acquired from several sources, in particular, a superior F-layer model based on the F-region method used by Raymond Fricker in IONPRED. The original product was improved and evolved to MINIPROP Plus and version 2. It included then the E-layer cutoff frequency, a gray-line map and an approximate auroral oval. A version has also been developed for Windows.

MICROMUF: This is a small program of 158 lines of code written in 1984 by Raymond Fricker (BBC World Service). MICROMUF calculates the MUF and LUF using only the SSN as input. The program was improved by Hans Bakhuizen, Technical Policy Adviser of Radio Netherlands. Contrary to MINIPROP, in MICROMUF the E-cutoff is associated to the LUF, although the LUF is normally considered to be a D-region matter. It uses Fricker's "mini F-region" algorithm constituting 13 mathematical functions (instead of only one in MINIMUF) to simulate the ITU database for the critical frequency.

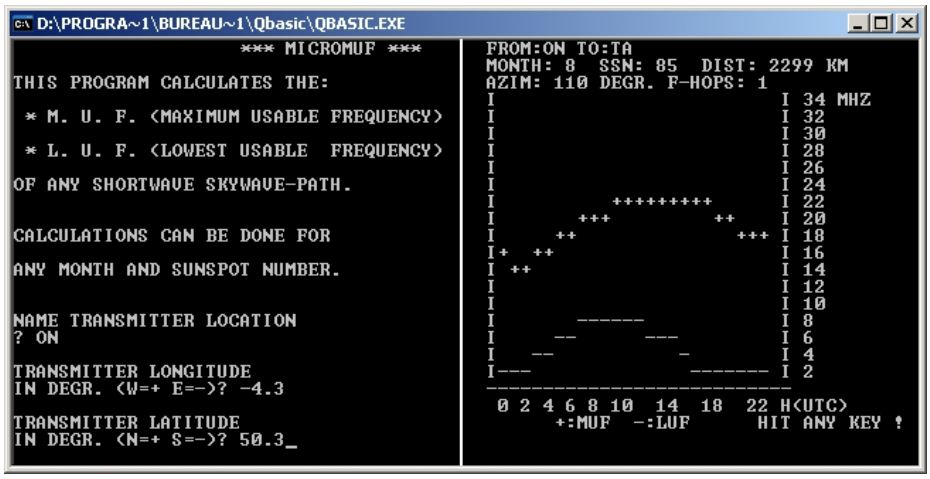

Figure 131. Example of text output from MICROMUF

A1.6 Appendix Summary

This appendix has examined a number of propagation prediction and planning tools used to predict:

- The condition of the ionosphere in terms of Electron Density at different heights. The backbone of these programs is a climatological or monthly median ionospheric model, which does not account for short-term variability;

- The parameters required for use in radio communications (MUF, LUF, Ray path, hops, etc).

The tools have been classified into three different categoties:

a. Tools based on IONCAP/VOACAP;
b. Tools based on ITU methods;
c. Other tool not covered by a) or b) above.

While a few of the tools can be adapted to real-time and short-term forecasting the majority are used for long-term planning purposes. For example, based on the requirements of users and the international regulatory structure long-term predictions are likely to be required for broadcast planning for some time to come. They are also worthwhile for system studies and planning for military operations.

The empirical basis of many methods are formulated taking into account mid-latitude data and hence do not include adequate transmission loss calculations to deal with high-latitude features, with the notable exceptions of AMCOM, and ICEPAC. Although most of the tools listed have crudely taken some high-latitude features (e.g. auroral absorption) into account, the following have not been included in the calculation of basic circuit reliability:

- Sudden ionospheric disturbances;
- Polar cap absorption (Solar proton events);
- Geomagnetic storms;
- Ionospheric Storms (effects of plasma clouds);
- Short wave fadeout;
- Blackouts.